Proceedings

ASPE 2015 Spring Topical Meeting

Achieving Precision Tolerances in Additive Manufacturing

April 26-29, 2015

American Society for
Precision Engineering

P.O. Box 10826, Raleigh, NC 27605-0826
(919) 839-8444 | Fax (919) 839-8039

Proceedings of

Achieving Precision Tolerances in Additive Manufacturing

ASPE Spring Topical Meeting

April 26-29, 2015

North Carolina State University
Raleigh, North Carolina, USA

The American Society for Precision Engineering (ASPE) is a multidisciplinary professional and technical society concerned with research and development, design, manufacture and measurement of high accuracy components and systems. ASPE activities encompass relevant aspects of mechanical, electronic, optical and production engineering, physics, chemistry, and computer and materials science. Membership is open to anyone interested in any aspect of precision engineering.

Founded in 1986, ASPE provides a new focus for a diverse but important community. Other professional organizations have covered aspects of precision engineering, always as a sideline to their principal goals. ASPE is based on the core of generic concepts necessary to achieve precision in any application; independent of discipline, ASPE intends to be the focus for precision technology, and to represent all facets from research to application.

ASPE – The American Society for Precision Engineering
301 Glenwood Avenue, Suite 205, Raleigh, NC 27603
P.O. Box 10826, Raleigh, NC 27605
Telephone: (919) 839-8444 Fax (919) 839-8039
Web site: aspe.net

Preface

This book comprises the proceedings of the ASPE 2015 Spring Topical Meeting entitled **Achieving Precision Tolerances in Additive Manufacturing**. The contributions reflect the authors' opinions and are published as presented to ASPE without change. Their inclusion in this publication does not necessarily constitute endorsement by the ASPE or its editorial staff.

Individual readers of this book and nonprofit libraries acting for them are permitted to make fair use of the material contained in this book to be used in teaching or research; provided they copy said paper in total, as written by the author. Permission is granted to quote excerpts from the scientific or technical works in this book with proper acknowledgment of the source to include: The author's name, the book name, and the ASPE tag line. Reproduction of figures and tables is likewise permitted from the contents of this book, provided that the same acknowledgment of the same source and content is permitted.

Any other type reproduction, systematic copying or multiple reproduction of any material in this book is expressly prohibited except with the written permission of the ASPE editorial staff, addressed to the Society's headquarters.

ISBN 978-1-887706-67-4

2015

American Society for Precision Engineering
301 Glenwood Avenue, Suite 205
Raleigh, NC 27603

Printed in the United States of America

Table of Contents

Preface ii

Contents iii

Schedule iv

Foreword v

Meeting Sponsors vi

Sustaining Corporate Sponsors vii

Corporate Sponsors viii

Tutorials . . . . . ix - xi

Technical Paper Index . . . . . xii - xvi

Technical Papers . . . . . 3 - 169

Author Index . . . . . 171 - 172

Program & Schedule

	Sun., April 26 Engineering Bldg III (EB III)		Mon., April 27 Hunt Library Auditorium, Rm 1103 *(unless otherwise noted)*		Tues., April 28 Hunt Library Auditorium, Rm 1103 *(unless otherwise noted)*		Wed., April 29 Hunt Library Auditorium, Rm 1103 *(unless otherwise noted)*
7:00	Registration and Continental Breakfast						
		7:30	Registration and Continental Breakfast	7:30	Registration and Continental Breakfast	7:30	Registration and Continental Breakfast
8:00	**KUHN TUTORIAL** EB III, Room 2232 **LEACH TUTORIAL** EBIII, Room 2236	8:30	**WELCOME** **DEAN OF NCSU ENGINEERING** LOUIS A. MARTIN-VEGA **OPENING REMARKS & SESSION I** PLENARY 1	8:30	**SESSION III** DESIGN AND OPTIMIZATION	8:30	**SESSION VII** PROCESS VALIDATION AND OPTIMIZATION
10:00	Coffee Break						
10:30	**KUHN & LEACH TUTORIALS** CONTINUED	10:30	Coffee Break	10:35	Coffee Break	10:35	Coffee Break
		11:00	**SESSION II** PLENARY 2	11:05	**SESSION IV** IN PROCESS SENSING	11:05	**SESSION VIII** CT METROLOGY OF AM COMPONENTS
12:00	Lunch EB III, Room 3120	12:30	Boxed Lunch Outside or Rooms 4101, 4105	12:45	Boxed Lunch Outside or Room 4105	12:00	Lunch On-Your-Own *(See List in Registration Package)*
1:30	**KUHN/VAN KEULEN TUTORIAL** EB III, Room 2232 **BAUZA/BROWN TUTORIAL** EBIII, Room 2236	2:00	**COMMERCIAL SESSION**	2:15	**SESSION V** Modeling and Microstructure	1:30	**SESSION IX** CONVERGENCE TO TIGHT TOLERANCES
3:15	Coffee Break					3:00	Coffee Break
3:45	**KUHN/VAN KEULEN** **BAUZA/BROWN TUTORIALS** CONTINUED	3:45	Coffee Break & **TECHNICAL POSTER & NETWORKING** Rooms 4101, 4105	3:55	Coffee Break	3:15 4:15	**SESSION IX** Continued
5:30		5:15		4:25	**SESSION VI** Characterization of Surface Finish	4:30	**Panel Discussion** What Did We Learn? *End of Conference*
				5:40		5:00	
6:00	**WELCOME RECEPTION** EB III Atrium	6:30	**DINNER AT CITY CLUB RALEIGH** 150 Fayetteville Street Raleigh, NC 27601 *Attire is Business Casual*		Free Evening		**INFORMAL CLOSING RECEPTION** 6:00 PM Clouds Brewing 126 N West St. Raleigh, NC 27603
8:00		9:00					

Foreword

The Second ASPE Topical Meeting on **Achieving Precision Tolerances in Additive Manufacturing** will be held in the auditorium of the James B. Hunt Jr. Library, located on the Centennial Campus of North Carolina State University.

This series of Topical Meetings on dimensional accuracy and surface finish is crucial to putting additive manufacturing (AM) onto the factory floor. The topics highlighted during this Meeting are as follows:

- Dimensional Accuracy and Surface Finish
- Design for Manufacturing
- Heat Treatment for Achieving Dimensional Tolerances
- Secondary Machining, Grinding and Polishing
- Characterizing the Performance of AM Machines
- Machine Capabilities and Standards
- Integrating AM into Manufacturing Processes
- In situ Process Metrology
- Metrology of External and Internal Features

The program will feature 4 tutorials, technical sessions with invited talks, a poster session, a commercial session, a panel discussion and many networking social events, including a dinner. We encourage presentations of a tutorial nature which elaborate principles essential to achieving high performance. We aim to bring together specialists and practitioners from industry, government, and academia for the exchange of ideas and to identify topics for further research.

Meeting Co-Chairs

John S. Taylor, Lawrence Livermore National Laboratory
Shawn P. Moylan, National Institute of Standards and Technology
Thomas A. Dow, North Carolina State University
Richard K. Leach, University of Nottingham, UK

Organizing Committee:

Vivek G. Badami, Zygo Corporation
Marcin B. Bauza, Carl Zeiss Industrial Metrology
Christopher A. Brown, Worcester Polytechnic Institute
Pete J. Fitsos, Lawrence Livermore National Laboratory
Hans N. Hansen, Technical University of Denmark
Ola L. A. Harrysson, North Carolina State University
Edward D. Herderick, GE Aviation
Allister W. James, Siemens Energy, Inc.
Bradley H. Jared, Sandia National Laboratories
Wayne E. King, Lawrence Livermore National Laboratory
Howard A. Kuhn, University of Pittsburgh
Thomas R. Kurfess, Georgia Institute of Technology
Yu Liu, Chengdu Green Energy and Green Manufacturing Technology R&D Center
Stephen J. Ludwick, Aerotech, Inc.
Andreas Fischer-Ludwig, Siemens Energy AG
Antonius T. Peijnenburg, VDL Enabling Technologies Group
Alexander H. Slocum, Massachusetts Institute of Technology
Fred van Keulen, Delft University of Technology

Sponsors of the

ASPE 2015 Spring Topical Meeting

on

Achieving Precision Tolerances in Additive Manufacturing

ASPE gratefully acknowledges the generous contributions by the following sponsors:

Thank you to

VDL Enabling Technologies Group

For sponsoring the Closing Reception

Closing Reception

Wednesday, April 29, 2015

6:00 PM

Clouds Brewing

126 N. West St, Raleigh, NC 27603

(located in Downtown Raleigh and within walking distance of downtown hotels)

ASPE 2015 Sustaining Corporate Sponsors

3M Company
St. Paul, MN 55144
Phone: (888) 364-3577
www.mmm.com

Aerotech, Inc.
101 Zeta Drive
Pittsburgh, PA 15238-2897
Phone: (412) 963-7470
www.aerotech.com

Ametek Precitech, Inc.
44 Blackbrook Road
Keene, NH 03431
Phone: (603) 357-2511
www.precitech.com

Carl Zeiss Industrial Metrology LLC
6250 Sycamore Lane North
Maple Grove, MN 55369
Phone: 763-744-2400
www.zeiss.com/metrology

Chardon Tool
115 Parker Court
Chardon, OH 44024
Phone: (440) 286-6440
www.ChardonTool.com

Cranfield Precision
Division of Fives Landis Ltd.
Woburn House
3 Adams Close
Kempston, Bedford, MK42 7 JE
United Kingdom
Phone: +44 (0)1234 312820
www.cranfieldprecision.com

Keysight Technologies
5301 Stevens Creek Boulevard
Santa Clara, CA 95051
Phone: (408) 553-7975
www.keysight.com

Lion Precision
563 Shoreview Park Road
St. Paul, MN 55126-7014
Phone: (651) 484-6544
www.lionprecision.com

Makino
7680 Innovation Way
Mason, OH 45040
Phone: (513) 573-7200
www.makino.com

Mitutoyo America Corporation
945 Corporate Boulevard
Aurora, IL 60504-9102
Phone: (630) 723-3619
www.mitutoyo.com

Moore Nanotechnology Systems LLC
230 Old Homestead Highway
Swanzey, NH 03446
Phone: (603) 352-3030
www.nanotechsys.com

Professional Instruments Company
7800 Powell Road
Hopkins, MN 55343
Phone: (952) 933-1222
www.airbearings.com

ASPE 2015 Corporate Sponsors

ADCOLE Corporation
669 Forest Street
Marlborough, MA 01752
Phone: (508) 485-9100
www.adcole.com

Alicona
1261 Humbracht Circle
Suite G
Bartlett, IL 60103 USA
Phone: (630) 372-9900
www.alicona.com

Contour Fine Tooling, Inc.
143 Jaffrey Road
Marlborough, NH 03455
Phone: (603) 876-4908
www.contour-diamonds.com

Center for Precision Metrology
University of North Carolina at Charlotte
9201 University Blvd.
Charlotte, NC 28223
Phone: (704) 687-8499
cpm.uncc.edu/

Corning Inc.
Corning, NY 14831
Phone: (607) 974-3842
www.corning.com

K & Y Diamond
2645 Diab St. Laurent
Quebec H4S 1E7
CANADA
Phone: (514) 333-5606
www.kydiamond.ca

Philips Innovation Services
High Tech Campus 7
5656 AE Eindhoven
The Netherlands
31-40-27-48060
www.innovationservices.philips.com

Specialty Components, Inc.
14 Village Lane
Wallingford, CT 06492
Phone: (203) 284-9112
www.specialtycomponents.com

VDL Enabling Technologies Group USA
3758 Spinnaker Court
Fremont, CA 94538
(510) 996-4660
www.vdletg.com

Zygo Corporation
Laurel Brook Road
Middlefield, CT 06455-0448
Phone: (860) 347-8506
Toll-free: (800) ZYGO-NOW
www.zygo.com

Tutorials

Tutorials will be held on Sunday, April 26 in the Engineering Building III on NCSU's Centennial Campus. For Regular Participants, tutorials are $275 each and for Student Participants, tutorials are $165 each.

Tutorial 1, Sunday, April 26, 2015

8:00 AM - 12:00 Noon

Dr. Howard A. Kuhn, University of Pittsburgh
Engineering Building III, Room 2232

Additive Manufacturing Fundamentals

The basics of additive manufacturing (AM) will be presented to provide essential information for design decisions. In particular, an engineering overview will explore the essential features of the seven primary classes of AM processes, as defined by ASTM: 1) Extrusion (fused deposition modeling); 2) Polymerization (stereolithography); 3) Lamination (layered object modeling); 4) Material Jetting (multi-jet modeling); 5) Powder Bed Fusion (selective laser sintering, selective laser melting, electron beam melting); 6) Powder Bed Binder Jetting; 7) Directed Energy Deposition (powder and wire) by laser and electron beam; plus 8) Hybrid processes (additive and subtractive).

For each process we will describe the pertinent fundamental science and analyses underlying each unit process and their effects on quality of the finished product – dimensional accuracy, repeatability, distortion, surface finish and feature resolution. Polymers, metals, and ceramics used in each process will be listed along with their test properties and the effects of setup and process parameters on their functional properties. In addition, geometric flexibility and limitations of the AM processes will be illustrated through application examples in mechanical structures, energy components, transportation vehicles and propulsion, medical and dental devices, direct write electronics, art and architecture, and consumer goods. Considerable attention will be given to applications of additive manufacturing of tooling for conventional processes, such as machining, sand casting, investment casting, composite forming, and injection molding. Case studies will be presented to illustrate the impact of this approach on design of parts for conventional processes.

Tutorial 2, Sunday, April 26, 2015

8:00 AM - 12:00 Noon

Dr. Richard K. Leach, University of Nottingham
Engineering Building III, Room 2236

Surface Topography Measurement and Characterisation

The seminar will discuss the fundamental principles of surface topography measurement. Profile analysis and the stylus method will be presented, including the most common ISO parameters. Common optical instruments and their limitations will briefly be presented. Lastly, the basics of areal characterisation will be discussed. The seminar will mainly focus on principles which are covered by ISO specification standards.

Tutorial 3, Sunday, April 26, 2015

1:30 PM - 5:30 PM

Dr. Howard A. Kuhn, University of Pittsburgh
Dr. Fred van Keulen, Delft University of Technology
Engineering Building III, Room 2232

Design for Additive Manufacturing (Howard A. Kuhn)

This tutorial will apply lessons learned from the fundamentals of each additive manufacturing process to construct a concurrent product and process design methodology. Considerations of materials, processes, and geometry will be integrated into a framework supporting product design. Methodologies for initial material and process selection will be presented. Sources of distortion, warping and delamination as well as micro-cracks and porosity will be reviewed, leading to design guidelines for product design and process specification for sound structures. Attention will also focus on design for function and tooling applications using current additive manufacturing processes augmented by innovative functional gradient materials, gradient meta-structures, and embedded systems. Advanced analytical models will be presented that enable prediction of distortion, microstructure, and properties. Use of these models for in-process quality control systems will also be described. Geometric design for additive manufacturing through topology optimization and shape optimization will be introduced.

Topology Optimization (Fred van Keulen)

After pioneering research in the late eighties, topology optimization gained major interest from the structural optimization community. In contrast to size- or shape optimization, with topology optimization the layout of a structure is optimized. Topology optimization typically leads to complex 3D architectures which can only be manufactured economically with traditional techniques after rigorous re-engineering and simplification. However, these complex 3D architectures are in general easy to manufacture using additive manufacturing techniques. Another perspective is to look at topology optimization as a design tool which will help to gain the maximum benefit from additive manufacturing. In this tutorial the basics of topology optimization will be explained. Aspects which will be discussed are selection of design variables, (adjoint) sensitivity analysis, checker boarding, solution techniques and formulation of the optimization problem. The tutorial will provide examples showing the capabilities and also pitfalls of the method.

Tutorial 4, Sunday, April 26, 2015

1:30 PM - 5:30 PM

Dr. Marcin B. Bauza, Carl Zeiss Industrial Metrology
Christopher A. Brown, Worcester Polytechnic Inst.
Engineering Building III, Room 2236

Metrology of Parts Made Using Additive Processes (Marcin B. Bauza)

Additive manufacturing (AM) shows significant promise towards revolutionizing discrete parts manufacturing. Traditional subtractive manufacturing offers a variety of capabilities which can be carried out at a high level of precision, however the range of shapes that can be produced is limited by the access of cutting / abrasive tools to designed features. With AM, forms and shapes that once were difficult or impossible to achieve with subtractive manufacturing are now feasible enabling a new level of design freedom. With increased complexity of AM parts the metrology and inspection requirements are changed as well, focusing less on increasing accuracy and more on the ability to access and properly measure internal and external AM features. Simultaneously dimensional tolerances are becoming more critical, therefore ensuring the part quality becomes necessary. Latest techniques for AM metrology will be discussed, including tactile, optical, and high accuracy and high speed CT.

Topographic Measurement and Multi-scale Geometric Analyses for Additive Manufacturing (Christopher A. Brown)

This section of the tutorial covers measurement experience by scanning laser confocal microscopy of AM parts, as well as analyses using scale dependent geometries properties. The objectives are to find correlations with and to discriminate between topographies and their processing conditions and their performance. These objectives support the design of processes and products, as well as quality control and assurance. Examples for scale based analyses of length, area, filling and curvature include highly confident discrimination and strong, scale-specific correlations with fatigue limit, friction, and adhesion for conventional manufacturing. Examples of measurements and analyses of FDM and laser sintered will be presented as well. The use of analysis software for scale specific discrimination and correlation will be reviewed and developments proposed. A broader perspective on scale and surface metrology, which goes beyond the limitation of current standards, will used to provide a scientifically logical basis for understanding the methods and results presented.

Technical and Poster Sessions

Session I
Welcome & Opening Remarks & Plenary 1
Monday, April 27, 2015, 8:30 AM - 10:30 AM

Session Chair: John S. Taylor, Lawrence Livermore National Laboratory and
Shawn P. Moylan, National Institute of Standards and Technology

1. **Digital Photonic Production... Opportunities and Challenges in Gas Turbine Manufacturing**
   Khanna, M. (Siemens Energy, Inc.) 3
2. **Progress In Additive Manufacturing**
   Herderick, E. C. (GE Aviation). 4
3. **Flexible Manufacturing with an Additive Process Chain: Design, Production and Surface Finish**
   Uhlmann, E.; Rethmeier, M.; Graf, B.; Kersting, R.; Bergmann, A. (Fraunhofer-Institute for Production Systems and Design Technology (IPK)) 5

Session II
Plenary 2
Monday, April 27, 2015, 11:00 AM - 12:30 PM

Session Chair: Thomas A. Dow, North Carolina State University and
Richard K. Leach, University of Nottingham

1. **Typical Requirements for Precision Mechanical Parts in Relation to Additive Manufacturing**
   Peijnenburg, A. T.; Oosterhuis, G.; Goudsmit, F. -W. (VDL Enabling Technologies Group). 10
2. **Considerations for AM Modelling in the Context of Topology Optimization**
   van Keulen, F.; Ayas, C. (Delft University of Technology) 15
3. **3D Systems' Perspective on the Future of Additive Manufacturing**
   Moussa, K.; Nguyen, H.; Tummala, P.; McDonough, J. (3D Systems Corporation) 17

Commercial Session
Monday, April 27, 2015, 2:00 PM - 3:30 PM

Session Chairs: Vivek G. Badami, Zygo Corporation and
Pete J. Fitsos, Lawrence Livermore National Laboratory

Session III

Design and Optimization

Tuesday, April 28, 2015, 8:30 AM - 10:35 AM

Session Chair: Thomas R. Kurfess, Georgia Institute of Technology and Antonius T. Peijnenburg, VDL Enabling Technologies Group

1. **Complexity Isn't Necessarily Free: Opportunities and Challenges in Additive Manufacturing**
   Jared, B. H.; Boyce, B.; Battaile, C. C.; Lim, H.; Tran, H. D.; Robbins, J.; Clark, B. W.; Blacker, T. D. (Sandia National Laboratories) 22

2. **Analysis and Optimization of the Dimensional Accuracy for FDM Parts Manufactured with ABSM30**
   Knoop, F.; Schoeppner, V. (University of Paderborn) 26

3. **Proportional Topology Optimization Method for Frequency Optimization of 3D Printed Parts**
   Wang, X.; Biyikli, E.; To, A. C. (University of Pittsburgh) 32

4. **Long-Term Positioning Effectiveness of Additive Manufactured-Monolithic Double Compound Notch Type Flexure Stage**
   Lee, C.-B.; Tarbutton, J. (University of South Carolina); Lee, S. K. (Gwangju Institute of Science & Technology) 36

5. **Features and Tolerances in Additive Manufacturing – an Extension to the AMF File Format**
   Srinivasan, H.; Harrysson, O. L. A.; Wysk, R. (North Carolina State University) 40

Session IV

In-Process Sensing

Tuesday, April 28, 2015, 11:05 AM - 12:45 PM

Session Chair: Ola L. A. Harrysson, North Carolina State University and Stephen J. Ludwick, Aerotech, Inc.

1. **Development of a Sensor Test Bed for In Process Sensing of Laser Powder Bed Fusion Additive Manufacturing**
   Kelly, S. M.; Boulware, P. C.; Cronley, L.; Firestone, G.; Jamshidinia, M.; Marchal, J.; Stempky, T.; Reichert, C. (EWI) 46

2. **In Situ Monitoring of Laser Powder Bed Fusion Additive Manufacturing Using Digital Fringe Projection Technique**
   Zhang, B.; Land II, W. S.; Ziegert, J. C.; Davies, A. D. (University of North Carolina-Charlotte) 47

3. **Current State and New Developments of Quality Monitoring**
   Leggett, P. (Concept Laser, Inc.) 53

4. **Dimensional Accuracy of Large and Complex Ti-6Al-4V Component Made via Electron Beam Melting**
   Bauza, M. B.; Bhogaraju, R. (Carl Zeiss Industrial Metrology); Kirka, M. M.; Richardson, B. S.; Love, L; Lowe, L. E.; Dehoff, R. R. (Oak Ridge National Laboratory) 54

Session V
Modeling and Microstructure
Tuesday, April 28, 2015, 2:15 PM - 3:55 PM

Session Chair: Howard A. Kuhn, University of Pittsburgh and
Bradley H. Jared, Sandia National Laboratories

1. **Modeling the Metal Additive Manufacturing Process at the Scales of the Part and the Powder**
   King, W. E.; Anderson, A. T.; Ferencz, R. M.; Hodge, N. E.; Kamath, C.; Khairallah, S. A.; Rubenchik, A. (Lawrence Livermore National Laboratory) 58
2. **Study on Additive Manufacturing of Inner Contoured Tools**
   Uhlmann, E.; Bergmann, A.; Gridin, W. (Fraunhofer-Institute Production Systems and Design Technology (IPK)) 59
3. **Mechanical and Microstructure Attributes of Inconel 718 Processed via Electron Beam Melting**
   Kirka, M.; Dehoff, R. R. (Oak Ridge National Laboratory); Medina, F. (Arcam AB); Sames, W. (Texas A & M University). 66

Session VI
Characterization of Surface Finish
Tuesday, April 28, 2015, 4:25 PM - 5:40 PM

Session Chair: Vivek G. Badami, Zygo Corporation and
Marcin B. Bauza, Carl Zeiss Industrial Metrology

1. **Physical Processes Linking Input Parameters and Surface Morphology in Additive Manufacturing**
   Taylor, J. S. (Lawrence Livermore National Laboratory). 70
2. **Characterization of the Optical Surface of Additively Manufactured Lenses**
   Browar, A. E. M.; Green, W. E.; Burns, S. J.; Ellis, J. D. (University of Rochester) 72
3. **Multi-scale Areal Curvature Analysis of Fused Deposition Surfaces**
   Bartkowiak, T. (Poznan University of Technology); Lehner II, J. T.; Hyde, J.; Wang, Z.; Brown, C. A. (Worcester Polytechnic Institute); Pedersen, D. B.; Hansen, H. N. (Technical University of Denmark) 77

Session VII
Process Validation and Optimization
Wednesday, April 29, 2015, 8:30 AM - 10:35 AM

Session Chair: Edward D. Herderick, GE Aviation and
Hans N. Hansen, Technical University of Denmark

1. **Quality Optimized Additive Manufacturing Through Measuring System Analysis**
   Uhlmann, E.; Bergmann, A. (Fraunhofer-Institute for Production Systems and Design Technology (IPK)); John, P.; Kashveko, V.; Gerlitzky, G. (IWF TU Berlin) 83
2. **Testing Workpieces for Selective Laser Sintering**
   Galovskyi, B.; Hausotte T. R. (Friedrich-Alexander Universität Erlangen-Nürnberg) 89

3. **Predicting Color Output of Additive Manufactured Parts**
Eiríksson, E. R.; Pedersen, D. B.; Aanaes, H. (Technical University of Denmark) 95

4. **Progress toward Standardized Additive Manufacturing Test Artifacts**
Moylan, S. P. (National Institute of Standards and Technology) 100

5. **Material Certification Through a Synergistic Experimental Monitoring and Microstructure Modeling Approach**
Elwany, A.; Karaman, I.; Arroave, R. (Texas A&M University) 106

Session VIII
CT Metrology of AM Components
Wednesday, April 29, 2015, 11:05 AM - 12:00 PM

Session Chair: Shawn P. Moylan, National Institute of Standards and Technology and Richard K. Leach, University of Nottingham

1. **Effects of X-ray Interactions and CT Algorithms on the Capability of X-ray CT Metrology of Additive Manufactured Parts**
Bate, D. J. (Nikon Metrology) 110

2. **Assessing Additive Manufacturing Processes with X-Ray CT Metrology**
Villarraga-Gómez, H.; Smith, S. T. (University of North Carolina-Charlotte); Lee, C.-B.; Corbett, T.; Tarbutton, J.; (University of South Carolina) 116

Session IX
Convergence to Tight Tolerances
Wednesday, April 29, 2015, 1:30 PM - 4:15 PM

Session Chair: John S. Taylor, Lawrence Livermore National Laboratory and Andreas Fischer-Ludwig, Siemens Energy, AG

1. **New Opportunities for Part Fidelity Using Hybrid AM + CNC**
Jones, J. (Hybrid Manufacturing Technologies) 122

2. **Post-Process Machining of Additive Manufactured Stainless Steel**
Lane, B. M.; Moylan, S. P.; Whitenton, E. P. (National Institute of Standards & Technology) 123

3. **Challenges in Tolerance Transfer for Additive Manufacturing**
Ameta, G. (Washington State University); Moylan, S. P.; Witherell, P.; Lipman, R. (National Institute of Standards & Technology) 129

4. **Laser Polishing of Laser Additive Manufactured Surfaces Made from Inconel 718 and ASTM F75**
Ross, I.; Kumstel, J.; Bremen, S.; Willenborg, E. (Fraunhofer Institute for Laser Technology ILT) 136

5. **Shape Adaptive Grinding (SAG) of Complex Additively Manufactured Parts**
Beaucamp, A. T.; Namba, Y. Y (Chubu University); Charlton, P.; Jain, S.; Graziano, A. A. (Zeeko Ltd.) 141

6. **Spatial Accuracy of Embedded Surface Coloring in Color 3D Printing**
Pedersen, D. B.; Hansen, H. N.; Eiríksson, E. R. (Technical University of Denmark) 147

Poster Session

Monday, April 27, 2015, 3:45 PM - 5:15 PM

Session Chair: Thomas A. Dow, North Carolina State University and
Marcin B. Bauza, Carl Zeiss Industrial Metrology

1. **In-situ Monitoring of Dimensional Accuracy in Additive Manufacturing by Layerwise Detection of Geometric Errors**
   Aminzadeh, M.; Kurfess, T. R. (Georgia Institute of Technology) 151

2. **Preliminary Study of Corona-Assisted Additive Manufacturing Process of Piezoelectric Thermopolymer**
   Lee, C.-B.; Mahamud, R.; Farouk, T.; Tarbutton, J. (University of South Carolina) 155

3. **Hydrogen Molecule Induced Surface Cross-linking for Enhancing Mechanical Stability of Printed Organic 3D Structure ***
   Liu, Y.; Zhan, H.-R.; Chen, Y.; Deng, Y.; Bao, C.; Lau, W.-M.; Mei, J.; Xu, K.; Tang, C. (Chengdu Green Energy and Green Manufacturing Technology R&D Center); Yan, H. (Beijing University of Technology)

4. **X-Ray Computed Tomography for the Characterisation of Pores in an Additive Manufacturing Process**
   Maskery, I. (University of Nottingham). 159

5. **Model – Support Material Interaction Inspection by X-ray Computed Tomography in FDM Additive Manufacturing Process**
   Ruiz-Huerta, L.; Caballero-Ruiz, A.; Vega-Alvarado, L.; Yañez-Sanvicente, R.; Castro-Espinosa, H. (Universidad Nacional Autónoma de México) 160

6. **Dimensional Metrology of Complex Inner Geometries Built by Additive Manufacturing**
   Villarraga-Gómez, H.; Smith, S. T. (University of North Carolina-Charlotte); Lee, C.-B.; Tarbutton, J. (University of South Carolina); Charney, S. P. (Carl Zeiss Industrial Metrology). 164

**** No Abstract Available***

Technical Papers

DIGITAL PHOTONIC PRODUCTION…OPPORTUNITIES AND CHALLENGES IN GAS TURBINE MANUFACTURING

Maneesh Khanna
Manufacturing Competitiveness
Manufacturing Development and Industrialization
Siemens Energy, Inc.

ABSTRACT

2015 International Year of Light
".....how optical technologies promote sustainable development and provide solutions to challenges in manufacturing, engineering, information technology, health and communications."

In a challenging energy market, Gas turbine product differentiation is driven by operational flexibility, fuel flexibility and product performance. This can only be achieved by innovation products, innovative business models and lead time to market. However, this is a major challenge for conventional manufacturing methods where the key to controlling cost and quality is driven by lot size and reduced product complexity. Hence, OE Ms are in need of agile manufacturing technologies that follow the market and business needs. Does the "Ray of Light" offer the agile manufacturing tool of the future? The current industry trend tends to say that "digital photonic production", where additive manufacturing plays an increasingly important role, is the key technology of the future. However, do we really understand the real opportunities it offers and the challenges it poses?

PROGRESS IN ADDITIVE MANUFACTURING

Edward D. Herderick
Advanced Manufacturing Initiatives Group
GE Corporate Supply Chain and Operations
Company or University
Cincinnati, OH USA

ABSTRACT
Additive manufacturing (AM) is among the fastest growing (1), most talked about manufacturing technologies on the planet (2,3) and it is providing diverse opportunities for new product design and manufacturing. At GE, efforts such as the additively produced LEAP engine fuel nozzle (4) and low pressure turbine blade manufacturing (5) are examples of how GE Aviation is leveraging these technologies in innovative ways.

The industrial excitement around this suite of processes is being driven by its capacity for empowering designers to focus on designing components for functionality rather than limitations of conventional processes such as casting, brazing, or forming processes. Furthermore, it is now enabling a whole new paradigm of rapid testing and product introduction wherein functional metal prototypes can be used for testing of individual components and manufacturing assembly processes (e.g. joining, forming, or machining). Using AM means product development cycles don't have to rely on traditional methods for manufacturing metallic prototypes, which can take months to produce. Any discussion of the technology needs to take into account the details of the resulting materials microstructure, surface roughness and ability to maintain engineering tolerances, as well as implementation details about reliability and cost, and potential supply chain issues.

This leads to the key question: *How* can ASPE community contribute to responsible, accelerated growth given the context of where the field is today? The key to industrial implementation for manufacturing technologies is a thorough understanding of the critical performance criteria in applications and the ability to consistently deliver reliable products. In order to realize the full potential of AM, further maturation of process control and finishing approaches including machining and heat treatment are essential. When that happens, AM adoption will accelerate as industrial designers become empowered to select tailored material and process combinations that drive performance improvement for demanding applications.

This presentation, Progress in Additive Manufacturing, will set the stage for the overall topical meeting, Achieving Precision Tolerances in Additive Manufacturing, by reviewing industrial requirements for maturation of unconventional technologies, presenting GE activities on additive manufacturing, and sharing views on where the field is going and needs from the supply chain.

1. 3D Printing and Additive Manufacturing State of the Industry Annual Worldwide Progress Report, Wohler's Associates Inc., 2014.
2. Hype Cycle for Leaders of Manufacturing Strategies, Jacobsen SF, Gartner Inc., 2013.
3. "Print me a Stradivarius", The Economist, February 10, 2011.
4. GE Reports, July 15 2014, "World's First Plant to Print Jet Engine Nozzles in Mass Production", http://www.gereports.com/post/91763815095/worlds-first-plant-to-print-jet-engine-nozzles-in
5. GE Reports, August 17 2014, "This Electron Gun builds Jet Engines", http://www.gereports.com/post/94658699280/this-electron-gun-builds-jet-engines

FLEXIBLE MANUFACTURING WITH AN ADDITIVE PROCESS CHAIN DESIGN, PRODUCTION AND SURFACE FINISH

Prof. Dr. h. c. Dr.-Ing. Eckart Uhlmann[1,3], Prof. Dr.-Ing. Michael Rethmeier[1,2]
Benjamin Graf[1], Robert Kersting[1], André Bergmann[1]

[1]Institute for Production Systems and Design Technology IPK
Fraunhofer-Gesellschaft, Berlin, Germany
[2]Federal Institute for Materials Research and Testing BAM
Berlin, Germany
[3]Institute for Machine Tools and Factory Management IWF
Technische Universität Berlin, Germany

INTRODUCTION

The industrial demand for flexible and innovative manufacturing technologies is continuously increasing [1]. These technologies have to be sustainable and resource-efficient, and have to allow the production of long-life capital goods. Consequently, the additive processes gain in importance as they offer an enormous potential of application, especially for the turbomachinery industry.

In order to use additive manufacturing technologies in industrial applications, it is necessary to consider the complete process chain, including all necessary pre- and postprocessing.

Although additive manufacturing is increasingly covered in scientific research [2-4], the linking between this technology and conventional industrial processes is rarely described.

OBJECTIVE

The aim of the study is the development of a ready-to-use process chain for additive manufacturing of highly-complex turbine components, such as blades and burners. The focus of the process chain is high dimensional accuracy and surface finish with secondary operations.

For this purpose, not only the computer-assisted preprocessing and the manufacturing by use of Selective Laser Melting (SLM) are considered, but also all downstream processes.

These include thermal treatment to adjust the microstructure, dry-ice cleaning to remove particles and shot peening in order to improve fatigue properties. Another focus of the study is the combination of different additive manufacturing technologies like SLM and Laser Metal Deposition (LMD), with the intention to increase build-up rates.

Finally, the results are discussed to describe the space of where additive manufacturing is beneficial.

PROCEDURES

In order to achieve the objective of this study, demonstrator parts from the turbine industry are chosen and the manufacturing along the process chain is described. FIGURE 1 shows a state-of-the-art turbine blade with an adapted internal design. Nickel-based alloy Inconel 718 is used in the experiments.

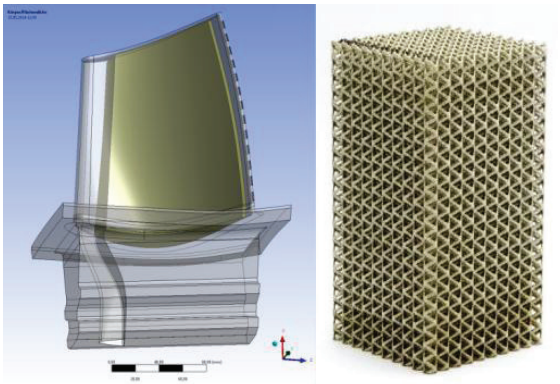

FIGURE 1: Left: Selected turbine blade with core; Right: Core is replaced by lightweight grid structure (right).

Additive processes

SLM is the most common additive technology to process weldable materials. SLM is a three-step layer-based process using a powder bed: 1) a thin layer of metal powder is placed on a platform using a mechanical coating system. 2) a focused laser beam selectively melts the topmost layer of the powder bed. 3) after solidification, the platform is lowered by the layer thickness and the cycle begins again. Complex parts can be built up, typically using thousands of layers.

LMD can be used as an additive technology to create a metallurgically bonded material deposition on a substrate, see FIGURE 2. A laser

beam melts the surface of a specimen, while powdery filler material is injected in the molten pool with a nozzle. Single weld beads can be deposited next to each other to form layers. Multiple layers on top of each other form volumes.

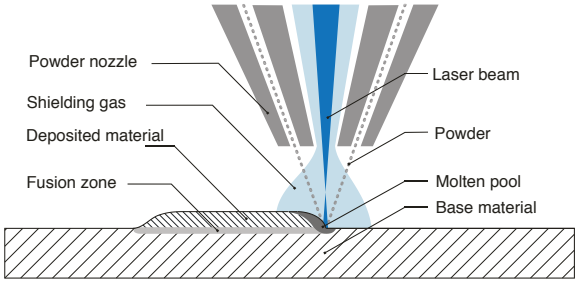

FIGURE 2: Laser metal deposition process

Table 1 shows a comparison of the two processes used. A combination of both SLM and LMD in an additive process chain is useful to get high deposition rate and material flexibility from LMD and high structural complexity from SLM.

TABLE 1: Additive processes SLM and LMD

	SLM	LMD
part dimensions	process chamber	machine working area
structural complexity	high, e.g. lattice structures	limited, e.g. walls
substrate	flat sheets	3D-surface
material flexibility	same powder for whole part	in-process modification

Turbine blade design

First, a conventional turbine blade design is adjusted according to additive manufacturing design rules [5]. The possibility to manufacture complex inner lightweight structures is used to reach higher functionality. By replacing full material regions with lattice structures, a lighter design with sufficient stiffness can be realized.

Turbine blade build-up

In the second step, demonstrator blades are built using two different manufacturing strategies. The first strategy uses a SLM- only-process, whereas the second strategy is a combination of SLM and LMD. For both strategies build-up rates and potential economic benefits are evaluated. The fir tree root of the blade is built up with LMD using two types of parameter sets. The first allows building up big volumes with a low number of layers, while the second set is chosen for high accuracy of the fir tree profile (TABLE 2).

TABLE 2: LMD parameter sets for Inconel 718. Laser power P, welding velocity v, spot diameter d, powder mass flow m

	P	v	d	m
	W	mm/min	mm	g/min
big volume	1000	600	1	6,5
high accuracy	800	800	1	6,5

Postprocesses

After manufacturing, additional finishing processes are needed to hit industry requirements. First steps are the manual removal of added support structures and a cleaning of the component: Adhering powder has to be removed. Different cleaning technologies such as shock-wave cleaning and dry-ice-cleaning are suitable. Once having a clean part, a double-stage age hardening is used to adjust the microstructure of Inconel 718 and to massively increase tensile strength. SLM-built surfaces in general have a relatively rough surface of Ra 8 - 10 μm. So in many cases surface finishing processes are necessary. Appropriate processes are metal-shot-peening and vibratory finishing. With the addition of compressive stresses from shot peening the metal fatigue strength can be increased.

RESULTS

Turbine blade design

FEM simulations show the advantages of lattice structures. Deformations on the tip of the blade, which are the result of radial forces during turbine operation, could be reduced by 30 %. Also, stresses in critical areas can be lowered by about 35 %. Another advantage of lattice structures is a more effective heat exchange between cooling air and blade wall due to an increased surface-to-volume-ratio. Using this potential the consumption of cooling air is reduced and thereby the degree of efficiency is increased.

Turbine blade build-up

FIGURE 3 shows a blade manufactured using the first strategy, only SLM. The complex trailing edge could be built with high accuracy.

FIGURE 3: Turbine blade built via SLM process (inner lattice structure not visible)

FIGURE 4 shows a detailed view on the built lattice structures: no cracks and deformations visible.

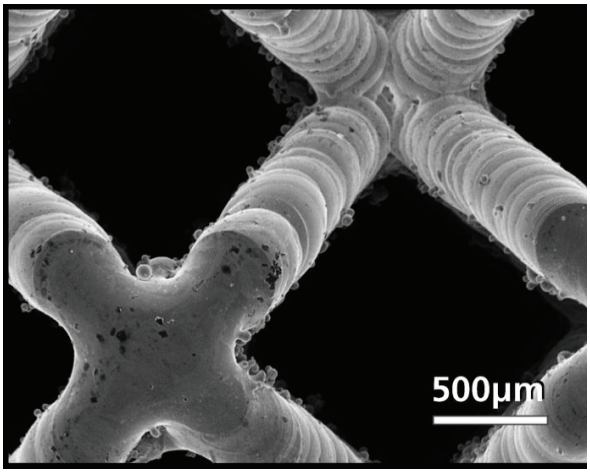

FIGURE 4: Detailed view on lattice structures

FIGURE 5 shows a turbine blade manufactured with the second strategy (SLM & LMD). Compared to pure SLM manufacturing, the technology combination decreased process time from 14 hours down to 5 hours.

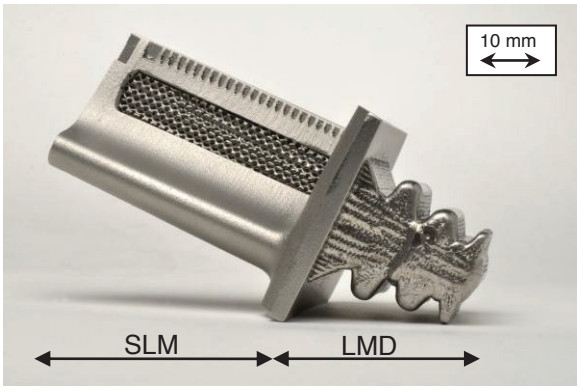

FIGURE 5: Turbine blade manufactured by SLM and LMD

The process duration for the different blade parts is shown in table 3. It is notable, that the LMD process achieved a deposition rate of 29 cm³/h, which is below the LMD machine specification of up to 250 cm³/h. The reason for this gap is that maximum deposition rate is measured with a parameter set using maximum laser power and powder mass flow. This parameter set is suited for a coating process of big parts (such as drill bits in the oil industry), but not feasible for the additive build-up of smaller and more complex parts like the fir tree profile.

TABLE 3: Process time

Part	Process duration
Complete blade with SLM	831 min
Airfoil portion with SLM	285 min
Fir tree root with LMD	36 min
Complete blade SLM-LMD combination	321 min

The LMD deposition rate of 29 cm³/h is measured for the welding process, while the laser is on. After a few layers are welded, part temperature increases, influencing melt pool dimensions and process stability. In order to achieve a constant welding process, cooling times between layers have to be applied. While one part is cooling down, the deposition process can continue on the next part. That way the process is used most efficiently. For the turbine blade, a batch size of 18 blades allows for a continuous material deposition.
The LMD-made blade's fir-tree roots were built near net shape. So further machining via CNC milling machine is required.

Postprocesses

FIGURE 6 shows lattice structures before and after cleaning using dry-ice-cleaning. About 90 % of the adhering powder particles could be removed.

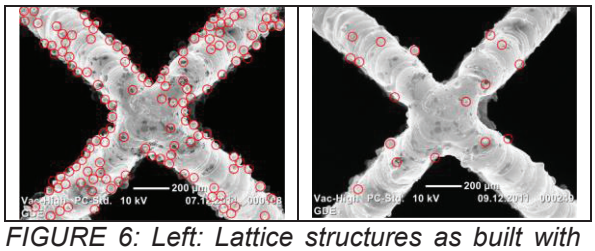

FIGURE 6: Left: Lattice structures as built with adhering powder (marked red); Right: After dry-ice-cleaning.

Due to double-stage heat treatment, the microstructure can be adjusted (See FIGURE 7).

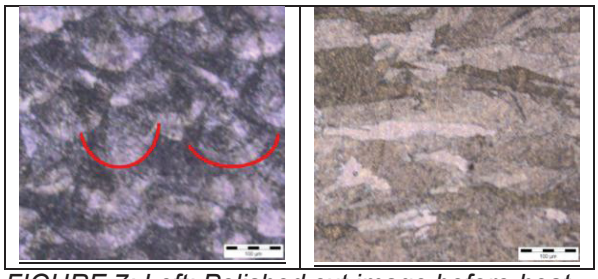

FIGURE 7: Left: Polished cut image before heat treatment (visible welding beads are marked red); Right: After heat treatment of SLM part.

By using well qualified SLM process parameters and heat treatment, very good material properties were achieved. Tensile strength was measured at 1450 MPa, while elongation at fracture remained at 14 %. The Young's modulus was measured at about 200 GPa.

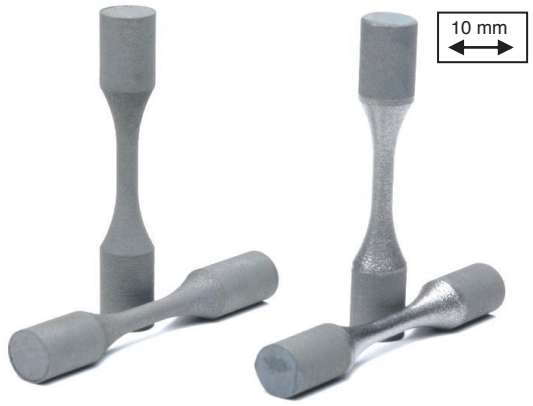

FIGURE 8: Left: HCF specimens before metal-shot-peening; Right: After metal-shot-peening

To improve surface quality and increase fatigue properties metal shot-peening was used to treat the built parts. Measurements show that roughness could be reduced massively from about Ra 8 μm down to Ra 4 μm. To investigate the improvement of fatigue properties, high cycle fatigue (HCF) test specimens were built (See FIGURE 8**Fehler! Verweisquelle konnte nicht gefunden werden.**).

Additive process chain SLM & LMD: Beneficial space

In order to evaluate in which areas the described additive SLM-LMD process chain is beneficial, the following criteria can be assessed:

- Part complexity
- Part geometry
- Materials
- Production scale

The SLM-LMD process chain is most useful when the part has both complex and simple features. In the turbine blade, *part complexity* is represented in the simple fir tree root and in the complex airfoil portion with lightweight structures. That way, the benefits of both technologies are used.

Part geometry relates to the platform of the blade, which is used as the boundary between the two processes. The platform provides a flat and stiff surface for LMD build-up. The stiffness is useful to reduce welding distortion effects.

Benefits regarding *materials* can be used whenever a multi-material design is advantageous. Using LMD, a change of material can be done easily during the build-up process. This allows to create a hard surface, while maintaining a core with high toughness.

The need for cool-down times during the LMD process means that high deposition rates can only be achieved, if multiple parts are processed during the same time. For the blade, a *production scale* of at least 18 blades leads to a continuous deposition process. The process combination is therefore most useful in small-batch production.

PROSPECT

The additive process chain presented in this paper allows manufacturing of fully operational turbine blades with excellent mechanical properties in strength and surface. By using a combination of SLM and LMD an increased deposition rate could be realized. This improves feasibility for small-batch production.

In future work, comparable parts made of Inconel 718 will be investigated in a helicopter turbine test rig. This should highlight the suitability of additive processes for dynamically and thermally highly-stressed components and prove the applicability of the developed process chain.
The target groups of this manufacturing chain are small and medium-sized enterprises (SMEs), particularly service contractors of Rapid Tooling and Rapid Manufacturing, as well as suppliers of the automotive and turbomachinery industry and mechanical engineering in general.

REFERENCES

[1] Wohlers Associates, Inc. (Hrsg.): Rapid Prototyping, Tooling & Manufacturing - State of the Industry. Annual Worldwide Progress Report, Colorado, 2003.

[2] Birger, E.M.; Moskvitin, G.V.; Polyakov, A.N.; Arkhipov, V.E.: Industrial laser cladding: current state and future. In: Welding International, Vol. 25 No. 3 (2011), p. 234-243

[3] Graf, B.; Gumenyuk, A.; Rethmeier, M.: Laser metal deposition as repair technology for stainless steel and titanium alloys, In: Physics Procedia, Nr. 39; 2012, p. 376-381

[4] Levy, G. N.; Schindel, R.; Kruth, J.-P.: Rapid Manufacturing and Rapid Tooling with Layer Manufacturing (LM) technologies, state of the art and future perspectives. CIRP Ann – ManufTechnol 52 (2), S. 589-609. 2003

[5] Uhlmann, E.; Bergmann, A.; John, P.; Kashevko, V.: Verification of Design Rules for Additive Manufacturing. Proceedings ASPE 2014 Spring Topical Meeting, American Society for Precision Engineering, p. 19-23, 2014.

Typical requirements for precision mechanical parts in relation to additive manufacturing

Ton Peijnenburg[1], Gerrit Oosterhuis[1], Frans-Willem Goudsmit[1] and Gerjan Veldhuis[2]
[1]VDL ETG
Eindhoven, The Netherlands
[2]VDL ETG USA
Fremont, CA, USA

INTRODUCTION

Additive Manufacturing (AM) of metal work pieces is establishing a position as viable option for the manufacturing of parts that are to be used in precision mechanical and precision mechatronic systems. The improvement of functional performance is the prime driver for considering this new manufacturing technology.

In addition, the use of AM has proven its worth for (rapid) prototyping of new designs. Critical parts can be build quickly, without having to worry about long lead times e.g. due to the need for tooling, and using metal or in other materials like plastic, for geometric, lay-out and (partial) functional evaluation.

To properly assess the potential of AM, several fields of use have been selected for functional performance aspects. An example of such a test field is thermal control. For each field of use cases with key product features have been selected that determine the manufacturing processes. An example of such a key feature is an internal channel for coolant or gas supply.

This paper explores the test cases based on their key (manufacturing) features, and compares state-of-the art specifications for current manufacturing processes with estimated and/or achieved results for AM processes. It is an extension to a paper published at the 2014 Spring Topical Meeting of ASPE (see reference [2]). Since then, cases have been investigated further and new cases have been added.

CASES, FUNCTIONAL PERFORMANCE AND (MANUFACTURING) FEATURES

The following test case areas have been defined, based on functional performance areas typical for precision mechanical and precision mechatronic systems.

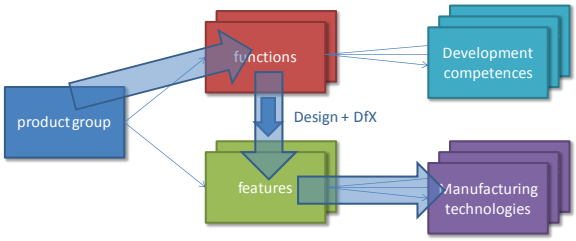

FIGURE 1. From functions to (manufacturing) features

The functional areas in our test cases are connected to product groups that we have introduced in VDL ETG for our technology roadmapping process. They are:

- Heat and flow
- Integrated mechanisms
- Structural dynamics
- Odd materials

In FIGURE 1, a mapping is created from product groups to product functions on the one hand and product features on the other hand.

- The *product functions* (e.g. “condition temperature” or “prevent contamination”) are in the design domain and related to development competencies such as thermal control.
- The *product features* (e.g. “a flat surface”, or “a clean internal channel”) are in the manufacturing technology domain and related to manufacturing technologies such as AM.
- The *design process* projects the product’s functions on one or more features. A manufacturing technology like AM greatly enhances the possible projections for a certain functionality, at improved levels of performance.

Heat and flow

Parts for thermal control become more prominent in precision equipment and the functional performance requirements are getting more stringent. The functionality is subcategorized based on the objective of thermal control: creating a uniform temperature (where K/m is the measure of performance) or exchanging heat (mainly cooling, where K/W is the measure of performance). Typically, internal channels and flow structures are used to implement thermal control functionality. So an important *product feature* of this functional group is “internal geometry”. Smoothness of flow, flow resistance, corrosion resistance, heat transfer coefficient, density (permeation) and cleanliness are requirements for this key feature. They translate to geometry, surface roughness and cleanliness.

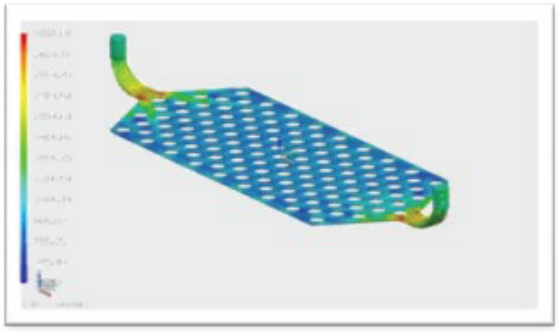

FIGURE 2. Heat removal part with flow speed calculation.

Internal channels are also used for (process- or purge-) gas delivery. In the context of this function, flow resistance and cleanliness are the most important requirements of the key feature.

In addtion, additive manufactuing allows these functional blocks for gas distribution to be designed and manufactured in a “sparse” manner, where material is only put where it is required – in this case, to seal the gas delivery channels and steer the flow of the medium, see FIGURE 3.

FIGURE 3. Gas delivery structure optimized for functionality.

Integrated mechanisms

Mechanisms for precision motion are often based on flexures, see FIGURE 4. Combining degrees of freedom is achieved by assembly of multiple parts that offer one or two degrees of freedom. AM holds the promise to further integrate, by allowing integration of all required degrees of freedom into one part, elminating internal interface- and reference features as well as allowing improved motion and stiffness profiles e.g. eliminate cross-coupling between axes. The functionality is subcategorized between no- or limited motion (“static”, e.g. adjustment mechanisms for optical components or sensors), and repetitive motion (“dynamic”).

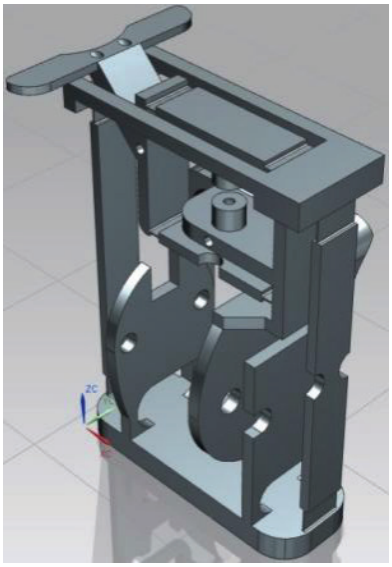

FIGURE 4. Integrated flexure mechanism.

Key features are flexures and the requirements for these features are (minimum) wall thickness

(for flexures), density, finish (roughness, related to fatigue) and stability (related to adjustment mechanisms).

Structural dynamics

Structural parts with functional requirements regarding dynamical stability, may benefit from design freedom offered by AM. Computational tools be may used to optimize topology of parts, optimizing their dynamic behavior. Weight, stiffness and damping are functional properties. Key features are thin walls and optimized shapes. Requirements include material density, material damping, (minimum) wall thickness and freeform capabilities.

When considering wafer tables, additional key features include a flat (burled) surface and additional key requirements include form and finish of the surface.

Odd materials

Core functionality of high-end equipment may rely on parts made from odd materials that support fuctions such as electron emission, X-ray absorption, high-voltage insulation, particle moderation etc. Metals with high atomic weights are often used for radiation or high-temperature heat shielding purposes, but are often quite difficult to machine. AM holds promise to more freely design and more economically manufacture parts out of materials such as tungsten, molybdenum and tantalum.

KEY PARAMETERS AND DISCUSSION

This section discusses findings on the key parameters for the various (manufacturing) features.

Form: surface flatness, minimum wall thickness and smallest feature size

Feature sizes allow for internal channels as well as flexures to be additively manufactured according to our design requirements.

For thermal conditioning, we have achieved improvements in thermal time constant (bulk material to cooling liquid) from 20 s to 1 s by use of a more dense channel structure that can be manufactured well using additive manufacturing (see references [3] and [4]).

In a specific case illustrated below, FIGURE 5 and FIGURE 6, it is important to realize that the high R_a (R_a = 15 µm) that comes with the SLM process makes it difficult to design miniature parts for SLM with tight tolerances. The peak-to-valley range of the roughness is in same order of magnitude as the overall profile form tolerance which is +/- 0.1 mm. The example below clearly illustrates the problem: The profile tolerance alone would allow a workaround, however the combination with the roughness makes it impossible to use for the current application.

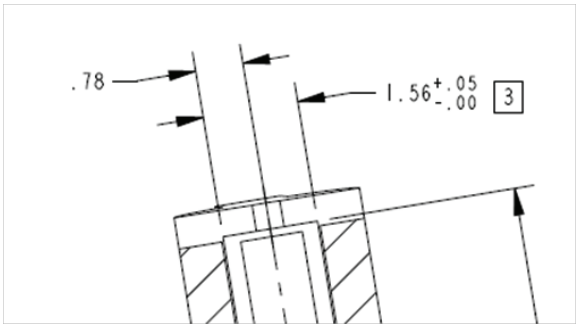

FIGURE 5 Small part with narrow form tolerance

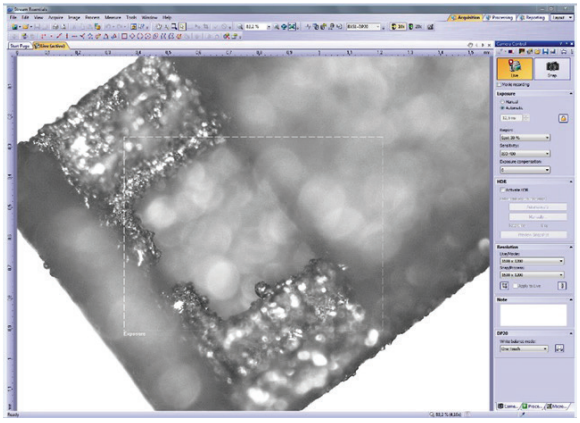

FIGURE 6 Microscopic image of feature as manfauctured using SLM

Surface finish: fatigue

Fatigue is investigated for a flexure mechanism. Samples were ordered and post-processed in three ways: no additional post-processing except for some level of powder blasting (surface roughness of flexure sections Ra of 15 □m), post-processing by our part supplier and EDM post processing in our own machine shop to resemble a traditionally manufactured flexure part. In all cases, more than 10 million cycles were achieved in our test set-up operating at a about 10 cycles per second.

Our feasibility study will be extended to achieve statistical relevance. First results however are encouraging. A high number of cycles is

possible with limited post-processing of flexure features. This is important for the flexure mechanisms that combine multiple degrees of freedom, since not all flexures will be readily accessible for post machining after AM.

One batch of flexures was poorly manufactured with high roughness and high stiffness and failed after some 100,000 cycles, see FIGURE 7. Important differences exist between SLM process recipes and their according heat treatments. As a result, majojr differences can be expected between suppliers, especially in fatigure performance..

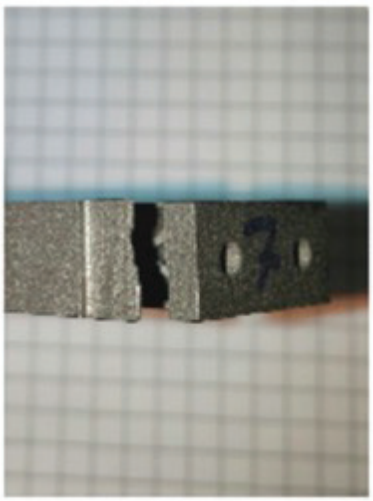

FIGURE 7 Early fatigue failure of poorly manufactured flexure

Leak tightness

To guarantee leak tightness for applications in UHV conditions, a minimum wall thickness is required depending on the material which is used for printing. Leak tight is defined as He leak rate of less than $5 \cdot 10^{-9}$ mbar.l/s. Wall thickness in titanium should be > 0.2 mm, in 316L it should be > 0.6 mm and in aluminum we use > 1.0 mm. Titanium and Aluminum cooling structures have been manufactured and proven to be leak tight acoording to the above specification, with – for Titanium - a wall thickness of 0.3 mm and (water) channel height of 0.6 mm.

Contamination

When post-machined surfaces of AM parts are similar to traditionally manufactured parts, no differences in cleanability and cleanliness for both molecular as well as particle contamination have been observed so far.

Cleaning of internal channels is still under test. We expect test results to be available by Summer 2015. Already, some lessons learned have been collected.

During a study test case of an heat exchanger, a virtual loop inside the product for the fluid flow was designed accidentally, leading to remaining powder being recirculated inside the channels when pressurized air was applied. Not all powder was removed and heat treatment after powder removal fixated the remaining powder by sintering of the small powder particles.

It appeared difficult to determine whether the powder was completely removed, especially for the first build, when no pressure/flow relation is known as a rerefence. Hence, it is important to establish process flows that allow for a robust qualification of the powder removal during production.

Quality control is needed for powder removal to validate channels being open. For complicated channel routings, the use of 2D X-ray or X-Ray CT inspection may be inevitable.

UHV compatible cleanliness levels for e-beam or EUV appliations have been demonstrated by a supplier of titanium AM parts.

ECONOMIC FEASIBILITY

At the moment, economic feasibility of some, precision engineering applications is questionable. This mainly holds for larger parts, where there are not many SLM machines and/or know-how to manufacture these parts. One example will be illustrated here below.

Within the thermal control group, for the development of a thermal wafer table, AM has recently been considered as one of the manufacturing options that would lead to superior thermal performance when compared to the best conventional alternative.

However, the manufacturing risks led to development cost and an increase of time to market that was unacceptable for this specific development project. As a result, the project decision was to choose a concept based on known technology. The according lower thermal performance was accepted as an acceptable loss.

This case study clearly illustrates the urgent need for industrialization of the AM process up to a level where manufacturing risks are low enough to apply AM in actual product developments.

CONCLUSION

For our test cases that were selected based upon product functions, we have demonstrated successful prototypes using AM. Requirements for key (manufacturing) features as defined for our test cases have been achieved using AM. The quality demonstrated is at a level that is acceptable for production of precision mechanical parts and systems. However, there are still manufacturing risks that affect the economics of using AM as manufacturing technology for volume production.

REFERENCES

[1] Vayre, Benjamin, Frédéric Vignat, and François Villeneuve. "Metallic additive manufacturing: state-of-the-art review and prospects." Mechanics & Industry 13.02 (2012): 89-96.

[2] Frans-Willem Goudsmit et.al. Typical requirements for precision mechanical parts and opportunities for additive manufacturing. ASPE spring topical meeting, Berkeley, CA: 2014

[3] Gerrit Oosterhuis et.al. AM design of a wafer conditioning table. ASPE spring topical meeting, Berkeley, CA: 2014

[4] Gerrit Oosterhuis et.al. Channels and Pillars. Mikroniek nr. 6, 2014, pages 36-40

Considerations for AM Modelling in the Context of Topology Optimization

Fred van Keulen & Can Ayas
Department Precision and Microsystems Engineering
Mekelweg 2,
2628CD Delft, The Netherlands
A.vanKeulen@tudelft.nl

Abstract

Recent developments in additive manufacturing (AM) have shifted its focus from rapid prototyping with low melting point polymers to production of advanced products from a wide range of materials, including metallic alloys and ceramic. The quality of these products is gradually improving. For instance, the density of products is increased by way of reducing porosity which in turn increases the strength and fracture toughness. Also the range of products and materials (combinations) which can be processed via AM is growing rapidly.

A major advantage of AM technologies is that complex structures can be manufactured, where the complexity is not one-to-one translated into cost of production. This is in contrast to subtractive manufacturing techniques. For example, with AM we may produce complex 3D architectures with embedded cooling channels. Moreover, the layout of these channels is then governed by the functional requirements rather than manufacturing considerations. The versatility of AM also implies mass customization and enhanced integration. The latter, can eliminate costly assembly steps. As a drawback, AM may require support structures which need to be removed during post-processing. This might be very challenging for internal architectures.

Although AM provides an enormous freedom in design, care should be taken to satisfy all manufacturability constraints and to account for process induced effects. As an example, many AM processes demand certain overhang constraints to be satisfied. The repeated heating-cooling cycles and the associated phase transformations which are an essential part of many metal based AM processes cause distortion of the products and/or an accumulation of residual stresses. The latter may give rise to deterioration of the mechanical properties or damage the product.

The unprecedented design freedom provided by AM is difficult to be exploited by manual design techniques. This holds in particularly if the design problem at hand requires multiple physical phenomena to be accounted for, such as heat transport, fluid and solid mechanics. In those cases, the designer is facing the challenge to fully exploit the design freedom in a 3D and multi-disciplinary setting, whereas at the same time manufacturability constraints and manufacturing-induced effects should be taken into account.

An elegant approach to take full advantage of the AM design freedom is to use topology optimization (TO). TO techniques are capable to optimize the full layout of a structure. Over the last decades TO has become a mature technique for simple linear and mono-disciplinary problems, in particular statics and dynamics. Rapid developments are taking place to make TO suited for transient, nonlinear and multi-disciplinary problems. We may conclude, that TO is a natural counterpart to AM.

Today's applications of TO techniques for AM products are still hindered by the fact that AM constraints and AM-induced effects are not integrated within the TO yet. Consequently, TO-based

designs often require manual adaptation before they can be used for AM production. This has two main drawbacks: (i) the designs created by TO will be eroded by the manual adaptations and (ii) the redesign steps are costly. For these reasons, AM constraints and AM-induced effects need to become integral components of TO techniques.

Integration of AM constraints into TO techniques requires the correct and efficient formulation of these constraints. Much more involved will be the integration of AM-induced effects. Here it is important to realize that TO techniques are iterative processes which rely on so-called adjoint design sensitivities. The latter are difficult to extract for transient simulations. If we incorporate AM-induced effects into TO, we are facing some kind of AM process simulation as integral part of the evaluation of an intermediate design. This process simulation should, for example, provide information on distortions and residual stress levels. Unfortunately, AM process simulations are of transient type, whereas also adjoint sensitivities must be evaluated. This implies that we cannot permit high resolution AM process simulations as integral components of TO techniques.

In this paper we present a review of existing AM-process models. In this review we focus in particular on the applicability of these models to be integrated with TO techniques. Aspects that will be highlighted are (i) computational costs, (ii) accuracy and (iii) ease of implementation and computational costs of adjoint sensitivities.

3D Systems' Perspective on the Future of Additive Manufacturing

Khalil Moussa, Hop Nguyen, Praveen Tummala, Jake McDonough
Advance Materials and Process
3D Systems Corporation
Rock Hill, South Carolina, USA

Since the early days, 3D Systems, has been focused on studying and improving the accuracy of 3D printing. Since 1984, StereoLithography been the first AM technology that saw a concerted effort to characterize and control the accuracy of 3D printed parts. In addition, MultiJet printing, Laser Sintering, Laser Melting and ColorJet Printing present unique opportunities as it open up a wider range of material to use in AM. Some of the most successful AM applications were the results of close collaboration between 3D Systems and the end users. This required an open mind from the traditional manufacturers to design the final parts for manufacturability using AM while benefiting from the design freedom that AM offers.

Procedure Of Measuring Accuracy

The process involves many aspects of obtaining statistical data. These aspects include machine types, material selection, part-building parameters, post processing and measuring methods. The data presents general accuracy of the machines which obtained by measuring Userpart, it also defines the accuracy and tolerances achieved in dental applications.

System set-up must pass quality control, acceptance tests. The material and build style are selected, the post processing such as part cleaning, post curing, etc., have to follow pre-determined standard operating procedures. After being post curing, the parts under test are put in a controlled environment room of a CMM system in a sufficient time for temperature stabilization before measurement are taken. The line width compensation and shrinkage factors are determined, the optimization conditions are defined before starting data collecting.

User-Part Accuracy

The User-Part

The test part has its name because it was created by StereoLithography User Group in 1990. 3D Systems, Corp. subsequently adopt the part as the standard for establishing the accuracy level achieved by StereoLithography machines. The part is designed with 170 dimensional measurements and range from 0.250" to 9.500". Of these, 78 are in x direction, 78 are in y direction and 14 are in z direction.

The User-Part:

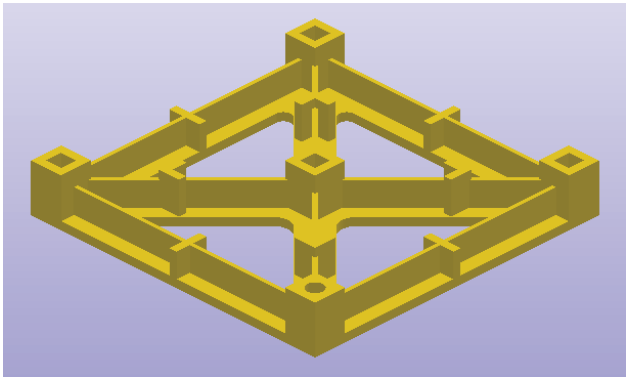

X, Y and Z dimensions of the User-Part

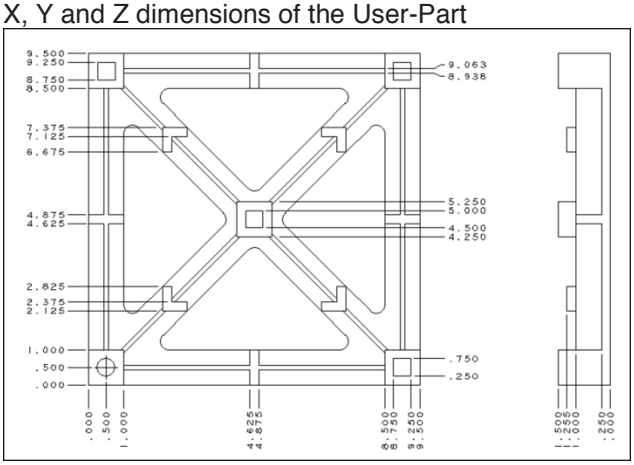

The Accuracy and Repeatability Statistics

The error distribution function (EDF), cumulative error distribution (CED) and value of Ɛ(90) are used to quantitatively measure accuracy and for repeatability the measurement of 10 parts are repeated.

The error is defined as in the following equation.

$$\varepsilon_i = S_i - S_d$$

Where S_i is the measurement of dimension identification i^{th} and S_d is the design value.

Ɛ(90) is specifically defined as tolerance value that 90% of the measurements fall within this limit.

Error Distribution Function (EDF)

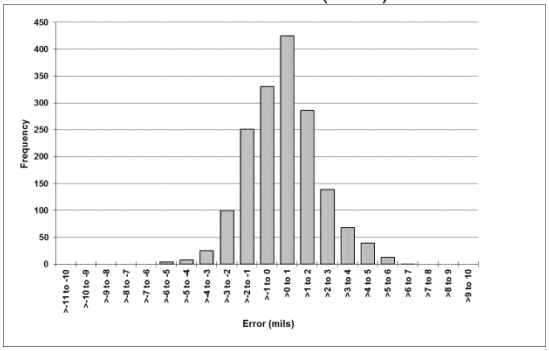

CED and Ɛ(90)

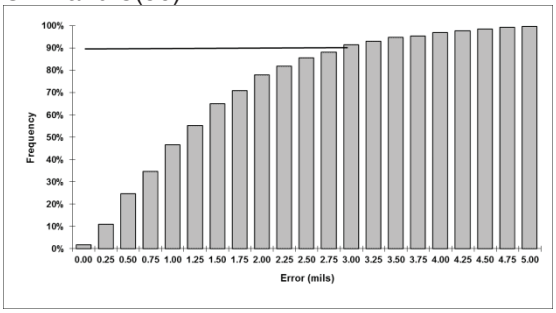

The User-Part Accuracy Achieved

The table below are the results of more than 10 years of studying, analyzing and tracking accuracy, repeatability of SL systems and materials such as SLA250, SLA 3500, SLA 5000, SLA7000, Accura 25, Accura 60 Bluestone etc.

Compiled UserPart Accuracy Results

ACES

Date	Machine Type	Machine SN	Resin	Zs (mils)	RMS (mils)	ε 90 (mils)
May-94	SLA-250/30	940015	SL 5170	6	1.80	2.89
May-98	SLA-250/50	940081	SL 5220	4	2.98	4.90
Oct-00	SLA-250/50	940081	SL 5240	4	2.43	3.85
May-04	SLA-250/50	940081	Accura 45	4	2.22	3.28
Dec-96	SLA-350/10	950222	SL 5190	4	2.15	3.48
Dec-97	SLA-350/10	960270	SL 5510	4	1.87	2.95
May-98	SLA-350/10	960270	SL 5520	4	2.82	4.63
Nov-98	SLA-350/10	950222	SL 5530	4	2.41	3.73
Apr-99	SLA-350/10	960270	SL 7510	4	2.05	3.37
Feb-00	SLA-350/10	960270	SL 7540	4	2.49	4.09
May-94	SLA-500/30	930004	SL 5180	6	2.54	4.18
Oct-96	SLA-500/30	Ciba500	SL 5410	6	2.36	3.80
Aug-99	SLA-500/30	920047	SL 5430	6	4.01	6.59
May-02	SLA-500/30	920047	AccuGen100	4	3.22	5.30
Oct-97	SLA-5000	POD2	SL 5195	4	3.43	5.64
May-98	SLA-5000	970229	SL 5520	4	3.74	6.15
Jul-98	SLA-5000	970230	SL 5510	4	2.34	3.77
Mar-99	SLA-5000	POD1	SL 5530	4	3.35	5.49
May-99	SLA-5000	POD2	SL 7510	3	2.92	4.78
Mar-00	SLA-5000	POD1	SL 7540	4	3.97	6.52
Jan-02	SLA-5000	POD1	AccuDur100	4	3.85	6.16
Mar-02	SLA-5000	POD2	AccuGen100	4	2.76	4.54
Aug-02	SLA-5000	P1	Accura SI 20	4	3.13	5.08
Dec-02	SLA-5000	P1	Accura SI 40	4	3.30	5.02
Jan-03	SLA-5000	P1	Accura SI 10	4	2.86	4.71
Jul-04	SLA-5000	P1	Accura 50	4	2.86	4.66
Aug-05	SLA-5000	7000-01	Accura 25	4	3.83	5.86
May-99	SLA-7000	98EA0003	SL 7510	3	4.45	7.21
Sep-99	SLA-7000	S1	SL 5530	4	5.91	9.64
Jan-00	SLA-7000	S1	SL 7520	3	4.98	7.98
Feb-00	SLA-7000	S3	SL 7540	4	5.83	9.46
Oct-01	SLA-7000	S1	AccuGen100	4	4.37	7.17
Jan-01	SLA-7000	S4	AccuDur100	4	5.93	9.75
Jul-02	SLA-7000	S4	Accura SI 20	4	5.49	9.03
Sep-02	SLA-7000	S3	Accura SI 40	4	5.44	8.97
Jan-04	SLA-7000	7000-3	BlueStone1365	4	3.10	5.00
May-04	SLA-7000	7000-3	Accura 50	4	4.66	7.50
Jul-05	SLA-7000	7000-2	Accura 25	4	3.27	5.37
Mar-06	SLA-7000	7000-0	Accura60	4	7.50	12.30
Mar-08	SLA-7000	7000-1	GreyStone 3371	4	4.60	7.40
Jun-01	Viper	POD2	SL 5510	4	1.83	3.01
Apr-02	Viper	POD2	AccuDur100	4	3.29	3.37
Apr-02	Viper	POD1	AccuGen100	4	2.67	4.38
Jan-03	Viper	POD2	Accura SI 40	4	2.85	4.66
Feb-03	Viper	POD 2	Accura SI 30	4	4.06	6.69
Mar-03	Viper	POD 2	Accura SI 20	4	2.98	4.58
Mar-03	Viper	POD 1	Accura SI 10	4	2.84	4.43
May-04	Viper	Viper-02	Accura 50	4	2.56	4.23
Jul-04	Viper	Viper-01	Bluestone1659	4	3.18	5.22
Jul-05	Viper	Viper-02	Accura 25	4	2.98	4.89

iPro 8000/9000 Accuracy and Tolerance

User-Part accuracy and tolerance provide overall, general performance of SL systems. If the accuracy is focused on one part and some critical dimensions, all SL system types can achieve accuracy to the resolution of the imaging module. The resolution ranges from 0.3 mils in SLA 250, Viper systems to 1 mil in SLA 7000 system. However, in applications which involve in "mass production", hundreds of parts being built on one platform which covers entire X/Y build envelop, the dimensional consistency within the build envelop is as important as accuracy. The examples of these types of manufacturing are dental and hearing aid applications. As many as 2 hundreds parts are built within two or three hours.

Dental and Hearing Aid parts

The dimensions of parts range from 0. 040" to roughly 3.000"

Hearing Aid Application

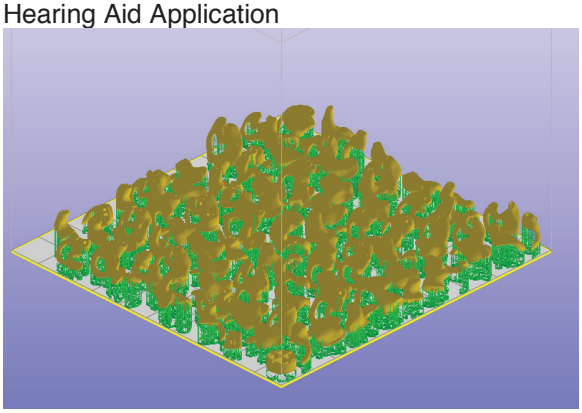

Dental Application

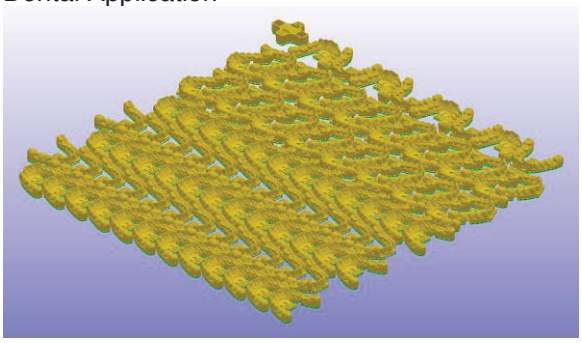

Accuracy Tolerance and Consistency.

The only difference in the procedure for measuring the accuracy and consistency in this case is test parts are built at many locations on the platform that covers whole X Y build envelop. The total range of the variation of the same dimensional ID of all parts in the same build is used for consistency measurement.

SLA® 7000 (for reference)

X or Y dimension to 1.2", dimensional repeatability = ± 5 mils across platform

iPro 8000 achieved:

X or Y dimension up to ~1.2", dimensional repeatability = ± 2.5 mils across platform

X or Y dimension up to ~0.040", dimensional repeatability = ± 1.5 mils across platform

SELECTIVE LASER SINTERING (SLS)

In SLS, the accuracy is best measured using a part that is typically referred to as a 'Scale Part.' This part is not only used to measure accuracy but also to determine the shrink values in X and Y of a material. Since the SLS laser beam is an elliptical beam, this part is also used to determine the beam offset values in order to be able to print fine features precisely.

SCALE PART

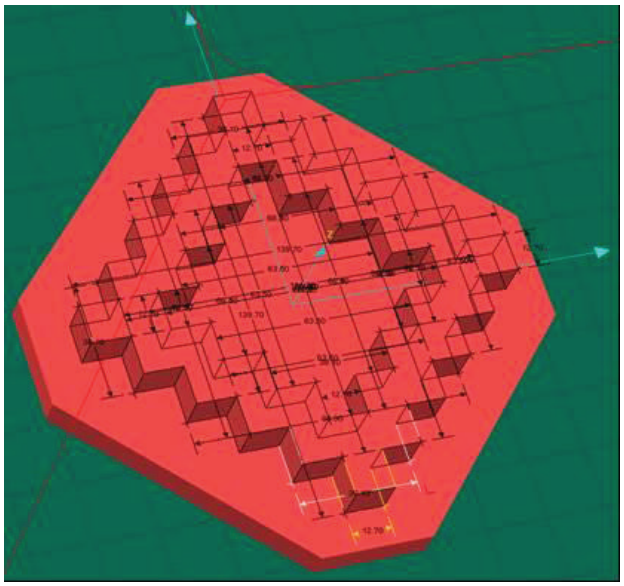

The image above shows a SLS Scale part. The Scale part has a stepped diamond shaped feature in X and Y. The Scale part is printed using the optimized SLS parameters for a particular platform and material combination.

MEASURING THE SCALE PART

The Scale part has 11 outer dimensions in X, 11 outer dimensions in Y, 7 inner dimensions in X and 7 outer dimensions in Y. The outer dimensions range from 12.7 mm to 139.7 mm in increments of 25.4 mm both in X and Y. The inner dimensions range fron 12.7 mm to 88.9 mm in increments of 25.4 mm both in X and Y. All the "outside" and "inside" dimensions of the stepped diamond shaped feature of the Scale part are measured using a pair of calipers. It is recommended to take three dimensions per step feature. The measured dimensions are entered in the SLS Build Setup software. In the Build Setup software, there is a tool called 'Measure and Enter Dimensions.' The Scale Part is selected from this tools option and the measured dimensions are entered on the left panel of the Scale Part as shown in the image below.

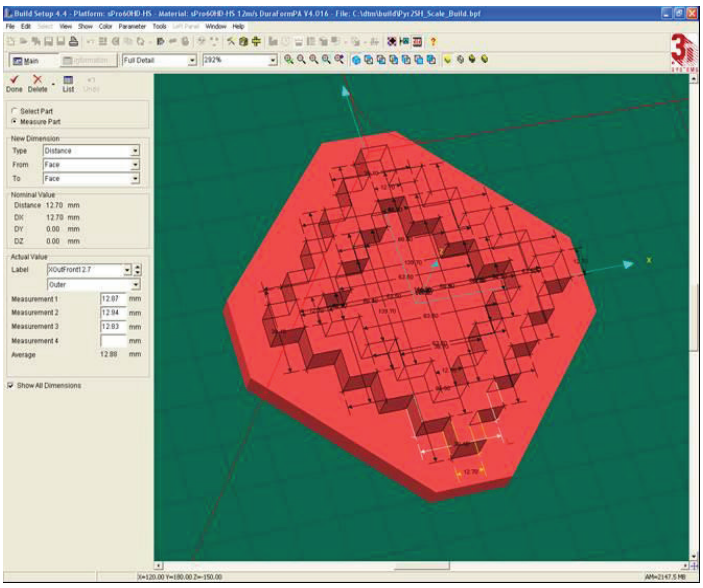

Once all the dimensions are entered, the 'list feature' can be selected to bring a spreadsheet view of the measured values as show in the image below.

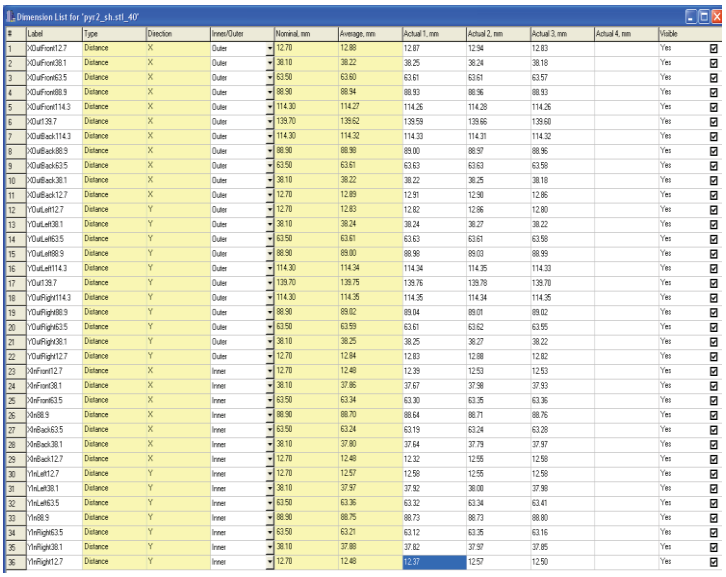

#	Label	Type	Direction	Inner/Outer	Nominal, mm	Average, mm	Actual 1, mm	Actual 2, mm	Actual 3, mm	Actual 4, mm	Visible
1	XOutFront12.7	Distance	X	Outer	12.70	12.86	12.87	12.94	12.83		Yes
2	XOutFront38.1	Distance	X	Outer	38.10	38.22	38.25	38.24	38.18		Yes
3	XOutFront63.5	Distance	X	Outer	63.50	63.60	63.61	63.61	63.57		Yes
4	XOutFront88.9	Distance	X	Outer	88.90	88.94	88.93	88.96	88.93		Yes
5	XOutFront114.3	Distance	X	Outer	114.30	114.27	114.26	114.28	114.26		Yes
6	XOut139.7	Distance	X	Outer	139.70	139.62	139.59	139.66	139.60		Yes
7	XOutBack114.3	Distance	X	Outer	114.30	114.32	114.33	114.31	114.32		Yes
8	XOutBack88.9	Distance	X	Outer	88.90	88.98	89.00	88.97	88.96		Yes
9	XOutBack63.5	Distance	X	Outer	63.50	63.61	63.63	63.63	63.58		Yes
10	XOutBack38.1	Distance	X	Outer	38.10	38.22	38.22	38.25	38.18		Yes
11	XOutBack12.7	Distance	X	Outer	12.70	12.89	12.91	12.90	12.86		Yes
12	YOutLeft12.7	Distance	Y	Outer	12.70	12.83	12.82	12.86	12.80		Yes
13	YOutLeft38.1	Distance	Y	Outer	38.10	38.24	38.24	38.27	38.22		Yes
14	YOutLeft63.5	Distance	Y	Outer	63.50	63.61	63.63	63.61	63.58		Yes
15	YOutLeft88.9	Distance	Y	Outer	88.90	89.00	88.99	89.03	88.99		Yes
16	YOutLeft114.3	Distance	Y	Outer	114.30	114.34	114.34	114.35	114.33		Yes
17	YOut139.7	Distance	Y	Outer	139.70	139.75	139.76	139.78	139.70		Yes
18	YOutRight114.3	Distance	Y	Outer	114.30	114.35	114.35	114.34	114.35		Yes
19	YOutRight88.9	Distance	Y	Outer	88.90	89.02	89.04	89.01	89.02		Yes
20	YOutRight63.5	Distance	Y	Outer	63.50	63.59	63.61	63.62	63.55		Yes
21	YOutRight38.1	Distance	Y	Outer	38.10	38.25	38.25	38.27	38.22		Yes
22	YOutRight12.7	Distance	Y	Outer	12.70	12.84	12.83	12.88	12.82		Yes
23	XInFront12.7	Distance	X	Inner	12.70	12.48	12.39	12.53	12.53		Yes
24	XInFront38.1	Distance	X	Inner	38.10	37.86	37.67	37.98	37.93		Yes
25	XInFront63.5	Distance	X	Inner	63.50	63.34	63.30	63.35	63.36		Yes
26	XInBack88.9	Distance	X	Inner	88.90	88.70	88.64	88.71	88.76		Yes
27	XInBack63.5	Distance	X	Inner	63.50	63.24	63.19	63.24	63.28		Yes
28	XInBack38.1	Distance	X	Inner	38.10	37.80	37.64	37.79	37.97		Yes
29	XInBack12.7	Distance	X	Inner	12.70	12.48	12.32	12.55	12.58		Yes
30	YInLeft12.7	Distance	Y	Inner	12.70	12.57	12.58	12.55	12.58		Yes
31	YInLeft38.1	Distance	Y	Inner	38.10	37.97	37.92	38.00	37.98		Yes
32	YInLeft63.5	Distance	Y	Inner	63.50	63.36	63.32	63.34	63.41		Yes
33	YIn88.9	Distance	Y	Inner	88.90	88.75	88.73	88.73	88.80		Yes
34	YInRight63.5	Distance	Y	Inner	63.50	63.21	63.12	63.35	63.16		Yes
35	YInRight38.1	Distance	Y	Inner	38.10	37.88	37.82	37.97	37.85		Yes
36	YInRight12.7	Distance	Y	Inner	12.70	12.48	12.37	12.57	12.50		Yes

CALCULATING THE SCLAE AND OFFSET VALUES USING SLS SOFTWARE

The Build Setup SLS software has a tool called 'Scale and Offset Wizard.' This tool uses the measured dimensions of all the step features of the Scale part and calculates the recommended X and Y Scale and Offset values to use in order

to be able to print parts accurately and as close as possible to the actual dimensions. Below is a screen shot of one of the steps in the wizard which displays the quality of regression fitting.

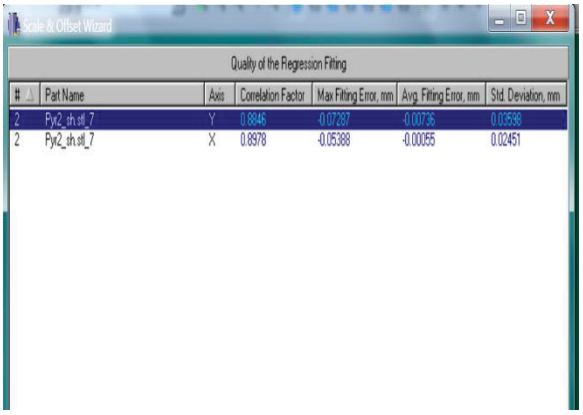

The correlation factors values for X and Y need to be greater than 0.75. If the correlation factors are less than 0.75, the entered dimensions need to verified for any measurement or input errors. The closer the correlations factors are to 1.0, the more likely the calculation will provide a scale and offset result that will improve the accuracy of parts.

Below is the screenshot of the final step in the Scale and Offset wizard. This step offers the recommended scale and offset values to use for a particular material on a particular platform in order to print accurate parts.

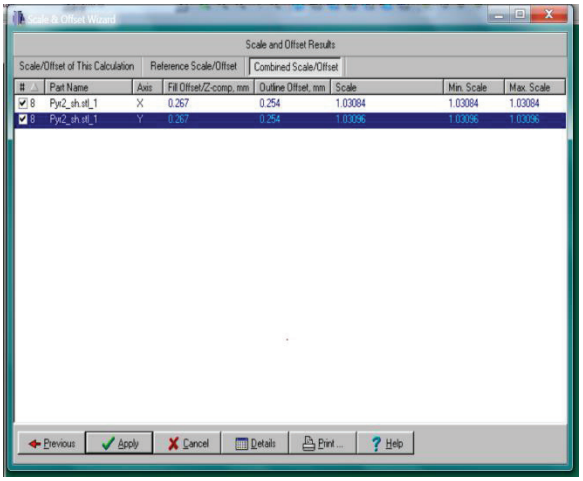

Z DIMENSIONAL ACCURACY

SLS employs a similar step feature part like the XY Scale part in order to measure and determine the recommended offset/compensation values to use to achieve the Z dimensional accuracy.

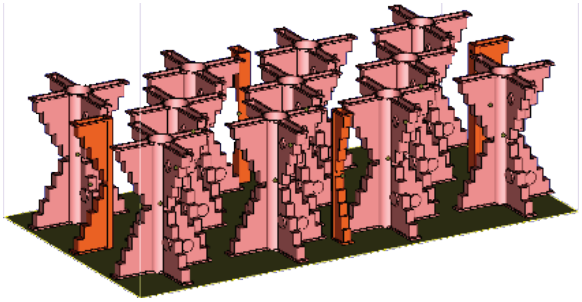

Build set up view

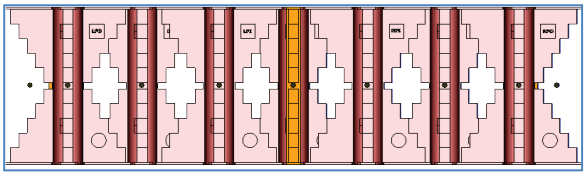

Front view of the parts.

The measurements of the various Z dimensions show variability across the build envelope. With the shorter dimensions having the least variability. A inverse dome model didn't show the desired accuracy outcome. However, a ellipsoid theory is been investigated and the data will be presented at a later date.

Conclusions:
The Additive Manufacturing technologies have made steady progress in understanding and controlling the process variability and have achieved tight tolerances in many mass production applications. In addition to SLA and MJP, Metal Printing, PolymerJet printing and Laser sintering are opening additional opportunities in manufacturing with wide range available materials and the design freedom afforded by AM.

COMPLEXITY ISN'T NECESSARILY FREE: OPPORTUNITIES AND CHALLENGES IN ADDITIVE MANUFACTURING

Bradley H. Jared[1], Brad Boyce[1], Corbett C. Battaille[1], Hojun Lim[1], Hy D. Tran[2], Joshua Robbins[3], Brett W. Clark[4] and Ted D. Blacker[4]
[1]Materials Science & Engineering
[2]Metrology & Sandia Production
[3]Computational Sciences & Math
[4]Computational Simulation
Sandia National Laboratories
Albuquerque, NM

OPPORTUNITIES

Additive manufacturing represents a new paradigm for component design and development. While multiple process variants exist among additive techniques, they all generate part material concurrent with part geometry; typically in a layer-by-layer fashion [1]. Access to discrete locations within each layer introduces the revolutionary capability for voxel level control of both materials and geometries within a three-dimensional volume. Such freedom motivates the claims from a burgeoning industry that "complexity is free" and indicates the potential to radically change how part geometries and materials are designed, fabricated and validated. Integrated Computational Materials Engineering (ICME) and the Materials Genome Initiative [2] are similar efforts with visions of developing materials using computational tools and methodologies akin to mechanical design, not through the traditionally empirical methods. The voxel level control of additive manufacturing provides one compelling path whereby these visions may be realized. Foundational work at Sandia in the Predicting Performance Margins (PPM) program [3] has developed multiscale material models useful for this ICME framework. Work to date has focused on laser welding processes, but is now being leveraged for a laser metal powder bed process.

In principle, voxel level geometrical control also introduces the capability to fabricate arbitrarily complex geometries containing both internal and external freeform features. Such geometrical freedom presents numerous opportunities to improve design performance by offering new functionality and/or by eliminating parts and interfaces with single monolithic structures.

Additive manufacturing has prompted

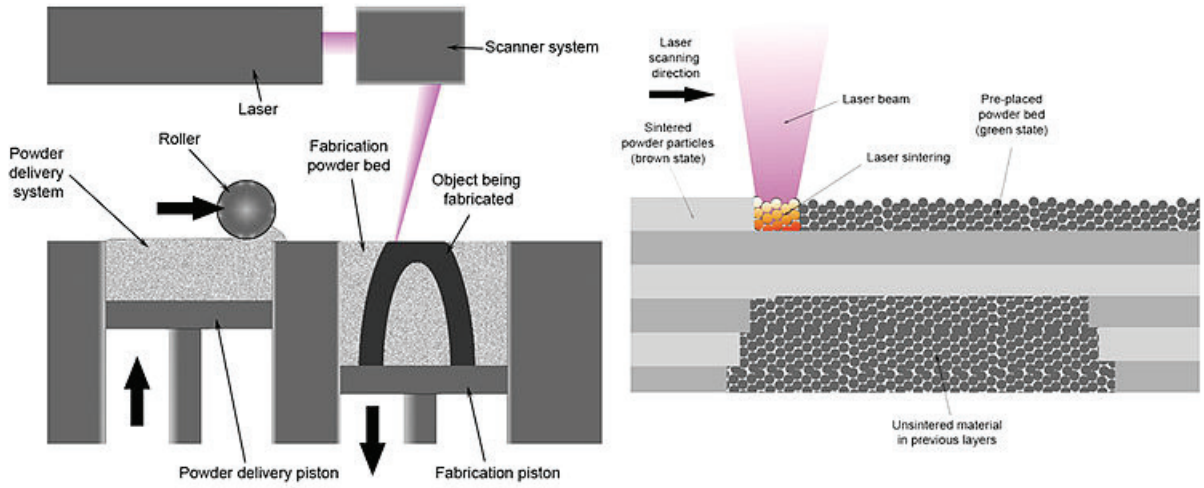

FIGURE 1. Layer-by-layer additive manufacturing in selective laser sintering demonstrates the opportunity for voxel-level material and geometry control (www.wikipedia.com).

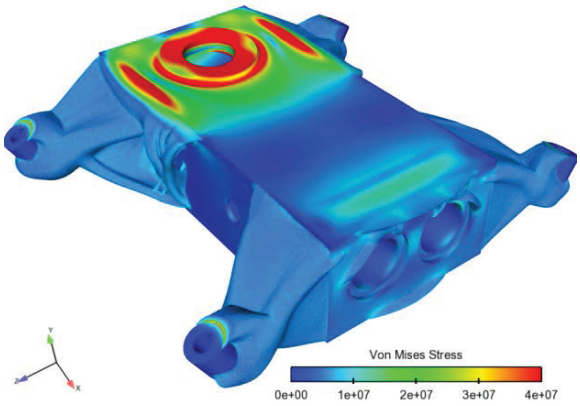

FIGURE 2. Housing designed using ATO with optimized stiffness to minimize vibration modes and amplitudes.

FIGURE 3. A 26-sided polyhedron with 3D Siemen stars on each face is relatively easy to print, but much more difficult to measure.

resurgence in computational design techniques such as adaptive topological optimization (ATO) where design and analysis are performed concurrently to generate geometries based predominantly on functional requirements, not manufacturing constraints. While ATO has existed for 25 years in the literature and academic circles [4], additive techniques are necessary to realize many of the resulting design solutions which are often non-intuitive and mimic biological constructs. Sandia started work in ATO in the mid 2000s [5], and has invested in the development of optimization algorithms and most recently, a design environment. Current capabilities address elasto-static and thermal optimization problems and are based on the Sandia Redsky high performance computing platform. Figure 2 demonstrates a housing designed using the Sandia code where stiffness was optimized to minimize the amplitude response in a vibration environment. On-going research includes efforts to incorporate process constraints, material anisotropy, uncertainty quantifications, multi-physics constraints and improved computational efficiency.

CHALLENGES

While the potential and future of additive manufacturing is exciting, real challenges exist. Most additive processes provide near net shapes, particularly for metal, which require post processing. Finish machining, polishing, powder or support removal, heat treating and hot isostatic pressing are all commonly performed to address problems with dimensional accuracy and repeatability, surface finish, residual stress, porosity and material microstructures. Such processing steps are time consuming and expensive, often eliminating anticipated cost or schedule gains. Arbitrary geometries are also not fully realistic as bounds and limitations exist in every process.

While “complexity is preferred” may be a more accurate assessment of part formation in additive (ex. a hollow lattice requires less time or material than a solid), the cost of metrology and/or inspection increases dramatically with complexity and can often become impractical or impossible. Freeform surfaces can no longer be measured as or represented by relatively simple shapes such as planes or cylinders. Figure 3 shows a complex geometry that was printed in PH17-4 on a metal powder bed machine. While fabrication of the part was relatively simple, metrology has proven challenging and measurement of the entire surface in a single setup remains elusive. Internal structures provide compelling advantages for applications such as light-weighting or conformal channels. Such structures, regardless of scale however, can only be characterized destructively or through cost and/or time prohibitive techniques such as neutron diffraction or computed tomography. Large data streams, whether for design, fabrication or metrology, present additional challenges as they must be managed efficiently and effectively during each aspect of the lifecycle. Furthermore, model based design definition and manufacturing becomes a requirement, not an option.

The use of computational based design techniques offers the promise of radically new design solutions that are optimized for maximum

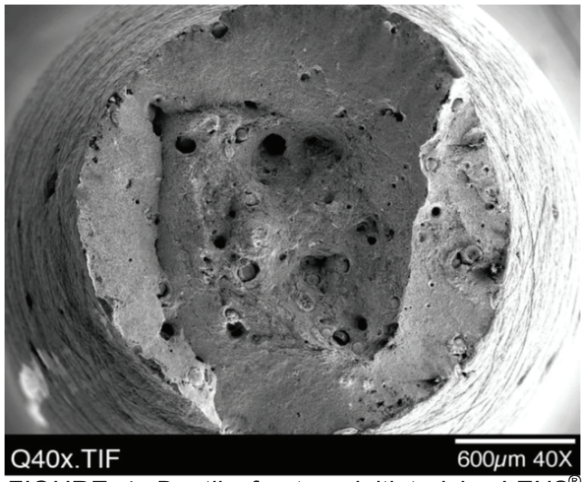

FIGURE 4. Ductile fracture initiated by LENS® porosity and unmelted particle defects in PH13-8Mo [6].

performance. Uncertainty quantification (UQ) is a common challenge in the computational sciences and generally refers to simulation accuracy. Optimization requires some maxima or minima so computational UQ must verify that a final solution is truly optimal. Material properties introduce additional uncertainty, however, and additive introduces new forms of anisotropy and property variations which depend on process inputs, feature size and feature orientation. Functional requirements and operating scenarios are often indeterminate and introduce additional uncertainties. New design tools must manage each of these uncertainties to provide designs that are truly optimized and that accurately represent design margins.

The concurrent formation of material and geometry introduces new design and process freedoms, but also introduces new requirements for managing and ensuring part and material performance. Material assurance, i.e. whether a material performs as designed and required for its intended application, is a fundamental question that must be addressed at some level for every application. Traditional material certification methodologies focused on feedstock materials are inadequate since internal defects can now be introduced through the manufacturing process not just the raw material. The introduction of engineered material complexity and internal structures further exacerbates the problem since existing metrology techniques generally presume isotropic bulk material properties and external surfaces. New metrology paradigms are

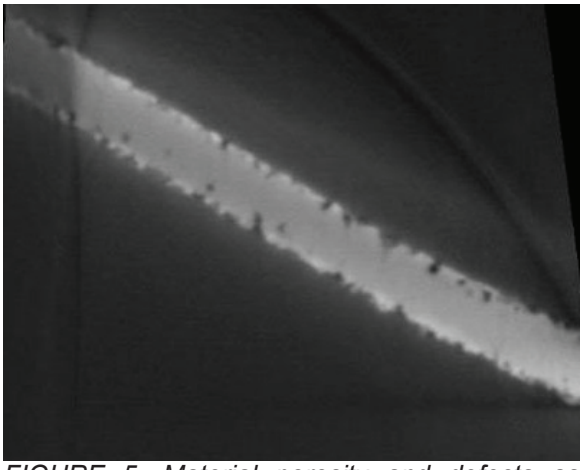
FIGURE 5. Material porosity and defects as observed via computed tomography in 17-4PH stainless steel.

therefore necessary as existing methodologies are too slow, too expensive and, in the case of defects, too late. In-situ process monitoring and control are clear needs for additive processes to meet the opportunities and demands of high consequence applications such as structural materials. Such work exists for LENS® and has already demonstrated improved material performance and margins [7].

Sandia is performing work that will be discussed in the midst of these opportunities and challenges for additive, particularly in areas of material and component design, materials assurance and process control. The larger precision engineering community, however, is uniquely situated to address many of these challenges. Systems level engineering and integration must be married with the computational and material sciences to develop design tools, materials and process equipment that satisfy the demands of a wide range of industries and applications. Precision engineering experience and expertise from error budgets, machine design, process control, thermal management and metrology are all needed in additive manufacturing and present opportunities for on-going research, collaborations and contributions.

ACKNOWLEDGEMENTS
Sandia National Laboratories is a multi-program laboratory managed and operated by Sandia Corporation, a wholly owned subsidiary of Lockheed Martin Corporation, for the U.S. Department of Energy's National Nuclear Security Administration under contract DE-

AC04-94AL85000. This document has been reviewed and approved for unclassified, unlimited release under SAND2015-2791C.

REFERENCES

[1] ASTM F2792, “Standard Terminology for Additive Manufacturing Technologies”.
[2] Materials Genome Initiative, www.whitehouse.gov/mgi.
[3] Sandia Predicting Performance Margins program, www.sandia.gov/PPM.
[4] Bendsoe, M. Optimal Shape Design as a Material Distribution Problem. Structural Optimization. p. 193-202, 1989.
[5] Gill G, et al. Titanium Cholla: Lightweight, High-Strength Structures for Aerospace Applications. SAND2007-6775. 2007.
[6] Zheng, B. et al. Microstructure and Properties of PH13-8Mo Steel Fabricated by LENS®. PowderMet 2006, San Diego, CA.
[7] Aggarangsi, P, et al. Transient Changes in Melt Pool Size in Laser Additive Manufacturing Processes, Solid Freeform Fabrication Symposium, Austin, TX, 2004.

ANALYSIS AND OPTIMIZATION OF THE DIMENSIONAL ACCURACY FOR FDM PARTS MANUFACTURED WITH ABS-M30

Frederick Knoop[1, 2] and Volker Schoeppner[1]
[1]Kunststofftechnik Paderborn (KTP)
[2]Direct Manufacturing Research Center (DMRC)
University of Paderborn
Paderborn, North Rhine-Westphalia, Germany

INTRODUCTION

Fused Deposition Modeling (FDM) is an Additive Manufacturing (AM) technology which is used for prototypes, single-part-production and also small batch productions. It is one of the most used technologies in the AM market. This production technique has the huge benefit that no forming tool is needed and thermoplastic parts can be built out of the CAD model in only a few steps [1]. For use as a final product, it is important that the parts have good mechanical properties, smooth surfaces and a high dimensional accuracy. The knowledge about dimensional deviations of the FDM process is necessary for determining tolerances. Tolerances are needed for designing interactions between two or more parts or for calculating fittings [2].

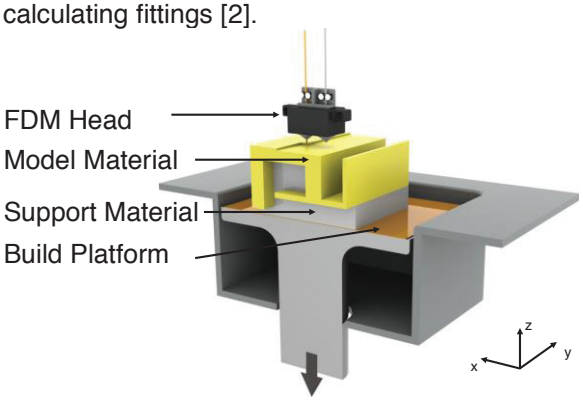

FIGURE 1. FDM process.

The FDM Process is shown in Figure 1. The strand shaped raw material is heated up in the FDM head. The molten material is deposited defined in X- and Y-direction on the build platform. After one layer is completed, the building platform is lowered by one layer thickness and the next layer will be deposited. There are two extrusion nozzles in the FDM head, one for the model and one for support material. The model material is used for the final part and the support material is necessary for bottom surfaces and to support overhangs and cavities. This support material can be removed in an additional post-processing step by breaking away or dissolving in an alkaline bath. The deposited material bonds with the layer beneath due to thermal fusion. This results in a strong and permanent bond between the layers [3].

The structure of a component layer is carried out in two steps. First of all the contour of one layer is deposited with one filament. Then the inner geometry is completed. The inner filling is done by default through a 45° raster. This raster angle changes for every layer by 90° so that there is an alternating raster fill for the parts. The Insight software from the manufacturer Stratasys is used for the data preparations. That includes the slicing of the STL file, generating support structures and the material extrusion path (toolpath).

There are several factors in the FDM process which may have an influence on the dimensional accuracy. These influence factors have been worked out in the project “Dimensional Tolerances for Additive Manufacturing” at the Direct Manufacturing Research Center (DMRC), University of Paderborn. The influence factors can be divided into six groups: geometric, material, measurement, machine-specific, environmental and procedural. But only a few parameters can be modified using Insight. Process parameters such as extrusion temperature or chamber temperature are fixed. In contrast, some parameters of the FDM process such as layer thickness or toolpath can be changed. The toolpath parameters define how the filling of the component is realized. The adjustable toolpath parameter include, but are not limited to: number of contours, filament width, raster angle and air gap between the filaments. Every change of the toolpath parameter results in a change of the mechanical behavior [4] [5]. To avoid this, it is possible to set a shrink factor (SF) in X-, Y- and Z-direction

independently. With this numerical factor the shrinkage of the polymer should be compensated during cooling to ambient temperature. The reason for this is, that polymers have a higher specific volume with increasing temperature. This effect is higher for semi-crystalline polymers than for amorphous polymers. The shrink factor is defined as follows:

$$Shrink\ Factor = \frac{L_{CAD} - L_{Part}}{L_{CAD}} \quad (1)$$

L_{CAD} is the drawing length of the part and L_{Part} is the real, measured length. In this work, the shrink factor is analyzed and optimized by a parameter variation.

MATERIAL AND MACHINE

In this work, the FDM system "Fortus 400mc" from Stratasys Inc. is used. This machine has a construction volume of 406 x 355 x 406 mm and there are 11 different thermoplastics available. These materials have different characteristics like high-performance, biocompatibility or resistance to heat, chemicals or UV radiation [6]. All specimens of this work are made with the material ABS-M30. This amorphous polymer is based on an acrylonitrile butadiene styrene copolymer and it is up to 25 to 70 % stronger than standard ABS [7]. In addition to good strength and stiffness properties, it has a very good impact resistance at low temperatures. The characteristics dimensional stability, hardness and scratch resistance make ABS very interesting for electronic housings or for applications in the toy and automotive industries. A disadvantage of this polymer is the low UV resistance [8]. ABS-M30 can be processed with four different layer thicknesses, which are realized with different tip sizes. By adjusting the tip size, it also leads to changes of temperatures in the FDM process. The layer thickness and the temperature for the four used tip sizes can be seen in Table 1.

TABLE 1. Tip sizes and the resulting layer thicknesses and temperatures.

Tip Size	Layer Thickness / mm	Model Temp. / °C	Chamber Temp. / °C
T10	0.127	320	85
T12	0.178	315	90
T16	0.254	315	95
T20	0.330	315	95

The model temperature corresponds to the set temperature of the heating element. The real melt temperature in the FDM process is unknown.

EXPERIMENTAL SETUP

To determine the dimensional accuracy of FDM parts manufactured with ABS-M30, test specimens have to be specified. For these investigations cuboids with a base area of 5 x 8 mm were chosen. The length of the cuboids will be varied in 8 steps between 3 mm and 100 mm. These nominal lengths were determined according to DIN EN ISO 286-1. In this DIN standard the nominal length is divided into classes. Here the maximum of each class is taken as the nominal length (except 100 mm). The test specimens are arranged on the build platform as seen in Figure 2.

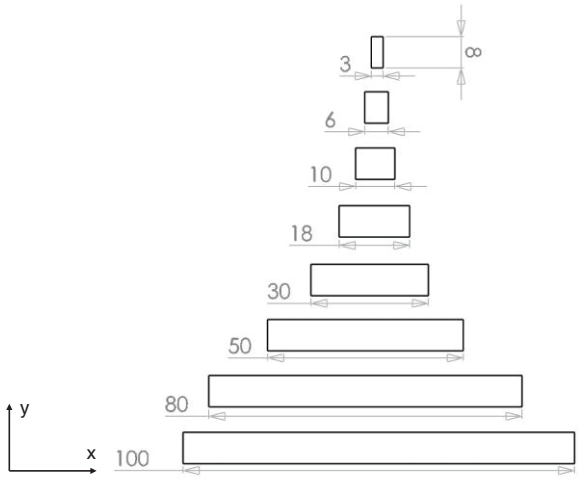

FIGURE 2. Test specimens with their nominal lengths.

For every direction in space three of these arrangements are built. Furthermore, the three test specimens of every direction are distributed over the entire build platform. Thus, a possible influence of the temperature distribution in the build chamber can be avoided. All in all there are 72 specimens (24 per orientation) in one build job. After building, the test specimens are conditioned for 88 hours at 23°C and a humidity of 50% (according to DIN EN ISO 291). The bottom support structures are removed by breaking away and not in alkaline bath. The specimens were measured with an outside micrometer for the respective measuring range. The used outside micrometer have an accuracy of ± 0.01 mm. Thus, a two-point measurement

was conducted on a defined measuring point. With this method, reproducible measurements are ensured.

ANALYSIS OF THE DIMENSIONAL ACCURACY

In the first step, the dimensional accuracy for the four different layer thicknesses is analyzed. This is the basis for further optimizations with the shrink factor. The standard parameters of the Insight software version 9.1 were used for these investigations. The parameters are shown in Table 2.

TABLE 2. Standard toolpath parameters.

Tip Size	Shrink Factor		Filament Width / mm
	XY	Z	
T10	1.0051	1.0059	0.3048
T12	1.0055	1.0059	0.3556
T16	1.0059	1.0059	0.5080
T20	1.0059	1.0059	0.6604

With these parameters the previously described test specimens were built. The dimensional accuracy is analyzed differentiated for each direction.

X-direction

The dimensional accuracy in X-direction is shown in Figure 3. The horizontal axis shows the nominal length of the test specimens from 3 to 100 mm. On the vertical axis the deviations from the nominal dimension are plotted. The four graphs represent the different layer thicknesses. All deviations are positive and they are in the range of 0.04 mm to 0.23 mm. It is visible that low layer thicknesses of 0.127 mm and 0.178 mm achieve very small deviations of around 0.05 mm for nominal lengths up to 50 mm. From a nominal length of 50 mm, the deviations increase slightly.

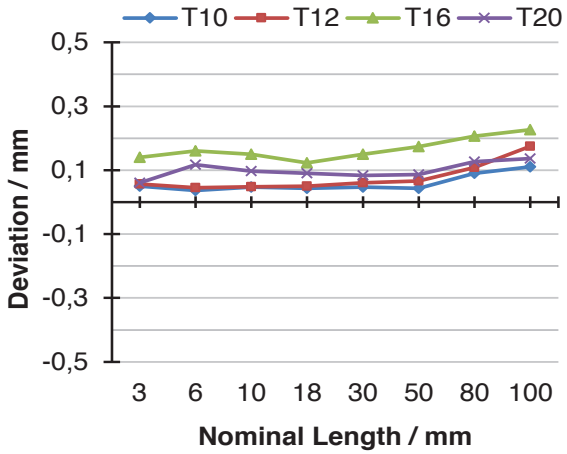

FIGURE 3. Dimensional accuracy in X-direction.

However, the T10 tip achieves for all specimens the smallest deviations. The highest deviation for the T10 tip size occurs for a nominal length of 100 mm and amount 0.11 mm. Unexpectedly, the dimensional accuracy of the T20 tip is better than the T16 tip. The diagram shows that the T16 tip has the highest deviations over the entire nominal lengths range. The standard deviation is very low for all layer thicknesses and averages around 0.02 mm. Only the standard deviation for the 100 mm specimens is slightly higher with an average value of 0.04 mm.

Y-direction

Next, the dimensional accuracy in Y-direction is discussed. The results of the measurement can be seen in Figure 4. In this direction the deviations are positive up to a nominal size of 30 mm. From a value of greater than 30 mm, the deviations tend to negative values. As described previously in the X-direction, the smallest deviations are achieved with a T10 and T12 tip. Up to a nominal length of 30 mm the 0.127 mm slice height provides the best results. From a nominal size of 50 mm the 0.178 mm slice height has a very good dimensional accuracy. The T12 tip has an average deviation of 0.03 mm. The highest deviations are recorded for the nominal size of 6 mm with an average of 0.12 mm. It can be noted that the slice height 0.254 mm and 0.330 mm have the highest deviations for all nominal lengths. The standard deviation is very low for nominal lengths up to 30 mm with an average of 0.02 mm. For specimens greater than 30 mm the standard deviations increase slightly and averaged circa 0.04 mm.

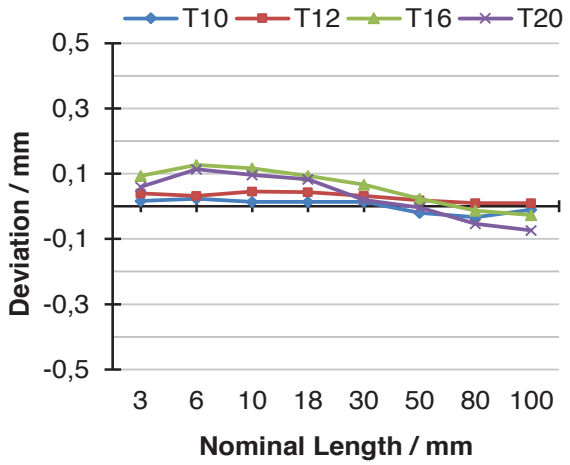

FIGURE 4. Dimensional accuracy in Y-direction.

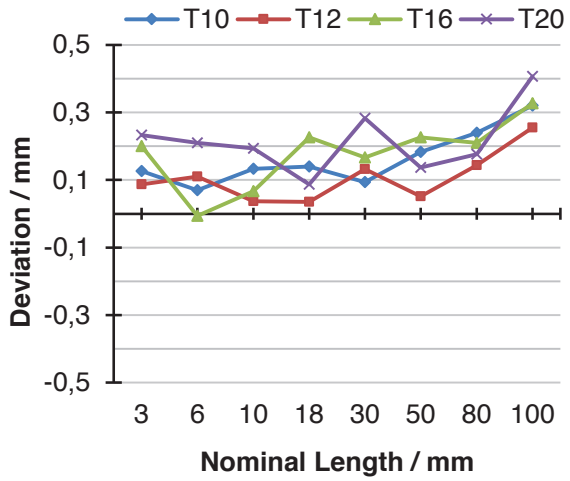

FIGURE 5. Dimensional accuracy in Z-direction.

Z-direction

In Z-direction it is visible that the deviations vary greatly for all slice heights (compare Figure 5). It is also recognizable that there are only positive deviations between 0 mm and 0.4 mm. The reason for this is that only whole multiples of the layer thickness can be realized. Another important point is the questions how many layers are generated by the Insight software. It has been observed that for some nominal lengths more layers are used as required. For a nominal length of 100 mm and a slice height of 0.178 mm 563 layers are calculated. Mathematically, only 561.8 (562) layers are required. Over the entire nominal dimension a layer thickness of 0.178 mm achieves the best accuracy. Then the T10 tip and then the tip sizes T16 and T20 follow. These tips tend to higher deviations due to their greater slice height. The standard deviations are very low with an average of 0.02 mm for the entire nominal dimension range.

PARAMETER OPTIMIZATION

After the initial state of the dimensional accuracy for all tip sizes is determined, a parameter variation of the shrink factor is conducted. In this paper only the T12 tip will be considered but of course the variation is also done for the other tip sizes. Within the parameter variation the shrink factor was adjusted to 1. This should determine which deviations occur when no shrink factor is set. Furthermore the shrink factor was set smaller and larger than the default value of 1.0055 (X- and Y-direction) respectively 1.0059 (Z-direction).

Optimization in X-direction

Figure 6 shows the influence of the shrink factor variation on the dimensional accuracy in X-direction. The purple graph indicates the standard shrink factor of 1.0055. It is visible that a shrink factor of 1 leads to huge negative deviations if the specimen is larger than 18 mm. In the small nominal deviation range up to 18 mm, all shrink factors behave similarly and the deviations are between 0 and 0.07 mm. Here, the shrink factor of 1.0035 has to be mentioned explicitly, because of the very low deviations. From a nominal length of 50 mm the deviations are negative for this shrink factor. The best accuracy for specimens from a nominal length of 50 to 100 mm is achievable with the shrink factor 1.0045. Thus, lower shrink factors obtain better dimensional accuracy in X-direction. The standard deviations for all measurements are slight with values between 0.01 and 0.05 mm.

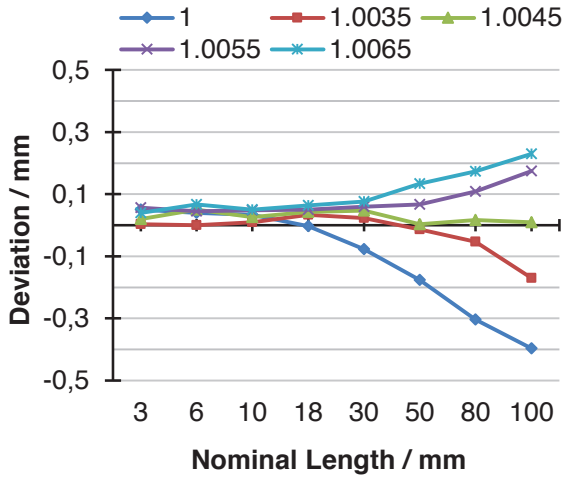

FIGURE 6. Influence of the shrink factor on the dimensional accuracy in X-direction (T12).

Optimization in Y-direction

As described previously, the dimensional accuracy in Y-direction is already good for all layer thicknesses. Hence, the standard shrink factor of 1.0055 has a good accuracy especially for larger nominal lengths (compare Figure 7). The shrink factors of 1, 1.0035 and 1.0045 have negative deviations for nominal lengths from 30 mm up to 100 mm. Only in the smaller nominal dimension range up to 10 mm, these parameters are useful to avoid dimensional deviations. A shrink factor of 1.0065 is not a good choice because the deviations over the entire nominal dimension range are too large. The standard deviations in Y-direction are slightly higher than in X-direction. The highest observed standard deviation is 0.07 mm, however on average it is 0.03 mm.

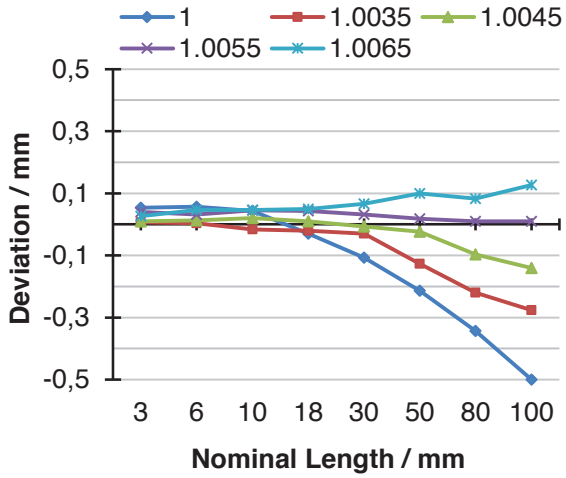

FIGURE 7. Influence of the shrink factor on the dimensional accuracy in Y-direction (T12).

Optimization in Z-direction

In the initial state, the dimensional accuracy in Z-direction for the T12 tip was already very good (compare Figure 5). Figure 8 shows the results from the parameter variation in Z-direction. The blue graph indicates the shrink factor of 1. This results in negative deviations for almost all nominal lengths except 3 and 6 mm. For these lengths the shrink factor 1 achieves the best results. With the shrink factors 1.0049 and 1.0039 the best dimensional accuracy is achieved for lengths from 50 mm to 100 mm. The standard deviations are very low with an average value of 0.02 mm.

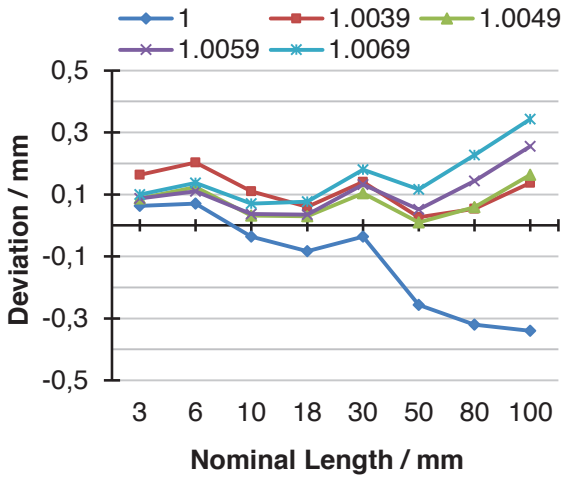

FIGURE 8. Influence of the shrink factor on the dimensional accuracy in Z-direction (T12).

CONCLUSIONS

In this paper the dimensional accuracy of FDM parts manufactured with ABS-M30 was analyzed and optimized. For this purpose, test specimens were defined that have different nominal lengths. The nominal dimensions were chosen in accordance to DIN EN ISO 286-1. The deviations from the nominal dimension were measured with outside micrometer on specimens, which were built with standard parameters of Insight version 9.1. The test specimens were built with four different tip sizes and in X-, Y- and Z-direction. Over the entire nominal dimension range from 3 mm to 100 mm, the T10 and T12 tip achieved the best results. The tip sizes T16 and T20 showed higher deviations. These investigations were done as a basis for further optimization. The optimization was conducted by a variation of the shrink factor for a T12 tip size (layer thickness of 0.178 mm).

The determination of optimal shrink factors was successful for all three dimensions. Therefore, optimized shrink factors have been found for specific nominal dimension. These results show that the FDM process can be used to build accurate parts if a sound knowledge is available. In order to use the FDM process for the production of final parts, tolerances must be identified and defined more precisely through in-depth research.

ACKNOWLEDGEMENTS

The authors want to thank all industry partners of the DMRC as well as the federal state of North Rhine-Westphalia and the University of Paderborn for the financial and operational support.

REFERENCES

[1] Wohlers T.: Wohlers Report 2014. Annual Worldwide Progress Report. 2014
[2] Jorden W., Schütte W.: Form- und Lagetoleranzen. Carl Hanser Verlag. Munich: 2012
[3] Wendel B.: Prozessuntersuchung des Fused Deposition Modeling. Dissertation, Friedrich-Alexander-University of Erlangen-Nürnberg: 2009
[4] Ahn S. H., Montero M., Odell D., Roundy S., Wright P. K.: Anisotropic Material Properties of Fused Deposition Modeling ABS. Rapid Prototyping. 2002; 8-4: 248-257.
[5] Es-Said O. S., Foyos J., Noorani R., Mendelson M, Marloth R.: Effect of Layer Orientation on Mechanical Properties of Rapid Prototyped Samples. Material and Manufacturing Processes. 2000; 15-1: 107-122
[6] Product Information Fortus 400mc. http://www.stratasys.com/3d-printers/production-series/fortus-360-400mc. Last Access: 02.04.2015
[7] ABS-M30 Specification Sheet. Stratasys. http://www.stratasys.com/~/media/Main/Secure/Material%20Specs%20MS/Fortus-Material-Specs/FortusABSM30MaterialSpecSheet-US-09-14-Web.pdf. Last Access: 28.03.2015
[8] Domininghaus H.: Kunststoffe - Eigenschaften und Anwendungen. Springer Verlag. Heidelberg: 2012

Proportional Topology Optimization Method for Frequency Optimization of 3D Printed Parts

Xue Wang[1], Emre Biyikli[1], and Albert C. To[1]

[1]Department of Mechanical Engineering and Materials Science
University of Pittsburgh
Pittsburgh, Pennsylvania, US

INSTRUCTIONS

Topology optimization is a branch of structural optimization which regards material distribution as the primary objective. With the advancement of computers, topology optimization experienced rapid growth in recent decades. Because of its ability to save materials significantly, it has already been applied to the design process of mechanical engineering, aerospace engineering, and architecture and some other engineering structures.

Frequency topology optimization has an important role in engineered structures. During the operation of this kind of structures, certain factors such as wind incentive, vibration generated by the engine or even waves from earthquakes cannot be avoided. In these cases, dynamic damage has become the main failure mode. Compared with compliance and stress optimization problems, very few research works have focused on frequency problems. In the work of Tenek (1994), he presents an optimization on isotropic and anisotropic plates for single or multiple eigenfrequency maximization problems using homogenization method [1]. After that Zhengdong Ma (1995) used this method to maximize eigenvalues as well as frequency response optimization problem [2]. As the traditional solid isotropic material with penalization method (SIMP) is not suitable for dynamic problems, research conducted by Pedersen (2000) proposed a modified SIMP model to optimize frequencies [3]. Also by using this method, Du et al (2007) discussed topology optimization involved both single and multiple eigenfrequencies [4].

All the methods that have been mentioned above are gradient-based method, but calculating gradients introduces computational burden and also other implementation concerns. This paper introduces a new topology optimization method called the Proportional Topology Optimization (PTO) [5] that minimizes the total mass of the system in order to reduce the material consumption as well as keep the resonant frequency away from external excitation frequency range.

This paper will present PTO algorithm, frequency problem, numerical examples and conclusions.

PROPORTIONAL TOPOLOGY OPTIMIZATION (PTO) METHOD.

PTO is a non-gradient algorithm that aims to solve the difficulties associated with gradient-based methods. It is easy to understand and the main idea of this algorithm is to assign the design variables to elements proportionally to the value which has a relation with the target function. The classical constrained stress and minimum compliance problems have been solved using this algorithm and this paper would focus on the frequency optimization.

Based on TOP99 computer program, the method had already been implemented into two MATLAB programs which aim to solve the constrained stress and minimum compliance problems. In this paper, the frequency optimization algorithm would be implemented into those programs.

FREQUENCY CONSTRAINED PROBLEM.

The frequency topology optimization problem involves minimizing the whole mass of structural while satisfying the frequency constraints, as

described in Figure 1. This optimization problem takes the following mathematical form:

$$\begin{aligned} &min\, M_{tol} = \sum_{i=1}^{N} \rho_i v_i \\ s.t. &\begin{cases} f^* \le f_{min} \\ 0 \le \rho_{min} \le \rho_i \le \rho_{max} \le 1 \end{cases} \end{aligned} \tag{1}$$

where M_{tol} is the target function which indicates the total mass of the structure, *N* the total number of elements, ρ_i the density of element i, v_i the volume of element *i*. The first constraint means that the minimum natural frequency of the structure f_{min} must be no less than the given frequency f^*. The second constraint indicates that the relative density is bounded by the minimum and maximum relative densities ρ_{min} and ρ_{max}, respectively. Note that these two parameters are usually set as 0 and 1, respectively, in conventional topology optimization problems.

The optimization process is implemented via updating the density of each element according to the following scheme:

$$P_i = elind^q$$

$$P_i = P_i \Big/ \left(\sum_{i=0}^{N} P_i \right)$$

$$\rho_i^{dis} = M_{rem} P_i \tag{2}$$

$$\rho_i^{new} = \rho_i^{new} + \rho_i^{dis}$$

$$\rho_i^{new} = max\{min(\rho_i^{new}, \rho_{max}), \rho_{min}\}$$

$$M_{rem} = M_{tar} - \sum_{i=0}^{N} \rho_i^{new}$$

where P_i is the proportional value for element *i*, *q* is the proportion exponent, ρ_i^{dis} is the part that should be assigned to *i* element, M_{rem} is the remaining material amount, M_{tar} is the target material amount which would change during the optimization process, ρ_i^{new} is the updated density for this element. elind is the indicator which is defined as:

$$elind = u_s^T k_e u_s$$

where k_e is the local stiffness matrix of element, u_s is the corresponding eigenvector of the minimum natural frequency.

Algorithm

- Setup FE and dynamic analyses and filtering
- Until convergence
  - Perform FE and dynamic analyses
  - Calculate indicator values
  - Check stop criteria, break if satisfied
  - Run optimization algorithm
    - Determine TM
      - Distribute RM
        - If frequency limit is exceeded, TM = CM - MM
        - Else, TM = CM + MM
    - Set RM = TM
    - Until RM is small enough
      - Distribute RM to element proportionally to their indicator
      - Apply filter
      - Apply frequency limits
      - Calculate AM
      - Update RM = TM – AM
    - Update density

where TM is the target material amount, CM is the current material amount, MM is the material move amount, RM is the remaining material amount,

FIGURE 1. PTOfc algorithm to solve the frequency problem.

Until now, it seems that the optimization problem Eq. (1) can be conducted through the algorithm shown in Eq. (2). However, solution control must be enforced in order to obtain reasonable results. There are mainly two reasons why this is necessary. The first one is already well-known, that is, the convergence and checkerboard problem may occur due to the intrinsic deficiency of FEA when used for topology optimization [7]. The second one is the localized modes phenomenon that occurs at low density area. At present, there are many proposed algorithms to handle these two problems [6][8]. A density filter is employed to relieve or eliminate the checkerboard problem which is shown in Eq. (3) and a new polynomial interpolation function which is used to avoid localized modes is shown in Eq. (4):

$$\rho_i = \frac{\sum w_{ij} d_j}{\sum w_{ij}}$$

$$w_{ij} = \begin{cases} \frac{r_0 - r_{ij}}{r_0} & for\ r_{ij} < r_0 \\ 0 & for\ r_{ij} \geq r_0 \end{cases} \quad (3)$$

where w_{ij} is the filtering weight of elements *i* and *j*, d_j is the non-filtered density of element *j*, r_{ij} is the distance between elements *i* and *j*, r_0 is the filter radius.

$$E(\rho) = E_{min} + E_0 g(\rho) \quad (4)$$

where $E(\rho)$ is the density dependent Young's modulus, E_{min} is a small Young's modulus assigned to void elements, E_0 is the Young's modulus of solid material, $g(\rho)$ is the penalization factor which is a polynomial interpolation function of density. In the following examples, function (5) will be used.

$$g(\rho) = \frac{4}{3}(\rho)^3 - \frac{2}{3}(\rho)^2 + \frac{1}{3}(\rho) \quad (5)$$

NUMERICAL EXAMPLES.

The example is a double-clamped beam with dimensions of 15 cm× 5 cm× 5 cm as shown in Figure 2. Material is assumed to have Young's modulus E_0=1.747 GPa, Passion's ratio v = 0.3 and mass density ρ=1.15 g/cm^3. This model is divided into 50 × 17 × 17 hexahedron elements. Calculation begins with a volume fraction of 0.7 and the initial fundamental frequency is 81.81Hz, set the frequency constraint for this problem to be $f_c \geq 92$ Hz.

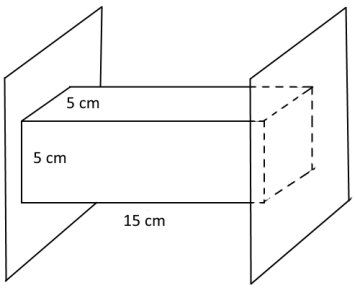

FIGURE 2. a double clamped beam

Figure 3 (a) shows the final configuration of the beam after optimization, the volume fraction becomes 0.67. Figure 3 (b) is the half structure corresponding to (a). Iteration curve of optimization is shown in figure 4. During the first 25 iterations, the total mass keeps stable but the frequency is growing until reach almost 96 Hz, then as mass decrease step by step.

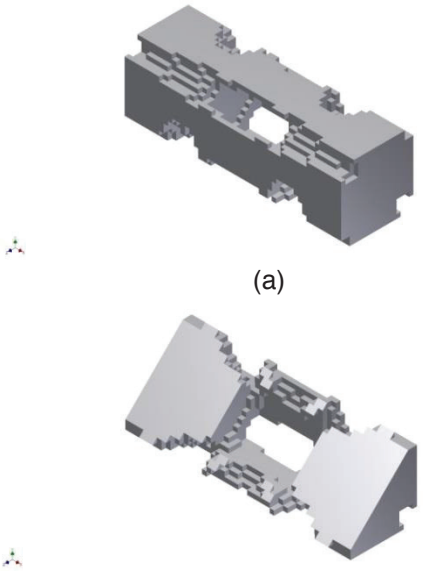

(a)

(b)

FIGURE 3. (a) The final design with $f_c \geq 92$ Hz. (b) half of the structure

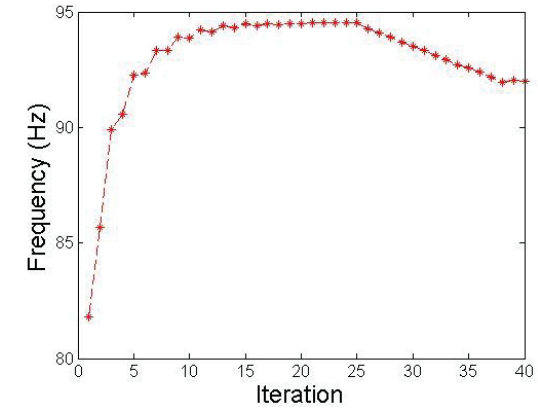

(a)

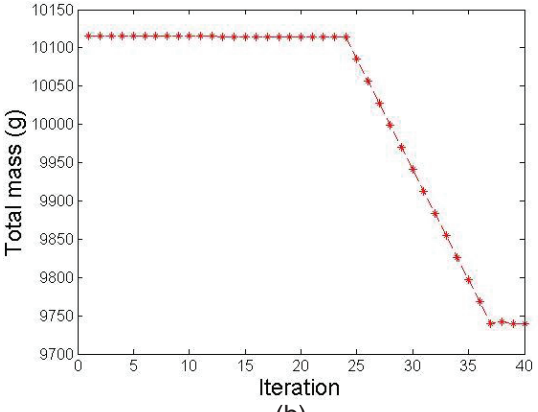

(b)

FIGURE 4. Iteration process

The final optimized structure has been successfully printed using a 3D printer and a picture of it is shown in Figure 5.

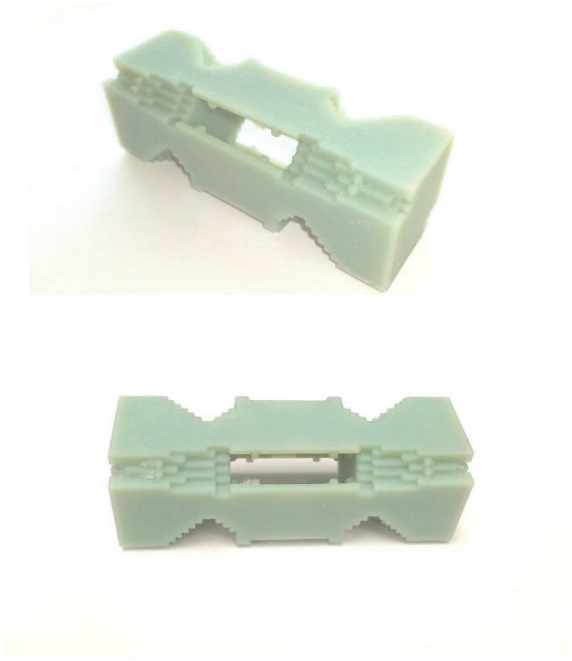

FIGURE 5. Model that printed by a 3D printer

CONCLUSIONS

A new non-gradient method called PTO is introduced in this paper to solve frequency optimization problem. One 3D example is used to prove the validity of this method for minimizing the total mass while constraining the fundamental frequency. This method will be applied to optimize several other structures in the future. Some experiment will also be done to test the printed structure for validation purpose.

REFERENCES

[1] Tenek H Lazarus and Hagiwara Ichiro (1994). Eigenfrequency maximization of plates by optimization of topology using homogenizatio mathematical programming. JSME Int J.37:667-677.

[2] Zhengdong Ma, Noboru Kikuchi and Hsienchile Cheng (1995). Topologycal design for vibrating structures. Computer Methods in Applied Mechanics and Engineering.121:259-280.

[3] Jianbin Du, Niels Olhoff (2007). Topologycal design of freely vibrating continuum structures for maximum values of simple and multiple eigenfrequencies and frequency gaps. Computer Methods in Applied Mechanics and Engineering.121:259-280.

[4] Niels Leergaard Pedersen (2000). Maximization of eigenvalues using topology optimization. Struct Multidiscip Optimiz.20:2-11.

[5] Emre Biyikli, and Albert C. To (2014). Proportional Topology Optimization: A new non-sensitivity method for solving stress constrained and minimum compliance problems and its implementation in MATLAB, under review.

[6] Bin Wang (2010). Multi-performance optimization of structures and its application in aerospace structural design. Ph.D. Thesis. Dalian university of technology.

[7] Martin. P. Bendsoe, Ole Sigmund (2003), Topology optimization: theory, methods and applications: Springer.

[8] Tyler E Bruns, Daniel A Totorelli (2001). Topology optimization of non-linear elastic structures and compliant mechanisms. Computer Methods in Applied Mechanics and Engineering 190:3443-3459.

LONG-TERM POSITIONING EFFECTIVENESS OF ADDITIVE MANUFACTURED-MONOLITHIC DOUBLE COMPOUND NOTCH TYPE FLEXURE STAGE

ChaBum Lee[1], Sun-Kyu Lee[2], and Joshua A Tarbutton[1]
[1]Department of Mechanical Engineering
University of South Carolina
Columbia, South Carolina, United States
[2]School of Mechatronics
Gwangju Institute of Science and Technology
Gwangju, South Korea

INSTRUCTIONS

Precision linear translation stages in general utilize flexures to provide linear or angular motion without friction or stiction. These flexure mechanisms are typically machined with a mill or electro-discharge machines (EDM) from solid blocks of metal resulting in a mechanism with precise linear motion with minimal off axis error motion for high positioning accuracy and resolution [1-4]. The monolithic flexure mechanism is the key to major breakthroughs in broad research areas and industrial applications including bio-nanotechnology, nanometrology, semiconductor manufacturing, chemical science and engineering, nano-machining and nanofabrication, material science, and high-density data storage systems [3-8].

For precision translation and positioning systems, most of the mechanisms manufactured today exploit the versatile capabilities of CNC machine tools, EDMs or waterjet. Nearly all flexure systems are fabricated using conductive materials, primarily metal. Flexure system fabrication uses methods planar processing methods to remove material. However, metal-based flexure stages are not only time consuming and expensive to manufacture but also difficult to use in chemical, electrical and electromagnetic environment, and in bio-tissue-handling work. Metallic flexure systems are subject to corrosion, interference with electromagnetic field distributions and can suffer from biocompatibility issues [2,4]. In addition, system bandwidth of the commercially-available metal-based flexure stages is approximately 100*Hz* because most flexure stages have a low first resonance frequency (less than 400*Hz*) [9]. Recently, with progress of microelectromechanical system (MEMS) technology, many MEMS motion stages have been introduced [10,11]. However, the total displacement is limited to a few tens of *μm* even though those are promising for compactness, high bandwidth and high resolution.

The use of polymer as a material for flexure stages can be an alternative method to explore various biological, electrical and magnetic applications because general polymers are biocompatible and electrically insulating. Also, it can provide a large deflection with low force compared to the metal flexures, and the polymeric materials have a higher damping than the conventional metal.

In this paper, the concept of a polymeric flexure mechanism for a long working range and low cost is presented by using AM technology. The double compound notch flexure mechanism made of photopolymer is explored to demonstrate this concept and the effects of its geometry on the flexural deflection and stress are investigated. The optical position sensor for displacement measurement is embedded into a monolithic linear translation stage to control the positioning of the stage. In addition, the positioning and thermal characteristics are empirically studied by actuating the stage over millions of cycles.

SYSTEM CONFIGURATION

The design of a double compound notch type flexure mechanism was employed in this study. This double compound kinematic design is well-known in precision engineering. It has a symmetric design configuration consisting of four compound springs attached at the shuttle. The use of four compound springs joined together constrains the stage motion to prevent deviation from rectilinear motion. The translation of the shuttle is controlled by the elastic deformation of two identical four-spring mechanisms. The use of two symmetrical four-spring mechanisms offers an additional

advantage that the system can self-compensate for thermal expansion [3]. The voice coil motor (VCM) was used as an actuator and was assembled with the flexure stage and aligned along the moving axis of the stage to mitigate Abbe error [5].

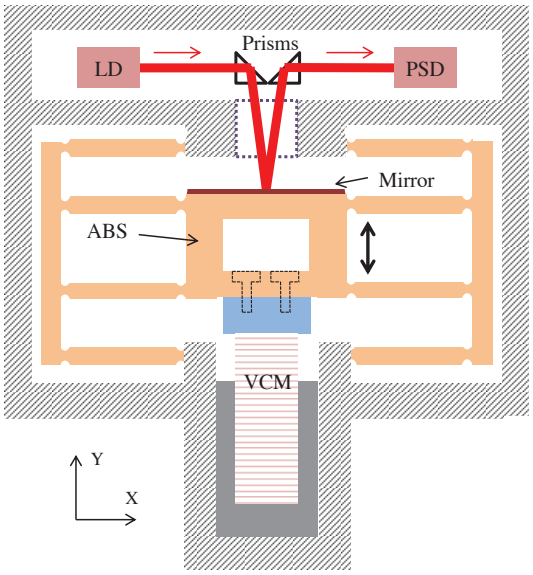

Figure 1. Schematic illustrations of sensor and actuator-integrated flexure stage.

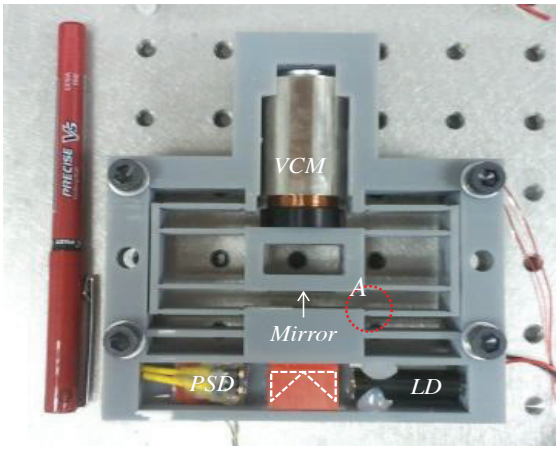

Figure 2. Image of the flexure stage.

An optical measurement system was incorporated to measure the stage position in real time as depicted in Figure 1. The displacement measurement system consists of a laser diode (λ 650nm), two right angle prisms, mirror (100nm thickness Au-evaporated on 500μm-thick Si substrate) and a position sensitive detector (PSD, 1×6mm^2) as seen in Figure 2. The laser light reflects off the prism surface by total internal reflection and travels to the mirror surface attached with the shuttle. As the shuttle moves, the light reflects off the mirror with offset distance, the reflected light is incident on the other prism and reflects toward the PSD. All optical components were firmly fixed with the flexure stage and aligned along the moving axis of the stage to mitigate Abbe error [5]. PSDs are commonly used because they are inexpensive and capable of measuring lateral displacement in one or two dimensions. PSDs contain two, four or more segmented photodiodes positioned symmetrically around the center of the detector. Each segment is separated by a narrow gap and has anode and common cathode contacts. Position information is derived from the optical signal powers received by the segmented photodiodes and defined by the relative position of the beam spot with respect to the center of the devices [12]. Two prisms were used to mechanically amplify the displacement by adjusting the angle at installation.

The parasitic motion of the flexure stage is critical for precision positioning applications [5,6]. It is expected that the designed polymeric flexure stage somehow has the parasitic motion along the out-of-plane directions because the shuttle is likely to bow under load from the coil weight and mirror even though they are light-weight. In this study, it was assumed that the voice coil attached with the shuttle is firmly fixed along the center line of the stage motion and moves along its center line because of magnetic force.

The polymeric material properties of AM parts are highly dependent on fabrication conditions such as photopolymer materials, printing layer-to-layer thickness, printing temperature and post-curing temperature and time. Thus, the elastic modulus of the AM flexure was experimentally measured by using stress-strain testing machine, and this result was used to estimate the flexural deflection and stress at a given condition. The flexure specimens (H12.7×W127×T3.3mm^3) made of photo-sensitive photopolymer (Visijet® SL Tough) were fabricated by stereolithography process (Projet®6000HD, 3D Systems Inc.). The layer-to-layer printing thickness, printing temperature and curing temperature and time were set to 125μm, 29°C, room temperature and 50min. with UV light, respectively. According to the datasheet [13], the elastic modulus of photo-polymer is 1.85GPa, but the strain-stress test result showed 795MPa.

Flexure hinges experience both bending and shear stress and their magnitude depends on the geometry of the flexure mechanism and the

nature of the applied loads. The commercially-available software package, Ansys, was used. The target displacement of the flexure stage is set to ±2.0*mm* in the study. The maximum applied force was limited to 1.375N per flexure because the VCM can produce 11N and the stage consists of total 8 flexures. In a double compound notch type flexure mechanism, the displacement of each flexure becomes a half of the total displacement of the shuttle under an identical flexure geometry condition [3]. The flexure was designed (see Figure 3).

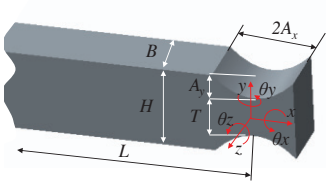

Figure 3. Hinge configuration: A_x=0.75mm, A_y=0.15mm, T=1.2mm, H=1.5mm, B=20.0mm and L=25.0mm

The maximum displacement and stress of the flexure stage were estimated approximately 3.0mm and 10.2MPa.

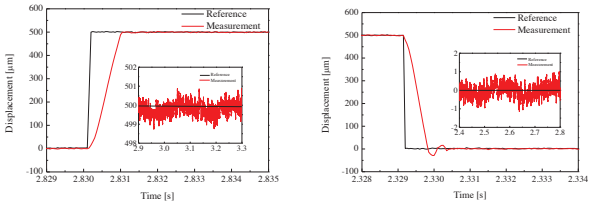

Figure 4. Results of step response of the flexure stage: forward(left) and backward (right).

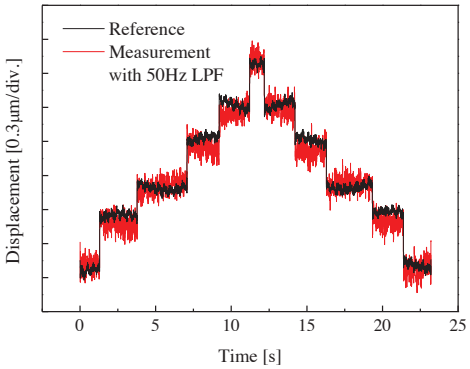

Figure 5. Resolution test of the flexure stage.

RESULTS

The PSD was calibrated with a coordinate measuring machine (CMM) with resolution 0.01μm. The PSD showed with sensitivity 4.398*V/mm* within the total working range 4.5mm. The displacement error due to nonlinearity of the sensor was estimated 3.6μm over the full range. This sensor was used for positioning feedback control of the stage.

The VCM and PSD-based displacement sensor were assembled with the flexure stage and aligned along the moving axis of the stage to mitigate Abbe error. The stage positioning was feedback-controlled by using an analog proportional-integral-derivative (PID) gain tuning. As seen in Figure 4, the stage showed good fast response characteristics (settling time approximately 0.9msec) and positioning performance (steady-state positioning accuracy less than ±0.3μm) to a 500μm displacement square-wave step command. The positioning resolution was evaluated by applying a stepwise signal as shown in Figure 5. The displacement of each step was set to the noise of the measurement system because it is in general affected by the noise in the measurement system. The resolution of the input signal (function generator) is 1mV (total working range -10V ~ +10V), which corresponds to approximately 0.2μm. The stepwise test results show that the noise level of the PSD sensor has approximately 0.3μm, which can be understood and the stage system has a resolution of 0.3μm at an ambient condition. It is considered that the use of high resolution digital controller can show a further improvement in positioning resolution and accuracy.

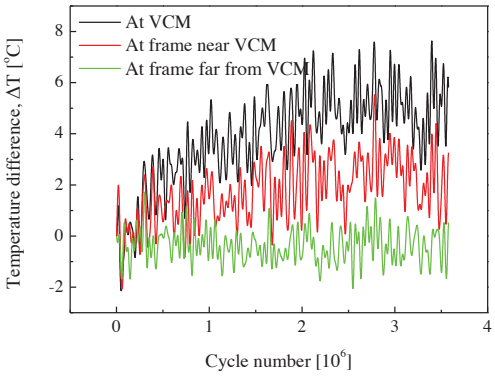

Figure 6. Temperature measurement of the flexure stage during 3.6 million cycles.

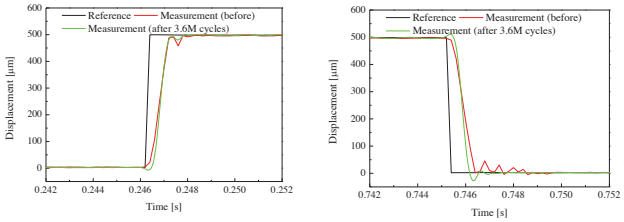

Figure 7. Results of step responses before and after 3.6 million cycles: forward(left) and backward (right).

A preliminary investigation of thermal effects was performed and the temperature was measured at the following three points: at the VCM, at the frame near VCM and at the frame far from VCM (PSD area). The temperature was monitored while the flexure was being subjected to cyclic loading of 3.6 million cycles in a temperature-controlled lab environment. The temperature of VCM and the frame near VCM rapidly increased and saturated at 6.0ºC and 2.5ºC after approximately 2 million cycles as shown in Figure 6. However, the temperature at the frame far from VCM remained constant with a small fluctuation. The results of step response before and after 3.6 million cycles were compared, and positioning accuracy and control performance showed no significant difference in steady-steady response characteristics between two step response results as seen in Figure 7. However, small difference in rising time and falling time between two results was found. It was thought that changes in temperature and material property of the flexures have an influence on the dynamic characteristics of the stage.

CONCLUSION

The low cost polymer-based monolithic flexure stage for millimeter-level working range was designed and the effect of its geometry on the deflection and stress of the flexures were investigated. As a result of the AM surface quality of the flexures, the AM approach to the flexure fabrication can replace a conventional EDM process because AM process can create the flexures made of polymer as well as metal. As a result of experiment, 0.3μm positioning resolution of the stage was achieved. Compared to the conventional metal-based flexure stage, the proposed polymeric stage showed high frequency operation and high bandwidth due to low mass density and the damping effect of the polymeric material, which are considered to provide design flexibility in flexure stages. From preliminary studies, it was found that material properties of AM parts are highly dependent on the fabrication conditions such as printing layer-to-layer thickness, printing temperature and post-curing temperature and time. Thus, the thermal, environmental and fatigue issues of the polymeric flexure stage as well as detailed material property characterization is subject of ongoing research.

REFERENCES

[1] Stuart T. Smith, Vivek G. Badami, Jami S. Dale, and Ying Xu, “Elliptical flexure hinges,” Rev. Sci. Instrum. Vol. 68, No. 3, pp. 1474-1483, 1997.

[2] Ki Woon Chae, Wook-Bae Kim and Young Hun Jeong, “A transparent polymeric flexure-hinge nanopositioner, actuated by a piezoelectric stack actuator,” Nanotechnology, No. 22, 335501, 2011.

[3] Smith, S., Flexures: Elements of Elastic Mechanisms, Taylor & Francis, London, England, 2002.

[4] Y. K. Yong, S. O. R. Moheimani, B. J. Kenton, and K. K. Leang, “Invited Review Article: High-speed flexure-guided nanopositioning: Mechanical design and control issues,” Rev. Sci. Instrum. Vol. 83, 121101, 2012.

[5] ChaBum Lee, Gyu-Ha Kim and Sun-Kyu Lee, “Uncertainty investigation of grating interferometry in six degree-of-freedom motion error measurement,” Int. J. Precis. Eng. Manuf., Vol. 13, No. 9, pp. 1509-1515, 2012.

[6] ChaBum Lee, Gyu-Ha Kim and Sun-Kyu Lee, “Design and construction of a single unit multi-function optical encoder for a six-degree-of-freedom motion error measurement in an ultraprecision linear stage,” Meas. Sci. Technol. Vol. 22, 105901, 2011.

[7] A. M. Hoover, S. Avadhanula, R. E. Groff, Ronald S. Fearing, “A rapidly prototyped 2-axis positioning stage for microassembly using large displacement compliant mechanism,” Proc. 2006 IEEE Intl. Conf. Robotics and Automation, Orlando, Florida, USA, May 2006.

[8] ChaBum Lee, Sun-Kyu Lee and Joshua A. Tarbutton, “Novel design and sensitivity analysis of displacement measurement system utilizing knife edge diffraction for nanopositioning stages,” Rev. Sci. Instrum., Vol. 85, 095113, 2014.

[9] Yuen Kuan Yong, Sumeet S. Aphale, and S. O. Reza Moheimani, “Design, Identification, and Control of a Flexure-Based *XY* Stage for Fast Nanoscale Positioning,” IEEE Trans. Nanotechnol., Vol. 8, No. 1, pp. 46-54, 2009.

[10] Y-S Kim, N G Dagalakis and S K Gupta, “Design of MEMS based three-axis motion stage by incorportating a nested structure,” J. Micromech. Microeng., Vol. 24, 075009, 2014.

[11] Lining Sun, Jiachou Wang, Weibin Rong, Xinxin Li and Haifei Bao, “A silicon integrated micro nano-positionoing Xy-stage for nano-manipulation,” J. Micromech. Microeng., Vol. 18, 125004, 2008.

[12] Akihide Kimura, Wei Gao and Satoshi Kiyono, “Design and construction of a surface encoder with dual sine-grid,” Int. J. Precis. Eng. Manuf., Vol. 8, pp. 20-25, 2007.

[13] Material information: VisiJet® SL Tough, Available http://www.3dsystems.com/sites/www.3dsystems.com/files/projet_6000_7000_0514_us_web.pdf, 3DSystems, Inc., Retrieved on Aug. 6, 2014.

FEATURES AND TOLERANCES IN ADDITIVE MANUFACTURING - AN EXTENSION TO THE AMF FILE FORMAT

Harshad Srinivasan[1], Dr Ola L. A. Harrysson[1], and Dr Richard A. Wysk[2]
[1]Industrial and Systems Engineering
North Carolina State Univertisy
Raleign, North Carolina, USA, 27695

THE NEED FOR FEATURES AND TOLERANCES IN ADDITIVE MANUFACTURING

In the traditional manufacturing paradigm, the features which comprise a part are assigned tolerances of position, orientation, size and form. This information is used to drive the selection and sequence of processes used to produce the part, in order to ensure that the part meets it's design specifications. Additive manufacturing (AM), however, has traditionally been a featureless manufacturing activity; the standard file format for AM – STL – describes the part as a single surface representation with no support for features and tolerances.

As AM transitions from a means of producing prototypes to a means of producing parts for end use, it is increasingly important for dimensional and surface requirements to be met. This observation is reinforced by the existence of a significant number of process planning systems that aim to improve the dimensional and surface properties produced by AM processes [1] [2] [3] [4] [5]. In many such approaches, process planning is performed at the feature level; process parameters such as build orientation and slice thickness are optimized to ensure critical features are produced to within a specified tolerance.

However, due to the featureless nature of current file formats for AM applications, process planning systems for AM have not reached significant prevalence in actual usage. Without a standard data exchange format that supports the demarcation of features and tolerances, process planning systems are forced to either use overly complicated formats such as STEP, use vendor specific CAD formats or resort to systems in which an operator is required to input the required tolerances at the point of manufacture. Past data formats designed to address this need, such as STA [6], have not been widely adopted.

THE AMF FILE FORMAT

The additive manufacturing file format, AMF, is a new format for additive manufacturing which attempts to address many of the deficiencies of STL while still maintaining the overall simplicity of STL's tessellated representation [7] [8]. Improvements in AMF include a more robust and efficient point-triangle representation, support for multiple distinct part volumes, which can each be assigned separate properties, greatly improved means for representing mesh structures and an XML based file structure for simplified processing.

TOLERANCE EXTENSIONS TO AMF

The current version of the AMF format does not include a means of demarcating manufacturing features or indicating tolerances. The 2013 AMF standard recognises this, and lists **X2.1.1 Future Provisions for Dimensional and Geometric Tolerances** and **X2.1.2 future provisions for surface roughnes** as future goals in apenxix X2.1. In this work, we describe an extension to the AMF format for assigning tolerances by demarcating standard features in the part geometry and assigning ASME Y14.5 [9] tolerances to them.

This feature based approach was selected to match the traditional manufacturing paradigm and to tap into the considerable technology, expertise and body of knowledge that has been developed to address feature based process planning. In addition, an AMF file which includes standardized feature definitions and tolerances can also be used as a data format for finish machining, qualification and other post–processing applications, activities which are gaining importance due to industry requirements.

Structure of AMF and extensions

In AMF, a single *object* is represented by multiple *volumes* which each consist of a set of *triangles* forming a manifold tessellated surface. The triangles are defined by referencing three vertices by

their index (vertices may be shared between triangles for efficiency and robustness). Vertex index is implicitly assigned by the order a vertex appears in the XML structure. Triangles and volumes do not possess any explicit or implicit order. AMF also supports curved triangles for more accurate representation of non-planar surfaces.

The fundamental building block of an object in an AMF file is the triangle, since it represents the bounding space occupied by the object. In order to reflect this, this work defines a feature *as a group of demarcated triangles with an associated unique id, name, class and tolerances*.

Feature structure

The data pertaining to each feature is described in a section under $< object >$, denoted by a $< features >$ tag. Each feature under $< features >$ is denoted by a $< feature >$ tag which has a unique integer "id" attribute. This attribute is used to identify the feature. A feature contains a single $< class >$ and $< name >$ and zero or more $< note >$ and $< tolerance >$ tags:

$< class >$ holds a string descriptor of the feature class – cylinder, plane, sphere etc.

$< name >$ holds a string name for the feature. The primary purpose of a feature name is human readability.

$< note >$ holds a string note meant to contain any extra information pertinent to the feature. Multiple $< note >$ may be provided.

$< tolerance >$ holds an ASME Y14.5 tolerance callout for the feature.

Figure 1 shows the structure of an AMF file with the feature and tolerance extensions.

Demarcation of triangles

Since triangles in an AMF file do not possess an id or index that can be used to identify them, demarcation is performed by marking each triangle that is part of the feature with the feature's unique feature ID . This is performed by inserting a $< featureid >$ tag into the $< triangle >$ structure (Figure 2).

This approach was also selected as it is highly compatible with software that is not 'aware' of this

```
<?xml version="1.0" encoding="UTF-8"?>
<amf unit = "millimeter">
  <object "id" = 0>
    <mesh>
      <vertices>
       ...
      </vertices>
      <volume>
       ...
      </volume>
      <volume>
       ...
      </volume>
    </mesh>
    <features>
      <feature "id"= 1>
        <class> plane </class>
        <name> bearing surface </name>
        <note> Example note </note>
        <note> Another note </note>
        <tolerance>
         ...
        </tolerance>
        <tolerance>
         ...
        </tolerance>
      </feature>
      <feature "id"=2>
       ...
      </feature>
    </features>
  </object>
</amf>
```

FIGURE 1. Feature structure; Extensions to AMF are in bold; "..." used to represent tags/data not shown

extension to AMF as feature–triangle associations remain intact even if triangle order is changed or if volumes are manipulated. In addition, it is possible to demarcate triangles across multiple volumes (Figure 3)

Tolerances

Tolerances of form and position (position includes orientation) can be applied to features by means of the $< tolerance >$ tag. A single tolerance consists of:

$< callout >$ holds a string describing the tolerance callout. Examples include *orientation*, *cylindricity*, *planarity* and *Ra* (surface roughness). It is the responsibility of the user / software generating a toleranced AMF file to ensure the callout is compatible with the feature class.

```
<volume>
  <triangle>
    <v1> 1 </v2>
    <v2> 2 </v2>
    <v3> 3 </v3>
    <featureid> 1 </featureid>
  </triangle>
</volume>
```

FIGURE 2. Demarcation of triangle with $< featureid >$

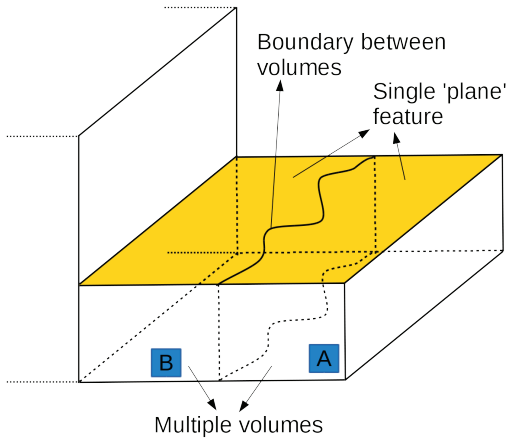

FIGURE 3. Single feature across volumes

$< maximum >$ holds a positive floating point maximum value for the tolerance in question.

$< minimum >$ holds a positive floating point minimum value for the tolerance.

$< condition >$ holds a string material condition at which the tolerance is applied. For example *mmc*, *lmc* and *rfs*

$< datum >$ contains information describing a single datum reference feature for this tolerance. Multiple datums may be specified with multiple instances of $< datum >$ in the $< tolerance >$

Acceptable values for the tolerance callout include all basic geometric characteristics described by ASME Y14.5 plus displacement, orientation and any intrinsic tolerances of form or size that may be applicable, such as *diameter* or *Ra*. These additions allow tolerances of position, form and surface quality to be represented in a manner similar to the standard tolerance callouts.

The values for $< maximum >$ and $< minimum >$ are always positive; using a negative value results in undefined behavior. When used with ASME Y14.5 basic geometric characteristics the $< maximum >$ value, without a paired $< minimum >$, is interpreted as the bilateral *tolerance value*. If both $< maximum >$ and $< minimum >$ are present, the tolerance value is the maximum value + the minimum value and $< maximum >$ represents the "in–space" portion of the tolerance zone while the $< minimum >$ value the "in–material" portion of the tolerance zone (Figure 4). This is equivalent to the unequally disposed profile modifier Ⓤ.

A similar interpretation applies when used with callouts denoting feature size , position or orientation. The $< maximum >$ value should be interpreted as the bilateral size of the tolerance zone if present without $< minimum >$. If both are present, $< maximum >$ is interpreted as the size of the tolerance zone in direction which increases the absolute value of the given callout while $< minimum >$ gives the size of the tolerance zone in the direction that decreases the absolute value.

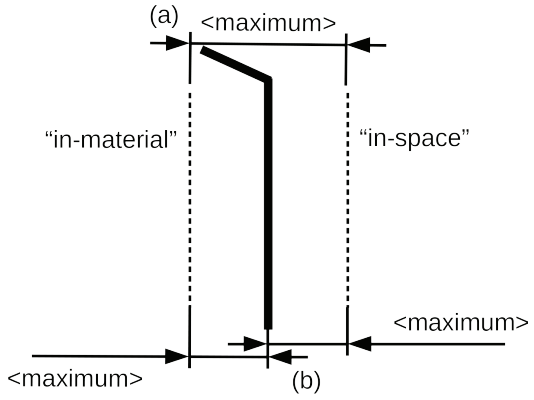

FIGURE 4. Interpretation of tolerance zone; (a) $< maximum >$ *alone (b) both* $< maximum >$ *and* $< minimum >$

All values are in the same units as specified in the header of the AMF file.

Figure 5 shows the tolerance callout for a cylindrical feature.

Nominal values and basic dimensions

All basic dimensions and nominal values must be determined by examining the actual features

geometry, I.e. the demarcated triangles. This approach was selected to more closely tie the dimensions and tolerances to the actual geometry of the part. A separate specification of the nominal values and basic dimensions lends itself to conflicts in interpretation if the part geometry is modified without also updating the specified nominal values.

Datums

A position or orientation tolerance must with respect to one or more reference features (datums). Each datum is specified by a $< datum >$ tag which contains a $< featureid >$ and optionally $< condition >$ and $< primacy >$ tags. All datums must be a valid feature, referred to by it's unique feature id.

The $< datum >$ tag contains:

$< featureid >$ is the required id of the features being used as a datum

$< condition >$ is the string material condition at which datum feature is referred to

$< primacy >$ is the boolean condition that indicated whether this datum has fixed precedence

The order in which datums are specified is important in cases where some datums have fixed primacy. When the primacy value of a datum is true, the datum's precedence (primary vs secondary vs tertiary) becomes fixed with respect to other datums. For example, in Figure 5, in the true_position callout, the primacy value of 1 (true) means that the tolerance should be interpreted as | ⌖ | 0.1 Ⓜ | A | B Ⓜ |. The same interpretation applies if the second datum's primacy were 1 (true). A primacy of 0 (false) or no primacy element should be interpreted as | ⌖ | 0.1 Ⓜ | A–B Ⓜ |. Where A refers to the feature with id '1' and B the feature with ID '2'.

No absolute coordinate system is provided similar to the approach adopted by ASME Y14.5. All tolerances of position and orientation must be specified with respect to other features within the same part.

It the responsibility of any software systems or users to ensure that datums have a valid interpretation. For example, a datum specified for a cylindricity callout has no meaning.

```
<feature "id"=3>
  <class> cylinder </class>
  <name> cylinder1 </name>
  ...
  <tolerance>
    <callout> Ra </callout>
    <maximum> 0.002 </maximum>
  </tolerance>
  <tolerance>
    <callout> diameter </callout>
    <maximum> 0.2 </maximum>
  </tolerance>
  <tolerance>
    <callout> true\_position </callout>
    <condition> mmc </condition>
    <maximum> 0.1 </maximum>
    <datum>
      <featureid> 1 </featureid>
      </primacy> 1 </primacy>
    </datum>
    <datum>
      <featureid> 2 </featureid>
      </primacy> 0 </primacy>
      <condition> mmc </condition>
    </datum>
  </tolerance>
</feature>
```

FIGURE 5. Tolerance callouts for a cylindrical feature

AMF-TOLERANCE ELEMENTS

Table 1 lists the tags introduced as a part of this extension to the AMF format.

FUTURE ADDITIONS

The current formulation of this extension to AMF does not address several important cases. These will be incorporated and specified in future work.

Constructed Features: Constructed Features are geometric entities, such as points and lines, that are constructed by the interaction of one or more surfaces. Such entities my be used as datums or may be used to control the form or position of the features (surfaces) that form them. A means for specifying constructed features and will be added in the future.

Compound Features: Compound Features are features that are formed by the combination of multiple geometric entities. Compound features are often of interest as manufacturing

Element	Parent Element(s)	Attributes	Multi Elements?	Description
$< features >$	$< object >$		No	The list of features of the object
$< feature >$	$< features >$	id	Yes	Container for all information pertaining to a single feature
$< featureid >$	$< triangle >$ $< datum >$		No	Id of a feature being referred to
$< name >$	$< feature >$		No	Name of features
$< class >$	$< feature >$		No	Class of a feature
$< note >$	$< feature >$		Yes	Any notes pertaining to the feature
$< tolerance >$	$< feature >$		Yes	A tolerance callout of the feature
$< callout >$	$< tolerance >$		No	The ASME Y14.5 tolerance callout
$< datum >$	$< tolerance >$		Yes	A datum feature for this tolerance
$< condition >$	$< tolerance >$ $< datum >$		No	The Material condition under which the callout or datum applies
$< primacy >$	$< datum >$		No	If this datum's primacy is fixed

TABLE 1. Elements of the AMF-Tolerance extension

features; for example counterbores and slots. Currently, these may be handled either as a single *surface* or must be handled as multiple independent features that are constrained by tolerances between them. The first approach limits the applicable tolerances while the second is inelegant and cumbersome. In the future, this scheme will be extended to include a concise means of grouping features into compound features and applying tolerances to them.

ASME Y14.5 compliance: The current form of this extension supports only a fraction of the ASME Y14.5 standard. While it is felt that complete support of the standard is not a priority, future additions will include increased support for important parts of the latest version of ASME Y14.5.

Formulations and definitions: The current form of this extension does not specify methods for mesh processing despite the reliance on interpretation of mesh geometry for the extraction of nominal dimensions and for interpreting tolerance zones. Developing and specifying these methods, perhaps based on the ASME Y14.5.1 standard, will be an important focus of future work.

Curved triangles and mesh structures: The AMF format supports curved triangles and mesh structures. It is expected that these can be incorporated into this scheme in the same way as normal triangles. However, further investigation into the interaction between tolerances and these constructs is necessary.

DISCUSSION AND CONCLUSION

Dimensions and Tolerances are fundamental to modern manufacturing. In this work we have described an extension to the AMF format that incorporates features, dimensions and tolerances. An XML tag structure that can hold ASME Y14.5 tolerances has been developed. The structure of this extension places very few constraints on the AMF format or on any software designed to handle it. It is expected that any software packages that are not 'aware' of these extensions will not be impacted by their presence. It is hoped that the AMF file format, with it it's improvements over STL, together with these extensions will help enable simplified data exchange and process planning for AM processes.

ACKNOWLEDGMENTS
The authors would like to thank the National Additive Manufacturing Innovation Institute and America Makes for supporting this work.

REFERENCES

[1] Cheng W, Fuh Jyh, Nee Ayc, Wong Ys, Loh Ht, Miyazawa T. Multi-objective optimization of part- building orientation in stereolithography. Rapid Prototyping Journal. 1995 Dec;1(4):12–23.

[2] Arni R, Gupta SK. Manufacturability Analysis of Flatness Tolerances in Solid Freeform Fabrication. Journal of Mechanical Design. 1999 Sep;123(1):148–156.

[3] Hanumaiah N, Ravi B. Rapid tooling form accuracy estimation using region elimination adaptive search based sampling technique. Rapid Prototyping Journal. 2007 Jun;13(3):182–190.

[4] Paul R, Anand S. Optimization of layered manufacturing process for reducing form errors with minimal support structures. Journal of Manufacturing Systems. 2014;.

[5] Zhang Y, Bernard A, Harik R, Karunakaran KP. Build orientation optimization for multi-part production in additive manufacturing. Journal of Intelligent Manufacturing. 2015 Feb;p. 115.

[6] Lynn CM, West A, Rosen DW. In: A process planning method and data format for achieving tolerances in stereolithography; 1998. .

[7] Hiller J, Lipson H. In: STL 2.0: a proposal for a universal multi-material Additive Manufacturing File format; 2009. p. 266278.

[8] ASTM. Additive Manufacturing File Format (AMF) 1.1. ISO/ASTM 52915:2013;.

[9] ASME. ASME Y14.5 2009 - Dimensioning and Tolerancing;.

DEVELOPMENT OF A SENSOR TEST BED FOR IN PROCESS SENSING OF LASER POWDER BED FUSION ADDITIVE MANUFACTURING

S. M. Kelly, P. C. Boulware, L. Cronley, G. Firestone, M., J. J. Marchal, T. Stempkey and C. Reichert
EWI
Columbus, OH USA

ABSTRACT
For certain metal additive manufacturing (AM) processes such as laser powder bed fusion, the build times involved can be on the order of days and weeks for parts less than 250 mm in size. In addition, the ability to perform post-process inspection may be compromised by the complex geometries afforded by AM. EWI is leading a team under America Makes, the National Additive
Manufacturing Innovation Institute to define sensors that can detect defects such as porosity, lack of fusion, cracking, and geometric variability that may compromise the quality of a part during the build process. The ability to know that a part quality is suspect or compromised early in the build process will lead to downstream cost savings and a more robust additive manufacturing process. In order to screen a wide range of sensor technologies for in process monitoring without interference from physical or software constraints from commercial L-PBF equipment, EWI has developed a sensor test bed. The test bed allows access to local and global process sensors mounted in ideal locations on the platform.

The ability of the sensor test bed to demonstrate equivalency to a commercial L-PBF machine (EOS M280) will be shown for nickel alloy 625. The presentation will provide an overview of the sensors, their characteristics, and various figures of merit for in process sensing. The results from the following sensors will be discussed: Local sensors including a photodetector, melt pool thermal camera, and high speed video; global sensors including high resolution vision camera, laser line scanner, and global thermal camera; and passive sensors which include various acoustic sensors. The results of an initial structured experiment to produce and detect porosity, lack of fusion, and geometric intolerance will be presented. In addition, other salient observations made about the L-PBF process using sensors such as the global thermal camera will be presented. This includes the variation of heat flow dependence on the scan and gas flow directions over the build platform, the transient layer to layer response of global heat flow, and the ability of the thermal sensors to detect lack of fusion/unfused powder regions.

Keywords: Laser Powder Bed Fusion, In Process Sensing, nickel alloy 625

In Situ Monitoring of Laser Powder Bed Fusion Additive Manufacturing Using Digital Fringe Projection Technique

Bin Zhang[1], William S. Land II[2], John Ziegert[2], and Angela Davies[1]
[1]Department of Physics and Optical Science
The University of North Carolina at Charlotte,
Charlotte, NC, USA
[2]Department of Mechanical Engineering and Engineering Science
The University of North Carolina at Charlotte,
Charlotte, NC, USA

INTRODUCTIONS

Laser powder bed fusion is a pioneering additive manufacturing approach for rapid prototyping [1]. The metal prototypes are directly fabricated from computer aided design (CAD) data, which makes the laser powder bed fusion additive process more time efficient and inexpensive comparing to conventional machine tooling. However, one challenge associated with improving the dimensional accuracy and optimizing the build process is the relative inability to measure the complete metal part, especially the internal features, by conventional metrology tools. One effective way to solve this problem is to continually monitor the build process as each layer is deposited. This paper demonstrates an in situ monitoring method for the laser powder bed fusion additive process. The procedure uses a digital fringe projection technique in combination with basic machine vision image analysis. This technique is capable of producing 3D point cloud measurements of fused metal powder surfaces, providing a large amount of data for characterizing the performance of the machine and improving the understanding of the process.

The digital fringe projection system contains three commercial DSLR cameras and a DLP projector (shown in FIGURE 1). However, only one of cameras (the one on the left) is used in the current study. Future work includes integrating data from all three cameras for better resolution and higher accuracy.

PRINCIPLES

The main operational procedures of the fringe projection system are as follows:

1. Obtain the wrapped phase of the object using a phase shifting algorithm.
2. Phase unwrapping.
3. Removal of carrier phase.
4. Conversion of phase maps to height maps (z calibration).
5. Conversion of pixel space to metered space (x-y calibration).

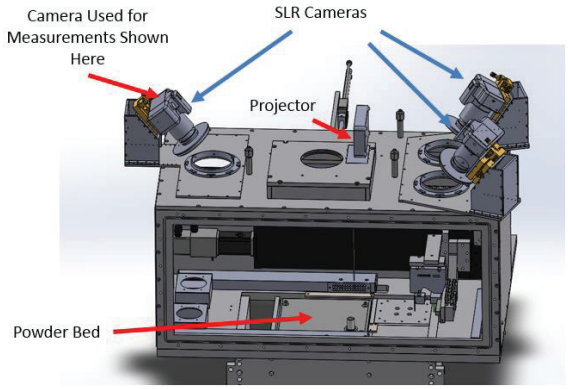

FIGURE 1. Configuration of digital fringe projection system on the laser powder bed fusion machine chamber.

When operating the digital fringe projection system, a sequence of sinusoidal fringe patterns are projected on the object surface. The irradiance distribution of the patterns are expressed as,

$$I_i(x,y) = I_0\left[1+\cos\left(\frac{2\pi x}{p}+\delta_i\right)\right] \qquad (1)$$

where i indiates the i^{th} image, I_0 is the Irradiance modulation, p is the period of the sine wave, δ is the step size which is given by

$$\delta_i = \frac{i-1}{N}2\pi, \qquad i = 1,\dots,N. \qquad (2)$$

Those fringe patterns are then captured by the camera at approximately a 50° angle, and the wrapped phase map is obtained by applying the phase shifting algorithm. The wrapped phase map is written as

$$\phi(x,y) = actan\left(\frac{-\sum_{i=1}^{N}\sin(\delta_i)I_i(x,y)}{\sum_{i=1}^{N}\cos(\delta_i)I_i(x,y)}\right) \qquad (3)$$

In the real computation process, the four-quadrant inverse tangent function, atan2(Y, X), is used to remove the ambiguity of sign of numerator and denominator. The result of atan2 function is limited in the range [-π, π], but the real phase of the sine wave is continuous. Thus, the next task is to expand the wrapped phase from [-π, π] to an extended range. This procedure is called phase unwrapping. In this paper, an Itoh phase unwrapping algorithm is used to obtain the unwrapped phase of the measured surface. Details of the phase unwrapping algorithm can be found in [2].

The unwrapped phase map contains both the object phase and the carrier phase. The carrier phase is a chirped sinusoidal wave, where the chirping is a result of the camera/projection angle. To estimate the carrier phase, simply fit the unwrapped phase map to Legendre polynomials (up to the third order is sufficient). Then, subtracting the carrier phase from the unwrapped phase map will give the object phase map.

Two calibration steps are needed in this study. The goals of calibrations are to achieve two conversions -- phase to z-height and pixel space to x-y metered space. The first procedure is called, z calibration or effective wavelength calibration [3], and the second one is called x-y calibration or machine vision calibration. In the z calibration, a coated piece of float glass is used as a diffuse flat surface. First, the phase shifting and phase unwrapping processes are used to obtain the unwrapped phase maps of the flat surface. Next, this step is repeated as the glass flat is moved to 10 different height positions as indicated by a separate external displacement measuring device. In doing so, the unwrapped phases can be related to the height values using a linear scaling factor, effective wavelength, given by

$$\lambda_{eff} = \frac{2\pi}{\Delta\phi/\Delta h} \qquad (4)$$

where Δϕ and Δh are the phase and height change between each height step for each pixel. At last, the height map is obtained by multiplying the effective wavelength map with the remaining phase map.

$$z(x,y) = \lambda_{eff}(x,y) \cdot \phi(x,y) \qquad (5)$$

The second calibration step is x-y calibration. The aim of this calibration is to convert pixels to millimeters. Conventionally, this is achieved by camera calibration [4]. Here a standard machine vision technique is implemented. The procedure uses a calibrated grid plate artifact. First, the images of the grid plate are acquired at a reference height level. Then the four corners of the grid are extracted to construct a projective transformation matrix T.

$$T = \begin{bmatrix} a_{11} & a_{12} & a_{13} \\ a_{21} & a_{22} & a_{23} \\ a_{31} & a_{32} & a_{33} \end{bmatrix} \qquad (6)$$

This matrix describes the position and orientation of the camera. By multiplying each pixel location (u,v) with the matrix, the perspective wrapping caused by the camera viewing angle can be removed. The new pixel space is given by

$$[x'y'w'] = [u\ v\ 1] \cdot T \qquad (7)$$

where (x'/w', y'/w') are the coordinates in orthogonal planar object space [5].

The lateral spacing of the reference grid is measured by a coordinate measuring machine (CMM). In doing so, the relation between the pixel number in transformed image space and the distance (in millimeters) of grid pitch can be established. This relation is described by

$$s = \frac{p_{ref}}{p_{orth}} \quad (\frac{mm}{pixel}) \qquad (8)$$

where p_{ref} is the pitch of reference grid, and p_{orth} is the pitch in pixels in orthogonal object space. Finally, the height map is converted from pixel space to millimeter space by multiplying the scaling factor (mm per pixel) with the height map in orthogonal object space.

$$[x\ y] = s \cdot \left[\frac{x'}{w'}, \frac{y'}{w'}\right] \quad (mm) \qquad (9)$$

One of the main noise sources in the digital fringe projection system is the nonlinear gamma curve of the projector/camera system [6, 7]. As a practical consideration, a gamma correction procedure is needed before the calibration and measurement to linearize the system input/output response curve. To improve measurement accuracy of the system, a generic gamma correction method [8] is used in this paper. In addition, a Fourier filtering technique is applied to further reduce the residual harmonic noise on the phase map.

EXPERIMENTS AND RESULTS

System Design

FIGURE 1 illustrates the final design of the digital fringe projection system mounted on top of the

laser powder bed fusion machine chamber. The projector (Qumi Q5) projects through a glass window which is approximately 560 mm above the powder bed top surface. The DSLR cameras (Canon T3i) are mounted on the three-dimensional adjustable stages. The angle between the camera and projector is about 50°. The lenses used in this experiment are 18-55 mm zoom in lenses, which are locked at 55 mm focal length by epoxy and connected by three specially designed lens mounts. The lens mounts ensure sealed connections between the cameras and the powder bed chamber. This seal is critical because the laser powder bed fusion process must take place in an Argon environment to minimize oxidation during the fusion process.

The projector and cameras are controlled by a personal computer. The projector is rotated by a small angle such that the projected fringes are rotated with respect to wiper blade that spreads new powder after each layer is fused. This rotation helps to prevent fringe bleedthrough noise (along the fringe direction) from being aligned with any potential texture or waviness of the powder layer caused by the wiper blade. In this study, an eight step phase shifting algorithm is applied to obtain the wrapped phase maps, and the pitch of the fringe pattern is approximately 3 mm/cycle.

Effective Wavelength Calibration

Conventionally, the effective wavelength is evaluated as one number in the entire field of view. This is reasonable when the angle between projector and camera is very small and when relatively low accuracy measurements are required. However, when measuring small height variations, such as powder/metal surface following fusion, it is necessary to consider the variation of effective wavelength over the field of view. Therefore, a separate effective wavelength is computed for each camera pixel.

In the effective wavelength calibration, the vertical stage is moved over a range from -0.5 mm to 0.5 mm in increments of 0.1 mm. FIGURE 2 shows the calibration result at the center pixel in the calibration region. The error bars are the standard deviation of the mean of 7 unwrapped phase measurements. This plot confirms the linear relation between the phase and height within the small height range. Thus, a straight line is fit to the data using the least square method [9], and the slope of the line is calculated to be 1.60 rad/mm. Putting this number into Equation 4 gives the effective wavelength, 3.92 mm/cycle. Repeating this process for all the pixels in the field of view, the effective wavelength can be mapped as a function of camera pixels. FIGURE 3 shows the effective wavelength map. As shown in this figure, the variation of effective wavelength is approximately 0.09 mm/cycle.

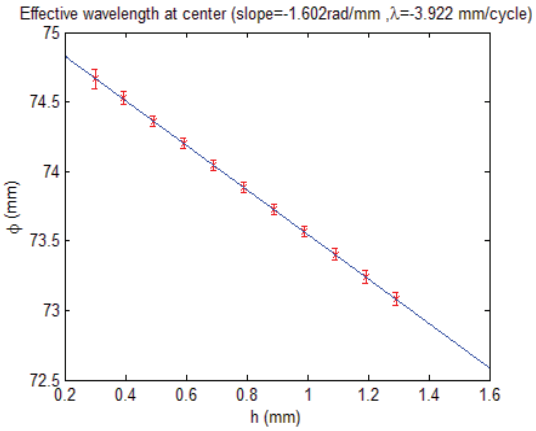

FIGURE 2. Plot of unwrapped phase as a function of height (at the center pixel)

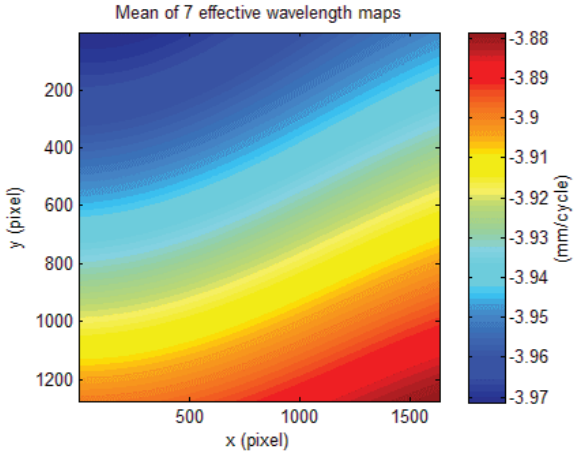

FIGURE 3. Effective wavelength map

Machine Vision Calibration

The lateral position calibration is achieved by imaging a calibration grid artifact. This technique is similar to the camera calibration technique [10] which can be seen in most digital fringe projection systems. The grid plate contains an 11 × 11 grid of 7.5 mm diameter reamed holes of nominally constant 15 mm pitch, covering an area of 150 × 150 mm. The centers of each of the black dots are extracted using standard machine vision techniques; and the four corner coordinates are used to construct the projective transformation matrix given in Equation 6. The original grid plate image and its transformed counterpart are shown in FIGURE 4. After the projective transformation

removes the perspective effect, the center of each hole is assigned with an x and a y scaling factor. These factors convert a point in pixel units to metered units. Between the hole centers, linear interpolation is implemented to determine the local scaling factor for each pixel.

In order to remove any distortions that may be generated by the projective transformation, the grid plate is measured with a CMM. FIGURE 5 shows the comparison of the grid generated by projective transformation and that measured by the CMM. The lateral error is intentionally magnified 10 times for visualization. The maximum image distortion is approximately 0.5 mm. The lateral distortion can be removed by subtracting the x and y errors from the transformed image.

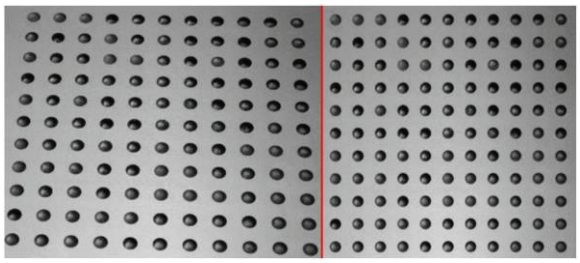

FIGURE 4. The left is the image of the calibration grid artifact in the camera coordinates. The right is the same image after passing projective transformation. The transformation converts pixels from camera coordinates to world coordinates.

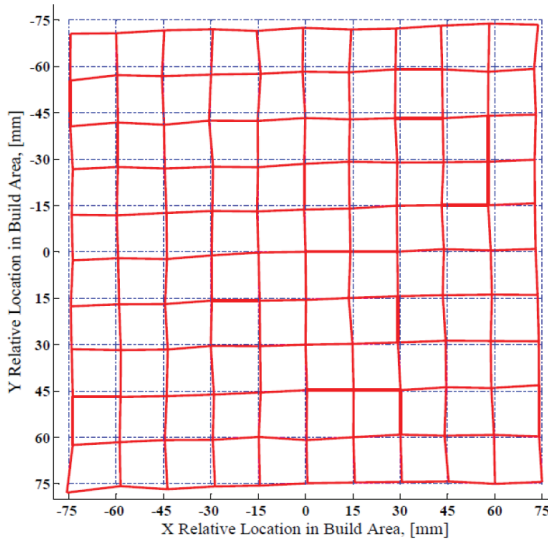

FIGURE 5. A visualization of the lateral distortions. The intersections of the red lines are the locations of each hole in the grad plate, while the blue lines are their location as measured by a CMM. (Note: the difference in hole position is magnified ten times for graphical purpose.)

In Situ Measurements of Build Area

The laser fusion powder bed process is a layer wise building process. Every step associated with one specific powder layer is referred to as a build cycle. FIGURE 6 gives one example of a typical build cycle. This cycle has four major steps. First, a layer of powder (typically 40μm thick) is dispensed by the wiper blade. Second, a high-power laser beam fuses a selected region in the powder. Third, the build platform drops 40 μm. Last, a new layer of powder is spread and the full cycle starts again. Measurements are taken at three critical moments in the build cycle to characterize the build process. As shown in FIGURE 6, the three measurements are taken 1) after a new powder layer is dispensed, 2) after laser fusion is completed, and 3) after the build platform is dropped down one layer height. The first measurement provides us with the overall flatness of the powder bed prior to layer fusion. The second measurement gives the surface profile of the fused powder. The third measurement monitors the height drop of the build platform and estimates the thickness of the new powder layers.

FIGURE 7 shows the three height maps of the metal/powder surface in the first build cycle. The build area is a 110 mm × 40 mm rectangle, and the fused regions are ten squares and one circle. Here, the shade of gray indicates the height of the surface, and the three measurements all use the same grayscale to height range for easy comparison.

FIGURE 8 gives a more detailed view of the square at the upper right corner. The main graph is the height map, and the right and bottom plots are the height profiles of the vertical and horizontal line traces indicated in the main graph. As shown in these profile plots, the fused area has a much larger height variation when compared to the powder bed pre-fusion. The standard deviation of height variation in the unfused area is estimated to by 10 μm, while that of the fused area is 31 μm.

More useful information can be discovered by analyzing different portions of the height maps. For instance, FIGURE 9 illustrates the height drop of the build platform through 30 build cycles. The height drops are estimated by subtracting the average height values for the powder at the

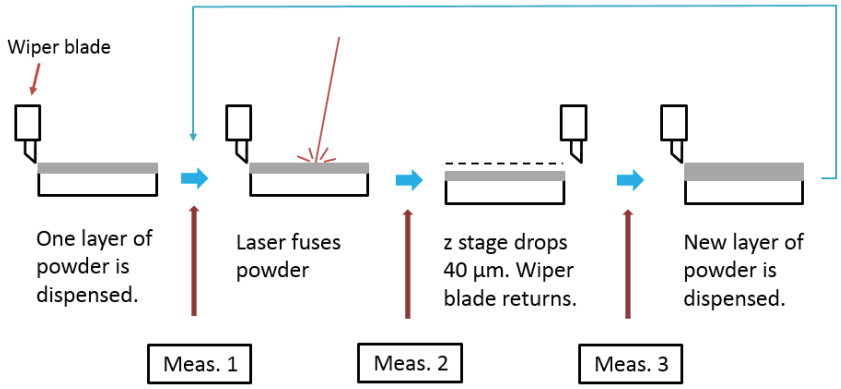

FIGURE 6. Schematic of one build cycle in the laser fusion powder bed process

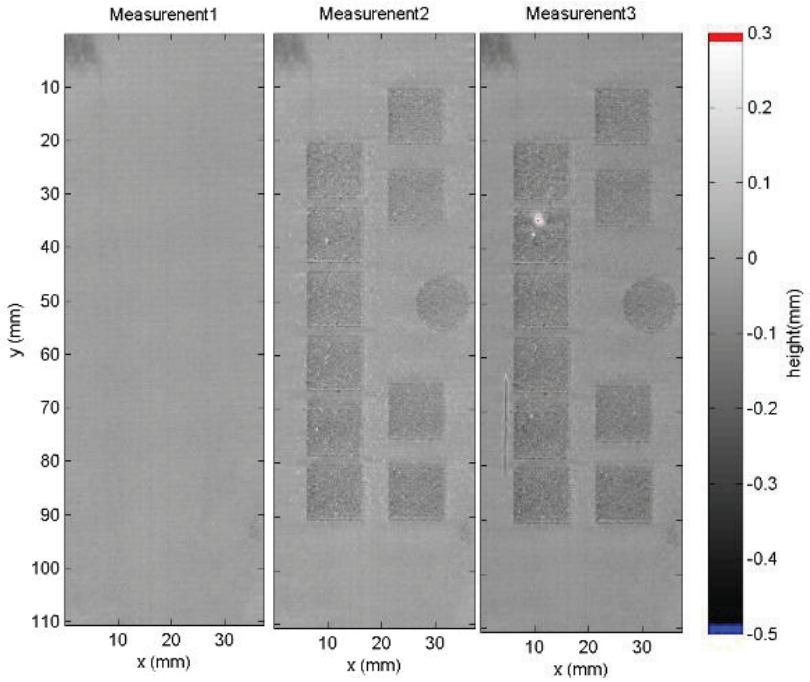

FIGURE 7. Three height maps of build area in the first build cycle.

bottom portion of measurement 2 and 3. As shown in FIGURE 9, this height drop of build platform is consistently around 40 µm through the 30 build cycles. This results agree with the programed height drop of the build platform.

SUMMARY

This paper investigates in-situ layerwise metrology for the laser powder bed fusion additive process using a digital fringe projection technique. This study has succeeded in measuring the metal/powder surface height variation following fusion of each layer. These data are expressed relative to a fixed reference coordinate system through the entire build process. these measurements offer the potential for benefits in the analysis and characterization of the build area, including determining boundaries of the fused region, measuring the height variation of the fused surface, and tracking the vertical motion of the build platform. Using a commercial DSLR camera and DLP projector, the lateral resolution of height maps is approximately 60 µm when the camera and projector are mounted and adjusted to encompass a 250 X 250 mm field of view. However, for the 110 mm × 40 mm build area used in this study, only 8% of the camera pixels are used, implying that much finer lateral resolution is possible. The noise floor for vertical resolution is approximately 20 μm.

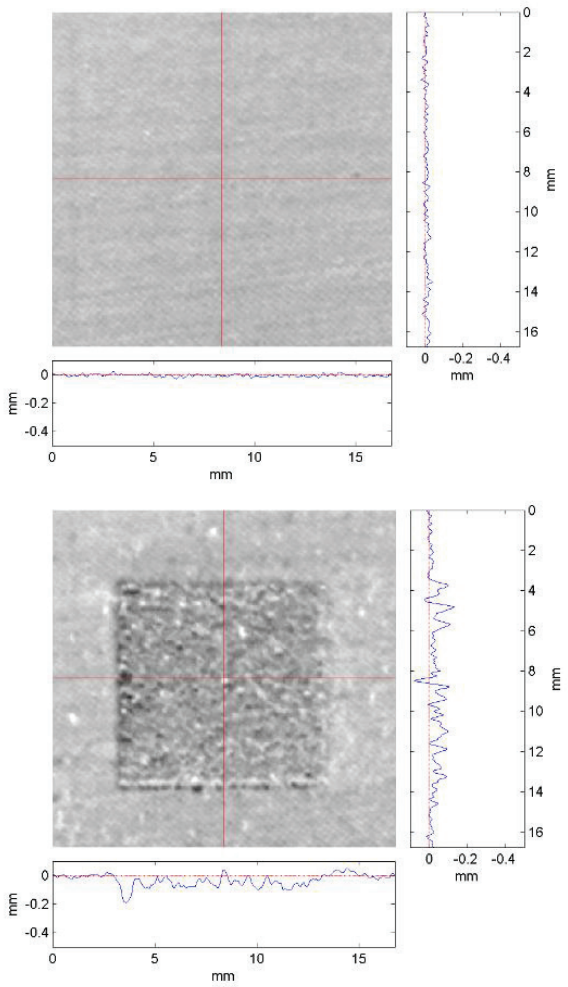

FIGURE 8. Local height maps with trace plots: the square at upper right corner in measurement 1 (top) and measurement 2 (bottom). First layer of powder is used as a reference height map.

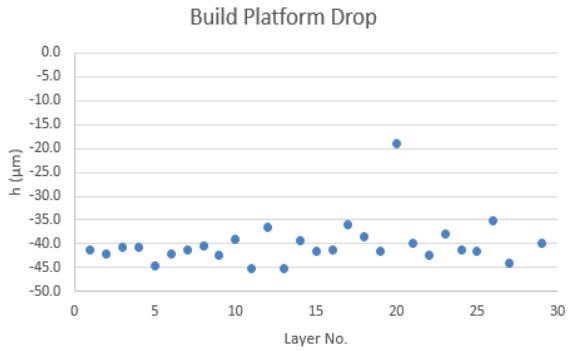

FIGURE 9. Average height drop of the build platform through 30 build cycles.

ACKNOWLEDGEMENT

This work is supported by funding from the National Institute of Standards and Technology, America Makes, and the Edison Welding Institute.

REFERENCES

[1] Simchi A, Petzoldt F, and Pohl H, On the development of direct metal laser sintering for rapid tooling. J. Mater. Process. Technol., 2003; 141: 319–328.

[2] Creath K. and Wyant J C, Moiré and Fringe Projection Techniques. Optical Shop Testing, 1992: 653.

[3] Purcell D, Davies A, and Farahi F, Effective wavelength calibration for moiré fringe projection, Appl. Opt. 2006; 45(34): 8629.

[4] Zhang S, Recent progresses on real-time 3D shape measurement using digital fringe projection techniques. Opt. Lasers Eng. 2010; 48: 149–158.

[5] Wolberg G, Digital Image Wrapping. Digital Image Wrapping. IEEE Computer Society Press. Los Alamitos,CA, USA: 1994: 41–56.

[6] Hoang T, Pan B, Nguyen D, and Wang Z, Generic gamma correction for accuracy enhancement in fringe-projection profilometry. 2010: 35;1992–1994.

[7] Hoang T M, Simple Gamma Correction for Fringe Projection Profilometry System. 2010; 1428: 4503.

[8] Guo H, He H, and Chen M, Gamma correction for digital fringe projection profilometry. Appl. Opt. 2004; 43: 2906–2014.

[9] Philip D, Bevington R. Data Reduction and Error Analysis for Physical Sciences. 3rd ed. McGrw-Hill, 2002.

[10] Bouguet J.-Y. Camera Calibration Toolbox. 2013. [Online]. Available: http://www.vision.caltech.edu/bouguetj/calib_doc/.

CURRENT STATE AND NEW DEVELOPMENTS OF QUALITY MONITORING

Perry Leggett
Concept Laser, Inc.
Grapevine, Texas USA

ABSTRACT

Additive manufacturing of metals provides means to fabricate complex components with geometries that were previously not possible. The unique components generated lead to challenges with qualification and defect detection within the part. A way to ensure part quality is through real-time monitoring of the additive process that provides a look inside the components and can detect defects that adversely affect part quality. Defects often occur within the part and are not observable from the exterior. By monitoring meltpool during the process, irregularities in the molten pool can be detected. These irregularities in the molten pool signal result in defects within the part. This presentation discusses the current state and new developments of Quality Monitoring utilized during the LaserCUSING process. Real-time monitoring of the molten pool is combined with geometric data of the sliced model to provide a virtual CT-like image of the component, highlighting any defects that may have occurred within a 3D model. The 3D Meltpool images are compared to CT scans of the finished part to compare the results. 3D Monitoring provides the ability to qualify components for critical applications and is crucial for the adoption of additive manufacturing in critical applications.

Dimensional Accuracy of Large and Complex Ti-6Al-4V Component Made via Electron Beam Melting

Marcin B. Bauza[1], Michael M. Kirka[2], Raghuram Bhogaraju[1], Bradley S. Richardson[2], Lonnie Love[2], Larry E. Lowe[2], and Ryan R. Dehoff[2]
Department or Division
[1]Carl Zeiss Industrial Metrology
Maple Grove, Minesotia, USA
[2]Manufacturing Demonstration Facility
Oak Ridge National Laboratory
Knoxville, Tennesee, USA

INTRODUCTION

Additive manufacturing (AM) shows significant promise towards revolutionizing the manufcature of discrete parts [1]. Traditional subtractive manufacturing offers a variety of capabilities which can be carried out at a high level of precision, however the range of shapes that can be produced is limited by the access of cutting / abrasive tools to designed features. With additive manufacturing, forms which could not be achieved before are feasible, making available a new level of functionality and capabilities to designers. However, the new technology brings new challenges in relation to inspection and metrology of produced parts, therefore significantly challenging a proper feed back on quality of printed components. In this paper we will discuss complexities of modern AM components and inspection procedures as well as capabilities for large AM parts.

MANIPULATOR ARMS

An example of the new design paradigm offered by AM and abstract design approaches by contemporaneity standards is that of the manipulator arms designed for the Office of Naval Research (ONR). These manipulator arms are designed for use in underwater salvage and repair work. Through employing AM techniques, significant weight can be removed and through the ingenious use of hydraulics [2], the hydraulic reservoir can be greately reduced when compared to commercial manipulator arms. This unique design methodology routes all electrical wires through internal pipes and the hydraulics through internal hoses. As a result, no electrical cables or hydraulic hoses are exposed on the exterior surfaces. This sort of revolutionary design only implementable through AM allows for the mitigation of water leakage into the structure, and for the overall assembly to become neutrally net buoyant through the removal of non-structural material. Shown in Figure 1 is a cross-section of a component of the manipulator arms depicting the internal electrical and hydraulic passages. Shown in Figure 2 is the fully assembled manipulator arms with the sections shown prior to submersion (a) and submersed for leak testing (b).

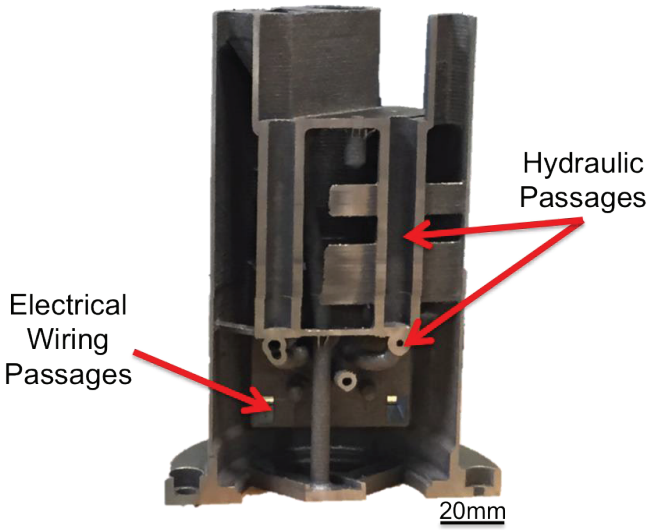

Figure 1: Cross-section of a manipulator arm component depicting the internal hydraulic channels and routings for electrical wires.

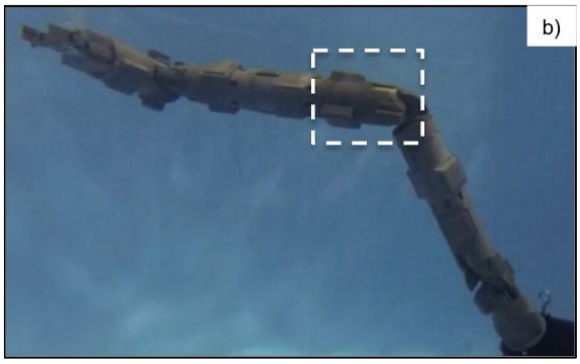

FIGURE 2. a) Assembled manipulator arms attached to hydraulic reservoir. b) Underwater testing and demonstration of manipulator arms. Dashed white box indicates the shoulder pinch point component examined in this work.

ELECTRON BEAM MELTING

In recent years metals AM processes such as the electron beam melting (EBM) process has emerged as one of the dominant methodologies for the manufacture of complex engineering components. EBM is a process, where fully dense metal components are built in a layer-by-layer fashion from metal powder within a powder bed. A raking mechanism spreads metallic powder across the build area for every layer. The Arcam EBM process utilizes a high power electron beam that generates the energy needed to melt the metallic powder. Electromagnetic optics allow for near instantaneous control over the electron beam and can result in simultaneous melt pools in a given layer and higher deposition rates over comparative laser AM systems [3,4]. For each build layer the electron beam pre-heats the entire powder bed to an optimal ambient temperature, specific for the material used. In addition the Arcam EBM process takes place in vacuum and at high temperatures. As a result, finishedEBM components contain low residuals stresses [5]. An overall schematic of a general Arcam EBM machine is shown in Figure 3.

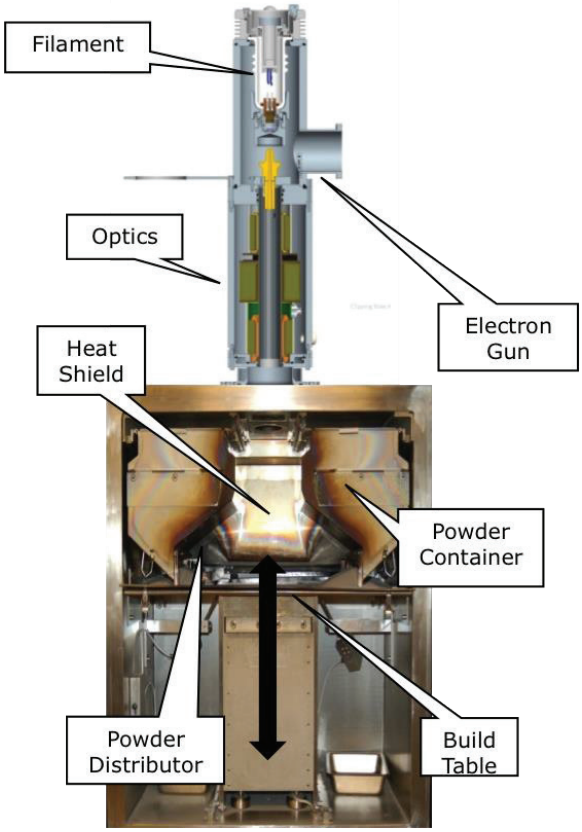

Figure 3: Interior cutaway depicting the various components of a generic Arcam EBM machine.

EXPERIMENTAL

For this work, examined was the shoulder joint of the manipulator arms. This particular component is the pivot point for the arms. The component was manufactured on an Arcam A2 EBM machine out of Ti-6Al-4V (Ti64). Ti64 was chosen due to its high corrosion resistance in sea water. The Ti64 powder was manufactured through gas atomization and had a size range of 40-120 μm. The layer thickness used in the component was 50μm. The build parameters used to build the shoulder pitch point component are the commercially released Arcam parameters for titanium.

COMPUTED TOMOGRAPHY FOR AM

AM parts are prone to substantial dimensional stress deformation [6]. AM building process requires significant experience to create dimensionally valid components. With high level of internal complexity AM parts have to be measured using Computed Tomography (CT) to allow internal metrology. Traditionally CT is used

for non destrictive testing (NDT) which typically is considered as qualitative rather than quantitative inspection. Therefore new techniques, and methods as well instrument designs were developed to enable quantitative inspection / metrology. Titanium alloys are very popular with AM, however those are more challenging materials that are difficult to measure with traditional CT. Latest advancements make such tasks possible and provide valuable information regarding dimensional accuracy of produced part.

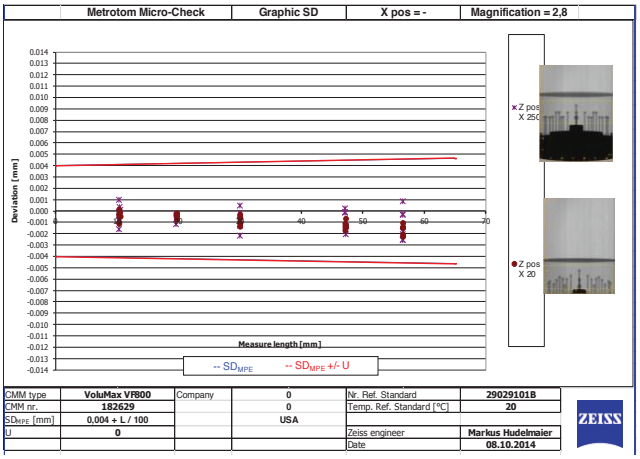

Figure 4: VoluMax 800 - the accuracy of distance measurement between multiple spheres based on VDI/VDE 2630 standard. The horizontal axis show increments of 20 mm as a distance between spheres, and vertical axis shows 1 µm increments as deviation from calibrated distance between spheres using high accuracy CMM. Red lines define manufacturer specification

Figure 4, shows curent capabilities and accuracy of CT system capable of qualitative analysis / metrology.

To validate the process, several repeatability measurements were performed to establish measurment baseline. Therefore, the part was measured multiple times over a period of few weeks. During this time other smaller or bigger parts were also measured, therefore the system was moved around its entire working volume. Since the CT used for this work is metrological, a separate calibration or comparison to known artifacts was not necessary, (Figure 5). Furthermore, every measurement was taken with part placed differently in the machine. As results show the measurements repeat within 20 µm, while measurement speed was only 3 min. (Figure 5)

MEASUREMENT RESULTS

Produced arm shows maximum dimensional deviations of 300 µm (Figure 6). Further analysis of results show several regions with higher deviations than some. Analyzing specific cross-sections (Figure 7) show that some features are created with accuracies below 0.001 inch and more than 0.004 inch for others (Table 1). In most cases, the regions of lower dimensional accuracy are not critical to the function of the component.

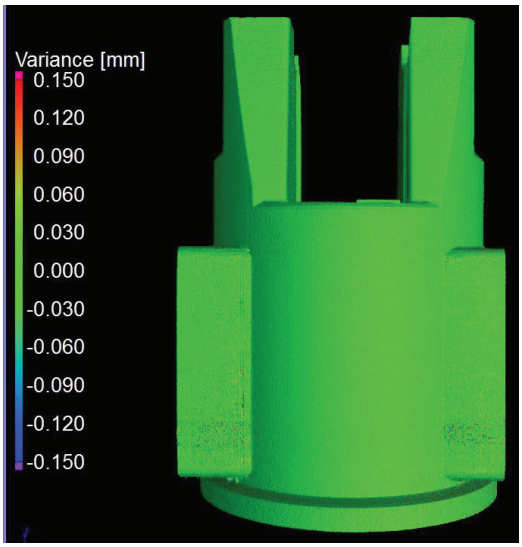

Figure 5: Measurement repeatability over several weeks without necessity of recalibration, Noise spots are contributed to a rough surface and different fixturing methods between scans.

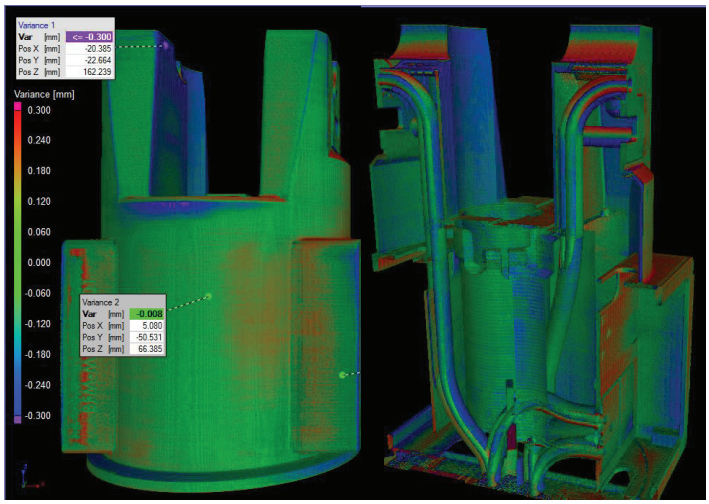

Figure 6: Measurement results showing external surfaces on the left and internal cross sections on the right.

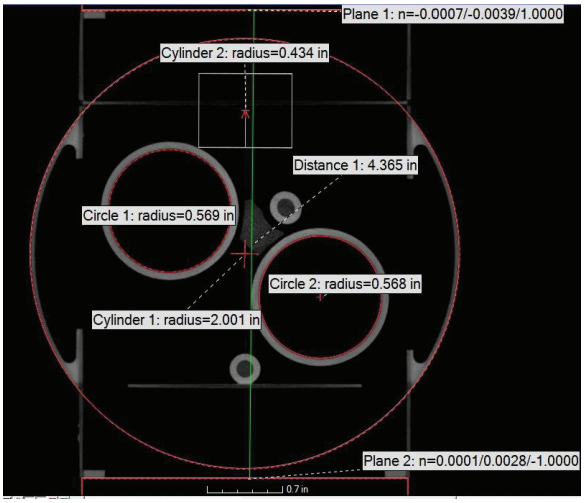

Figure 7: Measurement results of selected features.

Measurement	Nominal Value	Run 1	Run 2	Run 3	Average	Delta
Diameter -Outside Cover	2.0000	2.0010	2.0010	2.0010	2.0010	0.0010
Radius of the handle	0.4300	0.4344	0.4344	0.4343	0.4344	0.0044
Width of the part	4.3550	4.3550	4.3540	4.3550	4.3547	-0.0003
Radius of the internal hole1	0.5690	0.5690	0.5690	0.5680	0.5687	-0.0003
Radius of the internal hole2	0.5690	0.5680	0.5680	0.5680	0.5680	-0.0010

Table 1: Measurement repeatability results and comparrison to nominal values. All values are in inches.

Further analysis of cross sections reveals specific sections of the part to be either porous, or not completed or extra featers are created, (Figure 8).

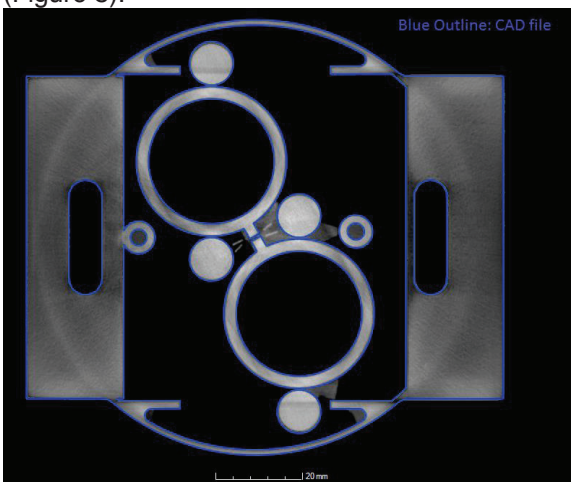

Figure 8: Cross-sectional view of measured part with blue overlay of CAD nominal shape

CONCLUSIONS

AM is enabling new ways of designing and manufacturing complex components. However, this freedom comes with a price of increased complexity of metrology process. Detailed metrological analysis provides valuable insight into the quality of the part and hint on possible corrections to mitigate some stress related dimensional deviations. In the case of the Ti64 EBM manipulator arm component analyzed in this work, generally good agreement between the desired component dimensions and tolerance and the final dimensions were obtained.

This research is sponsored by the US Department of Energy, Office of Energy Efficiency and Renewable Energy, Advanced Manufacturing Office, under contract DE-AC05-00OR22725 with UT-Battelle, LLC. The United States Government retains and the publisher, by accepting the article for publication, acknowledges that the United States Government retains a non-exclusive, paid-up, irrevocable, worldwide license to publish or reproduce the published form of this manuscript, or allow others to do so, for United States Government purposes.

The research that has resulted in the fabrication of the robotic arm components is sponsored by the Office of Naval Research, Ocean Battlespace Sensing S&T Department Code 32.

REFERENCES

[1] Gibson I, et al. Additive Manufacturing Technologies. Springer-Verlag New York: 2010.

[2] Dehoff R, et al. Freeform Fluidics. Patent US 20130331949A. 12 Dec. 2013.

[3] Arcam A2X: Setting The Standard for Additive Manufacturing. Arcam AB. Web. 2015.

[4] Brochure: The power of Additive Manufacturing. Renishaw. Web. 2015.

[5] Sochalski-Kolbus L, et al. Comparison of Residual Stresses in Inconel 718 Simple Parts Made by Electron Beam Melting and Direct Laser Metal Sintering. Metallurgical and Material Transactions A. 2015; 46: 1419-1432.

[6] Bauza M, et al. Study Of Accuracy Of Parts Produced Using Additive Manufacturing, ASPE 2014 Spring Topical Meeting: Dimensional Accuracy and Surface Finish in Additive Manufacturing, Berkeley, CA, 2014

MODELING THE METAL ADDITIVE MANUFACTURING PROCESS AT THE SCALES OF THE PART AND THE POWDER

Wayne E. King[1], Andrew T. Anderson[2], Robert Ferencz[2], Neil Hodge[2], Chandrika Kamath[3], Saad Khairallah[2], Alexander Rubenchik[4]
[1]Physical and Life Sciences Directorate, , [2]Engineering Directorate[3], Computations Directorate, [4]NIF and Photon Sciences Directorate, Lawrence Livermore National Laboratory, Livermore, CA 94550, USA

INSTRUCTIONS

A physical understanding of the metal powder bed fusion process can provide insight into engineering margins, uncertainties in margins, and sensitivity of engineering margins to process parameters. Thus, a physical understanding of the process is an essential element of part qualification. Such an understanding should also enable increased control of the process, which in turn improves the likelihood of producing qualified parts. Modeling and simulation of the additive manufacturing process provides a mechanism to develop this understanding.

In this presentation we discuss recent progress in developing physics-based models for the metal powder bed fusion process. We discuss a model at the scale of the powder that is used to computationally model the melting of powder and its resulting densification. [1] It resolves randomly distributed individual powder particles in 3D. The laser-material interaction is treated via a physics-based absorption model. It models melting of the powder, flow and convection of the liquid, and morphology of the solidified metal. We also discuss a model at the scale of the part that is used to computationally build a complete part and predict properties such as residual stress in 3D. [2] It treats the powder as a lower density, low strength solid. The laser material interaction is treated using an energy source term. It models the melting/solidification transition and and includes material strength. We also discuss the role of data mining and uncertainty qualification in the modeling and simulation process and describe future applications. [3]

This work was performed under the auspices of the U.S. Department of Energy by Lawrence Livermore National Laboratory under Contract DE-AC52-07NA27344. This work was funded by the Laboratory Directed Research and Development Program at LLNL under project tracking code 13-SI-002.

REFERENCES

[1] Khairallah, S.A., Anderson, A.: Mesoscopic Simulation Model of Selective Laser Melting of Stainless Steel Powder. Journal of Materials Processing Technology 214, 2627-2636 (2014)
[2] Hodge, N.E., Ferencz, R.M., Solberg, J.M.: Implementation of a thermomechanical model for the simulation of selective laser melting. Comput Mech 54, 33-51 (2014)
[3] Kamath, C., El-dasher, B., Gallegos, G.F., King, W.E., Sisto, A.: Density of additively-manufactured, 316L SS parts using laser powder-bed fusion at powers up to 400 W. Int. J. Adv. Manuf. Technol. 74, 65-78 (2014)

STUDY ON ADDITIVE MANUFACTURING OF INNER CONTOURED TOOLS

Prof. Dr. h. c. Dr.-Ing. Eckart Uhlmann[1, 2], André Bergmann[2], Witalij Gridin[2]

[1]Institute for Machine Tools and Factory Management IWF
Technische Universität Berlin
Berlin, Germany
[2]Institute for Production Systems and Design Technology IPK
Fraunhofer-Gesellschaft
Berlin, Germany

INTRODUCTION

The manufacturing of inner contoured special tools using carbides undergoes a time- and cost-intensive multistage process. After the carbide has been directly pressed into a disk, a complex and multistage cutting process is applied in order to achieve the required geometric complexity. The integration of cooling channels leads to great difficulties in conventional production and is due to high initial costs only achievable in large scale and to a limited extent. Nowadays, there is an increasing demand for individual products. Companies therefore require manufacturing technologies which are customizable and allow the production of an increasing product range. One technology which meets the required criteria is selective laser melting. In a shortened process chain, near-net-shape and inner contoured special tools can be manufactured in batches, thus saving energy and resources. Furthermore, conventional preparatory work as well as production stages will be significantly reduced. An increase in the freedom of design as well as the degree of innovation and efficiency in production can be achieved.

EXPERIMENTAL INVESTIGATION OF LASER MELTING OF WC-CO 88-12

Overview of investigated process fields and, respectively the parameters

The initial point for the study was determined both by transfer of results from previous studies on laser melting of carbide and by boundary conditions of the SLM 250HL machinery. Furthermore, the economics of the process were considered, striving to achieve the highest possible build-up rate.

Consequently, for further investigations a process window was determined as illustrated in Figure 1. A variation of the focus position x_F, laser power P_L, scan speed v_s and scan line spacing h_s was carried out in the parameter study. The aim was to identify a set of parameters which allows a direct melting of the starting powder WC-Co 88-12 with a laser beam, achieving a relative density in the material compound of approx. 100 %. Measurement of out-come variables such as density, roughness and hardness was carried out on cuboid formed carbide specimens.

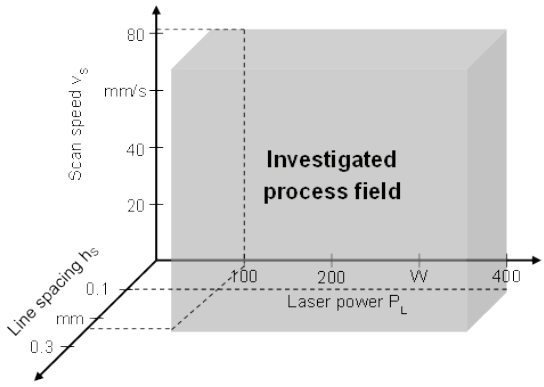

FIGURE 1. Overview of examined process fields as a function of laser power P_L, scan speed v_s and scan line spacing h_s

Variation of focus position

Focus position x_F affects the depth and width as well as the temperature of the melting pool. Focusing of the laser beam also regulates the focus spot diameter, on which all other exposure parameters are dependent. In the studies conducted, x_F was varied in the interval from 3 to -3 mm.

The additive manufacturing process ran extremely unstable. Already after 20 layers, traces were detected on the powder bed, caused by wearing out the wiper and irregular coating. This effect increased towards both extremes x_F 3 mm and x_F -3 mm. Many specimens showed an af-

terglow with a preceding spectacular spatter formation.

In the case of an unstable layer buildup, thermally induced tensions cause detachment of the test specimen, initially at its vertices, from the building platform. The contact surface to the substrate plate is reduced which leads to a delay in heat transmission. High temperatures dominate so that the impact increases and further areas of the specimen break their bindings. Furthermore, an additional phenomenon is seen. The heat remaining in the specimen is transferred to the surrounding powder, which leads to unwanted and uncontrollable powder adhesion. The body edges tend to form large elevations and wear out the wiper during each coating. Besides, the formed elevations are not covered with powder. The supplied amount of energy, which would have melted the powder, increases on the other hand any further powder adhesions. The overlapping of the mentioned phenomena and their mutual intensification leads to a snowball effect, which can result in complete detachment of the specimens. Minimum wear of the wiper was observed close to x_F=0 mm. Furthermore, fewer powder adhesions were indicated here in comparison to specimens positioned farther out. An optical assessment with a light microscope (Figure 2) was conducted as well as a tactile surface measurement (Figure 3). Specimens with focus position x_F=0,5 mm had the smoothest surface as well as the least powder adhesion at the edges. Hence, its focus adjustment was used in further studies and kept constant.

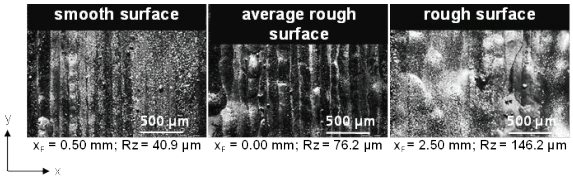

FIGURE 2. Formation of different surface qualities through varying the focus position x_F

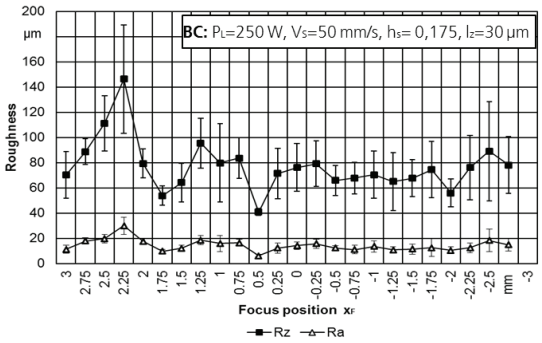

FIGURE 3. Roughness R_z and R_a as a function of focus position x_F

Variation of laser power

In order to achieve components with higher relative density, the low melting Co phase must be completely melted. Therefore the WC phase has to be wetted and cavities both inside and outside the WC-Co agglomerates must be filled. This requires a closed melting pool in the interaction zone.[1] The necessary amount of energy introduced into the powder bed is controlled primarily by the laser power P_L. With increasing laser power, higher temperatures are obtained in the melting pool and its viscosity is reduced. Similarly, the width and the depth of the melting pool increase with increasing power. In the studies conducted, P_L was varied within 125…350 W, by which the energy input area E_{FL} similarly changed from 14 J/mm^2 to 40 J/mm^2 at both extremes.

The additive manufacturing process was accompanied by a series of phenomena. A significant difference in the extent of spatter formation was detected as a function of laser power P_L. With equally increasing laser power and energy input, spatter formation increased (Figure 4). All specimens were seen with clearly visible spatter particles deposited on to the left, due to the flow direction of the processed gases. However, the effect was more pronounced at higher P_L (Figure 5)

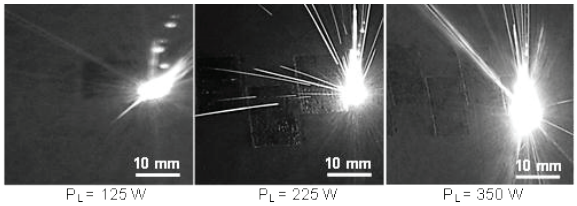

FIGURE 4. Characteristics of spatter formation as a function of laser power P_L

Additional phenomena regarding layer application were observed (Figure 5). Due to the pow-

der adhesion on the specimen edges, slight elevations were formed which caused wear on the wiper. The width of individual wear points increased with higher laser power. These were clearly visible in the form of traces in the building chamber area on the front tray. It was visible that the tray was not covered with powder at points where the wiper was worn out. The elevated specimen edges displaced the powder on both sides, which was simply shoved and smoothened by the intact part of the wiper.

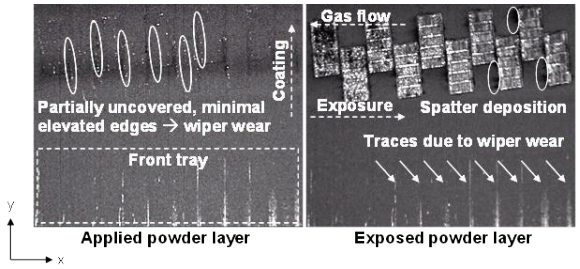

FIGURE 5. Snap shots of the building process after coating and exposure

Areas with detached corners were detected on specimens which were built with laser powers of 150 W, 175 W and 325 W. This fact was already identified during the variation of the focus position and explained in detail. In the course of this experiment, the partially detached specimens seemed to have a random character and could not be referred to the threshold value of the laser power or the energy input, from which process instability occurred.

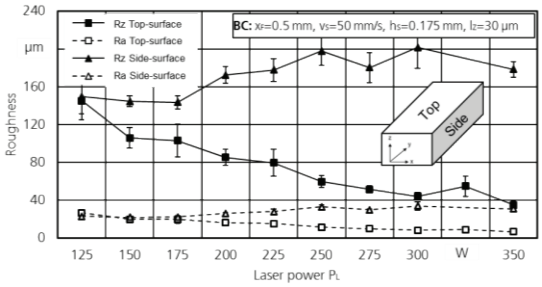

FIGURE 6. Roughness R_z and R_a as function of laser power P_L

The tactile measurement of the top as well as the side surface of the specimen showed clear tendencies (Figure 6). With increasing laser power P_L, the top surface of the specimen became smoother (Figure 7). By means of a broad melting pool at high laser power, the exposed track and the adjacent track were attached seamlessly to each other. At low laser power (e.g. 125 W), indentations and elevations were identified on the top surface of the specimen. A clear form of individual low-situated exposure tracks and elevations between them were visible to the naked eye.

However, increasing the laser power P_L caused another adverse effect. It came to a strong powder adhesion at the edges of the specimens which immensely increased the roughness of the side surfaces. This effect results from a broad melting pool as well as high temperatures. Partial heat dissipation took place at contact areas with loose powder particles (border areas). These were melted and attached to the specimen's side surface.

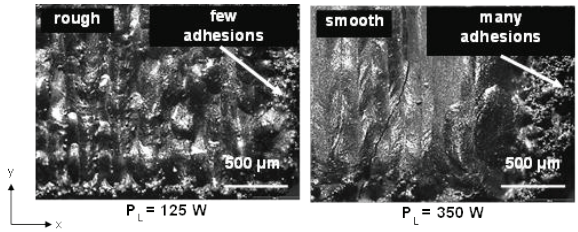

FIGURE 7. Formation of different surface characteristics on top- and side surfaces through varying the laser power P_L

Furthermore, a brown discoloration was noticed on the side surface of the specimens. The discolorations were more evident in the specimens that were exposed to higher laser power P_L. From 300 W onwards, the top surfaces were partially tinged with a bluish and violet color and were clearly identifiable under the light microscope. This was interpreted as a phenomenon of excessive input of energy. The exact description of the chemical reaction procedure coupled with a stringent explanation of the discoloration could however not be made.

Furthermore, increased laser power resulted in a pronounced brittleness (fragility) of the specimen. A few specimens broke apart at areas between the stripes due to cracks in the overlap region. The fracture region had the typical shape of a brittle fracture, which proceeds without plastic deformation. In addition, the tendency to fracture is due to unadjusted stripe spacing or stripe overlap, which occurs in stripe hatching. In order to eliminate this level of freedom, specimens in consecutive attempts were exposed with meander hatching and an angular increment. This ensures both rotation of the tracks and various positioning of the initial starting point of the exposure at each layer.

Measurement of the relative density ρ_{REL} of laser melted objects resulted in ρ_{REL} being approxi-

mately proportional to P_L (Figure 8). Increasing the laser power resulted in a high molten amount of Cobalt and in the reduction of its viscosity (increase of flowability), so that the available cavities could be closed. The dimensions of the melting pool were extended both in width and in depth, by which a widespread wetting of the tungsten carbide grains was possible.

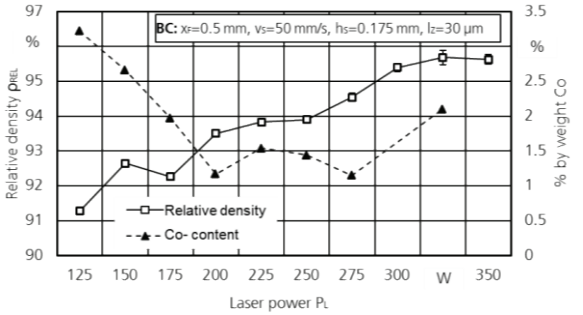

FIGURE 8. Relative density ρ_{REL} as a function of laser power P_L

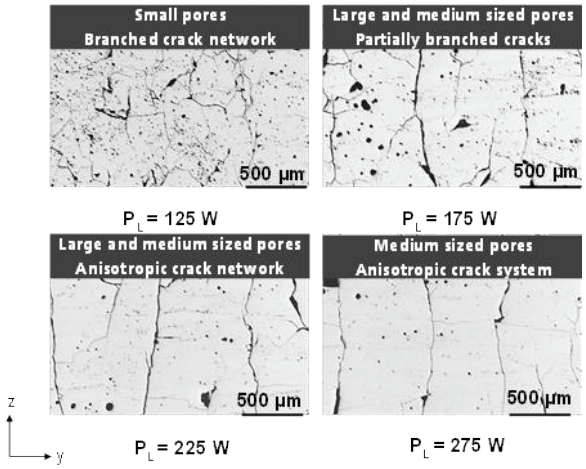

FIGURE 9. Formation of porosities of different degrees as well as differently pronounced crack networks as a function of laser power P_L

Measured values of relative density were qualitatively confirmed through metallographic examinations in build direction of cross-cut specimens. Inner porosity of the specimens sank with increasing laser power (Figure 9). Thereby, small pores were almost completely filled by larger amounts of molten Cobalt (P_L=275 W). A certain amount of average pores was available in all specimens. Furthermore, all specimens indicated clearly formed cracks. With increasing laser power, the anisotropy of the cracks increases from a complex, almost isotropic crack network of 125 W to a continuous crack network in build direction of 275 W.

Due to the layer by layer buildup of laser melting, all specimens showed an evident and unmistakable inhomogeneity (Figure 10). Periodic accumulations of coarsened WC grains (up to 10 μm) were identified between the layers. These were partially surrounded by larger cobalt accumulation. It is to be assumed that there will be WC grain growth in the upper area of the melting pool and, respectively in the laser welding bead. High temperatures and the longest cooling durations predominate there, due to primary heat dissipation in the already solidified layers. Furthermore, this area will be thermally stressed upon exposure of the top most powder layer as contact point between the melting pool and the solid object in order to transfer heat to the solid layers below.

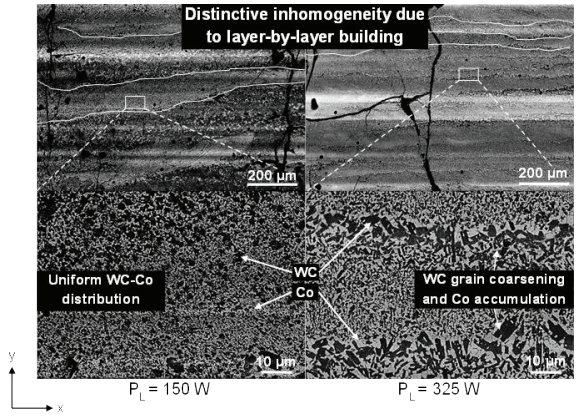

FIGURE 10. Formation of a different microstructure as a function of laser power P_L

Variation of laser power and scan speed

Scan speed v_S describes the relative movement between the focus spot of the laser beam and the powder bed to be exposed. It therefore determines the exposure time of the laser radiation on the powder bed as well as the formation rate of the melting contacts between the completely or only partially melted powder particles. With respect to minimal building time in manufacturing a component, a high density at maximum scan speed is aimed for.[1] However, a high scan speed may cause melting trade interruption which could lead to process instabilities.[2]

This experiment bears a crucial character and represents the interaction between laser power P_L and scan speed v_S at constant surface energy E_{FL}. The energy input of 28 J/mm^2 in the initially defined process window will be examined under the influence of the result quantity.

Determination of roughness (Figure 11) showed decreasing values with increasing laser power

and scan speed. The tendency towards higher surface finishing was, however, due to the increased laser power as in experiment “variation of laser power”. This increased the width of the melting pool, allowing for a seamless connection of the tracks. Simultaneous increase of scan speed v_S had a counteracting effect on the powder adhesion to the border areas, so that only a slight increase in R_z was registered on the side surface.

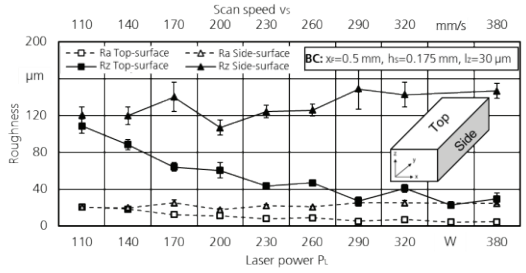

FIGURE 11. Roughness values R_z and R_a as a function of laser power P_L and scan speed v_s

Relative density ρ_{REL} was detected in the range of 140…200 W (Figure 12). The specimen that was exposed to 100 W had connections which were partially broken from the substrate plate, which resulted in high porosity due to structure instability. At 200 W, a clear decrease of relative density was verified. Based on the analysis of the grounded specimen, an increase of porosity was detected with the increase of scan speed from 40 mm/s onwards. Higher v_S reduces the permanence of a liquid phase. On that account, shorter flow distances were covered by molten cobalt, so that unclosed cavities in WC-Co texture are preserved.

The initial test weight of 30 kg was reduced to 10 kg at Vickers hardness test in order to reduce crack growth at the test indentation (Figure 13). Fluctuations of the measured values (Figure 14) are due to cracks and inhomogeneity. The greatest significance is the average value of 1350 HV10 from all measurements taken, since this is determined primarily through the material (Co content, WC grain size).

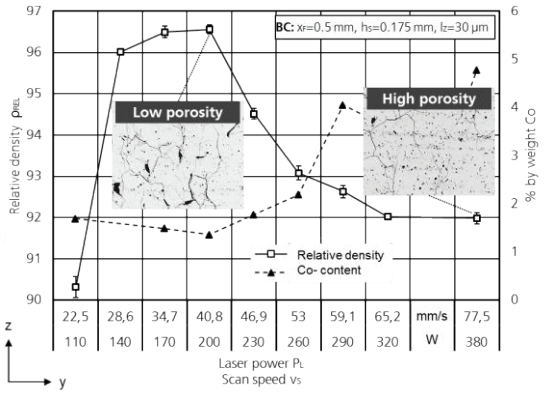

FIGURE 12. Relative density ρ_{REL} as a function of laser power P_L and scan speed v_s

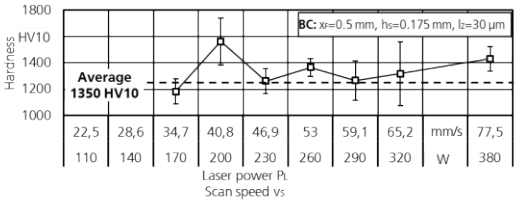

FIGURE 13. Hardness HV10 as a function of laser power P_L and scan speed v_s

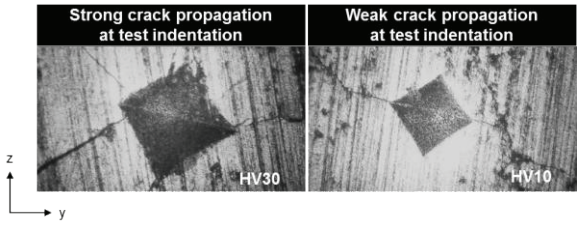

FIGURE 14. Crack propagation at test indentation at various test weights between 30 and 10 kg

The performed structure analysis of the laser melted specimens reinforced the depictions so far (Figure 15). Reducing v_S increases the permanence of the molten phase, which leads to a stringent formation of molten beads. Increasing v_S causes the contrary. Variation of P_L and v_S changes nothing on the already mentioned WC coarse grain formation, Co accumulation as well as presence of a WC-Co mixed phase.

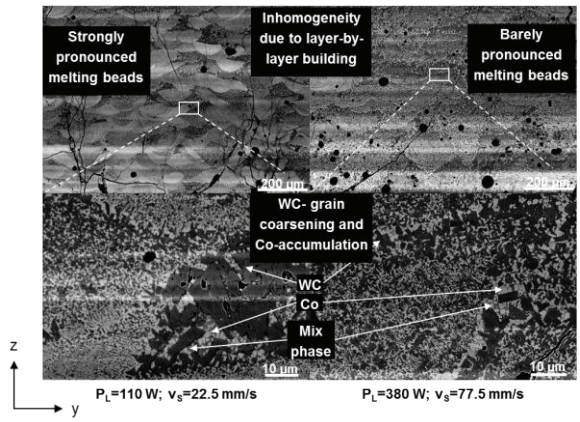

FIGURE 15. Formation of microstructures as a function of laser power P_L and scan speed v_s

A key finding was achieved in the EDX-analysis of laser melted specimens (Figure 16). It showed a clear loss of cobalt, through the SLM processing. The weight proportion of Co decreased from initially measured powder of 12% to 1…3%. The full evidence of this phenomenon was achieved through the EDX-analysis of the ring, which fastened the laser protective glass in the building chamber. The surface of the ring showed adhesions, which contained up to 52% Co. Approximately 3% Co was recorded over the entire surface of the ring.

FIGURE 16. Proof of evaporation of cobalt by means of Co adhesions on the laser protective glass

Variation of scan line spacing

The scan line spacing h_S represents the distance between adjacent scan lines. A proper setting is needed to ensure full accessibility to both scan tracks. Too widely selected scan line spacings cause interruptions in the molten areas as well as pores within the tracks. This decreases the density and strength of laser molten components. With too narrowly selected scan line spacing, cavities may form due to accumulation of meltings on the existing contours of the preceding tracks.

In the following study, the scan line spacing h_S is varied in the range 0,100…0,235 mm. This adjusts the degree of overlap of the exposed tracks, influencing the structural texture of the laser melted carbide body.

Due to the unstable process behavior triggered through the detachment of the specimen from the substrate plate, the building process could not be completed successfully. After 50 layers, all specimens were already seen with either cracks or powder adhesions, so that proceeding of the building process would result in a collision between the specimens and the layering system. This led to a manual abort of the building process.

A roughness test of the top surfaces was carried out. This however, did not yield any new insights of the effects of scan line spacing h_S. All determined values of the average surface roughness R_z fluctuated in the range of 40…50 μm without showing a clear tendency.

VALIDATION

A validation of the collected knowledge was carried out by laser melting an indexable insert, both with and without integrated cooling channels (Figure 17 and 18). The parameter selection was based on the highest measured relative density of the previous parameter optimization phase. The first prototypes could be built successfully. The building process was partially unstable as in the experimental phase, so that not all inserts were built on the substrate plate. The use of a powder with finer carbides gave no further information regarding the present process instability of laser melting.

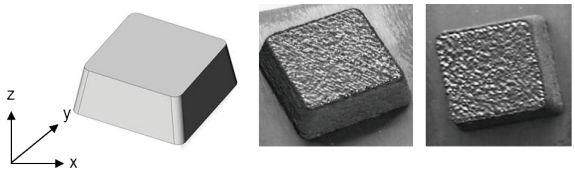

FIGURE 17. Laser melted indexable insert prototypes using WC-Co 88-12

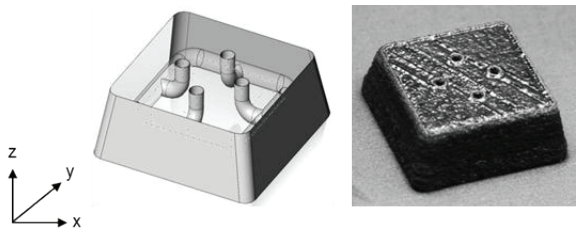

FIGURE 18. Laser melted indexable insert prototypes using WC-Co 88-12 with integrated cooling channels

CONCLUSION

In this study, the primary exposure parameters were varied and their influence on the result quantities such as relative density, roughness, hardness as well as microstructure was inspected. In addition to that, spatter formation and powder application of the coating system during the building process was recorded and analyzed. The total generated results can be summarized as follows:

- The focus position x_F affects the surface quality as well as the tendency of powder adhesion on the border area. A process safe area was in the range from -2...2 mm.
- Increasing the laser power P_L causes a proportional increase of the spatter formation. An improvement of the surface quality of the top surface, but a degradation of the surface quality of the side surface through increased particle adhesion is detected. On the one hand a higher relative density and on the other hand a embrittlement of the material due to cobalt depletion can be measured.
- A proportional increase of laser power P_L and scan speed v_S at constant surface energy input of 28 J/mm^2, induces a better surface quality of the top surface. In the region between <200 W and <40 mm/s, the highest relative density as well as the lowest porosity was achieved.

The microstructure of all specimens, regardless of exposure parameters, indicated an unmistakable inhomogeneity. This occurred due to layer by layer building of laser melting plus distinctive, both isotropic and anisotropic crack networks or systems, which were caused by cobalt depletion and thermally induced stresses. Additionally, WC grain coarsening, Co accumulations as well as a mixed phase of both components were identified. Furthermore, an average Vickers hardness of 1350 HV10 was recorded. In the validation stage, the first indexable insert prototypes were built out of WC-Co. A field test of the tools can only be performed after the existing cracks have been eliminated.

Purpose of further research studies on laser melting of carbide powders should include the following aspects: capturing an exact process field and determining post processes in order to achieve crack-free structures without pores.

REFERENCES

[1] Meiners, W.: Direktes Selektives Laser Sintern einkomponentiger metallischer Werkstoffe. Berichte aus der Lasertechnik. Rheinisch-Westfälische Technische Hochschule Aachen, Diss, Aachen: Shaker, 1999.

[2] Eisen, M.A.: Optimierte Parameterfindung und prozessorientiertes Qualitätsmanagement für das Selective Laser Melting Verfahren. Berichte aus der Fertigungstechnik. Universität Duisburg-Essen, Diss, Aachen: Shaker, 2010.

Mechanical and Microstructure Attributes of Inconel 718 Processed via Electron Beam Melting

Michael Kirka[1], Frank Medina[2], William Sames[3], Ryan Dehoff[1]

[1]Manufacturing Demonstration Facility
Oak Ridge National Laboratory
Knoxville, Tennesee, USA
[2]Arcam AB
Molndal, Sweeden
[3]Department of Nuclear Engineering
Texas A&M University
College Station, Texas, USA

INTRODUCTION

The recent surgence in capabilities of metals additive manufacturing (AM) has yielded great interest from all industry sectors. However, slowing adaptation and implementation of the technology is a lack of understanding of the microstructure-property relationships necessary for industrial component designs. Further, the microstructures obtained in metals AM processes differ greatly from those observed in identical alloys manufactured in the wrought and cast forms due to the high solidification rates and non-equilibrium phase formation. From an additive perspective, great interest has been given to high temperature alloys, specifically, Inconel 718 due to its workhorse status within the aerospace community. Of the AM processes, electron beam melting (EBM) produces components that contain low amount of residual stress, making the process particularly appealing for high temperature materials [1]. To be discussed in this manuscript is the mechanical behavior of Inconel 718 produced using the EBM process and the effect of post-processing on the monotonic tensile and high cycle fatigue (HCF) properties.

ELECTRON BEAM MELTING

EBM is a process, where fully dense metal components are built in a layer-by-layer fashion from metal powder within a powder bed. A raking mechanism spreads metallic powder across the build area for every layer. The Arcam EBM process utilizes a high power electron beam that generates the energy needed for melting the metallic powder and high build rates. Electromagnetic optics allow for near instantaneous control over the electron beam and can result in simultaneous melt pools in a given layer. For each build layer the electron beam pre-heats the entire powder bed to an optimal temperature. In the case of Inconel 718, the temperature is maintained above 850°C. Additionally, the Arcam EBM process takes place in vacuum and at high temperatures. A schematic overview of an Arcam EBM machine is shown in Figure 1.

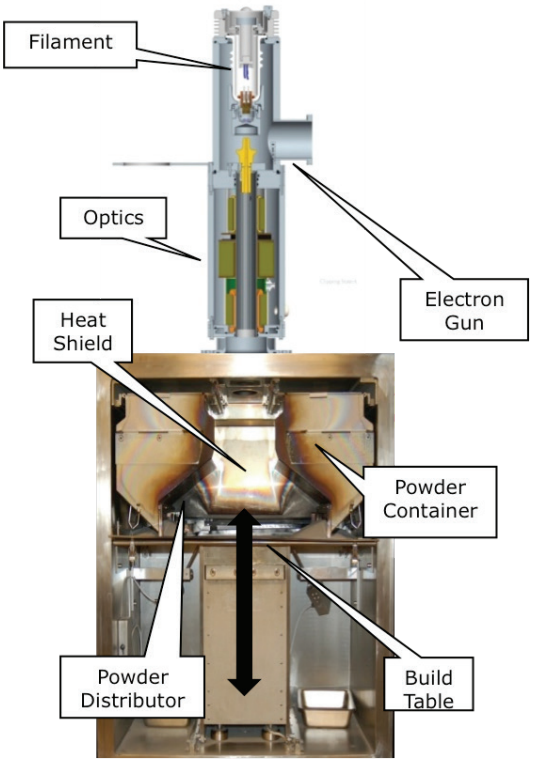

Figure 1: Interior cutaway depicting a generic Arcam EBM machine.

EXPERIMENTAL

Cylindrical and prismatic blocks were manufactured on Arcam S12 and A2X EBM machines from Inconel 718. The Inconel powder was manufactured through gas atomization and had a size range of 40-120 µm. Layer thicknesses of both 50 and 75µm were used. Throughout the builds, the temperature measured at the base plate was maintained above 850°C.

For mechanical experiments conducted, cylindrical dogbone specimens conforming to applicable ASTM standards were used. From the prismatic blocks, specimens were removed perpendicular to the build direction (XY), whereas specimens obtained from the cylinders were aligned with the build direction (Z). After machining, select groups of specimens were given post-process heat-treatments for optimizing the tensile properties and hot isostatic pressing treatments followed by a heat-treatment for removing any residual shrinkage porosity. The heat treatment and HIP conditions are listed in Table 1. For all tensile tests, ASTM E8M-13A standard was followed. Further, all HCF experiments were conducted with a stress ratio of R_σ=0.1 and frequency of 20Hz while conforming to ASTM E466-07. Fatigue life was determined by ultimate fracture of the materials.

Table 1: Post-processing conditions applied to EBM Inconel 718.

Heat-Treatment Cycle	
Solution Temperature	Precipitation Temperature
Hold at 1066 °C for 1 hour per 25 mm of thickness.	Hold at 760 °C for 10 hours Furnace cool to 649 °C and hold for 20 hours

HIP Cycle I	HIP Cycle II
Temperature 1200°C ±10°C	Temperature 1200°C ±10°C
Pressure 100MPa -0/+5MPa	Pressure 120MPa -0/+5MPa
Dwell time 120min 0/+30min	Dwell time 240min 0/+30min

RESULTS and DISCUSSION

During an EBM build, lower layers are exposed to high temperatures for greater periods of time than the upper layers. Ultimately this gives rise to microstructural gradients in the as-built material due to the precipitation and coarsening of secondary phases. While dependent on build conditions, secondary phase precipitation occurring in Inconel 718 can be roughly correlated to the time-temperature-transformation (TTT) digram for Inconel 718.

The as-built microstructure for a layer near the top of a build (Layer 1,900) and bottom (Layer 100) is shown in Figures 1a and c. In the uppermost layers of the build, the γ matrix is void of the γ′ and γ” strengthening precipitates, whereas at the bottom of the build γ’, γ”, and δ have precipitated throughout the γ matrix.

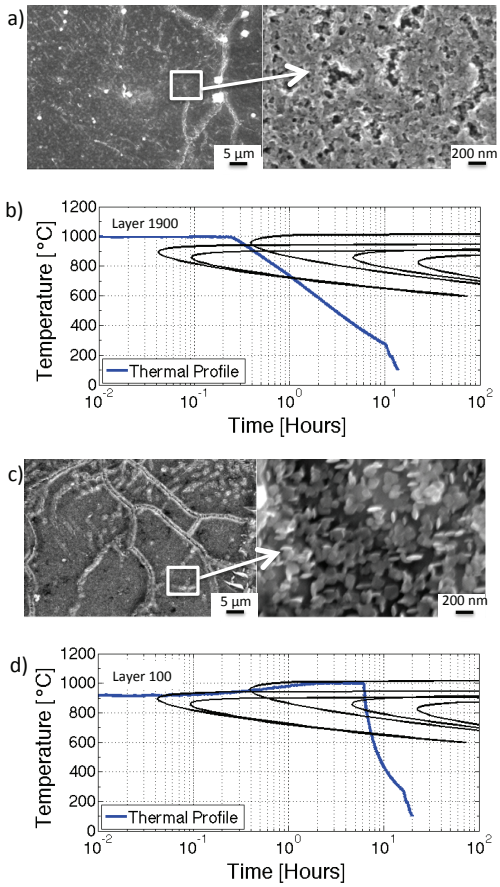

Figure 2: a) Microstructure observed at layer 100 b) TTT diagram thermal profile overlay at layer 100 c) Microstructure observed at layer 1,900 d) TTT diagram thermal profile overlay at layer 1,900.

Overlaying the thermal profiles of the respective layers onto the TTT diagram for Inconel 718, provides guidance on controlling the build temperature during the EBM process and an indication of the microstructure as a function of build height in a component. In precipitate strengthened alloys such as Inconel 718, understanding which phases are present and their respective sizes is critical due to their direct impact on the mechanical properties and the ability to properly heat-treat the material to obtain optimal properties [2].

Shown in Figures 3 and 4 are the average monotonic tensile results for EBM Inconel 718 in each of the material conditions. In each case 6 experiments were conducted to obtain the reported average values. For comparison, the Inconel 718 properties stipulated by ASTM E3055-14a in the as-built and post-processed states are indicated by red lines. In the as-built state, EBM Inconel 718 exhibits excellent tensile strength both parallel and and perpendicular to the build direction. However, the elongation at failure falls short of the required specifications.

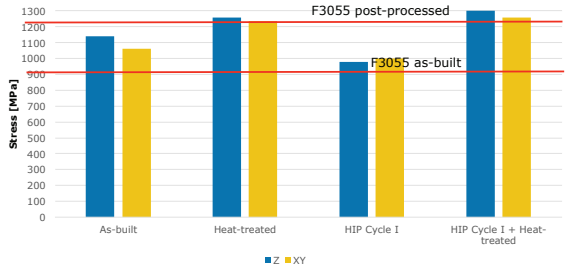

Figure 3: Average measured ultimate tensile strength for each of the Inconel 718 conditions at room temperature.

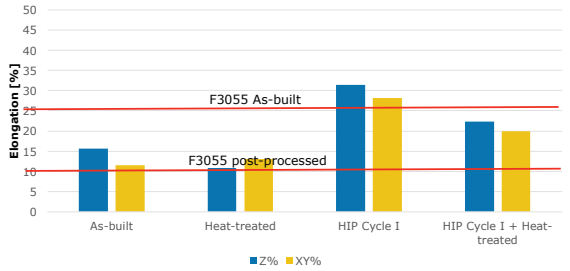

Figure 4: Average elongation at failure for each of the Inconel 718 conditions at room temperature.

With application of the heat-treatment described in Table 1, a peak aged condition is achieved resulting in acceptable average values for UTS and elongation at failure at room temperature. The UTS and elongation at failure for the heat-treated material tested at 650°C is shown in Figures 5 and 6. Between the build direction and perpendicular to the build direction the properties see a 10% decline.

To mitigate potential effects of shrinkage porosity associated with the rapid solidification occurring in the EBM process, HIP treatments were conducted according to Table 1 prior to heat-treating the material. Testing the material in the HIP state prior to heat-treating resulted in increases in both UTS and elongation to failure when compared to the as-built material. This is indicative of pore closure. However, as a result of the HIP cycle, the mechanical response is largely dominated by the matrix rather than the strengthening phases.

With application of the same heat-treatment the as-built material was given, similar UTS values were obtained with the added benefit of a 2x increase in the elongation to failure. When tested at 650°C, the HIP and heat-treated material yielded increases in the elongation at failure in both orientations as well as average UTS perpendicular to the build direction. Parallel to the build direction, the average UTS value remained unchanged from the as-built heat-treated material.

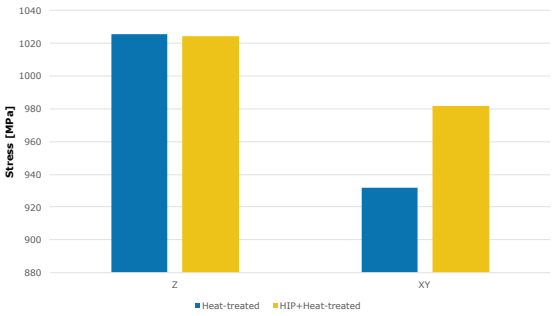

Figure 5: Average measured ultimate tensile strength for Inconel 718 in the heat-treated and HIPd and heat-treated condition at 650C.

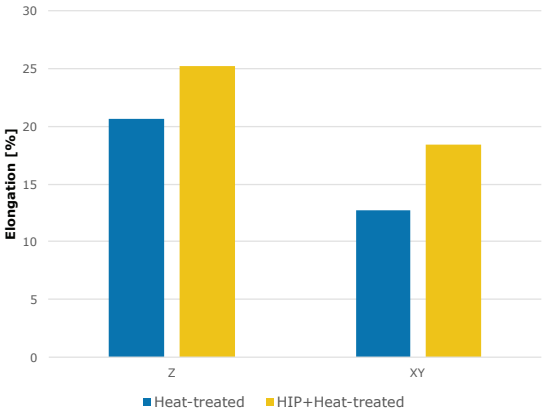

Figure 6: Average elongation at failure for EBM Inconel 718 in the heat-treated and HIPd and heat-treated condition at 650C.

High cycle fatigue results for EBM Inconel 718 material in various material conditions is shown in Figure 7. The EBM Inconel 718 material

(highlighted by the black box in Figure 7) largely under performs the traditional cast and forged Inconel 718 forms in all material conditions. This behavior is indicative that some level of micro-porosity remains present even after extensive HIP treatments. HCF behavior in the absence of porosity is governed by the ultimate tensile behavior. While the HCF results indicate much improvement in process control are required, instances where shrinkage and process induced porosity have been eliminated have resulted in excellent HCF life behavior in the EBM Inconel 718 material. These life results are highlighted by the dashed box in Figure 7.

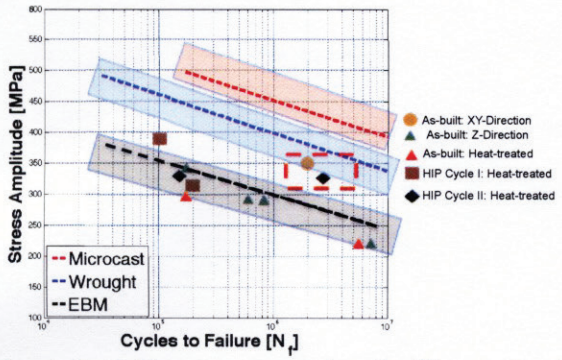

Figure 7: S-N curve comparing the life results of EBM Inconel 718 to cast and wrought Inconel 718 when tested at room temperature.

CONCLUSIONS

In the as-built condition, desirable tensile mechanical properties were obtained. However, the as-built properties are dependent on build parameters such as build temperature. Heat-treating the as-built material was found to provide the optimal microstructure for obtaining required tensile properties and satisfying the requirements of ASTM F3055 for AM Inconel 718. HIP treatments were given to material to mitigate the effects of shrinkage porosity on the HCF life behavior. It was observed that similar or superior tensile properties were obtained for HIP material in the heat-treated state when compared to that of the as-built heat-treated material at room temperature and 650°C. While the HCF fatigue life behavior of EBM Inconel 718 requires further improvement, desirable results have been obtained showing the promise of the material and process.

ACKNOWLEDGMENTS

This research was sponsored by the U.S. Department of Energy, Office of Energy Efficiency and Renewable Energy, Advanced Manufacturing Office, under contract DE-AC05-00OR22725 with UT-Battelle, LLC.

REFERENCES

[1] Sochalski-Kolbus L, et al. Comparison of Residual Stresses in Inconel 718 Simple Parts Made by Electron Beam Melting and Direct Laser Metal Sintering. Metallurgical and Material Transactions A. 2015; 46: 1419-1432.

[2] Oblak J, et al. Coherency Strengthening in Ni BaseAlloys Hardened by D022 Gamma Double Prime Precipitates. Metallurgical and Material Transactions. 1974; 5: 143-154.

Physical Processes Linking Input Parameters and Surface Morphology in Additive Manufacturing

John S. Taylor
Lawrence Livermore National Laboratory
Livermore, CA 94550
jstaylor@llnl.gov

University of North Carolina at Charlotte
Center for Precision Metrology

ABSTRACT

The morphology of surfaces that are newly-created by additive manufacturing shows a rich texture spanning varied spatial frequencies, patterns and motifs. The additive manufacturing process (e.g. selective laser melting of metals) employs a large number of input parameters, including powder size and shape distribution, laser power, laser scan spacing, pre-heat temperature, material assay, vertical step spacing, scan strategy, etc. Attempts to correlate input parameters with surface finish, typically described in terms of R_a, have shown some success, but often illuminate conflicting trends based on myriad combinations of input parameters. In this paper, it is proposed that a necessary step is to consider first the physical processes involved in creating the body and surface of the component. This is the essential rubric linking input parameters and output variables, such as those describing surface morphology. These physical processes or the resultant material properties span laser-powder interactions, plasma interactions, ablation and spatter, adhesion and sintering, phase changes, evolution of grain structure, gas ejection, local and global residual stress fields, hydrodynamics including Plateau-Rayleigh instability and Marangoni circulation, and the breadth of heat and mass transfer.

This paper draws from the literature to describe the physical processes that take place during additive manufacturing, with a focus on selective laser melting. The impact of each process on morphology is considered, and in some cases, the direct link between an input parameter and its signature on the surface. An argument is made for characterizing morphology using a richer language than R_a, particularly areal surface parameters, and perhaps a motif-based description, all following the path identified in the ISO and surface finish communities. Examples of surface morphologies on AM-fabricated components that have been measured on recently available optical surface metrology instruments are shown. Progress in predicting the 3D surface morphology of AM-fabricated components using multi-physics simulations of are also be described, with suggestions for describing resultant surface morphology. The plausibility of correlating physical processes in additive manufacturing with concomitant measured and simulated surface morphologies is discussed. Finally, it is proposed that characterization of

surface morphology on witness samples or fabricated components prior to finishing operations offers an opportunity for enhancing manufacturing process control with a view toward ensuring the stability of the essential physical processes.

AUSPICES
Lawrence Livermore National Laboratory is operated by Lawrence Livermore National Security, LLC, for the U.S. Department of Energy, National Nuclear Security Administration under Contract DE-AC52-07NA27344. LLNL-ABS-668593.

CHARACTERIZATION OF THE OPTICAL SURFACE OF ADDITIVELY MANUFACTURED LENSES

Allison E.M. Browar[1], William E. Green[1], S. J. Burns[1,2] and Jonathan D. Ellis[1,3]
[1]Department of Mechanical Engineering
[2]Materials Science Program
[3]The Institute of Optics
University of Rochester
Rochester, NY, USA

INTRODUCTION

Printoptical technology is an additive manufacturing technique consisting of specifically placed droplets to form a smooth surface with translucent bulk material without the use of post processing [1]. Pioneered by LUXEXCEL, it has gained momentum in the illumination industry for the ability to produce custom translucent optics. A recent (2015) press release revealed a collaboration between LUXEXCEL and Edmund Optics to produce custom plastic optics for the photonics industry [2]. Furthermore, recent studies have used Printoptical technology to fabricate a microlens array for photovoltaic solar concentrators [1]. However, there has not been research presented which identifies the dimensional accuracy of the finished surface. In this proceedings, we present ongoing work to characterize the specifications of Printoptical technology by presenting measurements of optical capabilities for both the LUX Standard and LUX-Opticlear materials manufactured as spherical lenses. Shape conformity was measured using an optical coordinate measuring machine [3] and local roughness with scanning white light interferometry (NewView 100, Zygo). The surface refractive index was measured using a prism coupling system [4].

SPECIFICATIONS

A CAD model depicted in Figure 1 was supplied to LUXEXCEL and was specified as a concave lens with a -45 $\pm$0.225 mm radius of curvature. The clear aperture was defined as 30 $\pm$0.050 mm with a 15 mm thick flat edge parallel to the substrate. A fiducial was placed on the flat edge for measurement purposes. The lens was ordered in both LUX-Opticlear and LUX Standard material with the required substrate. Figure 2 shows a picture of the LUX Standard (left) and LUX-Opticlear (right) lenses manufactured with Printoptical technology. This paper will characterize the experimentally measured shape and the optical properties of the lenses and compare them to the specifications provided.

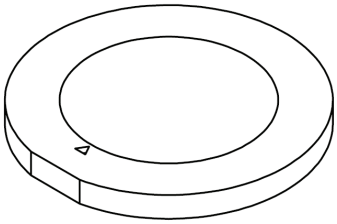

FIGURE 1. Solid model of the lens submitted to LUXEXCEL. *A fiducial consisting of a flat edge and triangular divot is positioned on the lens for orientation reference.*

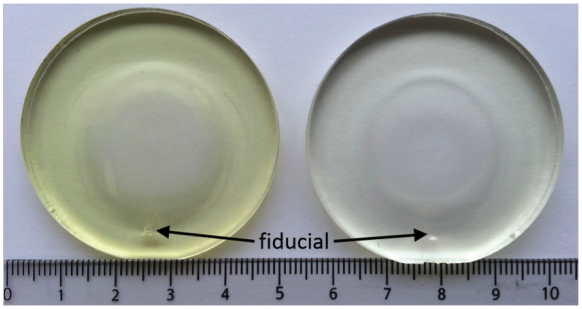

FIGURE 2. Photograph of LUXEXCEL *lenses printed with LUX Standard (left) and LUX-Opticlear (right) with specified 45 mm outer diameter, 30 mm clear aperture, and 45 mm radius of curvature. The fiducial is shown as an arrow marker and flat edge.*

As shown in the color photograph in Figure 2, the LUX Standard material has a yellow hue. In contrast, the LUX-Opticlear material is visibly transparent. Segurola, *et al.* [5] describe yellowing of the plastic material as common with UV cured photopolymers and is a result of chemical composition. This proceedings does not attempt to quantify the discoloration of the lenses but simply to note a difference.

MEASUREMENT METHODS

Various commercial devices were used to measure the surface of the LUXEXCEL lenses. The surface finish, shape conformity, roughness, and refractive index are described in the sections below. Statistical analysis is presented from four lenses of each material.

The results used to describe the surface in the next sections are defined by the MetroPro software. The arithmetic average (Ra) deviation is defined as the average deviation of each measurement point to the center line

$$Ra = \frac{y_1 + y_2 + y_3 + ... + y_N}{N}$$

where y_x is the absolute value of each measurement from the removed surface and N is the total number of measurements. The root mean square (RMS) is a common attribute in optical measurements which is defined as the standard deviation of the surface to the removed surface and is represented by

$$rms = \left(\frac{y_1^2 + y_2^2 + y_3^2 + ... + y_N^2}{N} \right)^{1/2}$$

where y_x and N are described above [6].

Shape Conformity

Traditional Fizeau interferometry was attempted to measure the surface conformity of the lenses. However, substantial high slope departures were present, leading to little useful data. While tactile probing methods were available, we opted to use a non-contact optical profilometer to prevent damage to the soft plastic optical surfaces. OptiPro Systems' UltraSurf is a non-contact five degree of freedom optical profilometer that uses three linear and two rotary stages with optical encoders to measure arbitrarily shaped optics [3]. The interferometric measurements were taken at the nominal normal vector to the optical surface via controlled motion of the optical probe. The UltraSurf was used to measure the overall shape conformity of the LUXEXCEL lens to the CAD drawing. Figures 3 and 4 show the overall surface error from the CAD model specifications. These figures show an uneven distribution of deposited material on the overall surface.

An optical probe with 0.2 mm spatial resolution was used to measure the surface of the clear aperture. Table 1 presents statistical data taken from measurements performed with the UltraSurf and the nominal 45 mm sphere removed. The

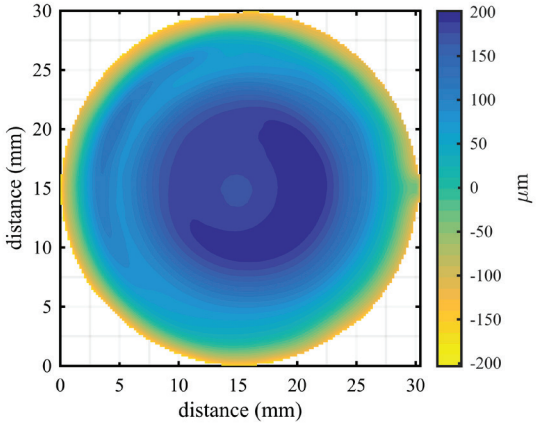

FIGURE 3. UltraSurf measurement of LUX Standard material with the nominal 45 mm radial sphere removed. The average deviation from the nominal sphere is 52.2 µm.

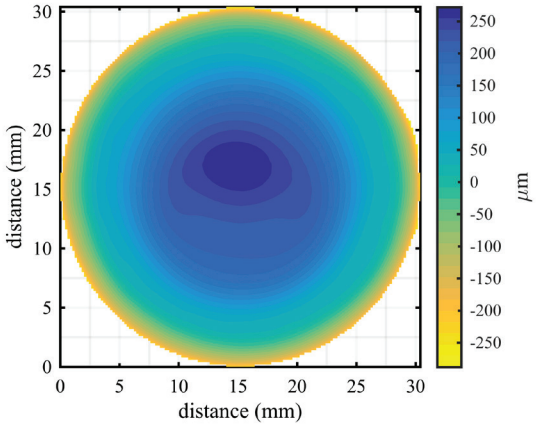

FIGURE 4. UltraSurf measurement of LUX-Opticlear material with the nominal 45 mm radial sphere removed. The average deviation from the nominal sphere is 84.9 µm.

LUX-Opticlear average error from the nominal radius is 24 % higher than the average error of the LUX Standard material. Similarly, the RMS deviation from the nominal surface is 22 % higher in the LUX-Opticlear material than the LUX Standard. However, the average radius of curvature of the LUX-Opticlear lens is closer to the nominal 45 mm than the LUX-Standard material. The relatively high standard deviation of the Ra and RMS compared to the average values indicates that the repeatability of the printoptical process may not be reliable.

TABLE 1. Statistical data taken from the UltraSurf measurements with the nominal 45 mm concave sphere removed. Data was taken from four lenses of each material. The table shows the average and standard deviation of the arithmetic average (Ra), root mean square (RMS), and radius of curvature.

Result	LUX Standard	LUX-Opticlear
Average Ra	26.93 µm	33.45 µm
Ra standard deviation	17.61 µm	28.32 µm
Average RMS	31.89 µm	39.03 µm
RMS standard deviation	19.92 µm	30.87 µm
Average radius of curvature (-45 ± 0.225 mm specified)	-48.36 mm	-46.43 mm
Radius of curvature standard deviation	0.21 mm	3.18 mm

Roughness

The local surface roughness was measured using a Zygo, NewView 600, white light interferometer with a 20X Mirau interferometric objective. Because of the field size, it is not suitable for measuring the overall form of the lens. Figures 5 and 6 show a portion of the LUX Standard and LUX-Opticlear surface, respectively, prior to cleaning with 15 Zernike terms removed.

It was found that the surface of the LUX Standard shows an 'orange peel' effect on the surface. An orange peel effect is characterized by the uneven texture on a plastic surface [7]. This texture can be the result of rapid cooling of the deposited polymer [8], or high viscosity caused by a decreased temperature of the melted polymer when forming the lens [7, 9]. Figure 5 shows the LUX Standard material measured with a 20X Mirau objective and the first 15 Zernike terms removed. There is clearly an orange peel effect; shown as a speckled pattern on the surface of the lens. In optics, the orange peel effect reduces sharpness and increases visual distortion, resulting in a low quality image [10]. In this study, the orange peel effect was absent on the LUX-Opticlear material.

Figure 6 shows the LUX-Opticlear material measured with a 20X Mirau objective and the first 15 Zernike terms removed. The residual surface exhibits corrugated lines parallel to the flat fiducial. The cause of these lines may be due to a raster process of the printoptical mechanism. The motion of the ink jet printer head is linear when depositing material droplets and inaccuracies in the drop positioning will be imprinted on the underlying structure.

To quantify roughness, the best fit sphere was removed to eliminate alignment errors and form. Figures 7 and 8 show the LUX Standard and

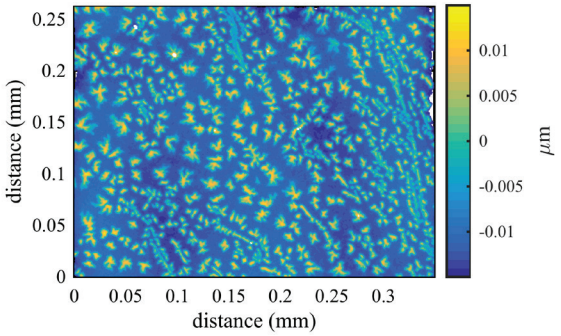

FIGURE 5. Areal profile of the LUX Standard lens measured with a 20X Mirau objective and the first 15 Zernike terms removed. It is clear that there is an orange peel effect.

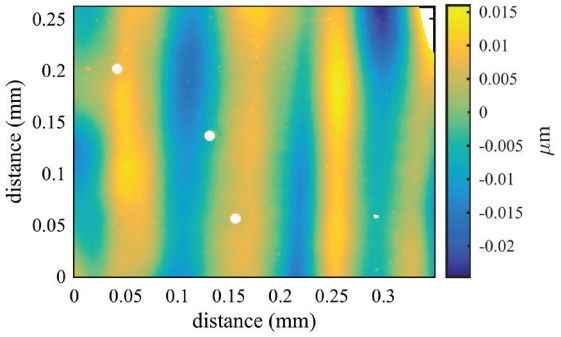

FIGURE 6. Areal profile of the LUX-Opticlear lens measured with a 20X Mirau objective and the first 15 Zernike terms removed. Vertical corrugated lines are parallel to the flat part of the fiducial.

LUX-Opticlear lenses, respectively, with the best fit sphere removed. It should be noted that two lenses were cleaned prior to measurement. Due to the soft material, after cleaning with an alcoholic based solvent and a lens cleaner scratches on the surface can be seen and the

TABLE 2. Statistical data taken from the NewView measurements with the best fit sphere removed. A 20X Mirau objective was used to take measurements with a NewView 600.

Result	LUX Standard	LUX-Opticlear
Average Ra	0.013 µm	0.019 µm
Ra standard deviation	0.013 µm	0.006 µm
Average RMS	0.017 µm	0.024 µm
RMS standard deviation	0.016 µm	0.007 µm

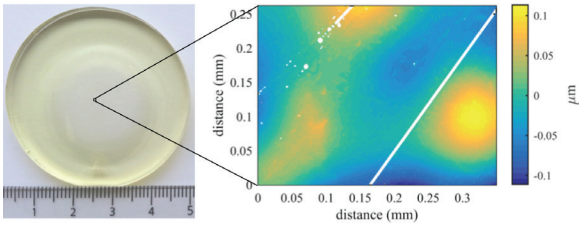

FIGURE 7. NewView 600 measurement of LUX Standard material with the best fit sphere removed.

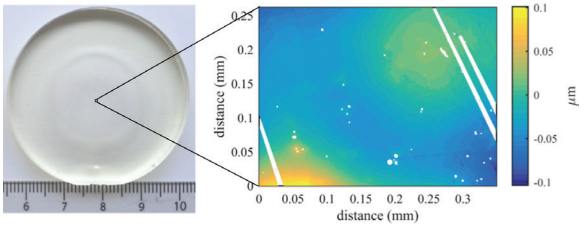

FIGURE 8. NewView 600 measurement of LUX-Opticlear material with best fit sphere removed.

apparent orange peel has decreased. Table 2 presents statistical data taken from measurements performed with the NewView 600. With the best fit sphere removed, the underlying roughness can be observed. The LUX-Opticlear material has a 46 % higher average roughness than the LUX Standard material and a 41 % higher RMS. There is a high standard deviation with respect to the average measurements, again indicating a low repeatability.

Refractive Index

The Metricon prism coupling system measures the refractive index of the surface [11]. The flat rim of each optic was placed in contact with the prism. A sensor measures the laser intensity reflected from the interface at various angles. When the critical angle is reached, the intensity drops dramatically. The Metricon software calculates the refractive index of the material surface using the critical angle and the known refractive index of the prism [4]. A 632.8 nm source was used in the Metricon. Each lens was measured in four equidistant positions. The rim on three of the LUX-Opticlear lenses were not flat enough to measure the refractive index with the Metricon system and the data was not collected. A single lens made with LUX Standard material had an average refractive index of 1.5287 with a standard deviation of 0.0026. The measurements of the other three lenses made with LUX Standard material had similar refractive index to the first measurement but was not consistent to the third decimal place. A single LUX-Opticlear lens had an average refractive index 1.5008 with a standard deviation of 0.0004. Both the refractive index of the LUX Standard and LUX-Opticlear material are higher than the common refractive index of PMMA which is 1.48 at 632.8 nm according to [12].

RESULTS AND DISCUSSION

We demonstrate preliminary optical metrology results of two different additive manufacturing techniques for Printoptical technology. The surface figure error, roughness, and refractive index was measured and analyzed. MetroPro software was used to subtract the nominal radius of curvature from the UltraSurf data and calculate the arithmetic average (Ra), root mean square (RMS), and best fit radius of curvature shown in Table 1. The NewView 600 data with the best fit sphere removed was analyzed in the same fashion as the UltraSurf measurements, shown in Table 2.

From these preliminary results, the LUX Standard material has a better surface conformity and roughness than the LUX-Opticlear material. The radius of curvature of the LUX Standard and LUX-Opticlear material was measured to have an 7.5 % and 3.2 % errors, respectively, which were both out of the specified tolerances. The refractive index of the LUX Standard and LUX-Opticlear materials were 2.7 % and 1.3 % higher than the conventional PMMA at 632.8 nm, respectively.

Although the lenses are visibly noteworthy

in terms of transparency and smoothness of additively manufactured lenses, the high standard deviation of the measurements in both tables indicate that the process of the printoptical technology may not have consistent repeatability. Additive manufacturing for optical components is a promising technology but the processes as demonstrated must be further optimized to meet tolerance specifications for imaging applications.

ACKNOWLEDGMENTS

The authors would like to acknowledge Brittany Taylor, Scott DeFisher (OptiPro Systems), and Kejia Fang for help with obtaining experimental measurements. We would also like to acknowledge funding support from the NSF Integrative Graduate Education and Research Traineeship (IGERT) Program: Distributed Renewable Energy: From Science and Technology to Entrepreneurship and Policy (NSF Award #0966089), NSF I/UCRC Center for Freeform Optics (IIP-1338877), Xerox Research Foundation, and Harbec Incorporated.

REFERENCES

[1] Price JS, Sheng X, Meulblok BM, et al. Wide-angle planar microtracking for quasi-static microcell concentrating photovoltaics. Nature Communications. 2015;p. 1–8.

[2] Edmund Optics and LUXeXceL Bring 3D Printed Plastic Optics to the Photonics Industry [press release]. Edmund Optics; 2015. Online.

[3] DeFisher S, Bechtold M, Mohring D. A Non-Contact Surface Measurement System for Freeform and Conformal Optics. In: Tustison RW, editor. Proceedings of SPIE. Window and Dome Technologies and Materials XII. OptiPro Systems; 2011. p. 80160W–1–80160W–6.

[4] Ulrich R, Torge R. Measurement of Thin Film Parameters with a Prism Coupler. Applied Optics. 1973 December;12(12):2901–2908.

[5] Segurola J, Allen NS, Edge M, et al. Photoyellowing and Discolouration of UV cured acrylated clear coating systems: Influence of Photoinitiator Type. Polymer Degredation and Stability. 1999;p. 39–48.

[6] MetroPro Reference Guide; 2006.

[7] Berins ML, editor. Plastics Engineering Handbook of the Society of the Plastics Industry. 5th ed. Kluwer Academic Publishers; 2002.

[8] Bichler M. Eliminate Surface Defects on Molded Parts. Plastics Technology. 2005;.

[9] Tordella JP. Fracture in the Extrusion of Amorphous Polymers Through Capillaries. Journal of Applied Physics. 1956 May;27(5):454–458.

[10] Spectrophotometry: Accurate Measurement of Optical Properties of Materials. vol. 46. Elsevier; 2014.

[11] Bulk Material or Thick Film Index. Metricon Corporation; 2015.

[12] Nikolob ID, Ivanov CD. Optical Plastic Refractive Measurements in the Visible and the Near-Infrared Regions. Applied Optics. 2000 May;39(13):2067–2070.

MULTI-SCALE AREAL CURVATURE ANALYSIS OF FUSED DEPOSITION SURFACES

Tomasz Bartkowiak[1], James T.Lehner[2], Joyce Hyde[2], Zhijie Wang[2], David Bue Pedersen[3], Hans Nørgaard Hansen[3], Christopher A. Brown[2]
[1] Institute of Mechanical Technology, Poznan University of Technology, ul. Piotrowo 3, Poznan, 60-965, Poland
[2] Surface Metrology Laboratory, WPI, Worcester, MA, USA
[3] Department of Mechanical Engineering, Technical University of Demark

INTRODUCTION

The objective of this work is to demonstrate the use of multi-scale areal curvature analysis to study surfaces created by FDM (fused deposition modeling), both as-deposited and as-polished with acetone vapor. Areal, multi-scale curvature analysis has been recently developed to better understand surface topographies, how they are manufactured and how they behave.

This is application of multi-scale areal curvature analysis is particularly important because surfaces made by additive manufacturing present new challenges for topographic characterization. Conventional topographic characterization has been developed primarily for characterizing surfaces created by machining and abrasive processing, because historically this is the way most surfaces of technological importance have been created. The new characterization methods might require new characterization methods.

It is difficult to control the surface roughness in AM (*Burns and Brown 2014*), especially during deposition by FDM (*Zeng et al. 2014*). The roughness is related to the layer thickness (*Zeng et al. 2014*). The roughness is modified by the inclination of the surface when it has been deposited by displacing the deposition of the successive external layers laterally compared to the underlying layer in order to form a surface that is inclined in a vertical plane (*Zeng et al. 2014*). When the deposited surface is inclined this way, more of the bead, or layer, is exposed, and can have an effect similar to increasing the layer thickness when it is measured tangential to the large slope (*Zeng et al. 2014*).

The layer thickness appears to be an important manufacturing process parameter for relating the process to the surface roughness. This would be similar to the feed in machining. It is easier, however, to change the feed in machining than to change the layer thickness in FDM. Surfaces made by FDM are nonetheless fundamentally different from machined surfaces. FDM surfaces have convex beads with sharp valleys in between, whereas machined surfaces have concave grooves separated by sharp ridges. Both surfaces could have similar values for conventional height characterization parameters, although each would have distinctly different behaviors, because they are essentially mirror images of each other. For example, the sharp positive curvatures on the FDM surfaces would be expected to cause stress concentrations and reduce fatigue limit.

Current practices, parameters and scales of measurement and analysis, in surface metrology have evolved primarily for their utility in characterizing surfaces created by abrasive and machining processes. Surfaces in additive manufacturing are distinctly different from machined surfaces. It should not be expected that the same practices will be similarly useful for additive manufacturing. The value in surface metrology is derived largely from the ability to discriminate surfaces based on parameters calculated from their measurement. Two things are important for discrimination, characterizing the appropriate features and characterizing them at the appropriate scale.

Previous work on FDM surfaces has used multi-scale length and areal analyses to discriminate AM surfaces deposited with different thicknesses and angles (*Zeng et al. 2014*). In order to better understand how to produce FDM that will behave in predictable ways other characterization methods need to be applied. Multi-scale curvature analysis of profiles has recently been developed and proved useful in fatigue (*Vulliez et al. 2014*).

In this work multi-scale curvature tensors are evaluated as a function of position on areal measurements of FDM surfaces as-deposited and as-polished with acetone vapor.

METHODS

Cubes having nominal dimensions of 20x20x20mm with a 10mm arc from one side to the top were manufactured on a Stratasys Dimension 1200 FDM and polished with acetone vapor (Fig. 1). The rounded portion is used to study the angle of inclination, or slope, from vertical on the side to horizontal on the top.

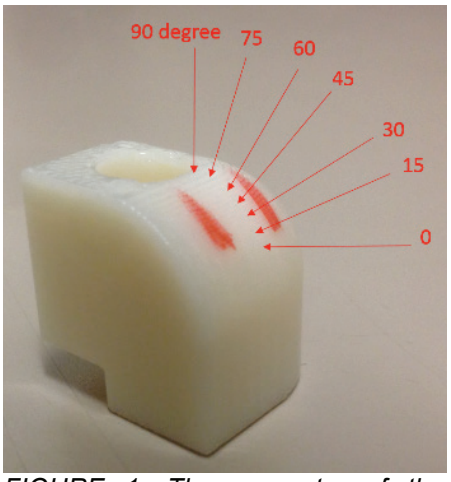

FIGURE 1. The geometry of the deposited block. The 0º surface is vertical and 90º is horizontal.

The vapor solvent polishing was done in a vacuum chamber, in which a saturated acetone vapor is formed when the pressure in the chamber is lowered to the vapor pressure of acetone. The process is cold and the atmosphere with its oxygen is pumped from the chamber; so it is a safe procedure.

Surfaces were measured perpendicular to the angle of inclination or deposition on the side around the curve with an Olympus scanning laser confocal microscope (OLS4100). Each surface measurement initially consists of over a million (1024x1024) height samples. These were made at locations every 15 degrees along the arc from vertical (0^0) to 75^0. Topographies (85x85µm) were measured on the top of the beads of the deposition layers with the 50x lens using 3X digital zoom. The region is reduced to 500x500 height samples to facilitate the calculation of the 3D curvature tensors, which is computationally intensive.

These surfaces were also evaluated with conventional height and hybrid parameters (ISO 25178 and ASME B46.1).

In this work curvatures are calculated using 3D normal based method. First of all, normal have to be computed prior curvature calculation. Our approach applies the covariance matrix method for computing normal. The closest 3×3 neighborhood is used for computations. The height samples on the edge are excluded from further analysis because they might generate high error value.

The curvature tensor **T** is a symmetric 3×3 matrix. The eigenvalues k_1, k_2, 0 represent the principal curvatures. The eigenvectors k_1, k_2 are the corresponding principal directions for the principal curvatures and **n** is the surface normal.

Theisel et al. (2004) presented a new technique for estimating curvature tensor **T** in a triangular mesh. That method shows better error behavior than a cubic fitting (*Goldfeather et al. 2015*) and is independent of rotations of the mesh and does not involve any parameterization or fitting. The accuracy of this method is dependent mostly on the accuracy of normal estimation. In the process of the curvature calculation for a particular scale the selection of points for the estimation of normals and the creation of triangular patches becomes an important issue.

In the present method, for each scale, height samples are extracted from the original measurement. Every iteration requires down sampling for the appropriate corresponding scale.

RESULTS

Renderings of the measured regions as-deposited and as-polished with acetone vapor, at deposition angle of 0º, i.e., a vertical side, are depicted in Figures 2 a) and b) respectively. Note that the vertical scale for the as-deposited surface is about five times larger than for the as-polished surface. The difference polishing makes is striking. The large curvature from the deposition bead is barely evident in 4b, after polishing, even with the more detailed scale.

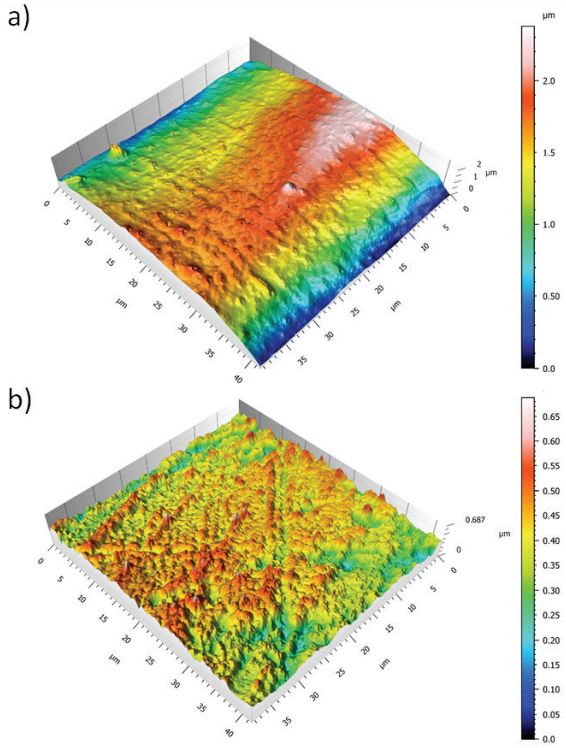

FIGURE 2. Renderings of the surfaces measured at deposition angle equal to 0°: a) as-deposited, b) as-polished.

The conventional height and hybrid parameters (ISO 25178-2) calculated for as-deposited and as-polished surfaces are shown in Table 1.

TABLE 1. Conventional and hybrid parameters calculated on the measured surfaces.

as-deposited

	Convetional			Hybrid	
Angle	Sa	Sv	Sz	Sdr	Sdq
0	*0.379*	*1.39*	*2.38*	*3.20*	*0.372*
15	*0.419*	*1.42*	*2.51*	*4.03*	*0.397*
30	*0.538*	*1.75*	*2.94*	*4.29*	*0.450*
45	*0.459*	*1.47*	*2.51*	*3.43*	*0.400*
60	*0.420*	*1.47*	*2.29*	*4.14*	*0.506*
75	*0.207*	*0.791*	*1.46*	*2.61*	*0.257*

as-polished

	Convetional			Hybrid	
Angle	Sa	Sv	Sz	Sdr	Sdq
0	*0.055*	*0.404*	*0.687*	*2.05*	*0.216*
15	*0.026*	*0.116*	*0.288*	*0.35*	*0.085*
30	*0.031*	*0.214*	*0.447*	*0.77*	*0.128*
45	*0.015*	*0.182*	*0.377*	*0.51*	*0.103*
60	*0.168*	*0.761*	*1.150*	*1.00*	*0.154*
75	*0.114*	*0.503*	*0.839*	*0.18*	*0.061*

Principal curvatures k_1 calculated for two different scales from regions measured at a 0º deposition angle are shown in Fig. 3. Negative curvatures represent convex surface features or valleys. Different scales of calculation show different features. For the as-deposited surfaces the convex bead is clearly visible as blue region at the larger scale, 4.17µm, about a tenth of the length of a side of the measurement shown in Fig. 2. Acetone polishing removes the much of the large scale convexity and adds fine scale complexity and fine scale details to the topography. Grooves visible at as-deposited surface rendering are visible on fine scale k_1 curvature plot as positive curvature regions.

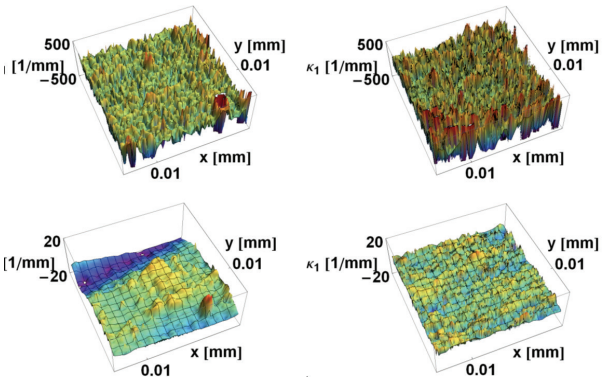

FIGURE 3. Maximum principal curvature k_1 calculated at each position for as-deposited (left column) and as-polished surfaces at deposition angle of 0°, calculated for two different scales of 0.417µm (top row) and 4.17µm.

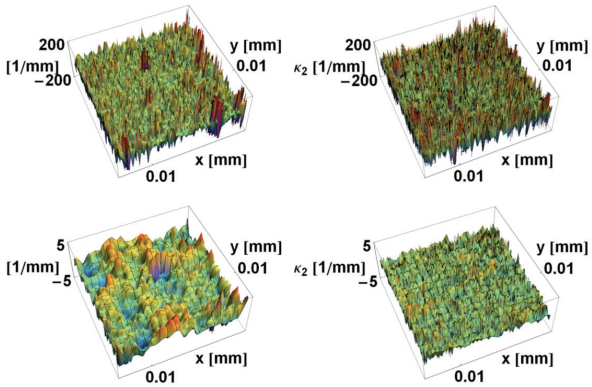

FIGURE 4. Minimum principal curvature k_2 calculated at each position for as-deposited and as-polished surfaces at deposition angle of 0°, calculated for two different scales of 0.417µm (top) and 4.17µm.

The minimum principal curvatures k_2 shown in Fig. 4 show the same tendencies as the maximums. The calculated values also show the influence of the processing. For the finer scales, the curvature values are smaller after the acetone treatment as some fine scale elements are removed.

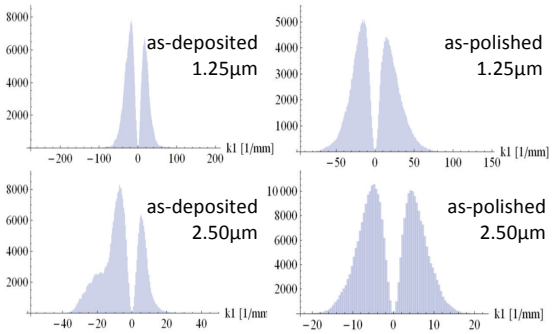

FIGURE 5. Distributions of maximum principal curvatures k_1 for as-deposited (left column) and as-polished surfaces measured at a deposition angle of 0°, calculated at two different scales 1.25 µm (top row) and 2.50 µm. Note that the x-axis for the as-polished surfaces is half as large as for the as-deposited surfaces.

Distribution of k_1 principal curvatures calculated for, measured at deposition angle equal to 0°, calculated for two scales 1.25µm *and* 2.50µm are presented in Fig. 5. It can be seen that the curvature values change with polishing. The distributions become narrower with polishing, tending towards zero for both scales. At the larger scale the as-deposited surface has the most negative curvatures, or convex regions.

Fig. 6 shows the mean and standard deviations of the maximum principal curvatures k_1 as a function of scale for several deposition angles, for as-deposited and as-polished surfaces. It can be noticed that the acetone vapor polishing reduces the magnitude of the mean principal curvature k_1 for all the calculated scales. Standard deviation follows the same pattern for all the angular orientations except 0º. The standard deviation increases markedly with decreasing scale.

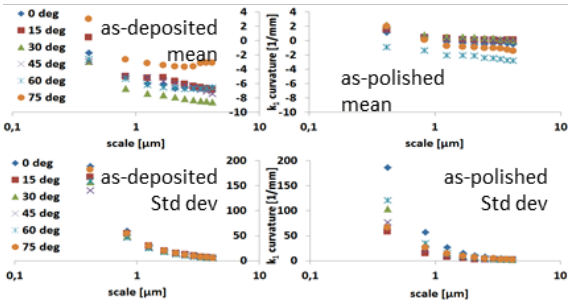

FIGURE 6. Statistical parameters: mean and standard deviation describing the distribution of principal k_1 curvatures calculated for various deposition angles.

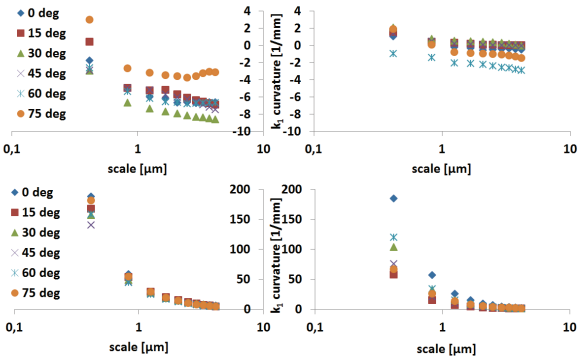

FIGURE 7. Statistical parameters: mean (top row) and standard deviation describing the distribution of minimum principal curvatures k_2 calculated for various deposition angles, as-deposited (left column) and as-polished.

Mean and standard deviation calculated for the distribution of principal k_2 curvatures calculated for the as-deposited and as-polished surfaces for several deposition angles are presented in Fig. 7. Acetone polishing clearly influences mean of the minimum curvatures. For the fine scale the magnitude is reduced and for the larger scales it tends to zero (indicating a tendency for flatness in one direction) for all the deposition angles. As for the standard deviation, the treatment decreases its values for the fine scales.

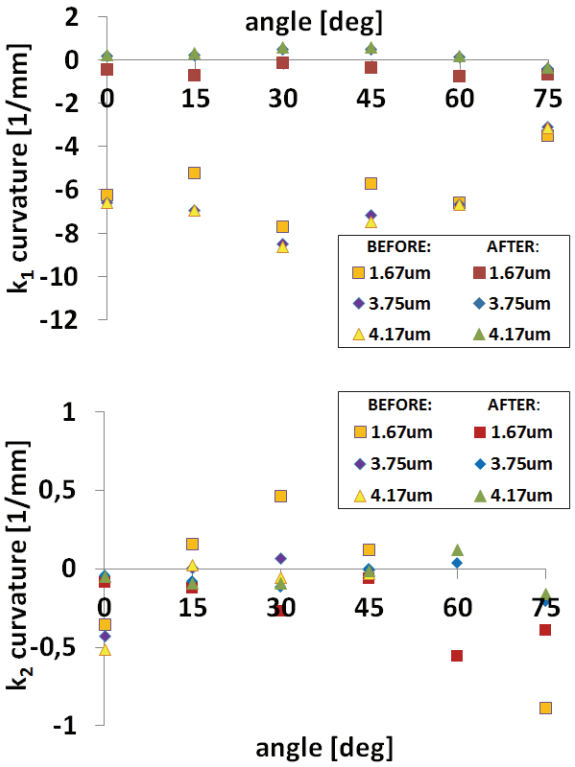

FIGURE 8. Mean of maximum and minimum principal curvatures (k_1 and k_2) plotted versus deposition angle for three scales. Before and after refers to as-deposited and as-polished surfaces respectively.

In Fig. 8, maximum and minimum principal curvatures, k_1 and k_2, are presented versus deposition angle for three scales: 1.67µm, 3.75µm and 4.17µm. It can be noticed that acetone polishing tends to decrease the difference of principal curvatures for most of the deposition angles making the surfaces more flat and less differentiated at most scales.

DISCUSSION

The plots of curvature versus position at different scales show things about the character of the differences between surfaces which are not evident from conventional height or hybrid parameters. The latter are calculated at specific scales and miss the transitions in nature of the topographies that are evident in multi-scale evaluation of the curvature.

CONCLUSIONS

1. Curvature describes surface topographies in a way that can identify convex and concave regions of a measured surface.
2. Different scales of calculation can show different surface features, e.g., fine scale analysis can indicate micro groves and holes, whereas large scale analysis can show general shape of the surface.
3. Distribution of principal curvatures is influenced by the acetone polishing. Both maximum and minimum principal curvature values decrease after the acetone vapor polishing. Acetone polishing also decreases the differences between the maximum and minimum principal curvatures between different deposition angles making the texture more similar at all scales.
4. The maximum and minimum principal curvature values are influenced by the deposition angles. Before treatment the maximum and minimum principal curvatures indicate greater for depositions at 30º and 45º. After treatment the maximum principal curvature also follows the same pattern. The minimum principal curvature acts similarly for 45º and 60º (for two scales).

ACKNOWLEDGEMENTS

The authors would like to thank Olympus for their generously allowing us to use of an OLS4100 scanning laser confocal microscope, and Digital Surf for their generously allowing us to use MountainsMap. The research into 3D curvature was partially supported by the Kosciuszko Foundation.

REFERENCES

[1] Burns C M, Brown C A, Form and Outlier Removal by Modal Filtering of Confocal Measurements of Laser-Sintered Additive-Manufactured Surfaces, 29th Annual Meeting of the American Society for Precision Engineering, November 9-14, 2014.

[2] Zeng Y, Wang K, Mello B C, Wang Z., Brown C A, Multi-Scale Evaluations of the Roughness of Surfaces made by Additive Manufacturing, ASPE Abstract: 3953, 2014 ASPE Spring Topical Meeting, Dimensional Accuracy and Surface Finish in Additive Manufacturing, April 13-16, 2014, University of California – Berkeley.

[3] Vulliez M., Gleason M.A., Souto-Lebel A., Quinsat Y., Lartigue C., Kordell S.P., Lemoine A.C., and Brown C.A., Multi-scale curvature analysis and correlations with the fatigue limit on

steel surfaces after milling, Procedia CIRP, 2014; 13: 308-313.
[4] Theisel, H.; Rossi, C.; Zayer, R.; Seidel, H.-P., "Normal based estimation of the curvature tensor for triangular meshes," Computer Graphics and Applications, 2004. PG 2004. Proceedings. 12th Pacific Conference on Computer Graphics and Applications, 6-8 Oct. 2004; 288-297.
[5] Goldfeather J., Interrante V., A novel cubic-order algorithm for approximation principal directions vectors, ACM Transactions on Graphics, 2004; 23(1): 45-63.
[6] ISO 25178-2:2012 Geometrical product specifications (GPS)
[7] ASME B46.1 Surface Texture (Surface Roughness, Waviness, and Lay)

Quality optimized Additive Manufacturing through Measuring System Analysis

Eckart Uhlmann[1, 2], Patrick John[1], Vasyl Kashevko[1], Georg Gerlitzky[1], André Bergmann[2]
[1]Institute for Machine Tools and Factory Management IWF
Technische Universität Berlin
Berlin, Germany
[2]Institute for Production Systems and Design Technology IPK
Fraunhofer-Gesellschaft
Berlin, Germany

INTRODUCTION

Additive Manufacturing (AM) processes are increasingly integrated into today's value-added chains and will be prospectively used for batch production. In comparison to conventional manufacturing processes, AM offers tremendous advantages such as feature-integration like undercuts as well as inner cooling channels [1], [2], [3]. However, the design process is limited by specific restrictions, that hinder tapping the full potential of AM [4].

Previous work focused on limits of the machinery, taking into account that every machine has different manufacturing limits depending on the material used and surrounding conditions [5], [6], [11]. However, each building process uses individual manufacturing parameters, which leads to a complex set-up. In order to monitor and analyze each building process, it would be an advantage to develop a testing method that could easily adapt to individual set-ups.

In most industries the importance to control every manufacturing step increases. For an appropriate analysis of additive manufactured parts, complex requirements need to be fulfilled by the measurement systems.

OBJECTIVE

The approach of this paper is, to develop a test component which is capable to quantify the process quality. Following previous investigations, the aim of this investigation is to develop an effective and inexpensive rapid test which allows an assessment of each building process.

In addition, a measuring system analysis of optical and tactile measuring systems for additive manufactured parts was realized. In Additive Manufacturing there is no standardized procedure for measurement of dimensional shape-, location- and surface accuracy. Besides, scientific uncertainty persists concerning the suitability of several optical and tactile measurement systems. On this topic research is needed, because some measuring systems are stretched to their limits due to the complex geometries that are created by Additive Manufacturing. This Paper compares the suitability of optical measuring systems with tactile measuring systems with different functionalities. Two tactile and two optical measuring systems were examined concerning different characteristics. The developed test component is used to ensure comparability of the measurements as well as validation of a suitable measuring method and measuring system covering the whole measurement process. This approach can be used to establish a method which makes Additive Manufacturing suitable for serial production and improve quality assurance.

PROCEDURES

First the geometry of the test component was developed, subsequently the powder was analyzed. Powder investigations and following mechanical strength analysis are important analytical steps and should be performed at the beginning of every Additive Manufacturing process [11].

Development of the test structure

This paper follows previous research activities at IWF and IPK concerning the assessment of additive manufactured parts. Up to now IWF and IPK used the test structure, shown in Figure 1, to assess selective laser melting (SLM) manufactured parts [11]. On this basis a more efficient and flexible structure is being developed. The implementation of a reference surface and the removal of the building platform were the first steps to improve the measuring conditions.

The authors analyzed several studies [4], [5], [6], [7], [8], [9], [10] as well as standards [12] regard-

ing geometry and positioning tolerances of AM and related processes like laser sintering and casting. A test structure of elementary geometric shapes like holes, angles, overhangs and radii as well as surfaces roughness measurements on inner and outer contours were developed (Table 1). The aim was to arrange as many structures as possible on the smallest possible volume, in order to examine shape characteristics, positional precision, dimension accuracy and surface quality.

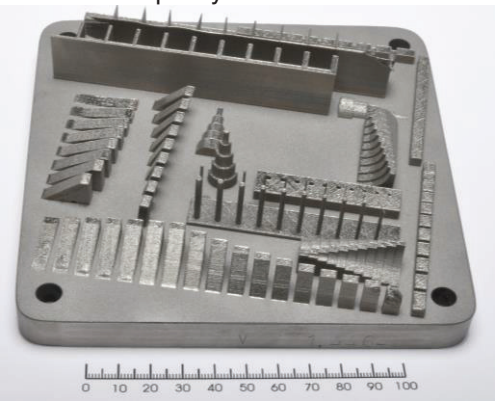

FIGURE 1. Previous test structure.

TABLE 1. Elementary geometric shapes and sizes.

shape	dimension	attribute
Round drilling	d = 10 mm	-
Angular drilling	d = 10 mm	-
Inclined drilling	d = 10 mm	45°
Inclined walls	l = 3.5..14.3 mm	75°;50°
Inner radius	r = 2.5..12 mm	2.5 mm
Outside radius	5..6mm	

These features and their predefined gradations were examined for surface characteristics. For this purpose, simple features and basic elements were identified which contain information of the attained process quality. Figure 2 illustrates the test component made of steel 1.2709. In order to save resources and machining time as well as to guarantee realisability for most machines, all elements were included in one cube with the dimensions 35 x 25 x 30 mm.

FIGURE 2. Developed test component to measure process quality for Additive Manufacturing.

Manufacturing Process with SLM

The component was produced with constant process parameters and without any support structures. Process parameters are shown in Table 2

TABLE 2. Process parameters.

condition	value	unit
Oxygen content	0-2	%
Laser wave length	1100	nm
Laser power	295	W
Scan speed	730	mm/s
Scanning strategy	chess	-
Coater velocity	500	min^{-1}
Layer thickness	50	μm
Average grain size	27	μm

To qualify the material for SLM, the necessary powder analysis on material 1.2709 was carried out according to DIN and VDI standards. The subsequent qualification of the material specific properties such as mechanical strength values and micrographs were also carried out [11].

Finishing

After the built process the test component was removed from the building platform via EDM. Due to corrosion after the eroding process glass bead blasting was necessary. Depending on the duration of blasting, this affects the surface quality of the test component.

Measuring Systems

Four different measuring systems were analyzed, the two tactile measuring systems Hommel Nanoscan and Zeiss O-Inspect as well as the two optical measuring systems, FRT Microprof MPR100 and Alicona InfiniteFocus. To quantify the quality of the test component, shape

characteristics, positional precision, dimension accuracy and surface quality were examined and assessed. All measuring systems feature a different suitability for the test component's inspection due to their specifications. It can be shown which measuring system is suitable for the examination of all measurement criteria. All measurements were also assessed concerning simplicity of handling and time needed for the measurement. The measuring of positional precision, shape accuracy and dimension accuracy with the FRT and the Zeiss O- Inspect showed no significant problems. Significant differences were found concerning the time needed for measurement and handling. Due to the Alicona Infinite Focus measurement method it needed a lot of time. Because the test component is designed as a rapid test the Alicona was no longer considered in this paper.
Additive manufactured parts consist of three different structures the area where the part was connected with the building platform, which was EDM-machined and the top of the part that shows the pattern of the scanning strategy. At the sides of the part different layers are visible. Figure 3 illustrates the different sides.

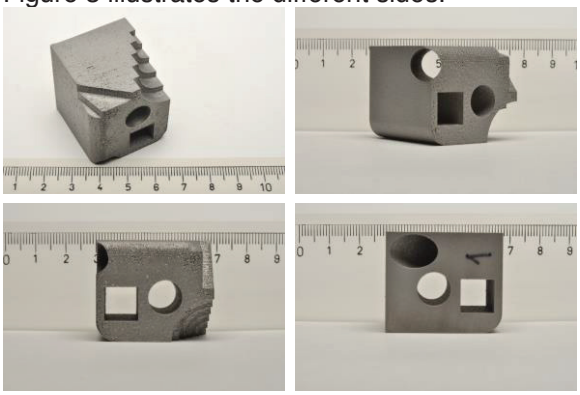

FIGURE 3. Different views of the developed test component to measure process quality for Additive Manufacturing.

The area that was connected to the building platform is not influenced by the AM process. So only the sides and top of the part are measured. On the area that was connected to the building platform only location and shape accuracy were examined, because the glass bead blasting affects the surface quality.

RESULTS

Test Structure

The test component was built error free with all features integrated, even though no support structures were used. The component only occupies a small amount of space so that other parts can be built simultaneously. This guarantees the use as a rapid test for process quality. The developed test component includes basic geometric features of work pieces. It gives a fast feedback concerning the possible surface and geometric quality. In addition, an alternate implementation of the test structure can be used for continuous documentation of the process quality for AM processes, systems and materials in general.

Measuring systems analysis

This paper investigates which measuring system is the most useful, regarding the examination of the selected measurement criteria.
Figure 4 shows the different measuring sections regarding positional accuracy. The first measuring section covered the distance between the edge of the cube and the apex of the round drilling. The nominal value is 8 mm. The second measuring section covered the distance between the edge of the angular drilling and the edge of the cube. The nominal value for this section is 6 mm. The Zeiss O Inspect is slightly overpredicting the positional accuracy with average values of 8.106 mm and 6.032 mm. These measuring results are slightly above the FRT average measuring values of 7.99 mm and 6.014 mm, shown in figure 5.

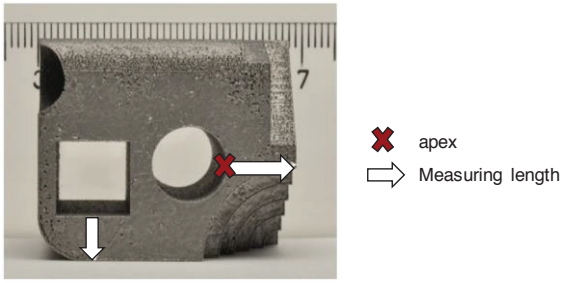

FIGURE 4. Measuring sections for positional accuracy.

Measuring system:
optical (FRT Microprof MPR100)
tactile (Zeiss O-Inspect)
Distance drilling apex to cube edge:
Nominal value = 8 mm
FRT = 7.999 mm
Zeiss = 8.106 mm
Distance canal edge to cube edge:
Nominal value = 6 mm
FRT = 6.014 mm
Zeiss = 6.032 mm
Material:
Steel 1.2709

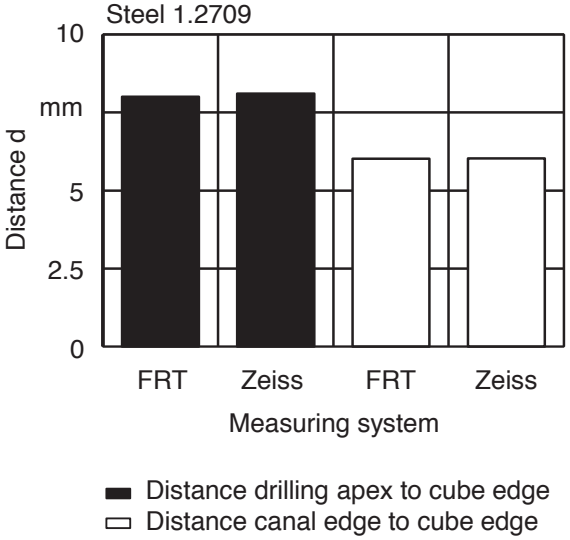

FIGURE 5. Results for positional accuracy.

Figure 6 illustrates the investigated geometrical shapes regarding diameter shape accuracy. First the angular drilling diameter and second the radius at the edge of the cube. The nominal value for the angular drilling diameter is 10 mm. The nominal value for the radius at the edge of the cube is 7.5 mm. Both measuring systems deliver acceptable results regarding the shape accuracy. The FRT measured an average diameter of 10.26 mm and an average radius of 7.55 mm. The Zeiss O- Inspect delivered an average diameter of 10.11 mm and an average radius of 7.49 mm, shown in Figure 7.

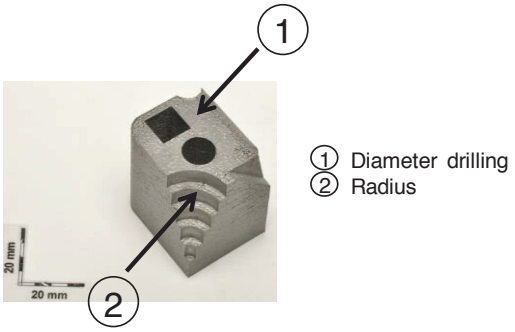

FIGURE 6. Measuring sections regarding diameter shape accuracy.

Measuring system:
optical (FRT Microprof MPR100)
tactile (Zeiss O-Inspect)
Drilling diameter:
Nominal value = 10 mm
FRT = 10.26 mm
Zeiss = 10.26 mm
Radius:
Nominal value = 7.5 mm
FRT = 7.550 mm
Zeiss = 7.499 mm
Material:
Steel 1.2709

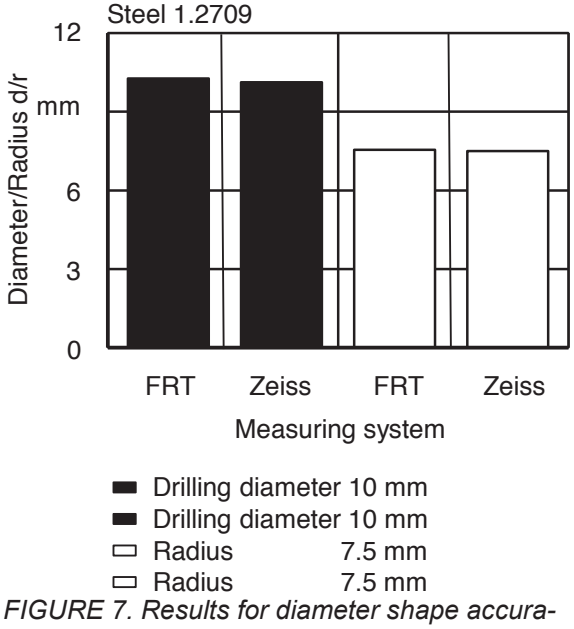

FIGURE 7. Results for diameter shape accuracy.

Figure 8 illustrates the two different angles at the side of the test component. The flatter, marked with 1, has a nominal value of 50°. The angle marked with 2 has a nominal value of 75°. Again both measuring systems proved to be suitable, with the FRT delivering average values of 50.32°

and 74.88° and the Zeiss O-Inspect 50.30° and 74.67°, illustrated in figure 9.

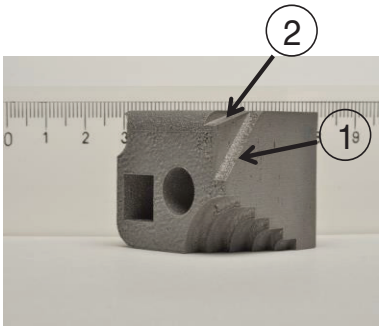

FIGURE 8. Measured angles.

Measuring system:
optical (FRT Microprof MPR100)
tactile (Zeiss O-Inspect)
Angle incline 1:
Nominal value = 50°
FRT = 50.32°
Zeiss = 50.30°
Angle incline 2:
Nominal value = 75°
FRT = 74.88°
Zeiss = 74.67°
Material:
Steel 1.2709

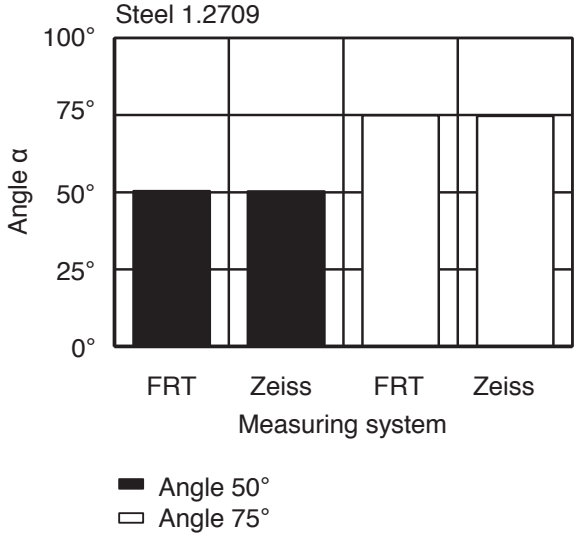

FIGURE 9. Results for angular shape accuracy.

Method
The test component has proven to be an easy to handle, resource saving and inexpensive rapid test.
The measuring system analysis showed that none of the examined measuring systems is suitable to validate the entire measurement criteria. However, the tactile measurement system Zeiss O-Inspect proved to be the most useful system regarding shape characteristics, positional precision and dimension accuracy. It was also the best system regarding handling. Concerning the required time it was 33 % better than the next best measuring system. Finally a classification of Additive Manufacturing in the ISO-Tolerance system is proposed according to standards [13]. Qualities between IT 12 and 16 were achieved (Figure 10).

PROSPECT

The necessity of monitoring the built process is a challenge which concerns all industries that are considering the application of AM. Therefore, different variances and improvements of the test component could be built with attention to specialized applications like horizontal holes or integration of support structures. The variety of measuring systems offers the possibility to extend the measuring system analysis.

ACKNOWLEDGEMENTS

This paper is based on results acquired in the project DFG UH 100/174-1, which is kindly supported by the German Research Foundation (DFG)

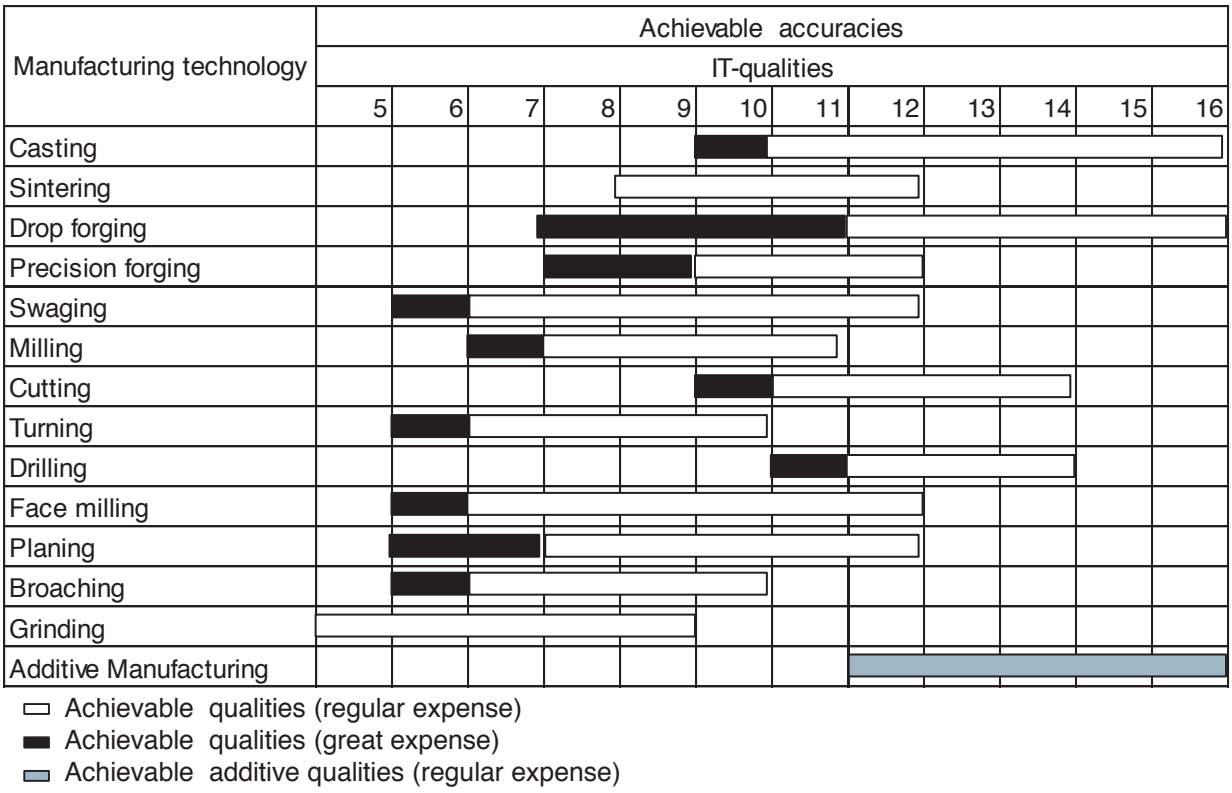

FIGURE 10. Proposed classification of AM according to ISO 286-1 [13], [14]

REFERENCES

[1] Uhlmann, E.; Bergmann, A.; John, F.: Generative Herstellung von Implantaten. Neue Konzepte für Werkzeugmaschinen. Fraunhofer Gesellschaft. 6. Berliner Runde, 2011.

[2] Gebhardt, A.: Generative Fertigungsverfahren. Hanser, 2007.

[3] Wohlers Associates, Inc. (Hrsg.): Rapid Prototyping, Tooling & Manufacturing - State of the Industry. Annual Worldwide Progress Report, 2003.

[4] Wegner, A.; Witt, G.: Konstruktionsregeln für das Laser-Sintern. Konstruktionstechnik, 2012.

[5] Wartzack, S.; Drummer, D.; Wittmann, S.; Stuppy, J., et al.: Besonderheiten bei der Auslegung und Gestaltung lasergesinterter Bauteile, RTejournal, Bd. 7 ,2010.

[6] Breuninger, J.; Becker, R.; Wolf, A.; Rommel, S.; Verl, A.: Generative Fertigung mit Kunststoffen. Springer, 2013.

[7] Seepersad, C., Govett, T., Kim, K., Lundin, M., Pinero, D.: A Designer's guide for dimensioning and tolerancing SLS parts. University of Texas at Austin, 2012.

[8] Hoeren, K.; Witt, G.: Konstruktive Möglichkeiten und verfahrensspezifische Grenzen in der additiven Fertigung. Konferenz und Tagungsband der 3D-Nord-Ost, 2012.

[9] Trenk, D.: Konstruktionsregeln für eine Rapid Tooling gerechte Gestaltung von Werkzeugen und Prototypen. IMW-TU-Clausthal Institutsmitteilung no. 25, 2000.

[10] Witt, G., Weckend, F., Köhler, P.: Wissenbassiertes Unterstützungssystem für Rapid Prototyping gerechte 3D-CAD-CAM-Prozesse. Abschlussbericht, 2009.

[11] Uhlmann, E.; Bergmann, A.; John, P.; Kashevko, V.: Verification of Design Rules for Additive Manufacturing. Proceedings ASPE 2014 Spring Topical Meeting, Hrsg.: American Society for Precision Engineering, 2014 pp 19- 23.

[12] DIN ISO 2768, Allgemeintoleranzen, Toleranzen für Form und Lage, 1991.

[13] DIN ISO 286-1, Grundlagen für Toleranzen Abmaße und Passungen, 2010.

[14] Paucksch, E., Holsten, S., Linß, M., Tikal, F.: Zerspantechnik. Vieweg, 2008.

TESTING WORKPIECES FOR SELECTIVE LASER SINTERING

Bogdan Galovskyi, Tino Hausotte
Institute of Manufacturing Metrology
Friedrich-Alexander-Universität Erlangen-Nürnberg (FAU),
Erlangen, Bavaria, Germany

INTRODUCTION

Improvement of manufacturing processes is often connected with the integration of the measurement technology and process control. The additive manufacturing (AM) became wider usable during recent decades. Nowadays this technology is also applicable in mechanical engineering, medicine, etc [1]. Selective laser sintering (SLS) technology has a great potential due to the fast and easy adjustable manufacturing of individual parts of different sizes and hidden structures. Nevertheless there are some limitations for wide usage of the SLS in industry. These are for instance: weak relation to the legal metrology and traceability to national standards [2, 3].

Manufacturing metrology provides control of conformity with specification for manufactured workpieces. Quality control, test methods for raw materials and process control are research directions in the field of standardization for AM [2, 3]. Methods for quality control of SLS were listed and divided into the following directions according to [4]: testing of the raw powder material, process control, testing of the part quality. Mechanical properties, dimensional accuracy as well as form, edges and surface quality are properties of the end product which should be confirmed in accordance with geometrical product specification. The quality of the process is of high importance for users and manufacturers of SLS machines. There are two basic approaches for evaluation of process parameters [1]:

- producing with the help of SLS machine some testing part with numerous structural elements (testing part, testing artifact);
- in-line monitoring of selected influencing parameters of the process (temperature deviation inside the process chamber, power of the scanning laser, scanning speed, etc.) [1].

Both methods have numerous disadvantages: the approach with the testing workpiece is subjective and represents process parameters indirectly; the monitoring of process parameters is too complex and cumbersome, because it requires implementation of several measurement systems. This method also requires complex analysis of the measured data. It is necessary to determine the aim of the process testing before choosing appropriate approach. Measurement and control of numerous parameters of the SLS process could improve geometric, as well as many other, parameters of the produced parts. The list of process parameters is given in one of the guidelines [4]. Such approach requires development and integration of different measurement systems. Main disadvantages of this approach are high cost and low flexibility (not all measurement equipment could be adopted for the using in different AM machines).

The approach based on testing workpiece is more appropriate for users of SLS machine. This approach meets lower expenses for development. All error sources of the SLS process make influence on the manufactured workpiece, which should be analyzed. After producing of the testing workpiece, repeatability of the SLS process, the so called manufacturing resolution and errors of the manufacturing can be studied [5, 6].

Both of the mentioned approaches are mentioned in [5] and the priority is given to the first one. During our work we have faced with the fact that industrial users of the SLS machines prefer to have simple and quick method to get information about the quality of the manufactured workpieces. Many researchers propose to use testing workpieces in order to evaluate manufacturing capabilities of AM [5-14]. Design of the mentioned in [5-14] testing workpieces has weak sides, like limited set of features for providing of geometrical form conformity.

The aim of our work is to compare and analyze the implementation big [16] and small testing workpieces in order to improve the post-process geometry testing.

DESIGN

The initial motivation of our work was to investigate some simple parts, which would

allow to determine manufacturing possibilities of the SLS machine (machine: DTM Sinterstation 2000; raw material: PA12 - Type: PA 2200, EOS GmbH). Three simple parts were designed, manufactured and measured in order to investigate: lateral and vertical manufacturing resolution (ability of the machine to reproduce detectable lateral and vertical elements), deviations inside produced parts (Fig. 1) [15].

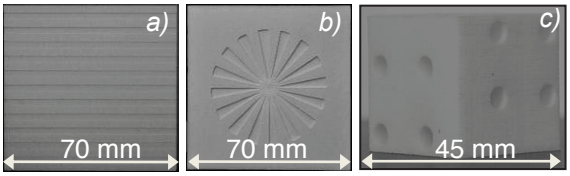

FIGURE 1. Example of testing parts [15].

There are step height testing parts (Fig. 1a) that were developed in accordance with ISO 5436-1:2000. The Siemens-Star testing workpieces (Fig. 1b) were designed to investigate the lateral resolution of SLS process. Few samples were oriented in different way inside the build space during the manufacturing. The reliable measurement results were evaluated [15]. The initial tests brought the information about the smallest reproducible by machine elements of the part. CT measurements allowed evaluating the form deviation inside the part (Fig.1c – part for CT measurements). After analysis of all parts it was concluded that using of such testing workpieces do not bring objective information, because: shape of the workpieces is affected by different temperature deviations inside the build space; location of the workpiece play important role; curving of the workpiece depends on its design [4, 5].

For reducing of all mentioned influences it was decided to develop new workpiece. The new design was developed taking into account the experience and recommendations set out in other studies [5-14].

It should be mentioned, that all manufacturing and design rules, as well as all our investigations were developed and conducted with using of mentioned SLS machine and raw material. Design and manufacturing rules were formulated [5] and improved:

- possibility to build a test area without support structures and post-process treatment;
- manufacturing of the artifact should require low amount of raw material;
- design of the artifact and positioning in the build space should prevent the influence of common distortions during the manufacturing process;
- structural elements should be measurable;
- structural elements should allow repeatability measurements;
- structural elements should have a form of “real” machine parts.

Guided by these rules the new designs were developed.

TESTING ARTIFACT

The first testing part with the multiple structural elements was designed and manufactured. The general approach is based on the analysis of other investigations [5]. All features of the artifact were designed taking into necessity to be measured with the surface measurement devices.

It should be noted that the testing artefact was manufactured in different scales and few times [16]. In this paper only the successful manufactured part is described.

Design of the testing artifact

The developed testing artifact is a rectangular hollow body with the active surface and many structural elements on it. Detailed description of all structural elements, design and process of its improvements is described in [16]. General view is presented in Fig. 2.

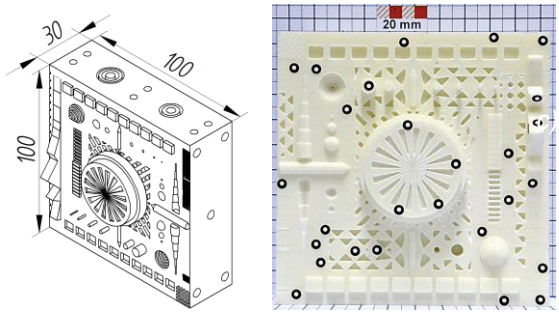

FIGURE 2. Testing artifact.

The active surface contains inclined and diagonal surfaces, pins and holes of different diameters, Siemens star and step height elements. It is covered with the cavities in order to reduce the melted area during the manufacturing process. Structural elements allow to:

- check the repeatability of the manufacturing process;

- determine the possibility to produce standard geometrical elements (point structure, spheres, cylinders, cones, etc.);
- confirm tolerances of form, orientation and location (established by users of the SLS machine).

The central element is the Siemens star, which is located on the central cylinder. Axes of this cylinder should be coincident with the Z-axis of the build space. The active surface should be parallel to the XY-plane of the build space. X and Y axes of the testing artifact should be 45° angled in respect to the correspondent axes of the build space. This requirement is caused by necessity to reduce the contact line between the sintered layers and the recoating element of the SLS machine. During the manufacturing the testing artifact should be located in the middle of the powder bed.

Analysis of the Testing Artifact

Two systems were used in order to measure the surface of the measurement artifact: ATOS Compact Scan – photogrammetric measurement system; Alicona Infinite Focus G4 – focus deviation measurement system. The artifact was cleaned with compressed air before measurements. For evaluation of measurement data were used software packages: PolyWorks, TalyMap Platinum and GOM Inspect. The general view of the inspected measurement data is presented (Fig. 3).

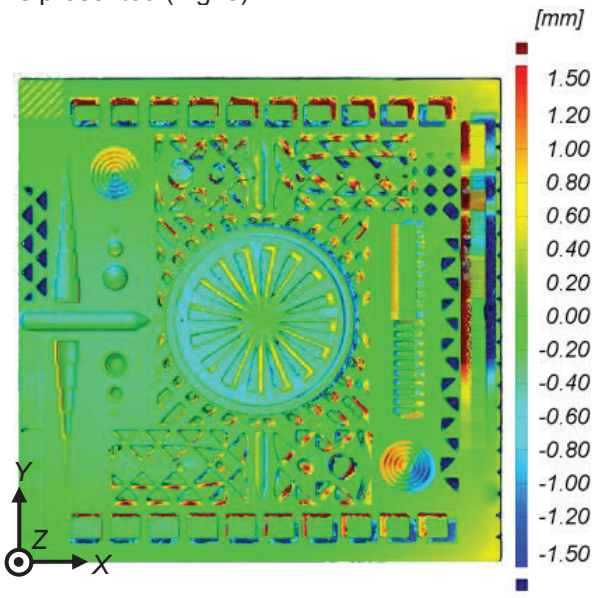

FIGURE 3. Testing artifact – measurement results.

The first thing is common for all manufactured samples: testing artifact was manufactured 4 times. They have the shrinkage of the body. This effect is usual for sintered polyamide parts, but in our case it's aggravated by the selected shape of the testing artifact – relatively big solid part. This effect is visible on the Fig.3. Nominal dimension of the artifact body in XY-plane (Fig.3) is 100 mm x 100 mm. The deviation between the nominal value and actual is up to 3.1 mm. Active surface of the artifact (lays in the XY-plane) has the deviation of the flatness up to 0.9 mm.

High shrinkage of the manufacture testing artifact makes impossible inspection, which is based on alignment of the nominal CAD model with the actual model (point clouds data of the measured workpiece). Nevertheless, the quality of the structural elements allows us to provide inspection of them. Analysis of the step height elements in previous investigations [15] has shown very high deviation between nominal and actual values of the steps. It is also caused by the shrinkage of the part. There are 40 step height elements: 10 negative and 10 positive with the nominal height from 50 µm to 500 µm (in increments of 50 µm); 10 negative and 10 positive with the nominal height from 10 µm to 100 µm (in increments of 10 µm). The difference between all this steps is traceable and corresponds to an increase or decrease of the nominal values. Nominal diameter of the smallest hole and pin is 0.5 mm. The pin was reproduced successfully. The hole is not detectable [15]. It is caused by merge of two sintering lines (point) located very close near to each other (sintered circle for each layer is only 0.5 mm). This effect has distorted the central area of the Siemens star. Which shows that so called lateral manufacturing resolution is around 1 mm (diameter of the manufacturing laser beam spot is around 0.6 mm).

Summarizing evaluation of the proposed testing artifact it should be mentioned its suitability, despite its shortcomings - excluding influence of the shrinkage on the measurement results evaluation.

SMALL TESTING WORKPIECES

After experience with the testing artifact it was decided to change strategy. Industrial users of the AM technologies need more simple method for the post-process testing – with lower expenses and time loss on manufacturing and testing of the workpieces.

The requirements for new approach are based on the main disadvantages of the mentioned above method. The temperature deviation on the powder bed as well as inside the build space is a serious influence on the quality of the manufactured parts. This effect brings much influence during the cooling of the build space. Intensity of the temperature decreasing is higher near the surface of the powder bed and on the borders of the build space [17]. There is a need to locate part in different areas of the build space. Using of big testing workpieces, like presented testing artifact, increases the expenses of the testing process.
It was decided to use a number of small parts.

Radar reflector testing workpiece

Design of the small workpiece is based on the geometry of the radar reflector. It is symmetric part which consists of three diagonal crossed square plates (each 40 mm x 40 mm x 3 mm). Such geometry creates 12 pairs of active planes (Fig. 4 E – one of the active planes).

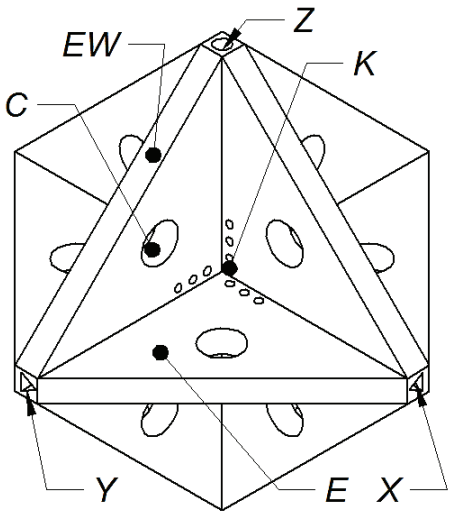

FIGURE 4. Radar reflector testing workpiece.

The radar reflector testing workpiece (RRTW) has the coordinate system (Fig. 4 X,Y,Z) and these axes should be aligned with the axes of the build chamber. All axes are labeled and this labeling elements are: two triangles and one circle indicate the positive direction of all axes. In order to prevent mix up of some amount printed parts design contains numbering [18] (Fig.4 K). This numbering allows locating in the build chamber the workpiece and identifying it after manufacturing. Presented numbering system allows identification of 27 workpieces in the build space and this number could be increased. In the middle of 12 walls located 12 holes with the nominal diameter of 5 mm. All mentioned elements allow providing inspection of: flatness, straightness, position, perpendicularity, parallelism, symmetry, roundness, cylindricity and repeatability of the elements. End planes (Fig. 4 EW) are also active surfaces. They allow evaluating of the stair stepping effect and inspection of angularity.
Presented RRTW was manufactured with the same machine like the testing artifact. The workpiece was located in the middle of the powder bed and in the top part of the build space.

Analysis of the RRTW

Measurements of the RRTW were conducted with the help of ATOS Compact Scan. The result of alignment and measured surface comparison with the CAD model of one artifact is presented on Fig. 5.

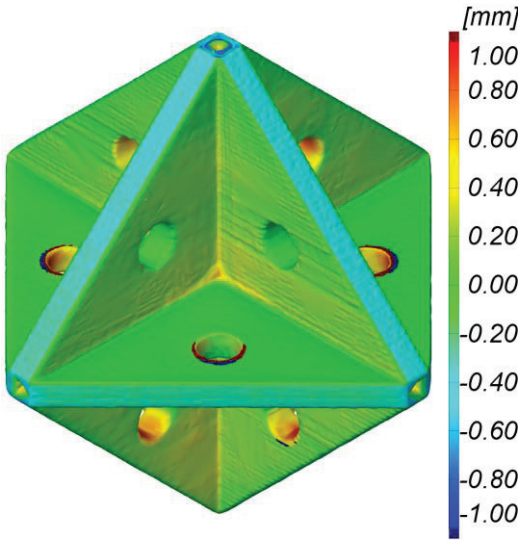

FIGURE 5. Inspection of the RRTW.

The first positive effect of the selected geometry is lower shrinkage. The deviation of the RRTW dimensions is 0.8 mm. Thickness of the walls has deviation 0.5 mm for vertical planes and 0.1 mm for horizontal planes. The maximal flatness deviation (0.2 mm) is detected on vertical planes (walls). Maximal cylindricity deviation is 0.4 mm. The most affected cylinders are located in the horizontal plane. This influence might be caused by recoating roller. Especially distortion is high on the edges of the

cylinders (Fig. 5). Angularity deviation: between end planes (Fig. 4 EW) is 0.4˚; between end planes and other planes (Fig. 4 E) is 0.1˚ (in accordance with: DIN EN ISO 14406-2:2012). Deviation of the perpendicularity between vertical and horizontal planes is up to 0.4˚ (in accordance with: DIN EN ISO 14406-2:2012). Parallelism of vertical and horizontal plane is nearly the same and it is 0.3 mm.
Measurement results show us that the shape of the RRTW is not affected so much as it was in case with the testing artifact. Nevertheless form deviation is different for horizontal and vertical elements (planes and cylinders).
The set of RRTW was manufactured in order to confirm the propriety of using multiple workpieces. For this manufacturing was used more modern SLS machine –FORMIGA P 110 (EOS GmbH). Multiple workpieces were manufactured in the center of the build space and near its edges [18]. Fig. 6 shows the set of inspected RRTW (top and bottom views are shown). The middle workpiece was manufactured in the center of the build space and other workpiece near the edges of it [18].

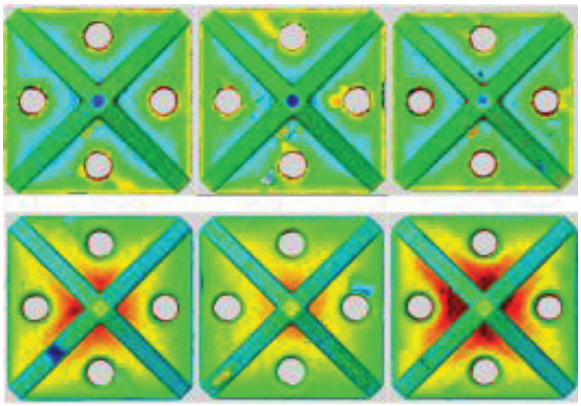

FIGURE 6. Set of the inspected RRTW.

This inspection brings us similar results [16]. The horizontal planes are the most affected, as well as cylinders in these planes. At the same time here clearly visible the advantage of multiple testing workpieces: parts which were manufacture near the edges of the build space have more affected middle part of the horizontal plane (red areas on Fig. 6). Measurement result of the manufactured RRTW confirms the consistency of the developed design. Using of large amount of testing workpieces will bring to uses of the SLS machine more information about the part form deviation in different areas of the process chamber.

CONCLUSIONS

In this work were considered two approaches for implementation of different testing workpieces in SLS post-process measurements of geometry. During our research two different designs were developed. Both types of workpieces are measurable.
Design of the large testing artifact should be improved. The hollow body of this artifact and fixing elements inside didn't bring the expected results – reducing of the active plane deviation [16]. Shrinkage of the body is too high. With the reducing of these distortions, better quality of the structural elements could be achieved. Nevertheless this approach can't be excluded, because even with the described distortions, structural elements are still measurable and bring information about the quality of the SLS process.
The second approach with the radar reflector testing workpieces is more reliable. Developed design allows providing investigations of parts quality in all volume of the build space. The small size of the workpiece reduces the manufacturing time and financial expenses for the post-process testing. Geometry of the RRTW could be measured with tactile measurement devices, different optical measurement devices and also with the CT. It brings the post-process testing to more high level and at the same time gives a possibility to provide procedure with the simple measurement equipment.
Overview of different research and development of own approaches bring us next conclusions: large testing workpieces with the solid body or common platform for structural elements are more affected. The big advantage of such testing workpieces is the possibility to build any kind of structural elements of models of real parts; set of small testing workpieces gives more objective information about the form deviation of the parts and about the repeatability of the process.
The disadvantage of simple and small parts is that it is impossible to reproduce complicated geometrical shapes. From the side of manufacturing metrology, the approach with the RRTW brings more objective and useful information.
Considering both proposed approaches we assume that the final solution should be done by the users of the AM.

ACKNOWLEDGMENT
The authors want to thank the German Research Foundation (DFG) for funding the Collaborative Research Center 814 (CRC 814), subproject C04. Additionally we would like to express our thanks to Prof. D. Drummer and Mr. R. Harder (CRC814, subproject B03) for producing of the testing workpieces.

REFERENCES

[1] Breuninger, J., Becker, R., Wolf, A., Rommel, S., Verl, A. Generative Fertigung mit Kunststoffen – Konzeption und Konstruktion für Selektives Lasersintern. ISBN 978-3-642-24324-0. Springer-Verlag Berlin Heidelberg: 2013.

[2] VDI 3404:2009-12 'Additive fabrication - Rapid technologies (rapid prototyping) - Fundamentals, terms and definitions, quality parameters, supply agreements'.

[3] Buining, H. Manufacturing trends. Standardisation for additive manufacturing. Presentation at the IMS Workshop, Barcelona: 2012.

[4] VDI 3405 Part 1:2013-10, 'Additive manufacturing processes, rapid manufacturing - Laser sintering of polymer parts - Quality control'.

[5] Moylan, S., Slotwinski, J., Cooke, A., Jurrens, K., Donmez M. Proposal for a standardized test artifact for additive manufacturing machines and processes. Proceedings of the Solid Freeform Fabrication Symposium. Austin, TX.: 2012; 902-920.

[6] Scaravetti, D., Dubois, P., Duchamp, R. Qualification of rapid prototyping tools: proposition of a procedure and a test part. The International Journal of Advanced Manufacturing Technology. 2008; 38 (7): 683-690.

[7] Moylan, S., Slotwinski, J., Cooke, A., Jurrens, K., Donmez M. Lessons Learned in Establishing the NIST Metal Additive Manufacturing Laboratory. NIST TN - 1801. 2012.

[8] Wegner, A., Witt, G. Ursachen für eine mangelnde Reproduzierbarkeit beim Laser-Sintern von Kunststoffbauteilen (Reasons of low reproducibility for laser sintered workpieces). RTejournal - Forum für Rapid Technologie. 2013.

[9] Campanelli, S.L., Contuzzi, N., Angelastro, A., Ludovico, A.D. Capabilities and Performances of the Selective Laser Melting Process. New Trends in Technologies: Devices, Computer, Communication and Industrial Systems. 2010; 233-252.

[10] Hoeren, K. P. J., Witt, G. Design-Opportunities and Limitations on Additive Manufacturing Determined by a Suitable Test-Specimen. IFIP - International Federation for Information Processing. 2013; 138–152.

[11] Vaezi, M., Seitz, H., and Yang, S. A review on 3D micro-additive manufacturing technologies. International Journal of Advanced Manufacturing Technology. 2013; 67: 1721–1754.

[12] Gregorian, A., Elliott, B., Navarro, R., and other. Accuracy Improvement In Rapid Prototyping Machine (FDM-1650). SFF Proceedings. 2001; 77–84.

[13] Raghunath, N., Pandey, P. M. Improving accuracy through shrinkage modelling by using Taguchi method in selective laser sintering. International Journal of Machine Tools and Manufacture. 2007; 47: 985-995.

[14] Kruth, J., Vandenbroucke, B., Vaerenbergh, J., Mercelis, P. Benchmarking of different SLS/SLM processes as rapid manufacturing techniques. Int. Conf. Polymers & Moulds Innovations (PMI). 2005.

[15] Galovskyi, B., Fleßner, M., Loderer, A., Hausotte, T. 'Systematic form deviations of additive manufactured parts - methods of their identification and correction. Proceedings of the 11th International Symposium on Measurement and Quality Control. Krakau - Kielce, Poland: 2013.

[16] Galovskyi, B., Hausotte, T., Drummer, D., Zhao, M. Model of a Measurement Artifact for Additive Manufacturing. Proceedings of the 5th International Conference on Additive Technologies. Wien, Austria: 2014; 90-95.

[17] Wegner, A., Witt, G. Ursachen für eine mangelnde Reproduzierbarkeit beim Laser-Sintern von Kunststoffbauteilen (Reasons for the lack of reproducibility in laser sintering of plastic parts). Proceedings of the Rapid.Tech 2013. Erfurt, Germany: 2013.

[18] Junginger, J. Measuring artefacts for additive manufacturing. Bachelor thesis Nr.: BA206-14. Erlangen, Germany: 2015.

PREDICTING COLOR OUTPUT OF ADDITIVE MANUFACTURED PARTS

Eythor R. Eiriksson[1], David B. Pedersen[2] and Henrik Aanaes[1]
[1]Department of Applied Mathematics and Computer Science
[2]Department of Mechanical Engineering
Technical University of Denmark
Kgs. Lyngby, Denmark

ABSTRACT

In this paper we address the colorimetric performance of a multicolor additive manufacturing process. A method on how to measure and characterize color performance of said process is presented. Furthermore, a method on predicting the color output is demonstrated, allowing for previsualization of parts prior to print. Results show that color prediction can be achieved with an average color difference error of $\overline{\Delta E^*_{00}} = 1.5$ and std.dev $\sigma = 0.75$, with similar order of magnitude as the literature defined threshold for „Just Noticeable Difference" (JND).

INTRODUCTION

Additive manufacturing has been an accepted means of production for the past decade and is a rapidly growing market. Today, additive manufacturing technologies are offering multi-color printed parts in an assortment of different materials[1]. Availability of print per order parts, where customers can supply their own high resolution color textures and geometries, has become a reality[1234]. Therefore, geometry and color quality assurance is required. So far, research focus has been placed on geometrical verification, giving promising results, whereas less effort has been placed on color verification[2][3]. Here we address the colorimetric performance aspect.

When converting 3D color models to the physical domain, through additive manufacturing, the enormous range of color available during modeling is not reproducible by the printer. The complete range of producible colors is known as the printers *gamut*. Any input colors outside the printable gamut will simply be constrained to a gamut boundary color, as illustrated in Figure 2. This is a known problem in the paper printing industry and is normally solved through printer profiling. Printer manufacturers sometimes offer these printer profiles which describe the printers color production capabilities according to a standard defined by the International Color Consortium (ICC).

In order to fully profile a printers color gamut, one would ideally define the input 3D model in terms of the printers native color space (*CMYK*). Unfortunately this is not possible, as color 3D mesh representations are derived from the *RGB* space. This is to be expected, as these data formats are mostly intended for use in *RGB* based devices such as a computer monitor. It is clear that the growing market of color 3D printing calls for a new or updated mesh format. To the authors best knowledge, no color 3D printing manufacturer offers color profiles or color management features. That being said and due to most printers proprietary nature, any color correction needs to be made at the 3D modeling level.

MATERIALS AND METHOD

In order to characterize the gamut of a ZCorp ZPrinter 650, a patched color plate was printed as seen in Figure 1.

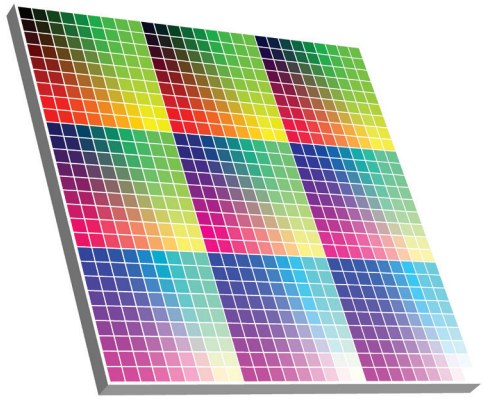

FIGURE 1. 3D model of the color calibration plate, providing 729 unique color patches.

[1]shapeways.com
[2]twinkind.com
[3]i.materialize.com
[4]figureprints.com

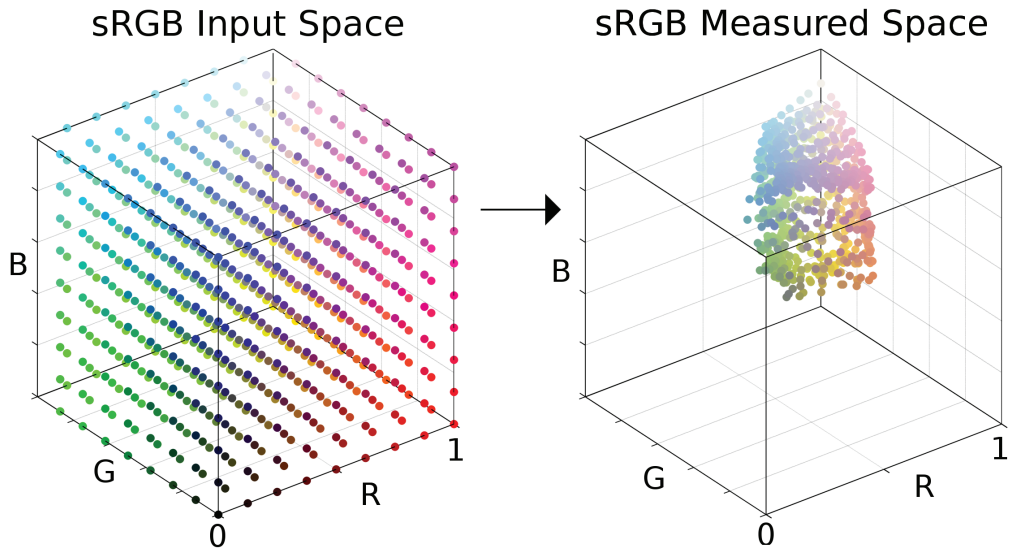

FIGURE 2. Comparison of input sRGB values to the actual measured values after print. The printers color generation limitations are apparent. Any colors outside of this printer gamut are not printable.

3D Model Generation

The color plate was generated in the Wavefront `.OBJ` format where each square in the plate was defined with a unique face color. This method was selected over applying a color image texture onto a blank plate. Thus, eliminating all uncertainties of texture handling and mapping in the printer software. The 729 unique color patches were sampled evenly from the entire three dimensional *sRGB* space, as visualized by Figure 2. This $9 \times 9 \times 9$ sample was selected due to physical size constraints set by the color measurement system used. The final plate dimensions are therefore $64.25 \times 64.25 \times 3$ mm with individual patch size of 2.15×2.15 mm.

Print Procedure

In order to capture the variability between prints, a set of 15 plates were printed in a stacked configuration, centered in the build volume. Layer thickness was set to 89 µm, bleed compensation enabled and the ZP150A powder was used. Special care was taken in thoroughly removing residual powder as to minimize color variations between prints whose effect can be seen in Figure 3. As it is known, infiltrating substances have significant effect on color vibrancy, and therefore the prints were not infiltrated in order to minimize additional variability. Modeling of this effect, dependent on infiltration type is a subject for future work.

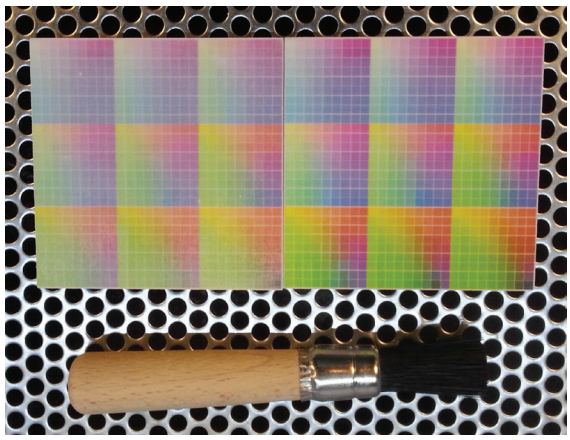

FIGURE 3. Two color plates, before brushing (left) and after brushing (right).

Measurement

Each color patch was measured using the multispectral imaging system *VideometerLab2*.[5] The VideometerLab2 allows for rapid color capture of an entire plate, contrary to other point sample based color measurement devices such as a colorimeter. Measurements were made in the device independent *CIELAB* color space under the D50 illuminant. Example output from the instrument can be seen in Figure 4. An automated color patch extraction algorithm was implemented

[5] www.videometer.com

and for each colored patch an average color value was computed, ideally simulating the perceptual integration as some color values are printed in dithered like patterns.

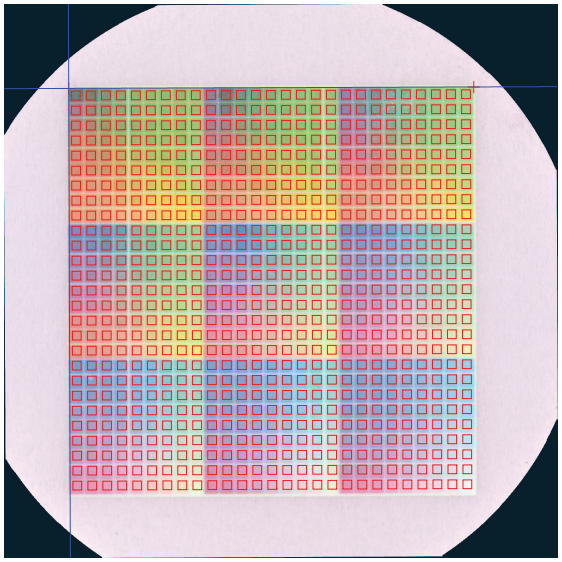

FIGURE 4. Automated patch extraction algorithm collects patches and computes their average color value.

RESULTS

An average plate was computed from all of the 15 measured plates. The color difference metric ΔE^*_{00} from the average color was computed for each color in the *CIELAB* space[4]. The color difference distribution from the mean for each plate is shown in Figure 5.

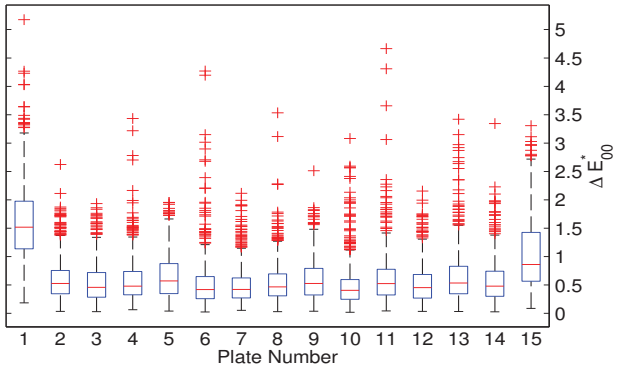

FIGURE 5. Boxplots illustrating color difference ΔE^*_{00} from the group mean. Median value is shown as a line in each box; Box edges are the 25th and 75th percentiles; Whiskers extend to the most extreme data points not considered outliers; Outliers are plotted individually.

It is apparent from the figure that the first and last plates in the stack differ significantly and are therefore omitted from the model. Further study is needed in order to evaluate whether this is a reoccurring trend. Figure 2 shows the transformation from the input *sRGB* values and the measured values. It is clear that the printer is not capable of printing a large majority of the input colors. Figure 6 clearly shows the printers inability to produce darker colors and the average color error is $\overline{\Delta E^*_{00}} = 21.4$, std.dev $\sigma = 4.15$. Several studies have tried to estimate the Just Noticeable color Difference threshold (JND) of the ΔE^*_{00} metric, however many are in disagreement. Documented JND threshold values range from 1 to 5.9[5]. The average systematic error was estimated by repeatedly measuring the same plate several times and an identical analysis performed. The measured systematic error difference was $\overline{\Delta E^*_{00}} = 0.11$ and std.dev $\sigma = 0.07$, orders of magnitude lower than the variations between prints.

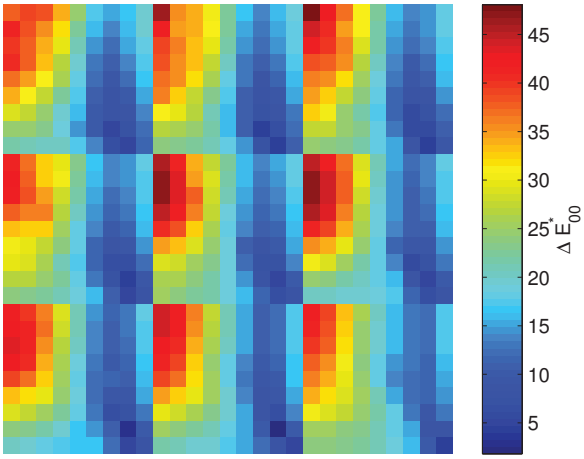

FIGURE 6. Color difference between the ideal plate and an average of the measured plates.

From the average color plate measurements, a 3D Look-Up Table (3D LUT) was constructed relating the input *sRGB* space to the measured *CIELAB* space. The input LUT is essentially a 3D lattice structure where each lattice corner contains *CIELAB* measurement data. From there, any intermediate points within a single lattice cube can be estimated using trilinear interpolation. This 3D LUT model can thus be used to predict resulting color measurements of a printed object given an input color. 3D LUTs are commonly used for this color conversion purpose and can be efficiently implemented on modern hardware.

MODEL EVALUATION

A week after the initial prints were made, a color plate as seen in Figure 7 was generated with random color values. A print prediction was performed using the 3D LUT model and the plate was printed using identical procedures as before. Post print, the plate was measured and compared to the predicted output. The color difference from the prediction obtained from the 3D LUT model and the measured plate is illustrated in Figure 8. The computed error mean was $\overline{\Delta E^*_{00}} = 1.5$ with std.dev $\sigma = 0.75$.

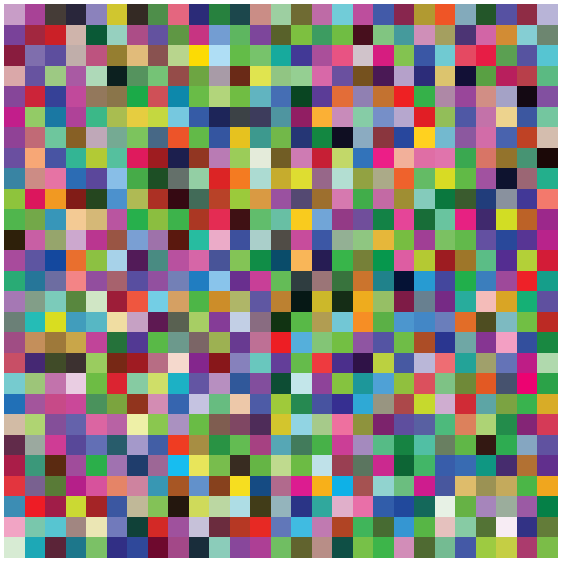

FIGURE 7. Plate with randomly generated colors, used for model verification.

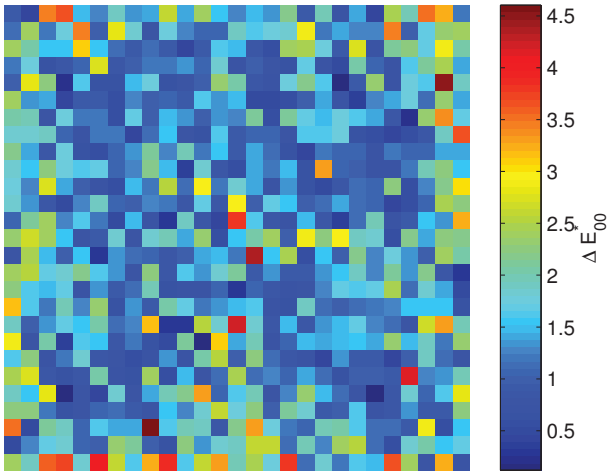

FIGURE 8. Color difference between prediction and actual measurements of the random plate.

DISCUSSION AND SUMMARY

The method described in this paper has been applied on an inkjet based 3D printer. Its variability and color limitations were visualized. When looking at the group statistics of the plates we observe the bottom and top plates to be statistically different from the rest. For the plate located in the bottom, we have two hypotheses. Firstly, the powder in the build chamber might not be compact enough in the bottom prior to print, thus yielding different surface textures. Secondly, the print head might not have reached a steady state of operation so early in the print. For the top plate, we believe it might be a factor of powder compression and drying as only a few extra layers of powder are deposited over the last plate. The remaining plates were measured using a multi-spectral imaging system with determined average systematic color measurement error of $\overline{\Delta E^*_{00}} = 0.11$ and std.dev $\sigma = 0.07$. Upon comparing the input data to an average of the measured data it was apparent that a large part of the input colors was not printed to specification. In fact, the average color error was $\overline{\Delta E^*_{00}} = 21.4$, std.dev $\sigma = 4.15$ and maximum color error greater than 45. Significantly exceeding the literature defined noticeable color difference threshold which ranges from 1-5.9. The largest error contribution was from the darker colors, particularly in the absence of red and green. These error regions are expected to somewhat heal by infiltration, where darker regions are known to benefit greatly. However, this might come at the price of the more lighter colors, as white will appear more grayish. A 3D Look-Up Table was constructed relating the input color values to the empirically measured color values. This allowed for a simple and efficient way to perform a color prediction given an input color value. If an input color value was not present in the table, trilinear interpolation was performed from the known values, yielding a color estimate. To evaluate the prediction model, a new color plate was generated consisting of randomly generated color patches. It was printed on the same printer and finally compared to the generated prediction model. The model captured the color conversion well with reasonable accuracy and an average color difference error of $\overline{\Delta E^*_{00}} = 1.5$ with std.dev $\sigma = 0.75$. This result lies within the noticeable color difference threshold range, making this method a promising candidate for color correction. Some error contribution is due to interpolation of color values, to which extent is unknown. The effect could be minimized by an even greater

sampling of the input color space. An important aspect of this study lies in the fact that the model and model verification was performed at a weeks interval, whilst the printer underwent normal use. It is therefore, interesting to see the stability of the print process and that the model holds, making this a candidate for longer term production runs utilizing the current setup.

FUTURE WORK

Reverse modeling methods will be attempted, relating the *CIELAB* output space to the *sRGB* input space. Color correction could thus be applied to the 3D modeled part prior to print. Furthermore, a further statistical analysis on the error components will be conducted.

ACKNOWLEDGEMENT

The work of this paper was supported and made possible by the Manufacturing Academy of Denmark (MADE).[6]

REFERENCES

[1] Wohlers T, Caffrey T. Additive manufacturing and 3D printing state of the industry annual worldwide progress report. 2014. Wohlers Associates. 2013;.

[2] Hansen HN, Nielsen JS, Rasmussen J, Pedersen DB. Performance Verification of 3D Printers. In: Proc. ASPE Spring Topical Meeting on Dimensional Accuracy and Surface Finish in Additive Manufacturing (13-16 April 2014, Berkeley, CA, USA) pp; 2014. p. 104–107.

[3] Pedersen DB, Hansen HN. Comparability of the performance of in-line computer vision for geometrical verification of parts, produced by additive manufacturing. In: Proc. ASPE Spring Topical Meeting on Dimensional Accuracy and Surface Finish in Additive Manufacturing (13-16 April 2014, Berkeley, CA, USA) pp; 2014. p. 179–183.

[4] Sharma G, Wu W, Dalal EN. The CIEDE2000 color-difference formula: Implementation notes, supplementary test data, and mathematical observations. Color Research & Application. 2005;30(1):21–30.

[5] Larraín R, Schaefer D, Reed J. Use of digital images to estimate CIE color coordinates of beef. Food Research International. 2008;41(4):380–385.

[6] www.made.dk

PROGRESS TOWARD STANDARDIZED ADDITIVE MANUFACTURING TEST ARTIFACTS

Shawn Moylan
Engineering Laboratory
National Institute of Standards and Technology[1]
Gaithersburg, MD, USA

Introduction

Users and buyers of additive manufacturing (AM) systems need to know system performance characteristics to make important, basic decisions such as whether or not the system is capable of manufacturing their parts. Unfortunately, there are no standard methods of evaluating the performance of AM systems so manufacturer specification sheets can often be ambiguous, confusing, or worse, misleading. Does the number specified for resolution mean the smallest feature achievable by the system or the finest scale on one of the machine's axes? Does the number specified for accuracy relate to the achievable tolerance of the machine or to the resolution? Can I achieve the specified accuracy with any material in any place in the build volume, or do I need to determine a very specific set of parameters and the one "sweet spot" in the machine? Standard test methods help to eliminate these questions by providing a common terminology and defined measurement procedures.

One method of evaluating the performance of manufacturing systems is to manufacture and measure a test part, often referred to as a test artifact. The errors measured in the test artifact give an indication of the system's performance. A standardized test artifact allows easy comparison between different machines or from the same machine over time. The ASTM F42/ISO TC 261 Joint Group (JG) for Standard Test Artifacts (STAR) is developing a standard describing test artifacts to assess AM system performance. This paper provides some background for AM test artifacts and discusses the progress made by the STAR JG.

Background

Additive manufacturing gained prominence in the late 1980s and early 1990s as layer manufacturing or rapid prototyping (RP) with stereolithography (SLA) as the first additive RP process. The so-called "user part" is one of the first test pieces designed to quantitatively assess the accuracy of SLA systems (see Fig. 1) [1]. This part was designed in 1990 by an SLA user group and focuses on assessing the machine accuracy in the x-y plane. As other RP technologies such as fused deposition modeling, selective laser sintering, and polyjet entered the market, users wanting to benefit from the advantages of RP had to choose which of the processes best fit their application. Many researchers proposed the use of test artifacts, often called benchmarking parts, to quantitatively compare the capabilities of the various processes [2]. Kruth was the first to mention a test artifact for comparing AM processes, citing a study done by two Dutch companies using a U-shaped artifact with various geometric features such as circular holes (in various orientations), circular bosses, square holes, and angled surfaces [3]. Other researchers built upon

[1] Official contribution of the National Institute of Standards and Technology (NIST); not subject to copyright in the United States. The full descriptions of the procedures used in this paper require the identification of certain commercial products. The inclusion of such information should in no way be construed as indicating that such products are endorsed by NIST or are recommended by NIST or that they are necessarily the best materials, instruments, software or suppliers for the purposes described.

these results, adding more and/or different features, including overhangs and freeform objects, to demonstrate some of the advantages of additive processes [2]. Recently, a test artifact based on successful geometries used for AM benchmarking parts and on machining test artifacts was proposed by NIST (see Figure 2) [4].

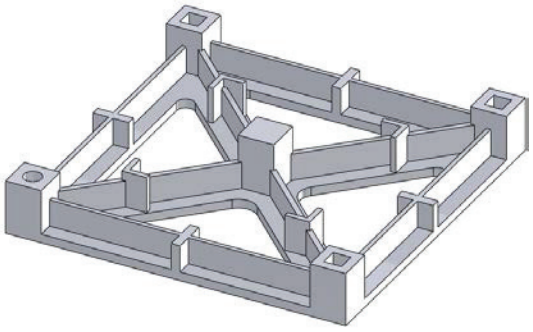

FIGURE 1. Solid model of the "user part."

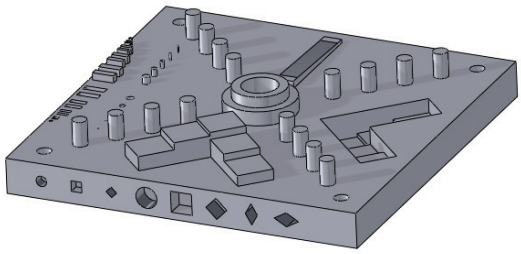

FIGURE 2. Solid model of the "NIST part."

Today there are literally thousands of test artifacts, most of which are never described in literature and are not available to the general public. AM-focused courses in technical, undergraduate, and graduate curricula often have projects or assignments requiring students to design test parts that demonstrate the capabilities of various AM technologies. AM users and machine developers working on material and process development likely have their own, sometimes proprietary, test part designs that demonstrate build quality with certain process parameter sets. And previously developed artifact designs are slightly modified (for example by adding a hemisphere to the NIST part) by individual users to address very specific requirements. These examples demonstrate the difficulty in standardizing a test artifact geometry: no single design will work for 100% of users or requirements.

In July of 2013, the two primary standards developing organization focused on AM, ASTM International's Committee F42 on Additive Manufacturing Technologies and the International Standards Organziation (ISO) Technical Committee (TC) 261 on Additive Manufacturing formally agreed to joint development and co-branding of standards [5]. As part of this agreement, pilot joint standards development groups were proposed in four areas, one being standard test artifacts. The JG STAR is convened by ASTM F42, and has 5 experts from ASTM F42 and 5 experts from ISO TC261 (maximum capacity). The group first met in January 2014 and has been working since to develop a draft standard.

Approach taken by JG STAR

In an effort to draft a standard that would benefit as many AM users as possible, the JG adopted a slightly different approach to avoid the problem that one part might not address the needs of many. The JG decided that the standard would describe a suite of test geometries that each tested a different characteristic of an AM system, and a user could configure the individual geometries to whatever best fit the current need. This approach had been proposed previously, by Smith [6], Jurrens [7], and most recently in a European AM standards project.

One of the main problems with one test artifact geometry is that AM systems come in many different sizes. Specifically, if a test part is too large or too small to adequately test an AM system, what is the user to do? Simply scaling the part up or down in size is often problematic because the absolute sizes and positions of features are often equally (or often more) important than the relative sizes and positions. To avoid this problem, the JG proposed to design test features that were easy to append (or trim) to accommodate different AM system sizes.

DRAFT

Finally, and most importantly, the JG decided that all artifact designs should allow for quantitative characterization of machine performance. Further, the standard should recommend what characteristics should be measured and not dictate the method of measurement. In fact, it was strongly preferred that any measurement should be able to be performed in several different ways, and not require users to own a particular measurement technology.

Artifact geometries

The JG is working toward 7 standard artifact geometries to characterize different aspects of machine performance: linear accuracy, circular accuracy, resolution pins, resolution holes, resolution ribs, resolution slots, and surface texture. Note that these geometries are still being debated and tested and are subject to change based on further review. Additional artifacts may be added in a future revision of the standard. The standard will thoroughly describe the artifact geometries, but it is also the intention of the JG to provide *.amf files (and *.stl files for a limited time) of each artifact for users to download, likely from the ASTM and ISO websites.

Linear accuracy

This artifact tests the linear positioning accuracy typically along a specific machine direction. Depending on artifact orientation and machine configuration, errors in the artifact may provide a basis for positioning compensation or diagnosing specific error motions in the machine's positioning system. Figure 3a depicts the artifact geometry; it is comprised of prismatic protrusions atop a rectangular solid base and is 55 mm in length. Spacing between the protrusions is non-uniform to avoid complications from periodic errors. If a longer test of linear accuracy is desired, multiple linear accuracy artifacts can be appended to one another. If the artifact is too large, a user can easily edit (or re-create) the geometry to remove the one of the end protrusions.

The primary measurement for the linear accuracy artifact is the positions of the protrusion faces relative to the primary datum at the end of the artifact. Alternatively, the lengths of each protrusion can be measured and the spacing between each protrusion can be measured. Further, after characterization for linear accuracy, this artifact can be used for characterization of part density, either by Archimedes method or by optical methods after sectioning/polishing the protrusion surfaces. Optional measurements on this artifact include straightness of the base and parallelism of the two sides of the base.

Circular accuracy

This artifact tests the ability of the machine to make arced contours and to produce arced features. Depending on artifact orientation and machine configuration, errors in the artifact may provide a basis for diagnosing specific error motions in the machine's positioning system, similar to a circular test performed on a machine tool [8]. Furthermore, this artifact tests the ability of the machine to create features in a specified location, specifically concentric features. The artifact geometry, shown in Figure 3b, is comprised of concentric rings that are each 3 mm in diameter atop base connecting all rings. The overall size of the artifact can easily be adjusted by adding or subtracting outer rings.

The primary measurements for this circular artifact are roundness/circularity of each face of each ring and the center position of a best fit circle to each face of each ring. Optional measurements include the thickness of each ring at several angular positions as well as the diameter of each face of each ring.

Resolution artifacts

There are 4 artifact geometries intended to characterize the minimum feature size achievable by the AM system: resolution pins, resolution ribs, resolution holes and resolution slots (see Figure 3c-f). Each

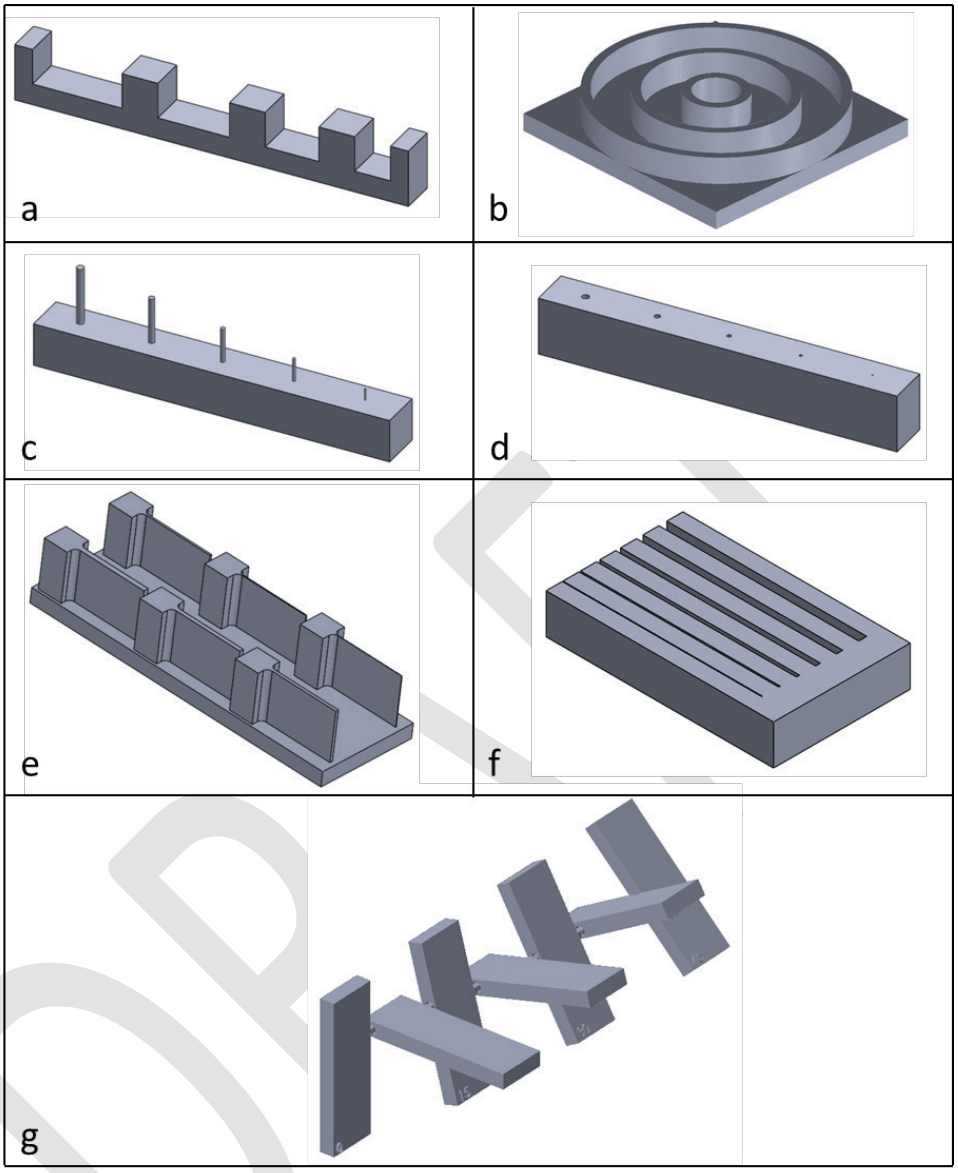

FIGURE 3. Solid models of the proposed standard test artifacts: a) linear accuracy, b) circular accuracy, c) resolution pins, d) resolution holes, e) resolution ribs, f) resolution slots, g) surface texture (scale is different for each model). Note that these geometries are still being debated and tested and are subject to change based on further review.

artifact is offered over three size ranges: coarse, medium and fine. In general, the coarse sizes are intended to test metal deposition and cladding type machines, with feature sizes ranging from a few millimeters down to 0.5 mm. The medium sizes are intended for the most commonly available AM systems, e.g., metal powder bed fusion, polymer material extrusion, etc. These features sizes range from 1 mm down to 0.1 mm. The fine features range from 0.2 mm down to 0.01 mm and are intended to measure the most accurate polymer AM machines or future machine capabilities. Further, the resolution pins artifact is offered at length to diameter ratios of 4:1, 6:1, 8:1, and 10:1. It is not intended for the user to build all resolution features available. The user should have an estimated resolution achievable by the system being examined and select the one feature set that spans that estimated resolution.

Surface texture

The surface texture artifact is actually a set of platens built at several inclinations, as shown in Figure 3g. While it may be thought that the stepwise nature of layer-by-layer processes would dominate surface texture, and the roughness could be mathematically determined based on layer thickness, initial research by JG members on metal powder bed fusion machines has shown this not to be the case. As such, it is intended that the user build all of inclination angles to give a thorough understanding of surface roughness achieved at each orientation. However, if a user is only looking for a quick check, or only needs to characterize a specific orientation, the artifact can be edited to only include the desired angles.

The primary measurement on surface texture artifacts is surface roughness. The standard discusses considerations for filtering the raw data obtained by either linear or areal roughness measurement and suggests that users report average roughness (R_a or S_a), mean roughness depth (R_z or S_z), skewness (R_{sk} or S_{sk}), and kurtosis (R_{ku} or S_{ku}). An optional measurement on the surface texture artifact is the inclination angle of each platen.

General guidance in the standard

Beyond descriptions of the artifact geometries and measurements to be taken, the standard also includes sections providing general guidance for building the artifacts as well as example artifact configurations. The standard intentionally does not prescribe specific protocols or recipes for building the artifact because these decisions by the builder might be important to the performance characterization (e.g., if using the standard geometries to compare between two AM service bureaus). However, the standard does require a builder to have documented material and process specifications (either standard or user-developed) describing the build. The standard does not require specific positions, orientations, or replicates for each artifact. However, general guidance text as well as example configurations are intended to get the user to consider important aspects of machine characterization. For example, none of the artifacts is more than 2.5D, so it is important to consider multiple orientations for each artifact to explore the performance of the machine in all directions.

The standard also includes general and specific guidance for measurement of each artifact. As previously mentioned, the standard does not require any specific measurement techniques and allows the user to measure each artifact in the most practical way available. However, the standard does require that the user disclose the measurement technique, any calibration information or certificates, as well as measurement uncertainty for all measurements. The standard includes a measurement appendix for informational purposes only. This appendix contains a table summarizing many alternative techniques for measuring each artifact (e.g., the linear accuracy artifact can be measured using a coordinate measuring machine, 3D scanner, dial indicator with calibrated motion axis, and handheld calipers or micrometers). This appendix also includes specific instructions for commonly used methods of measuring each artifact (e.g., a specific protocol for measuring resolution slots with slip or shim gages).

Expected next steps and timeline

Drafts of each section of the standard have been completed and initially reviewed by the JG. The first draft of the entire standard has recently been compiled and will be reviewed by JG members. Edits will be made to the draft based on JG member feedback before the draft will be distributed to the ISO TC 261 working group 3 on Testing and ASTM F42.01 subcommittee on Testing. Following this review (and subsequent revision) the standard will be fast-tracked for vote by both the ISO TC 261 as well as ASTM F42. It is

hoped that subcommittee review will be completed shortly after the next joint meetings of ISO TC261 and ASTM F42 in July 2015 in Berlin, Germany and that the standard can be approved around the time of the joint committee meetings in January 2016.

REFERENCES

[1] E. P. Gargiulo, Stereolithography process accuracy: user experience, Proceedings of the 1st European Conference on Rapid Prototyping, University of Nottingham, 1992, 187-207.

[2] Moylan, S., Cooke, A., Jurrens, K., Slotwinski, J., Donmez, M.A., A Review of Test Artifacts for Additive Manufacturing, NISTIR 7858, Gaithersburg, MD, 2012.

[3] Kruth, J.P., Material Incress Manufacturing by Rapid Prototyping Techniques, CIRP Annals, 1991, 40 (2), 603-614.

[4] Moylan, S., Slotwinski, J., Cooke, A., Jurrens, K., Donmez, M.A., An Additive Manufacturing Test Artifact, Journal of Research of NIST, 119: 429-459. http://www.nist.gov/el/isd/sbm/amtestartifact.cfm

[5] AM Standards Development Plan, www.astm.org/COMMIT/AM_Standards_Development_Plan_v2.docx

[6] Smith, R., Standard Test-Files for Benchmarking RP Systems, Third International Conference on Rapid Prototyping. (1992).

[7] Jurrens, K., Standards for the Rapid Prototyping Industry, Rapid Prototyping J., 1999, 5(4), 169-178.

[8] ISO 230-4, Test Code for machine tools—Part 4: Circular tests for numerically controlled machine tools.

DRAFT

Material Certification through a Synergistic Experimental Monitoring and Microstructure Modeling Approach

Elwany, A.[*], Karaman, I.[**], and Arroyave, R.[**]

[*] Department of Industrial & Systems Engineering, Texas A&M University

[**] Department of Industrial & Systems Engineering, Texas A&M University

1. Introduction

Qualification and certification (Q&C) of materials, processes, and parts in metal-based AM continue to be a high priority need, according to most research and industrial stakeholders as clearly conveyed in most published roadmaps such as the roadmap for additive manufacturing [1] and NIST's measurement science roadmap for metal additive manufacturing [2]. Q&C can be a lengthy and expensive process (e.g. $130M and take 15 years for some aircraft components in developing statistically substantiated databases and creating test coupons and specimens [3]). Accelerating this process is an ongoing effort; see for example Lawrence Livermore's initiative for accelerated certification of additively manufactured metals (ACAMM). A precise and standard definition of Q&C for AM has not yet been coined. Nevertheless, some enabling capabilities have been identified, such as developing accurate predictive process models for microstructure and properties [4]. Thermal process monitoring is a key element of this task, since it provides one of the important inputs to physics-based microstructure models.

We describe our recent integration of a thermal monitoring system with a commercial SLM platform, and then give a high level overview of how this will be used to contribute in the acceleration of Q&C for AM materials.

2. Monitoring System Integration

A two-wavelength imaging pyrometer (ThermaViz®) was integrated with a ProX 100™ SLM system by 3D Systems. ProX 100™ uses a 50-W fiber laser to selectively fuse metal powder. To enable this integration, the first step was to design a custom bracket to mount ThermaViz® inside the build chamber as depicted in Figure 1 and Figure 2 .

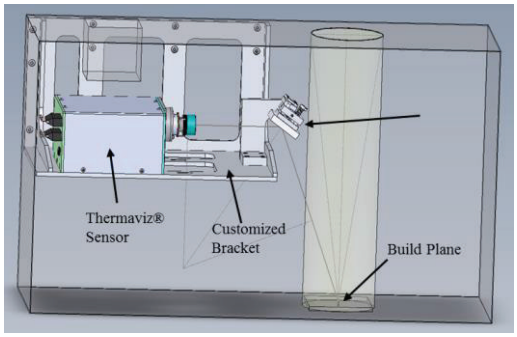

Figure 1 Solid model of ThermaViz installed in the ProX 100 build chamber

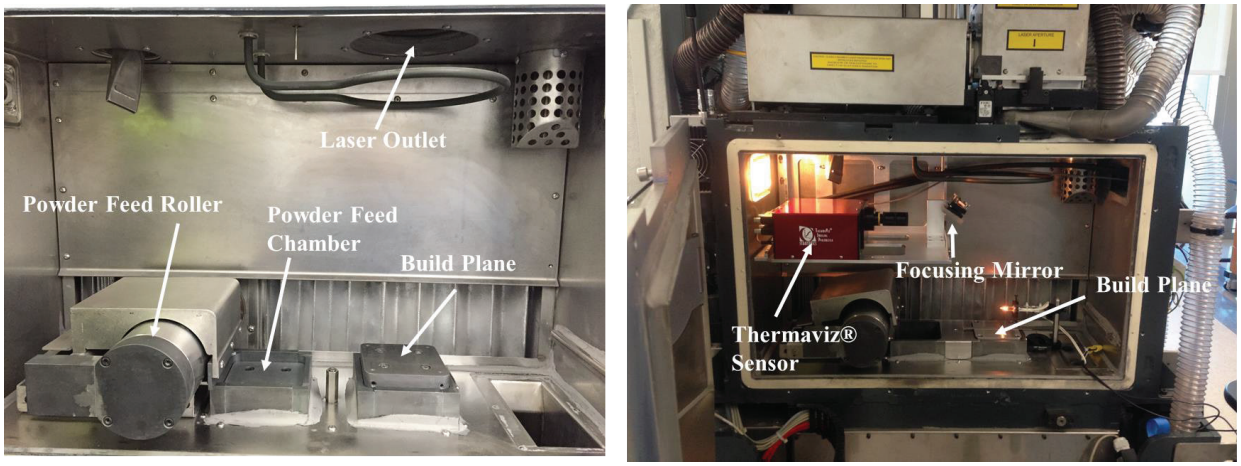

Figure 2 ProX 100™ build chamber with (right) and without (left) the ThermaViz® sensor installed

ThermaViz® focuses on the powder bed with a full field of view (FOV) of 26 mm × 20 mm. The sensor has spatial resolution of 1300 × 1000 pixels, at 20 μm per pixel and 150 frames per second. Monitoring the powder bed with two-wavelength pyrometry hedges against emissivity variation, which is one of the main practical challenges in using thermography for monitoring metal-based AM processes.

Five layers where created in 17-4 Stainless Steel, each layer with a 10 × 10 mm simple geometry. The laser power and scanning speed were set to 48 W and 350 mm/s, respectively to test the capabilities of the integrated monitoring sensor. Figure 3 displays snapshots of the melt pool images acquired within the first layer of the test build.

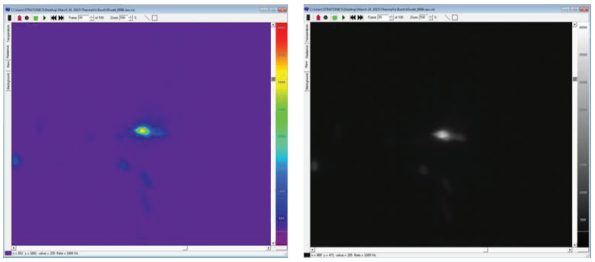

Figure 3 Metl pool images. Right frame shows raw data. Left frame shows pre-processed data after thresholding

In addition to melt pool images, thermal profiles and thermal histories across custom defined regions of interest are readily generated. Figure 4 shows the intensity profile for two cross sections across the width and length of the melt pool (top left and bottom left, respectively). The length of the melt pool, the region of interest (horizontal line in the bottom right figure) was set at 1 mm covering 40 pixels (25 μm per pixel). From the top left figure, the length of the melt pool is approximately 7 pixels = 175 μm. Notice that in order to get an accurate assessment of this length, we need to find the

intensity level corresponding to the melting temperature of the powder.

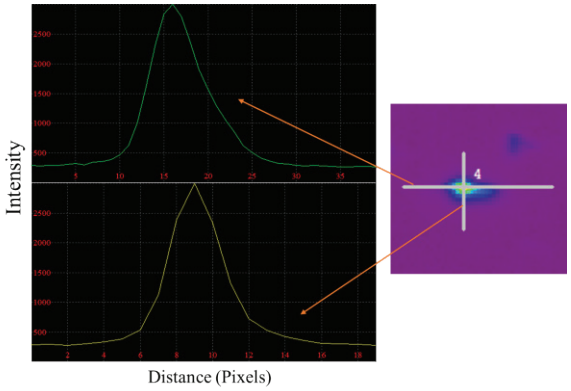

Figure 4 Linear region of interest (cross section through melt pool) with intensity profiles

Figure 5 shows a rectangular region of interest, and the intensity distribution (histogram) within that region. It is worth mentioning that these intensities are still input to an algorithm to interpret them into temperatures rather than pixel counts.

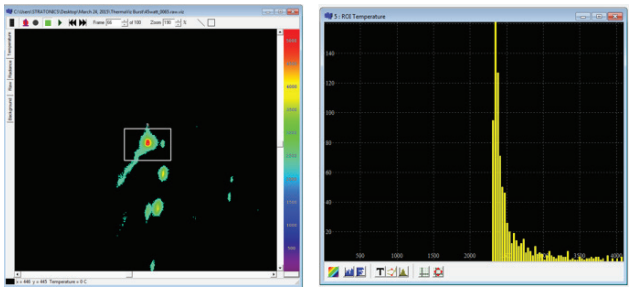

Figure 5 Rectangular region of interest (left) with intensity distribution (right)

The thermal history can also be output for subsequent use with physics-based models. Just for illustration, Figure 6 shows the melt pool peak intensity over 100 successive frames.

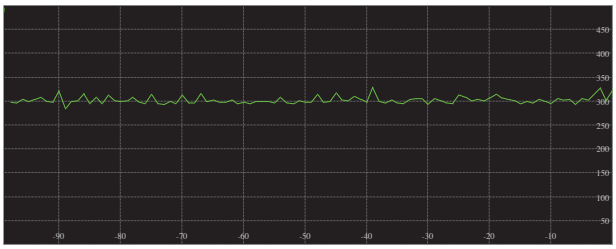

Figure 6 Peak intensity within region of interest over 100 successive frame

The above figures are only meant to demonstrate the type and structure of data that can be generated using the integrated monitoring system. To our knowledge, this effort is among the first in integrating a two-wavelength imaging pyrometer on an SLM system.

3. Next Step: Microstructure Modeling and Uncertainty Quantification

The thermal history captured using the integrated monitoring system will provide input to Phase Field models that we have developed to simulate microstructure evolution during SLM. Next, the microstructure of the fabricated samples will be experimentally characterized. Gaussian process models for uncertainty quantification can then use information from simulated and experimentally characterized microstructures to identify the sources of uncertainty in SLM. The proposed framework, summarized in Fig XXX, is invaluable in establishing a process-microstructure-properties relationship that is much needed to accelerate the material certification process in SLM.

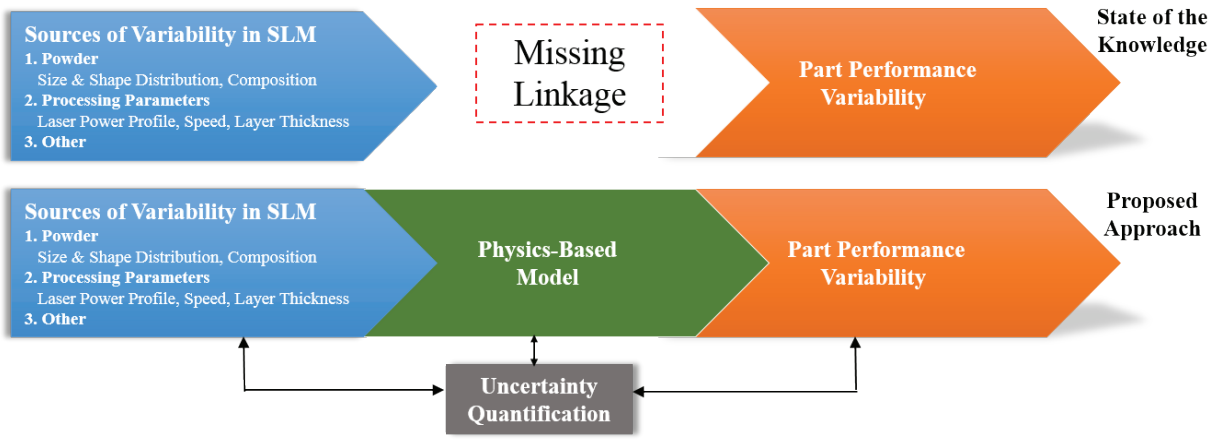

Figure 7 Proposed vision for Uncertainty Quantification in metal-based AM

References

1. Bourell, D.L., M.C. Leu, and D.W. Rosen, *Roadmap for additive manufacturing: identifying the future of freeform processing*. The University of Texas at Austin, Austin, TX, 2009.
2. NIST, *National Institute of Standards and Technology: Measurement Science Roadmap for Metal-based Additive Manufacturing*. May 2013, U.S. Department of Commerce: Maryland.
3. Frazier, W.E., *Metal additive manufacturing: A review*. Journal of Materials Engineering and Performance, 2014. **23**(6): p. 1917-1928.
4. Frazier, W.E., *Direct digital manufacturing of metallic components: vision and roadmap*. Direct Digital Manufacturing of Metallic Components: Affordable, Durable, and Structurally Efficient Airframes, at Solomons Island, MD, 2010.

Effects of X-ray interactions and CT algorithms on the capability of X-ray CT Metrology of Additive manufactured parts

David J. Bate[1],
[1]Engineering Department
Nikon Metrology
Tring, Hertfordshire, UK

Introduction

This paper will address how the interactions of the X-ray beam affect the output CT volume and hence the ability to make accurate measurements of the part, it will also consider the impact of the standard Feldkamp filtered back projection method normally used for CT reconstruction and the limitations on the measurement accuracy it introduces. The last section will show which of these have an impact on Additive manufacturing parts.

In doing this the issue of accurately finding the surface for measurement will not be addressed, it will be assumed that the reconstruction needs to have a well defined edge with good contrast and low noise that is representative of the object and can be calibrated to make a good measurement provided a good reconstruction of the data can be produced.

X-ray interactions

When an X-ray beam interacts with matter there are a number of processes involved, in the energy range for most AM parts the most important for the CT image reconstruction are the attenuation of the beam and the scattering (both coherent and incoherent) of the beam. Effects such as pair production only become an issue at much higher energies.

Scattering vs Attenuation

The X-ray CT reconstruction is based on the attenuation information and the process is captured in the Beer Lambert law:

$$I = I_0 e^{-\mu t}$$

Where I_0 is the intensity without the object, I is the intensity measured at that position on the detector with the object in place, μ is the attenuation coefficient of the material and t is the thickness of the material.

The second effect is scattering, X-ray photons which are scattered will arrive at pixels in the detector that do not correspond to the direct path and are not related to the attenuation. As such they do not contribute to the CT reconstruction and so appear as an additive term (noise like) in the Beer- Lambert law.

However, the scattering occurs only from material and is affected by the density and crystal structure of the material so these photons have a fixed pattern error rather than being truly random noise. Therefore, the size of the scattering problem will depend on the sample. At the extremes a very small low density object being scanned at low kV will have very little scattering whereas a crystalline high density part (such as an aircraft turbine blade) will have a lot of scattering.

The effect of scattering is to reduce the contrast between material and air in each radiograph collected and so to reduce the accuracy of the CT scan, in particular scattered artefacts that move with the rotation (due to crystal scattering) can lead to false material in the reconstruction and general scattering will lead to a lack of contrast on the edges. This assumes that a Filtered back projection reconstruction is used. Other reconstructions can handle scatter better as will be discussed later.

To reduce the effect of scattering collimators are used. These restrict X-ray photons to paths which will reach the detector in a straight line and so stop any photons from interacting with the cabinet and sample mounting contributing to the image. The effect of inelastic scattering can be reduced further by using post sample filtering as such photons are lower energy.

Beam hardening

The use of polychromatic X-ray sources in micro focus computed tomography means that the ideal Beer – Lambert law shown above:

$$I = I_0 e^{-\mu t}$$

Is modified further, in addition to the additive term required to cover the scattering and noise to a form which is integrated over the energy range of the polychromatic beam;

$$I = I_0 \int e^{-\mu(E)t} dE$$

However, the standard filtered back projection algorithms assume the standard monochromatic Beer Lambert law.

This leads to errors as the X-ray beam loses its low energy components first as they are attenuated fastest and so becomes harder as it travels through the object.

The effect of this is to generate two types of artefact; The first appears where two areas of high material density line up in some projections and not others, as the beam is hardened when hitting the second area after passing through the first is leads to 'streaks' or 'bridges' connecting areas;

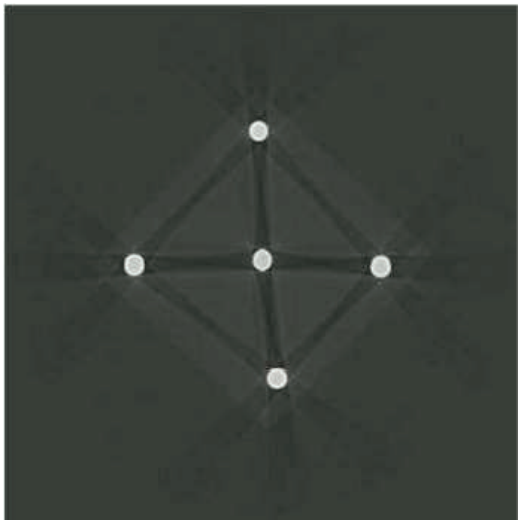

FIGURE 1. Image showing streak and bridging artefacts due to beam hardening.

The second effect is most clearly seen in cylindrical objects where the beam passing tangentially through the edges of an object is hardened less than the beam passing through the longest path length in the middle of the object, this leads to 'cupping' artefacts where the edges of an object are brighter than the centre (see Fig 1. For examples)

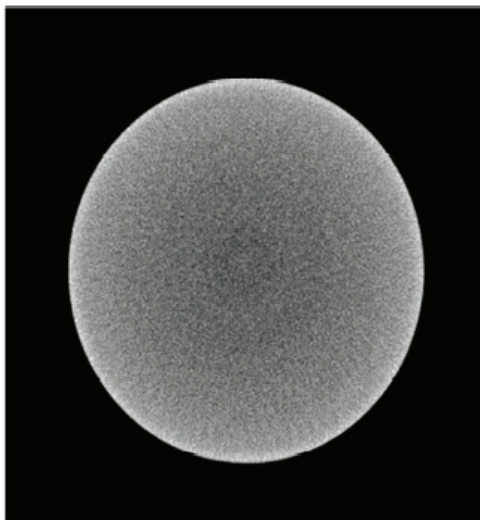

FIGURE 2. Image showing cupping artefacts due to beam hardening.

Clearly, such artefacts will affect the ability of any analysis to determine accurately the surface of the material so this effect will reduce the accuracy of any measurement in CT unless it is corrected for.

Finding the exact spectrum is very difficult in most practical cases and so there are two strategies used to correct the data; The first strategy is to use a physical filter to remove most of the lowest energies from the beam before it interacts with the sample; the second method is to use a 'Beam hardening correction'.

When the final object is single material either of these methods can work very well and so for many AM parts made with a single base material this issue can be solved either with correct physical filtering or with a post acquisition correction.

For a single material the post acquisition correction can be generated by pre scanning under the X-ray conditions to be used known thicknesses of the material (made by AM in the same manner as the main object) and constructing a graph of Apparent attenuation vs

actual attenuation by thickness (see Figure 3. For the results.)

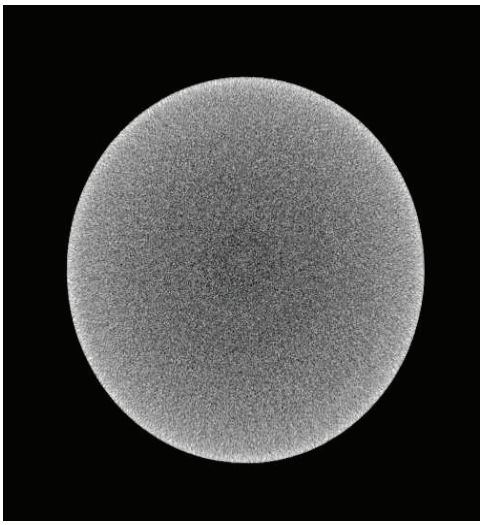

FIGURE 3.(a) CT slice with no physical filtering or post acquisition correction

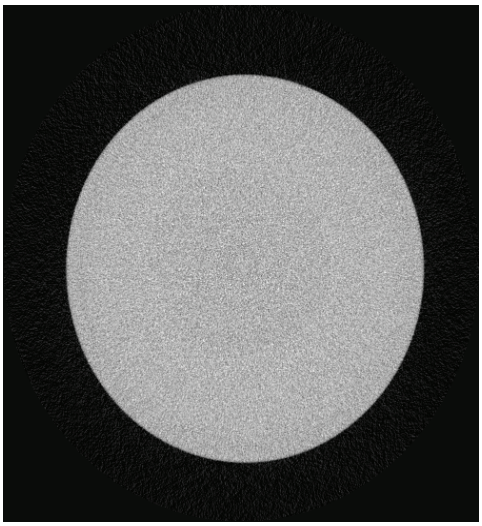

FIGURE 3.(b) Same CT slice with 1 mm of Cu physical filtering

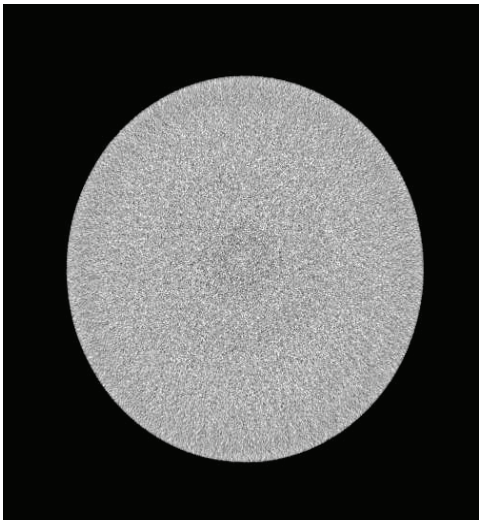

FIGURE 3.(c) CT slice with Post acquisition correction.

The situation is more complicated when two materials are present as they will harden the beam differently.

If the two materials are well known then it is possible to create a post acquisition correction similar to the single material case, although it is more complex.

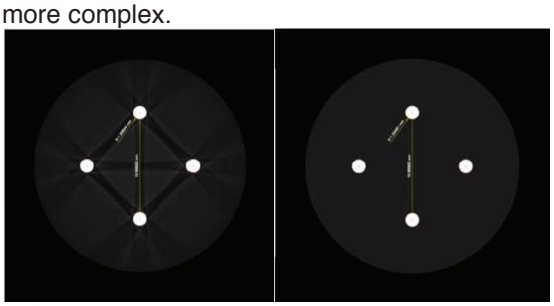

FIGURE 4. Dual material test sample with no correction (Left) and a two material post acquisition correction (Right).

The final method of removing beam hardening is to use a dual energy scan following the Alvarez technique [1]

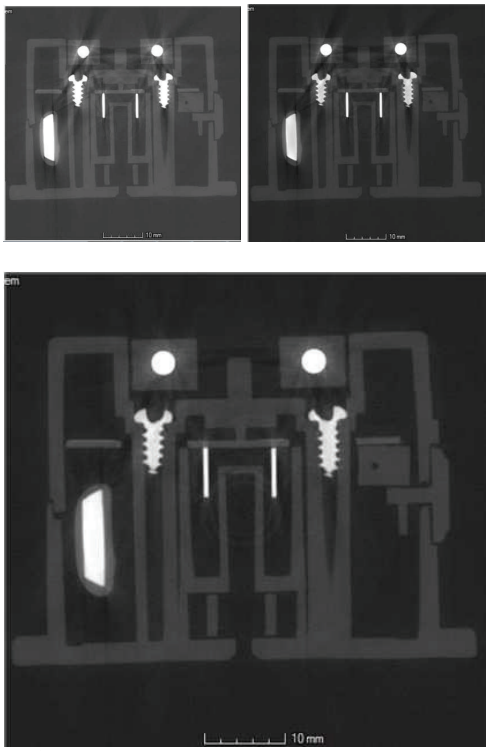

FIGURE 5. A high energy and low energy scan combined into a single corrected scan according to the Alvarez method [1]

Reconstruction algorithm

At present the most popular and common algorithm for CT reconstruction is based on Filter Back project, usually the Feldkamp algorithm. This has the advantage of being fast to reconstruct on large datasets and easy to use, but has the disadvantage that it is only strictly accurate on the central slice of the reconstruction.

Mathematically the algorithm takes each projection image and calculates the attenuation along the ray to each pixel, it then assigns that ray (back projects) to the ray path with the attenuation spread evenly over the whole ray. In order to do this Radon transform is used, these operations introduce a bluring and a filter is used in the transformed space to remove this blurring.

There are three major issues that need to be addressed with the algorithm to get high precision metrology; Number of projections, Cone beam error.and noise.

Number of Projections

When the reconstruction is performed and the attenuation from multiple projections are added then the image is buuilt up gradually, as can be seen in Figure 6 until enough projections are used the image is very poor.

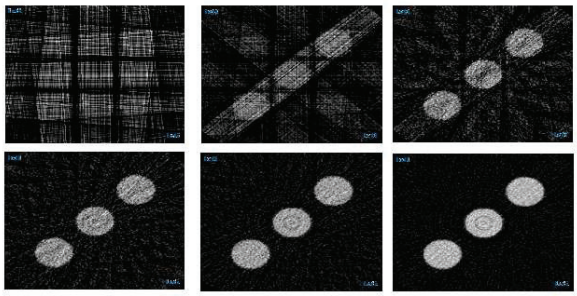

FIGURE 6. Build up of CT reconstruction showing the improvement from 4 (top left) to 128 (bottom right) projections

An estimate of the number of projection can be obtained by considering the circle that is swept by the widest part of the object. Its circumference is $2\pi r$ but also it is made up of the n projection steps. For good metrology you want the step per projection to be no larger than 1 pixel, so working in pixel space.

No. of Projections = 2π Width of object in Pixels

In general because the X-rays penetrate the object so that information is being generated on both side a value between π and 2π is best. E.g. if the object fills 1500 pixels on the imager, its radius is 750 pixels and so at least 2356 projections should be used.

Cone beam errors

The second major issue with the reconstruction is the cone beam error. This arises because the algorithm is only exact in the central plane as it needs to have ray paths to all parts of a given voxel, so as the voxels move off axis the top (or bottom) is not sufficiently covered.

This error is inherent in the algorithm and, in the long term, will be eliminated by other acquisition and reconstruction algorithms, such as helical (currently also inexact but trades a single error for a smeared error) or Iterative full solutions (currently extremely long reconstruction times).

At present the best way to minimize this error is to use a small vertical cone angle for measurement scans, best results are seen if the cone angle is less than 6 degrees, but depending on the precise shape of the object this can be varied.

Noise

The last error is the random noise. In the description of the algorithm the filtering in the transform space was mentioned, this filter is usually a simple ramp filter, which tends to over enhance high frequency noise.

This effect can be reduced by using a different filter but these filters will also reduce the high frequency components of the object and so reduce the accuracy of the reconstruction and in particular the edges.

Therefore, it is very important to make sure the projection images are low noise

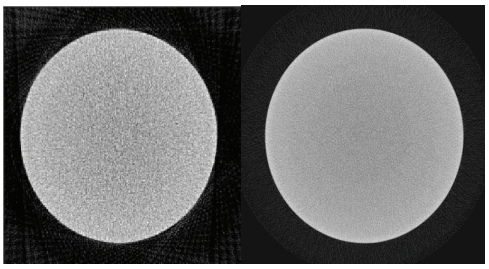

Figure 7. Two slices showing the effect of noise, the same X-ray conditions and number of projections were used in both cases,

The quality of a CT reconstruction is determined by the amount of X-ray photons detected and so it is often better to reduce the number of projections slightly in order to increase the averaging (noise reduction) per projection.

If time is no object then very high quality reconstructions can be achieved, but in a practical process there will be a time limit.

Impact on AM parts

All of the above issues are present in all X-ray CT. The nature of AM parts means that effects of using very high energy (pair production and extreme scattering) are avoided. It is also less likely that the object will be highly crystalline.

However, it is likely that the object will have small micro-structure due to the processes of production which will scatter X-rays.

Therefore, combining the above we can deduce a set of guidelines for good CT suitable for metrology measurement.

1. Make sure that the kV chosen penetrates the longest path in the object well
2. Make sure the beam current is chosen to give a good contrast between material paths and voids
3. Use physical filters to remove the low energy X-rays that will be stopped in a very short material path.
4. Spread the filter so that about 50% is before the sample and 50% after the sample (to reduce low energy scattered X-rays
5. Collimate the beam. X-rays from the source that won't hit the detector with no object in the way are only adding noise, remove them before detection
6. Collect each projection as long as practical to reduce noise
7. Take enough projections to avoid missing data around the edges of the sample and hence the edges of the reconstruction
8. If the object is tall, split it into small vertical sections and stitch them together afterwards to avoid cone-beam errors.
9. Use appropriate beam hardening corrections when reconstructing.
10. Do not apply noise filters that will remove data needed for the edge reconstruction (filters that remove high frequency components in the frequency space)

If these 10 rules are followed it should be possible to obtain a good quality CT reconstruction volume with sharp well defined edges with good contrast that will allow an edge finding routine to find them and use them for measurement.

The methods described in this abstract do not address the next two key issues which are to find that surface and how to measure from it and also, how to calibrate the CT system and obtain traceability back to standards. At present this

hampered by the lack of an ISO standard for CT metrology of any type, not just AM.

Both of these topics need further work to allow the final goal of accurate CT measurement of AM parts.

Acknowledgements
I would like to acknowledge the help in funding the beam hardening research from the EU on project Hi Micro. I would also like to acknowledge help from my colleagues in Nikon metrology in particular Ben Price, Sakaguchi-san and Andrew Ramsey

REFERENCES

[1] R E Alvarez and A Macovski. Energy-selective reconstructions in X-ray computerized tomography. 1976 Phys. Med. Biol. 21 733.

ASSESSING ADDITIVE MANUFACTURING PROCESSES WITH X-RAY CT METROLOGY

Herminso Villarraga[1, 2], ChaBum Lee[4], Taylor Corbett[4], Joshua A. Tarbutton[4], and Stuart T. Smith[1, 2, 3]
[1]Center for Precision Metrology, [2]Department of Physics and Optical Science, and [3]Department of Mechanical Engineering and Engineering Science
University of North Carolina at Charlotte, NC, USA.
[4]Department of Mechanical Engineering
University of South Carolina, Columbia, SC, USA.

In a recent review of CT metrology issues it was stated that, "Industry can no longer accept that intricate components produced by additive manufacturing or multi-material injection molding escape any geometrical and tolerance quality control for the only reason that there is no non-destructive method to measure the inner or internal geometry" [1]. Recently, with the development of X-ray computed tomography (CT) systems designed for applications of industrial metrology, CT has become the only commercially-available, non-destructive method to perform dimensional measurements of internal geometrical features [1, 2]. The aim of this study is to illustrate its applications for assessment of additive manufacturing (AM) processes. This paper presents a comparative study using CT for dimensional metrology (part to CAD comparison, wall thickness analysis, size) and for material inspection (void detection) to examine the outcome of two different AM processes that produced two identical flexure mechanisms. The flexures were fabricated by fused deposition modeling (FDM) and stereolithography (STL) methods at the Department of Mechanical Engineering from the University of South Carolina at Columbia. ABS (Acrylonitrile butadiene styrene) of elastic modulus 2.5GPa and a photopolymer material of elastic modulus 1.85GPa are used in with FDM and STL processes, respectively, and the two identical double-compound notch-type flexure mechanisms were fabricated by two different processes. Each leaf string is L25.0×W20.0×T1.0 mm^3. Because the approach in this work focuses on the applications of CT metrology as a tool for assessment of manufacturing processes, particularly AM, with the aim of generalization and for pedagogical purposes, the FDM method will be referred to as AM1 and the STL method will be referred to as AM2. For reference, the FDM and STL refer to processes by which digital 3D design data is used to build a component in layers by depositing various polymeric or composite materials. In general, FDM and STL have a printing resolution of approximately 100 μm and 0.5 μm, respectively. In this research, the hypothesis is two-fold: CT technology can be used as an inspection/metrology tool for AM products, and AM technology can be used for precision engineering applications.

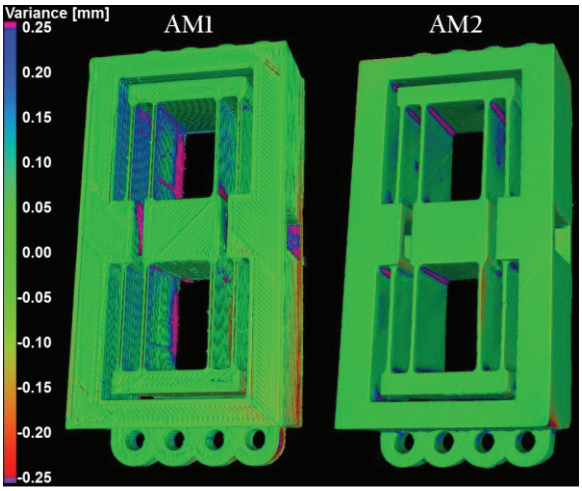

FIGURE 1. Part to CAD comparison for the outcomes of the AM1 and AM2 processes.

CT METROLOGY ANALYSIS

Figure 1 shows the variance analysis for the AM1 and AM2 flexures against the CAD model for the parts. Here, the testing surface's location for the part is generated from a three-dimensional voxel set of data (grey scales or absorption intensities) obtained by the CT scanning of the parts with X-rays. To allow dimensional measurements using the X-ray CT technique, the parts were scanned with a Zeiss Metrotom 800, CT machine [3, 4].

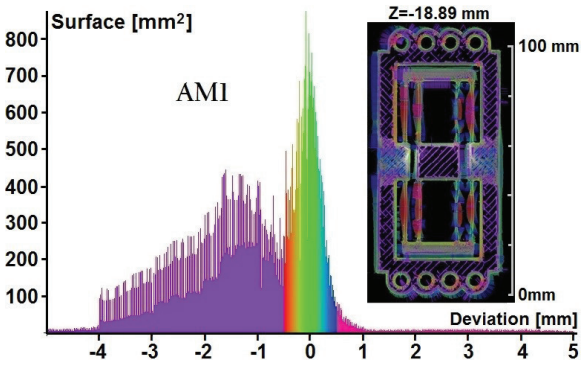

FIGURE 2. Full variance distribution for deviations of the CAD model in the outcome of the AM1 process. A cross section of the part-to-CAD comparison at a plane located at $Z = -18.89$ *mm from the top part's planar face is shown.*

Parts' surface determination was performed on the original scan voxel data with VGStudio MAX 2.2 [5]. This software uses the CT reconstructed data to create a three-dimensional model of the volume that can be used in 2 or 3 dimensions. From the measurements depicted in Figure 2 for example, it can be seen that deviations from the nominal geometry (CAD model) rise up to ± 0.25 mm and larger when using the AM1 process. In contrast, the AM2 process generated part-to-CAD deviations mostly between ± 0.1 mm with a few exceptions particularly around the edges or corners of the part's surface, see Figure 3. Deviations up to -4 mm were detected between measured and nominal dimensions of the CAD model of the part (flexure) for the AM1 process, Figure 2. These particular tolerance outcomes might be related to the printing resolution limits associated with the AM1 and AM2 processes, which have a printing resolution of approximately 100 µm and 0.5 µm, respectively. Individual components tolerances in the flexures can be tested, but the part-to-CAD comparison using the CT data offers the advantage of fully assessing the parts' surface everywhere. This comprehensive assessment allows for decreased inspection time when comparing the AM1 and AM2 processes. The representation of CT data is based on the original voxel data to avoid measurement uncertainties caused by a second data representation (Standard tessellation language or STL conversion, for example, add inaccuracies to the surfaces during the triangulation process). This representation based on voxels provides geometric evaluations in 2D or 3D such as, nominal/actual comparisons and all further geometric analyses like wall thickness analysis and dimensional metrology with uncertainties of less than 1/10th of a voxel [5].

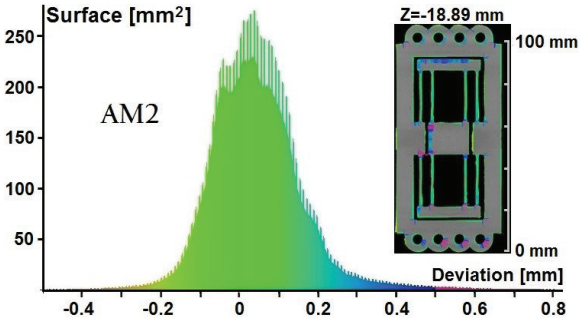

FIGURE 3. Full variance distribution for deviations of the CAD model in the outcome of the AM2 process. A cross section of the part-to-CAD comparison at a plane located at $Z = -18.89$ *mm (from the top) is shown.*

A cross section of the parts at a plane located at $Z = -18.89$ mm (from the top part's top planar surface) is presented in Figure 4, showing residual internal and spatial deformations detected in the flexure AM1 (top image). On the other hand, the manufactured part generated by the AM2 process does not reveal the presence of major deformations in the thin walled flexure leaf structures.

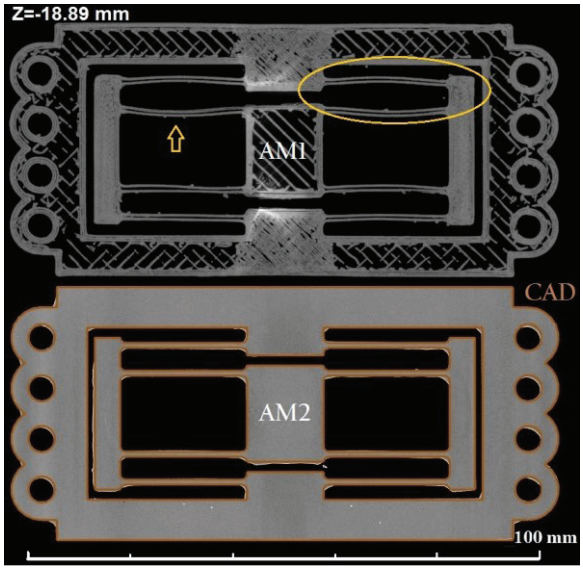

FIGURE 4. Transversal cross section for the AM1 and AM2 parts at $Z = -18.89$ *mm. A sketch of the CAD model is shown superposed on the AM2 part.*

A 3D wall thickness analysis on the CT volume data was also applied to locate the positions and size of the individual areas with thinner wall thicknesses, and the results can be visualized by color-coding as shown in Figure 5 and Figure 6. Due to the high density of porosity for the AM1 part, very thin wall thicknesses are generated with the AM1 process, as can be seen from Figure 5. Most walls for the manufactured part, in that case, are in the region of 0.3 to 1.3 mm thick. Only a small fraction of the total part's surface gets over the 2 mm thickness. On the other hand, the wall thicknesses generated with the AM2 process (see Figure 6) for an identical part's design range between 1 to 22 mm making the walls not only wider but stronger. Therefore, we do not see evidence in the AM2 part of the same kind of internal and spatial deformations detected in the flexure AM1 (top image from Figure 4). However, the method for wall thickness detections is inaccurate at any corner of the part under investigation [6], so those regions are not assessed.

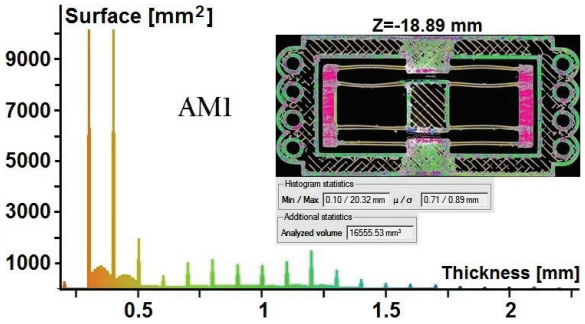

FIGURE 5. Full part's wall thickness distribution for the outcome of the AM1 process. A color coded distribution for the cross section of the AM1 part (at $Z = -18.89\ mm$) is also shown.

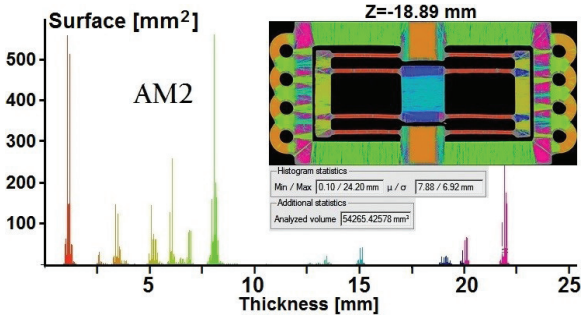

FIGURE 6. Full part's wall thickness distribution for the outcome of the AM2 process.

CT DEFECT ANALYSIS

CT provides defect volume analysis that determines voids within the manufactured parts, their position, their size, volume and morphology. Figures 7 and 8 show the porosity analysis or defect volume distribution for the outcome of the processes AM1 and AM2 respectively.

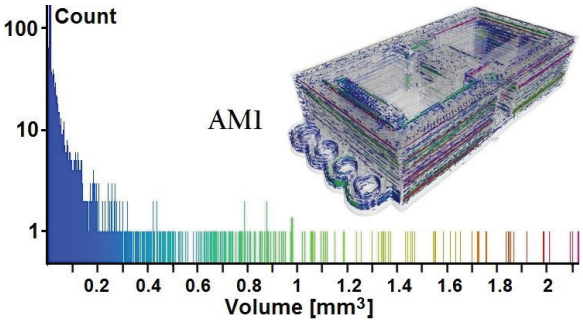

FIGURE 7. Defect volume distribution for the outcome of the AM1 process, voids count in function of their size. A transparent view of the AM1 part depicting the internal defects is shown.

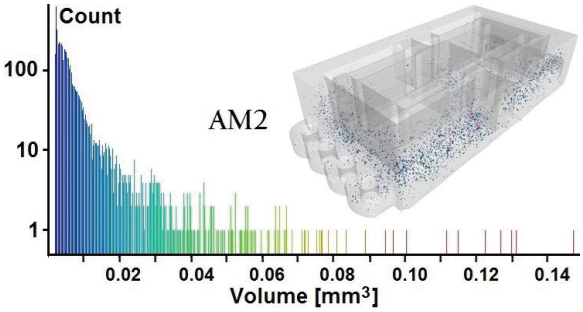

FIGURE 8. Defect volume distribution for the outcome of the AM2 process.

Statistical information for the full defect volume distribution within the whole part for each case (AM1 and AM2) is presented. Particularly, a higher density of porosity for the AM1 part is revealed apparent in contrast to the AM2 part, mainly distributed in planar layers stacked along the Z-axis, which is the same direction along which the manufacturing processes deposit the layers of (ABS) thermoplastic material. Figure 7 shows an accumulation of voids for the AM1 process mostly in the range of 0.002 mm^3 to 0.2 mm^3 volumetric size (0.08 mm to 0.36 mm radius), while for the AM2 process the majority of voids (fewer than for AM1) have a size major dimension of only between 0.002 mm^3 to 0.02 mm^3 (0.08 mm to 0.17 mm radius). These defects (sizes) during the manufacturing processes might be a reflection of the resolution limits of the AM

systems, or inability to produce very thin layers (stacks) of material while building the part. Thus, the printing resolutions of approximately 100 µm for the AM1 process and 0.5 µm for the AM2 process can be associated with larger volumes of voids or air bubbles inside the AM1 part than that of an identical part built by the AM2 process. Because those can affect material properties (elastic modulus), that determine stiffness and damping of the flexures. Moreover, fatigue and long-term reliability issues can be raised due to air-voids (or air bubbles).

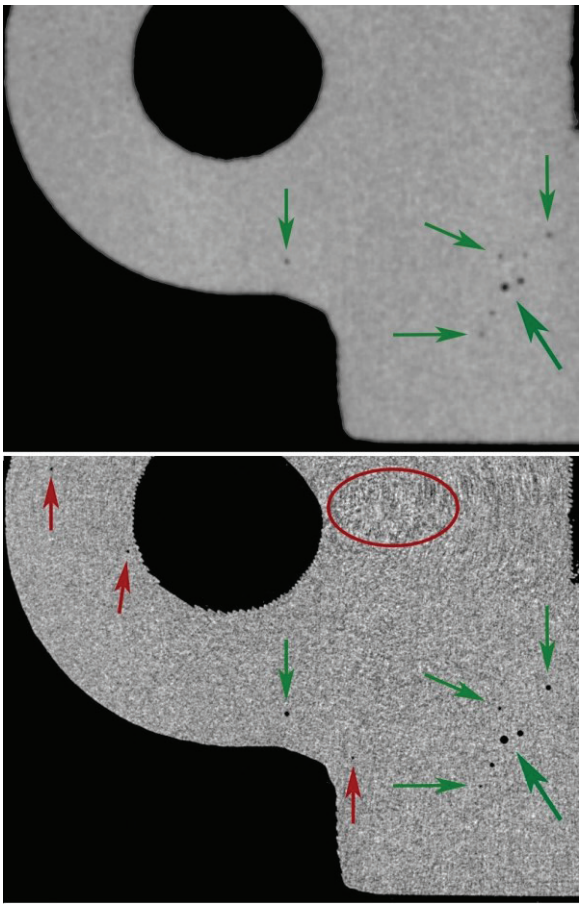

FIGURE 9. Region of interest for the AM2 part highlighting voids. 65 µm (up) and 20 µm (down) CT scan voxel sizes (resolution) were used.

Void detection is limited by the CT scanner resolution, and thus pores with a diameter of the order of one voxel or less cannot be detected or differentiated from noise in the CT image. VGStudio MAX 2.2 actually allows a user defined limit for void detection, which is recommended to be in a minimum size of 2 voxels in diameter to avoid false detection in the noise level of the data. Therefore, a default parameter set to a volume of approximately 8 voxels (=2x2x2) was applied for the AM1 and AM2 parts studied here, which were scanned with a voxel resolution of Vx=65 µm. Voids with volumes in the order of $(0.13\ \text{mm})^3 = 0.002\ \text{mm}^3$ or less cannot be assessed. Figure 9 shows a region of interest for the AM2 part scanned with two different resolutions, 65 µm and 20 µm voxel sizes, and this shows how the 20 µm scan not only makes the holes easier to detect but additional holes were found.

A COMPLEX PART MANUFACTURED BY THE AM2 PROCESS:

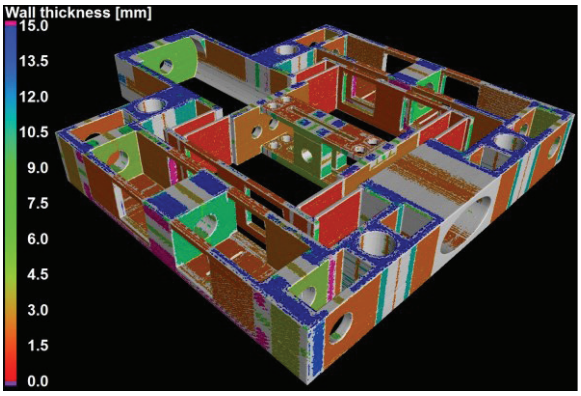

FIGURE 10. Wall thickness distribution for the monolithic double compound-type flexure mechanism manufactured by the AM2 process.

With the information acquired from CT analysis of the AM1 and AM2 parts in the previous section, the AM2 process was selected for manufacturing a complex part called the "monolithic double compound-type flexure mechanism." Figure 10 shows the thickness distribution for the monolithic double compound flexure with most of the walls being approximately 2 mm thick. On the other hand, part-to-CAD comparison for the same part is shown in Figure 11. Again exhibiting tolerances mostly around ± 0.1 mm from the nominal geometry of the CAD model. This is summarized in Figure 12 which also reveals the existence of a substantial portion of the flexures' surfaces outside of the ± 0.1 mm tolerance. Those regions are highlighted in Figure 11 (and Figure 12), with the purple color representing deviations from nominal geometry below the -0.1 mm, and a pink color representing deviations above 0.1 mm.

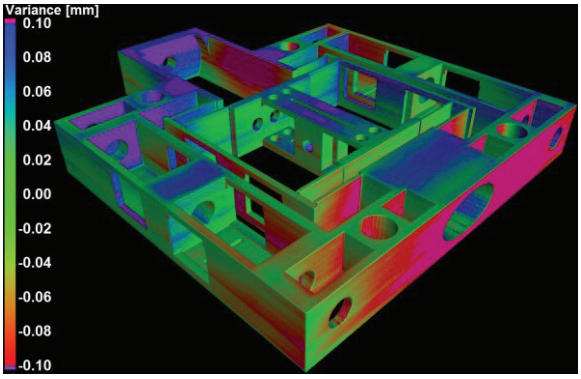

FIGURE 11. Part to CAD comparison for the monolithic double compound-type flexure.

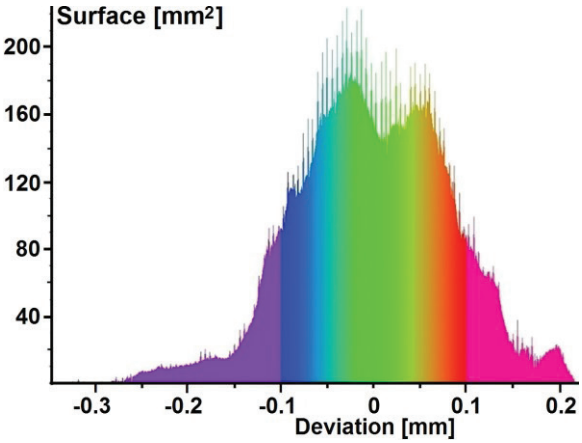

FIGURE 12. Variance distribution for deviations of the CAD model for the monolithic double compound-type flexure mechanism.

Recalling the approximate 1/10th of a voxel size for the uncertainty estimation of dimensional CT metrology [5], since the monolithic double compound flexure was CT scanned with a 91 µm voxel size, an uncertainty of around 9.1 µm for the geometrical evaluations presented here for this part (the monolithic double compound flexure) should be expected. However, this is a rough estimation, and could be an overestimation since the maximum permissible error (MPE) from the CT machine certificate used for the research presented here, is stated as $MPE = (8 + L/100)$ µm with the length L in mm [7]. The approximation $u_m \approx MPE/2$ might be a good estimation of uncertainty coming from the CT machine [8], but this estimation only accounts for uncertainty coming from the repeatability of the measurement instrument during its calibration process. A more thorough uncertainty analysis to include contributions coming from calibration, statistics (repeatability of measurements), systematic errors, and workpiece variations needs to be done. This is beyond the scope of this paper, and references [9, 10, and 11] provide a more detailed analysis of these issues. Still, it is important to note that for the AM tolerances reported here, mostly approximately ± 0.1 mm or more, uncertainties in the reported measurements in the order of 10 µm do not change the conclusions in this paper.

CONCLUSIONS

AM is capable of manufacturing highly complex 3D structures, layer by layer, that can be light and stable. CT provides a quantitative visualization of objects layer by layer as well as in 3D. This makes the CT technology particularly useful to study the outcome of an AM process, not only for inspection or material quality control but also for dimensional metrology. In particular, tolerances can be contrasted between different processes, with non-destructive measurement of the additive manufactured product. There is considerable benefit in measuring the products in the assembled state, not only for results comparison (as in this paper), but also for tracking dimensional changes after assembly of modifications deliberately applied to a single process or to a particular component. The artifacts, AM1 and AM2, presented in this paper could also represent two trials of a part that was evaluated and a modified in an AM process.

From this work, it is evident that residual internal deformations and spatial deformations were detected in the manufacture of flexures with the AM1 process (see Figure 4), and deviations up to -4 mm were detected between measured and nominal dimensions from the CAD model of the flexure (see Figure 2). Improvement in the manufacturing process for the part was observed by using the AM2 process, reaching tolerances down to ± 0.15 mm (see Figure 3). These particular tolerance outcomes might be related to the printing limitations associated with the AM1 and AM2 processes, which in general have a printing resolution of approximately 100 µm and 0.5 µm, respectively. Thus, as might be expected, a larger volume of voids inside the AM1 part (Figure 7) compared to the defect volume distribution for a similar part built by the AM2 process (Figure 8) was detected. However, void detection is limited by the CT scanner resolution, and thus pores with a diameter in the order of one voxel or less could not be detected or differentiated from noise in the CT images presented here. For reference, AM1 and AM2

parts studied here were scanned with a voxel resolution of Vx = 65 µm, while the monolithic double compound flexure was CT scanned with a 91 µm voxel size. The density of defect inclusions inside the AM1 and AM2 parts seems to correlate to the printing limitations associated with the AM1 and AM2 processes, which is also reflected in the respective measurements of part thickness distributions shown in Figure 5 and Figure 6.

With the information gained from this study, and additional research on characterization of polymers fabricated by AM processes [12], the monolithic double compound-type flexure mechanism was manufactured by the AM2 process. An initial characterization of the part by CT is shown in Figures 10 through 12, and in the future, additional dimensional metrology (measurements of size) will be performed on the features of interest in terms of functional performance of the flexure mechanism. Lastly, although a full uncertainty analysis has not been completed for the measurement results presented here, it is important to note that for the AM tolerances reported, mostly around ± 0.1 mm or above, typical CT uncertainties in the order of 10 µm are a factor of ten lower, therefore indicating that these tolerances are predominantly those of the AM process.

ACKNOWLEDGMENTS

The authors would like to express their appreciation to Carl Zeiss Industrial Metrology, LLC, for providing the CT measuring machine, and to Volume Graphics GmbH for providing VGStudio MAX. This study could not have been completed without their collaboration.

REFERENCES

[1] Kruth J. P., Bartcher M., Carmignato S., Schmitt R., De Chiffre L., and Weckenmann A. Computed tomography for dimensional metrology. CIRP Annals, Manufacturing Technology 60 (821-842), 2011.

[2] Villarraga H., Morse E. P., Hocken R. J., and Smith S. T. Dimensional metrology of internal features with X-ray computed tomography. Proc. of ASPE Annual Meeting, Vol 59, 2014.

[3] Benninger R, METROTOM 800 computer tomograph. Inovation Special Metrology 11 (6-7), The Magazine from Carl Zeiss, 2009.

[4] Lettenbauer H, METROTOM – Measure in a new dimension. Inovation Special Metrology 9 ((12-13), Magazine from Carl Zeiss, 2007.

[5] Reinhart C, Industrial computer tomography – A universal inspection tool. 17th World Conference on Nondestructive Testing, Oct 2008, Shanghai, China.

[6] Reinhart C., Poliwoda T, Guenther T., Roemer W., Maass S., and Gosch C. Modern voxel based data and geometry analysis software tools for industrial CT. 16th World Conference on Nondestructive Testing, 2004, Montreal, Canada.

[7] Lettenbauer H., Georgi B., and Weiβ D. Means to verify the accuracy of CT systems for metrology applications (in absence of established international standards). Symposium on Digital Industrial Radiography and Computed Tomography, 2007, Lyon, France.

[8] Gupta S. V. Measurement Uncertainties: Physical Parameters and Calibration of Instruments, 2012, Berlin Heidelberg: Springer-Verlag.

[9] Villarraga H., Thousand J. D., Morse E. P., and Smith S. T. CT measurements and their estimated uncertainty: The significance of temperature and bias determination. 15th International Conference on Metrology and Properties of Engineering Surfaces proceedings, 2015, Charlotte, NC.

[10] Villarraga H., Clark D. O., and Smith S. T. Strategies for coordinate metrology on flexible parts: CMMs vs CT. 15th International Conference on Metrology and Properties of Engineering Surfaces proceedings, 2015, Charlotte, NC.

[11] Villarraga H., Morse E. P., Hocken R. J., and Smith S. T. Dimensional metrology of internal features with X-ray computed tomography. ASPE 2014 Annual Meeting, pp. 684-689, Boston, MA.

[12] Corbett T., Kok T., ChaBum L., Smith S. T., Villarraga H., and Tarbutton J. A. Identification of mechanical and fatigue characteristics of polymers fabricated by additive manufacturing process. ASPE 2014 Topical Meeting, Apr. 13-16, Berkeley, CA.

NEW OPPORTUNITIES FOR PART FIDELITY USING HYBRID AM + CNC

Jason Jones
Hybrid Manufacturing Technologies
Dallas, TX USA

ABSTRACT
To enable the geometry and material freedoms afforded by AM, yet achieve the precision of CNC machining; hybrid combinations of these two machines have st arted to gain traction in the market. Subtractive milling or grinding of metal AM parts can eliminate "stair-step" surface texture effects (inherent in layered manufacturing) and improve dimensional accuracy by more than an order of magnitude. This presentation reviews the technical and cost benefits of hybrid and its complementary nature to conventional processing.

In addition to enabling in----process machining of metal AM parts, hybrid approaches afford further opportunities to improve the fidelity of parts including multi-scale deposition and conformal laser surface treatment. This presentation highlights the drivers and extend ed potential of hybridizing for parts made by directed energy deposition and powder bed fusion. In particular the effects of surface re--melting for parts made from metal powder is shown.

POST-PROCESS MACHINING OF ADDITIVE MANUFACTURED STAINLESS STEEL

Brandon M. Lane, Shawn P. Moylan, and Eric P. Whitenton
Intelligent Systems Division
Engineering Laboratory
National Institute of Standards and Technology[i]
Gaithersburg, Maryland, USA Company or University

INTRODUCTION

Due to the poorer surface finish and geometric accuracy of additive manufactured (AM) parts compared to machined parts, it is inevitable that parts fabricated through AM processes will require post-process machining. This problem was identified early by machine manufacturers that make hybrid additive-subtractive systems. Apart from these complex systems, many AM part designs will require drilling, tapping, and surface finishing to meet their specified geometric tolerances, to satisfy the required functionality or fit in an assembly.

There is already a substantial amount of research attempting to analyze, measure, model, and predict material microstructure and mechanical properties of AM materials [1]. However, the rapid growth of the AM industry and incorporation into the manufacturing landscape ensures the use of post-process or hybrid machining will outpace fundamental research and broad scientific understanding. However, some basic experiments can shed light on the potential challenges and pitfalls of post-process or in-process hybrid machining of AM materials. Machine shop personnel at the National Institute of Standards and Technology (NIST) have anecdotally reported more difficulty in milling, drilling, and tapping AM materials compared to their cast or wrought equivalent. This initiated an exploratory study into the machining characteristics of AM materials.

EXPERIMENT SETUP

AM disk specimens were fabricated in a laser powder bed fusion (PBF) machine from GP1 stainless steel powder (chemically equivalent to 17-4 stainless steel) with standard AM build parameters recommended by the machine manufacturer for this material. These parameters include two contour passes (laser exposures on the periphery of each build layer) before and after the internal areas are exposed: a pre-contour pass and post-contour pass respectively. These contour scans are conducted with a laser beam offset of 0.08 mm, laser power of 80 W, and scan velocity of 700 mm/s.

In conjunction, disks with similar geometry and 4.65 mm thickness were cut from wrought 17-4 stainless steel billet as baseline comparison. The AM disks were built on AISI 1045 steel build plates without support structure (directly fused to the build plates). Both AM disks (still attached to base plate) and baseline disks were put through a stress relief at 650 °C for 1 hour in Argon and allowed to air cool. . AM disks were separated from the build plates via wire electrical discharge machining (EDM), resulting in a thickness of 4.24 mm.

The periphery of the AM disks retained the sintered, powdery texture evident on all laser PBF parts. Both sets of disks were cut on the NIST orthogonal machining test center using the same instrumentation used in previous machining research at NIST [2]. Titanium-alumina-nitride (TiAlN) coated carbide grooving inserts were used to cut the disks. These had nominally 45 µm edge radius, 5° rake angle and 6° clearance angle.

Six total tests were conducted; two on the baseline material and four on the AM material. Table 1 gives the machining conditions for these tests. Further cuts on the baseline material were not pursued after two cuts since forces achieved relatively consistent steady state and were considered exemplary for those cutting conditions. Cuts on the AM disk increased feed-rate after the initial two cuts. Thickness of the disk workpieces were 4.65 mm for the baseline and 4.24 mm for the AM disks. Difference in thickness of the AM and baseline disk is accounted for in the force analysis by reporting force values per disk thickness. At the end of each cut, the tool holds position for 1.5 revolutions to clean up any radial runout in the

disk which occurs if the tool is retracted quickly. Spindle speed was increased in each test from 167 rev/min for Test 1 to 171 rev/min for Test 6 to maintain constant surface speed while the disk diameter is reduced by cutting.

Table 1. Test order and machining parameters. All tests used the same tool.

Workpiece		Machine Input		
Test Name	Material	Surface Speed (m/min)	Feed Rate (mm/rev)	Cut Surf. Distance (m)
Test 1	Wrought	60.00	0.070	1.500
Test 2	Wrought	60.00	0.070	1.500
Test 3	AM	60.00	0.070	1.500
Test 4	AM	60.00	0.070	1.500
Test 5	AM	60.00	0.140	1.500
Test 6	AM	60.00	0.280	1.500

A high speed visible light camera with macro lens was positioned normal to the tool rake face and captured video of chip formation at 4000 frames/s (a period of 0.25 ms/frame). In addition, a 3 axis dynamometer captured machining forces in the cutting, normal, and side directions at 1 MHz. Figure 1 shows the placement of the tool holder, camera, and workpiece in the machining test center. The AM disk was positioned on the spindle such that the EDM surface, which coincides with the bottom of the build during laser PBF fabrication, faces the front of the machine (viewed by the operator), and faces the right-hand side in the high speed videos.

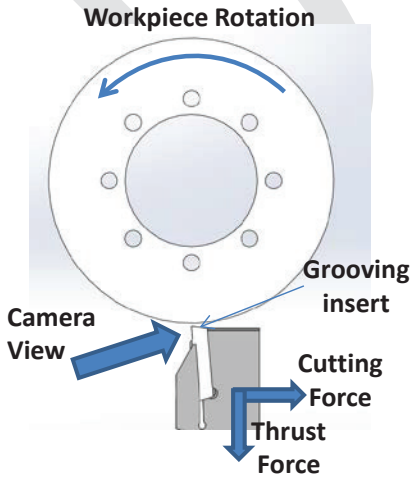

Figure 1. Schematic of workpiece rotation, tool and camera position. AM build direction is into the screen.

FORCE RESULTS

Figure 2 gives three example force plots from three tests. These show 1 MHz force data downsampled to 1 kHz. Mean side tool forces directed out of the machining plane were below < 2.5 N/mm and are not visible in Figure 2.

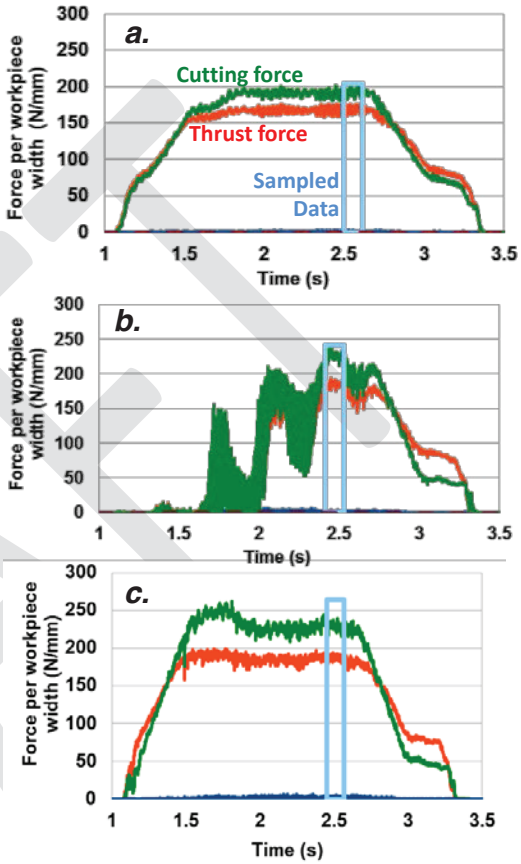

Figure 2. a. Test 2 (wrought material) showed relatively stable cutting which achieved steady state after one rotation. b. Test 3 (first cut on AM disk) showed noisy unsteady forces resulting from rough surface and radial runout. c. Test 4 (second cut on AM disk) showed stable cutting similar to wrought material, but noticeably higher cutting and thrust forces.

Table 2 gives summary statistics of the collected forces for the 'Sampled Data' regions shown in Figure 2. 'Mean Tool Forces' are defined as the mean of the 1 kHz data downsampled taken over 0.3 disk revolutions at a time subjectively chosen to be near a 'steady state' forces. The standard deviation was calculated for every 1 000 sample bin from the 1 MHz data, and the mean of this standard deviation data is defined in the 'Vibration' columns in Table 2. This gives a measure of force vibrations above 1 kHz.

Table 2. Summary of force statistics taken from 'sampled data region' consisting of 0.3 disk revolutions. Test 1 forces were not acquired due to faulty equipment triggering.

	Mean Tool Forces			Vibration		
Test	1 kHz downsampled			Mean of 1000-pt. std. dev.		
Name	Side	Thrust	Cutting	Side	Thrust	Cutting
	(N/mm)	(N/mm)	(N/mm)	(N/mm)	(N/mm)	(N/mm)
Test 1	-	-	-	-	-	-
Test 2	0.56	168.44	191.72	8.42	10.03	14.85
Test 3	1.02	183.57	225.68	13.72	20.63	27.09
Test 4	1.31	187.73	229.01	23.32	25.38	36.10
Test 5	2.42	221.73	371.97	26.40	39.51	65.56
Test 6	1.87	255.06	589.92	45.92	60.95	147.3

For the same cutting conditions, the per width thrust and per width cutting forces were approximately 11% and 19% higher, respectively for AM materials in Test 4 vs. Test 2. AM disks cause much more high frequency noise. As seen in Figure 2b, the first cut on the AM disk (Test 3) did not achieve a steady state, therefore the force statistics are not comparable to the wrought material.

HIGH SPEED VIDEO OBSERVATIONS

Tests 1 and 2 on the wrought material did not show any notable phenomena. Continuous chips formed immediately after the tool contacted the workpiece, as shown in Figure 3. Smoke can be seen stemming from the cutting region, likely due to heating of residual machining oils on the tool or workpiece. One of the fiber illumination sources was placed behind the tool towards the right in the movie frames, also seen in Figure 3. Videos for Test 4 through Test 6 on the AM material did not show any significant observations either. Chips were continuous from the beginning to end of cutting. Segmentation on the back of the chips was clearly visible in Test 5 and 6, with the segments being larger for Test 6. These segments, which increased from test 4 to 6 along with the feed rate, typically coincide with adiabatic shear banding, though also depend on cutting speed, tool rake angle, and coolant/lubrication [3].

Table 3 outlines the timing of observable phenomena of interest seen in Test 3, which was the first cut on the AM material. Chip formation on this material started with powdery debris and dislocated chips; transition into continuous chips which curled sharply to the right of the frame with visible, periodic dark striations on the back of the chip; then transitioned into normal chip curl.

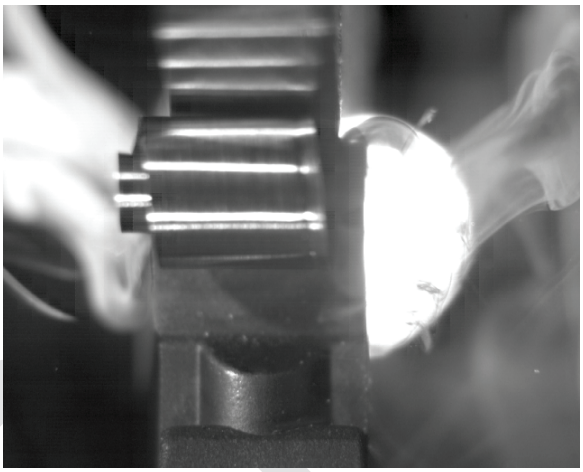

Figure 3. Test 1 showed continuous chips which curled nominally in the orthogonal cutting plane.

Table 3. Phenomena observed in Test 3 high speed video and their relative time of occurrences.

Frame	Time	Spindle Revs	Total Feed	Observations
	(ms)	(revs)	(mm)	
1400	0	0	0	Tool contacts workpiece.
-	-	-	-	Chips are powdery and dislocated.
2784	346.0	0.97	0.068	Continuous chip formation starts. Chips show tight curl with dark striations.
-	-	-	-	Continuous chips with striations
5430	1007.5	2.84	0.199	Striations disappear. Chip curl is less severe.
6522	1280.5	3.61	0.252	Tool stops feeding into workpiece.
-	-	-	-	Chip becomes thinner as effective depth of cut is reduced.
7662	1565.5	4.41	0.309	Chip formation stops

Variation in chip curl

Normally, during orthogonal cutting of wrought materials, chip curl occurs in the same plane as the cutting direction and workpiece rotation, as was observed in Tests 1 and 2 and shown in Figure 3. However, after continuous chips started forming in Test 3, these chips curled sharply to the right as seen in Figure 4b. After further cutting, the sideways chip curl subsided.

In laser PBF and other laser-based AM processes, residual stresses occur in the part after it is formed and cooled. Some stresses may still exist even after a stress relief heat treat cycle, as was done with the AM parts in this study. These residual stresses depend on the material, part geometry, laser scan strategy, and

multiple other factors. Generally, the top of the AM build forms tensile stresses, while the interior or bottom are compressive [4,5]. With regard to the sideways chip curl seen in Figure 4b, this may be a result of the release of tensile stresses on the left side of the chip, which coincides with the top of the AM build. It is theorized that plastic deformation of the chip causes the residual negative strain to normalize, which effectively causes expansion which pushes the chip to the side. As the tool cuts further and enters the interior of the part, the residual stresses may be lower, therefore resulting in reduced side bending of the chip seen in Figure 4c and in later Tests 5 and 6.

Striations on the back of the chip

As mentioned in the observations in Table 3 and evident in Figure 4b, periodically formed dark striations could be seen on the back of the chip in Test 3. Prior to the machining tests, the inner diameter of the AM workpiece disk was lathe turned in order to fit on the machining center spindle. These striations were also evident on the resulting interior surface, as shown in Figure 5a-b. The spacing of the striations (approximately 5 mm) coincided with the spacing of triangular faces formed when the solid part file is converted to a stereo-lithography (STL) file. This also results in slightly visible faceting on the periphery of the uncut AM disk, which causes high and low spots on the surface, and varies the effective depth of cut. However, striations were apparent over more than one disk revolution, and appeared up to 0.20 mm total feed. This is much larger than the effective high/low spots on the periphery of disk with 5 mm facets, and indicates that the striation features are formed or exist further into the interior of the disk at a distance affected by the contour exposure during the laser PBF build.

CONCLUSIONS

These machining tests were originally designed to make subjective observations, and guide development of future, more scientifically rigorous tests. Based on these results, two phenomena are of further interest: chip curl due to surface residual stresses and surface features due to part file tessellation. The following conclusions are made:

- Mean cutting and thrust forces and high frequency vibration were higher for the AM material.
- Chip curl on the AM material is likely affected by residual stress. The chip is pushed away from regions of tensile stress released after plastic deformation.
- Tesselated surfaces of STL part file is a likely cause of the observed chip surface striations. However, the striations appear at cut depths deeper than the effective high/low spots caused by faceted perimeter of the disk.

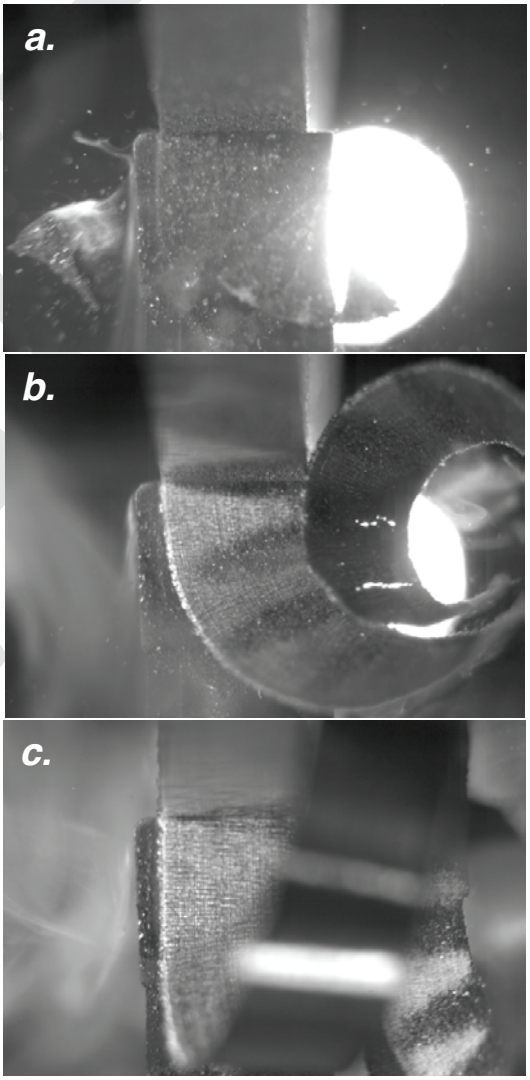

Figure 4. a. Test 3 frame 1920 shows powdery, dislocated chips and debris. b. Frame 3176 shows continuous chips which curl sharply to the right and have dark striations on the back. c. Frame 5634 shows continuous chips with less severe chip curl. The shiny, new cut surface is closer to the camera and out of focus. Striations can be seen further to the right on the previously formed chip surface.

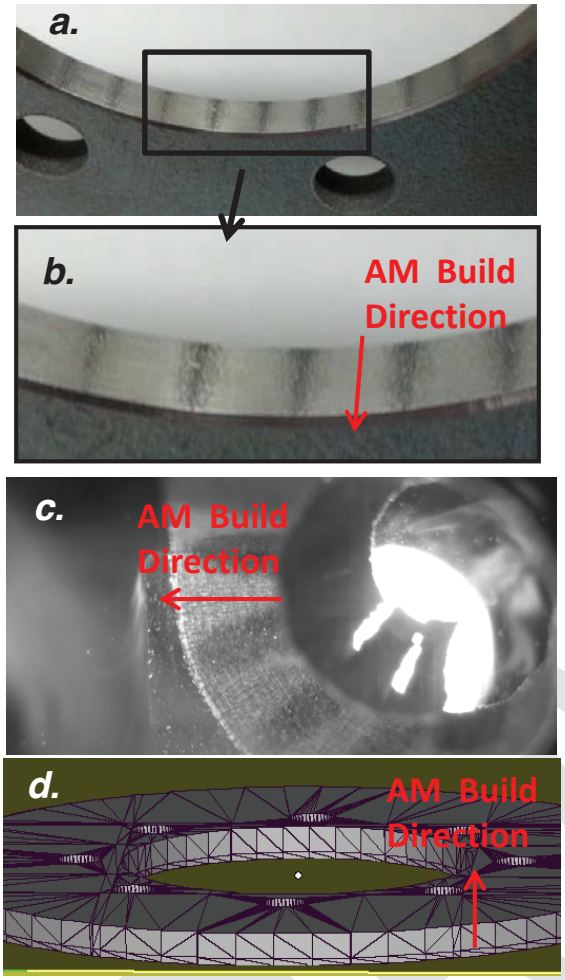

Figure 5. a. Lathe turned inner diameter of the workpiece showing light/dark striations. b. Enhanced view of striations on the workpiece. c. Striations appearing on the chip surface in high speed video (Test 3, frame 3154) and the relation to the build direction. d. STEP file of disk showing tesselated facets on the inner and outer periphery.

FUTURE WORK

Since near net-shape parts are possible with AM, it is presumed that only relatively shallow or finish machining would be of interest and the main objective being to optimize surface form and finish. It is presumed that manufacturers will not push tool life requirements for AM part machining and will absorb the added cost of potentially switching tools prematurely. This is due to the fact that AM parts have already accumulated high value based on the design and AM build times prior to any post-process machining, and tool cost is relatively low compared to the risk of scrapping an AM built part. However, tool breakage could be a potentially large cost factor of machined AM parts if they must be scrapped. Therefore, continued research on machining of AM materials should detail tool wear and tool forces. Apart from this, further machining experiments on AM materials conducted at NIST will focus on two phenomena based on the results of this preliminary study.

Chip formation vs. laser PBF contour scanning strategy

As previously mentioned, residual stresses in laser PBF parts are affected by multiple factors. Two factors; laser scan strategy and heat treatment, are candidate variables that manufacturers may choose to enable better conditions for post-process machining. It was observed in this study that the stress-affected chip curl mostly occurs closer to the part surface at depths primarily created during the pre- and post-contour scanning during the AM build. Further studies will attempt to observe how the chip curl is affected by different contour scan strategies. If residual stress release is a dominant factor in chip curl, then this may have an ultimate effect on surface form as well. Varying stress relief heat treat cycle, or observing the chip characteristics on fully annealed samples will also galvanize the idea that chip curl is largely affected by chip curl, and guide manufacturers towards an optimized heat treatment.

In addition, multiple methods and standards exist for stress measurement by material removal [4]. New methods for observing and quantifying residual stress by machining may be possible.

Surface finish vs. STL surface tessellation

Though surface finish of the disks were not measured in this preliminary study, the striations seen on the chip and machined surface in Figure 5 form an obvious periodic change in surface finish. Since one purpose machining AM parts is to improve surface finish, mitigating these striations is important. Varying the STEP file tessellation on machined parts may further elucidate the cause of the striations, and surface finish measurement will quantify their effect on overall surface finish. Another important factor is how deep into the workpiece material the striations appear and affect the surface, that is, how much material must be removed to negate their effect. Smaller feeds than those used in this study may better resolve the total cutting

depth at which the striations disappear. Results from this study will create part design rules if post-process machining for improved surface finish is necessary.

REFERENCES

[1] Mani M, Lane B, Alkan MA, Feng S, Moylan S, Fesperman R. Measurement science needs for real-time control of additive manufacturing powder bed fusion processes NISTIR 8036. Gaithersburg, MD: National Institute of Standards and Technology; 2015.

[2] Madhavan V, Lipczynski G, Lane B, Whitenton E. Fiber orientation angle effects in machining of unidirectional CFRP laminated composites. J Manuf Process n.d.;In Press - Corrected Proof. doi:10.1016/j.jmapro.2014.06.001.

[3] Deshayes L, Mabrouki T, Ivester R, Rigal J-F. Serrated chip morphology and comparison with finite element simulations. Proc. IMECE04, Anaheim, CA: American Society of Mechanical Engineers; 2004, p. 815–24.

[4] Kruth J-P, Deckers J, Yasa E, Wauthlé R. Assessing and comparing influencing factors of residual stresses in selective laser melting using a novel analysis method. Proc Inst Mech Eng Part B J Eng Manuf 2012;226:980–91. doi:10.1177/0954405412437085.

[5] Gnäupel-Herold T, Slotwinski J, Moylan S. Neutron measurements of stresses in a test artifact produced by laser-based additive manufacturing. AIP Conf. Proc., vol. 1581, Baltimore, MD: AIP Publishing; 2014, p. 1205–12.

[i] Official contribution of the National Institute of Standards and Technology (NIST); not subject to copyright in the United States. The full descriptions of the procedures used in this paper require the identification of certain commercial products. The inclusion of such information should in no way be construed as indicating that such products are endorsed by NIST or are recommended by NIST or that they are necessarily the best materials, instruments, software or suppliers for the purposes described.

CHALLENGES IN TOLERANCE TRANSFER FOR ADDITIVE MANUFACTURING

Gaurav Ameta[1], Shawn Moylan[2], Paul Witherell[2] and Robert Lipman[2]
[1]School of Mechanical and Materials Engineering,
Washington State University
Pullman, WA, USA
[2]National Institute of Standards and Technology
Gaithersburg, MD, USA

1. INTRODUCTION

For proper functioning of a product, specification of geometry, material, tolerances, surface finish and any other additional requirements are needed from a designer. The specifications necessary for such communication have well established standards, for example, the ISO 10303 [1,2] series of standards govern geometry specification while the ISO 1101 [3] and ASME Y14.5 [4] series of standards govern tolerance specification. Proper functioning of an "as designed" product relies on manufacturing the product within the specification, including allowable variations (tolerances).

Tolerance specification is the specification of the type and value of tolerances based on available Geometric Dimensioning and Tolerancing (GD&T) standards (e.g., ASME Y14.5 [4] or ISO 1101 [3]). GD&T is a language to communicate acceptable 3D variations of geometric elements in a part from design to manufacturing and inspection. GD&T is based on mathematical representations of the variation of geometric elements and manufacturing knowledgebases [5,6]. Different tolerancing activities that are part of the production process are shown in Figure *1*1 (adopted from [7]).

1.1. Tolerancing activities

Different tolerancing activities are undertaken at different stages of the production process to ensure that (i) appropriate tolerances are specified by the designer and (ii) the specifications are followed by the manufacturer. These activities include tolerance analysis, tolerance synthesis, tolerance specification, tolerance transfer, and tolerance evaluation.

To ensure functionality of a product after manufacturing, the designer must arrive at a satisfactory set of tolerances that will preserve the design intent to match manufacturing capabilities. A designer can arrive at a satisfactory set of tolerances by using one of two approaches: tolerance analysis or tolerance synthesis [8]. With *tolerance analysis*, the designer estimates values for individual part tolerances and then uses a software analysis tool to determine the resultant range of variations for a critical dimension or function of the assembly. With *tolerance synthesis*, often called tolerance allocation, the desired control at target features (e.g., a maximum clearance to ensure proper lubrication or control of noise) is chosen. Then, the tolerances are generated from a mathematically based tolerance model, also in an automated way, to meet that choice. The final *tolerance specification* to each feature is a tradeoff between tight tolerances, which usually result in better performance of the assembly, and loose tolerances, which result in lower cost to manufacture the individual parts but also in a lower probability of proper assembly and/or function. Arriving at satisfactory set of tolerances using tolerance analysis is an iterative process. With tolerance synthesis, often optimization techniques are applied using functionality related heuristics.

The manufacturing and inspection stages of the product life cycle very often use different datum features than those desirable for design and function. Therefore, tolerances suitable for design function must be transferred, i.e., related, to tolerances on different dimensions with different datum features in such a manner that the product's desired function is not compromised. This transformation of tolerances is called ***tolerance transfer*** [9–12].

Tolerance evaluation deals with the analysis of the data obtained from dimensional measurements and conformance of the part with the specified design tolerances. As is evident from the discussion presented. Each tolerance

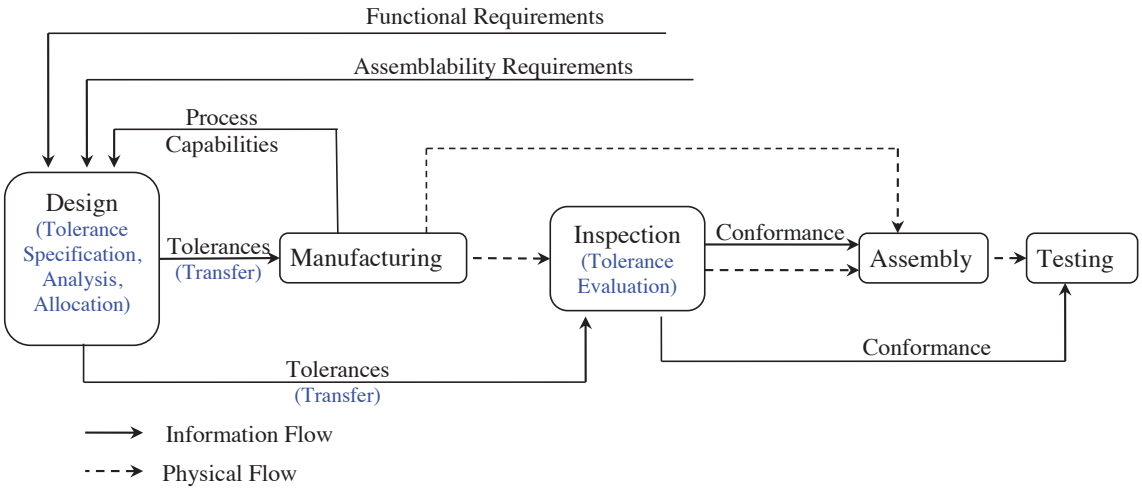

Figure 1: Modified figure from [7]*, showing different tolerancing activities in product life cycle.*

activity is conducted in a particular phase of the production process. Tolerance analysis or synthesis leading to tolerance specification occurs in the design stage. Tolerance transfer and subsequent analysis is conducted at the beginning of the manufacturing stage. Tolerance evaluation (if needed tolerance transfer too) is conducted in the inspection stage. The focus of this paper is tolerance transfer that is conducted at the beginning of the manufacturing stage and will be detailed in the next section.

1.2. Tolerance transfer

From the design point of view, datum features are used to imply design intent of particular function of the part or sequence of assembly of components in a product. Each feature in a part could potentially have different datum reference based on the design intent. In traditional manufacturing, datum references are used to identify positions of machining features. In order to save time and cost, the number of datum references used in creating features are reduced in manufacturing. As the datum references are changed, validity of the tolerance specification and design intent has to be verified. As these datum features are changed, manufacturer might conduct tolerance analysis to verify the design intent and validity of the transferred tolerances.

A simple example is presented in Figure 2 to illustrate tolerance transfer. Figure 2(a) indicates designer's intent, which is to control the location of surfaces C and B with respect to the surface A. The dimensions l_1 and l_2 have tolerances t_1 and t_2, respectively.
As the manufacturer changes the datum features from surface A to surface B, the location of surface C is now accomplished using dimension l_3. The tolerance t_3 on l_3 has to be computed in order to maintain the tolerance on l_2 that the designer required. From the simple chain of dimension in Figure 2(b), it is evident that $l_2 = l_1 - l_3$ and therefore $t_2 = t_1 + t_3$. This will lead to the computation of $t_3 = t_2 - t_1$. The result of changing the datum reference is that the manufacturer has to control the dimension with might tighter tolerance.

The above example demonstrates simple tolerance transfer. The purpose of this paper is to highlight the challenges in applying tolerance transfer to additive manufacturing (AM). The next section will present AM and tolerance related developments.

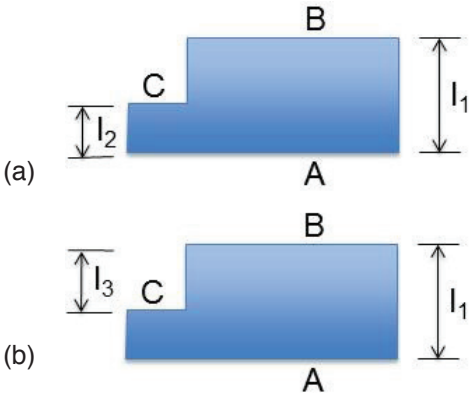

Figure 2: Simple part with linear dimension

2. ADDITIVE MANUFACTURING

Additive Manufacturing (AM) produces parts by joining materials in layer-by-layer fashion. There are many different types of AM processes. These are well classified and studied in the literature [13–15]. AM processes are capable of producing complex free-form surfaces and many different kinds of structural lattices using a large variety of materials, including plastics, metals, ceramics and biomaterials.

As in traditional manufacturing processes, tolerance analysis or synthesis leading to tolerance specification will be utilized in AM too. Tolerance transfer will be needed to economically produce parts with less setups and less post processing. Tolerance evaluation is needed to ensure that parts produced meet the designer's requirements.

Although, all the tolerancing activities will be useful in AM, they need to be adopted to the novelties that AM technology presents. For e.g. in tolerance specification, current GD&T standards do not have the right set of mechanisms to control the variations in geometric features that are feasible with AM. The need for new specification tools in tolerancing standards have been presented in [16]. These can be classified as (a) AM-driven specification needs and (b) specification needs highlighted by the versatility of AM processes. AM-driven specification needs include build direction, layer thickness, support structure related specification, and scan/track direction. Specification needs highlighted by the versatility of AM processes include, region-based tolerances for complex free-form surfaces, tolerancing internal functional features, tolerancing lattice and infills.

AM not only creates additional tolerance specification needs but also impacts how tolerance transfer is conducted. The purpose of this paper is to highlight these challenges in tolerances transfer. The next section will demonstrate a comparison of tolerance transfer activities between traditional and additive manufacturing.

3. TOLERANCE TRANSFER COMPARISON

In order to demonstrate tolerance transfer, the specification shown in *Figure 3* will be utilized. The specification shows a part with planar datum feature A, hole datum feature B, a pattern hole datum feature C and a side profile of the part. The datum feature B is toleranced with respect to datum feature A. The datum feature C is toleranced with respect to datum features A and B. The side profile is toleranced with respect to datum feature C. Specification to datum feature B and C also includes size tolerances besides position tolerances.

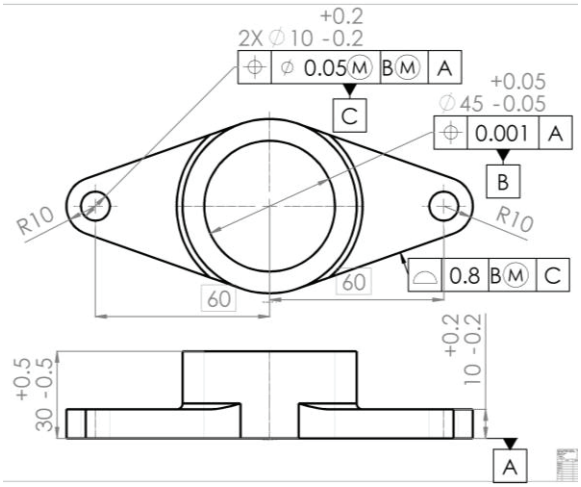

Figure 3: Part with GD&T specification to demonstrate the tolerance transfer.

3.1 Tolerance transfer in traditional manufacturing

Figure 4 and to create the side profile. Therefore, to create the side profile in process plan 1, the part needs to be mounted upside down with respect to hole

Table 1 show two potential process plan to machine the part from Figure 3. In order to avoid incurring additional costs of setups and related time loss in machining the part with datum feature A and center hole B, new and convenient datum features are generated in the two process plans shown in Figure 4. As is evident, both these plans do not conform to the design intent of controlling the side holes C with respect to the center hole B.

A rectangular stock larger than the dimensions of the part will be chosen to produce the part shown in Figure 3. Figure 4(a), step 1 shows the rectangular block machined close to the max dimensions of the part. Step 1 creates additional datum features labelled D, E and F that will be utilized in the subsequent steps. In process plan 1(Figure 4(a)), datum plane A will be created in Step 1. In the process plan 2 (Figure 4(b)), additional datum plane G is created in Step 1. The datum plane G provides for additional material to hold the part in the machine. This additional material will aid in machining the side profile in a later step 4. Figure 4(a) step 2 shows the rectangular block with machined holes, either from datum plane A or G (Figure 4(b) step 2). Figure 4(a), step 3 shows the machined top plane for holes B and C with respect to datum A or G (Figure 4(b)). In Figure 4(a), process plan 1, the part is currently secured with planes E and F that will be machined out as the side profile is created. Therefore, the part needs to be secured with another datum feature in order

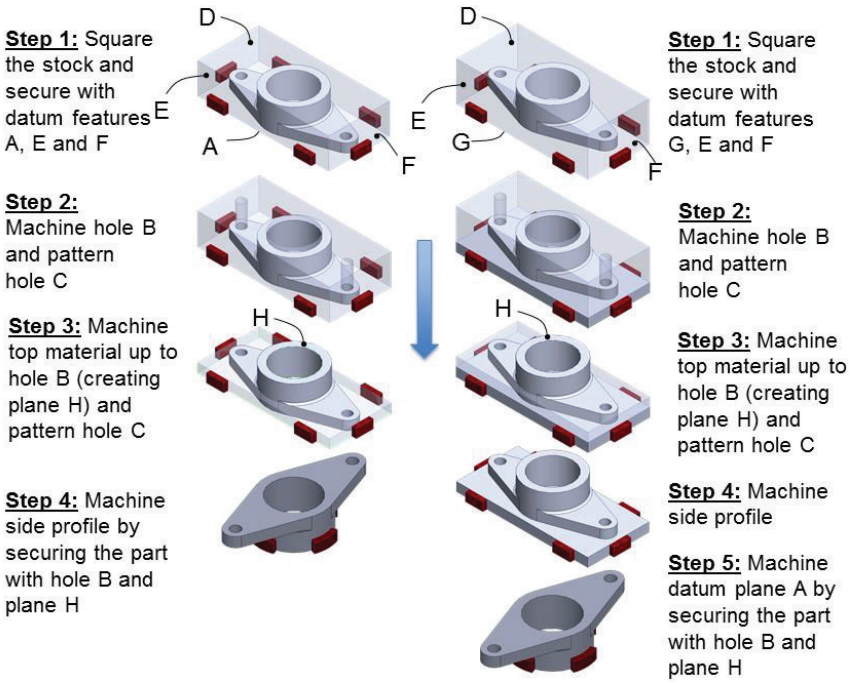

(a) Process Plan 1 (b) Process Plan 2

Figure 4: Steps and additional datum feature in a Process plan for machining the part shown in Figure 3.

to create the side profile. Therefore, to create the side profile in process plan 1, the part needs to be mounted upside down with respect to hole B and the top plane of hole B (labelled as datum plane H). In process plan 2, the side profile can be machined as is and then the part is inverted to create datum plane A (step 5, Figure 4(b)). As this process plan is created with modified datum features, new tolerances will be computed than the ones specified in *Figure 3*. The computation of tolerance values is similar to the example shown in section 1.2. These steps with corresponding tolerances are also shown in *Table 1*.

Table 1: Process plan options showing different datum features and tolerances than those specified in Figure 3.

Feature	Datum feature	Tolerance (mm)
Process Plan 1		
Datum plane A	D	0.0001
Center Hole B	A,E,F	0.025
Side Holes C	A,E,F	0.025
Top Plane of B	A, E, F	+/- 0.5
Top Plane of Side holes C	A, E, F	+/- 0.2
Side Profile	B, C	0.8
Process Plan 2		
Plane G	D	0.0001
Center Hole B	G, E, F	0.025
Side Holes C	G, E, F	0.025
Top Plane of B	G, E, F	+/- 0.25
Top Plane of Side holes C	G, E, F	+/- 0.1
Side Profile	G	0.8
Datum A	Top Plane of B	+/- 0.25

Both the process plans still require two setups to create the datum plane A and the side profile C. The tolerance values are modified so that the final variations in the worst-case would still meet the tolerance specified by the designer. For example, center hole B and side holes C are created with tolerances 0.025mm from datum features A, E and F. This is done so that in the worst case, the tolerance between center hole B and sides holes C remains 0.05mm as specified.

3.2 Tolerance transfer in AM

When the part shown in *Figure 3* is to be manufactured using additive manufacturing, first of all a build direction will be chosen. This build direction will then determine the primary datum.

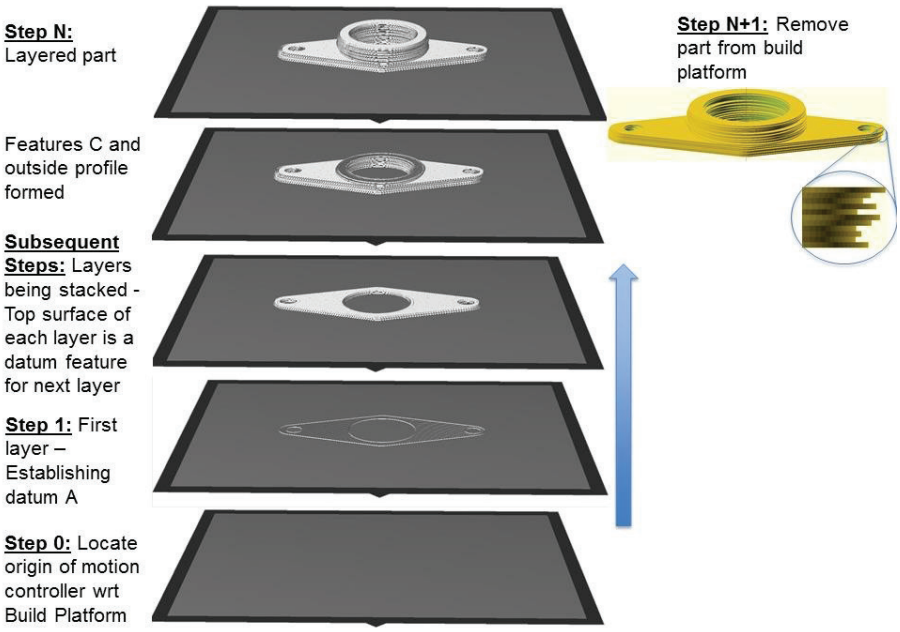

Figure 5: Process plan for producing part shown in Figure 3 in AM

In this case because of the planar nature and lateral size of datum plane A, build direction is chosen perpendicular to datum plane A. This choice of build direction and datum plane A leads the plan shown in *Figure 5*. At step 0, an origin and a coordinate system is established with respect to the motion controller in the AM process. Steps 1 through N will build part in a layer-by-layer fashion. In the end, the part is removed from the build platform and inspected to further processing. In certain situations, there might be support structures that needs to be removed followed by machining or abrasive process to finish the part.

In the build direction, the tolerances in *Figure 3* are 1mm for the height of datum hole B and 0.4 mm for the height of datum holes C. In the AM process, the number of layers to the top plane of datum hole B, are 81. Then, the required tolerance on the height of each layer can be computed as 1/81 = 0.01234mm (assuming all the layers have same thickness).

In the lateral direction, in each layer, location of holes will be independently controlled with respect to the coordinate system established with the motion controller. Assuming that the motion controller's accuracy for a particular AM process is given as 0.03 mm in the lateral direction. The location error for a layer of datum hole B will be 0.03mm. The location error for a layer of hole C will be 0.03mm. In the worst-case scenario, the variation between datum hole B hole C can be 0.03+0.03 = 0.06mm. This variation will be greater than the specified tolerance (0.05) between holes C and datum hole B, when the size of holes C and datum hole B are 9.8mm and 44.95mm, respectively.

Furthermore, as each layer can be produced offset with respect to the previous layer, the variation in form, orientation and position of the holes will be much greater. This can be rectified in sub-processing by enlarging the datum hole B and datum hole C. This is because the material modifier specified allows for greater tolerances (upto 1.4mm) when the holes are made larger (datum hole B at 45.05mm and holes C at 10.02mm).

4. CHALLENGES IN TOLERANCE TRANSFER FOR AM

There are many challenges related to tolerance transfer for AM. A few of them will be briefly discussed in this section.

As is evident from the example in section 3.2, the selection of the *build direction* also effects the selection of the primary datum feature for the process plan. Furthermore, based on the geometry, material and the AM process, special structures might be needed, (called *support structures*) to be able to produce the part layer by layer. These support structures would require additional post-processing to remove them and to finish the surface to the specification. The post-processing steps, when removing material, would

require attention when choosing layer thickness in the AM processes.

In many AM processes, parts are built hollow with internal structures to provide necessary strength while minimizing the weight. Parts built in this manner usually have a certain number of shells (outer surface profile before internal structure and hollow volume starts). Such, parts would require special attend when needed additional machining. as the additional machining would remove these shells in order to meet the tolerance requirement but reducing the structural strength.

As-built assemblies in AM will have a single datum reference for all the parts in the assembly. This would require tolerance transfer to change datum features and ensure that the AM system capability will meet the computed and required tolerances.

Furthermore, as-built assemblies are made with AM processes for assemblies that are in motion (**Error! Reference source not found.**). Usually these assemblies have large clearances between moving components. These are typically in the range of 0.15mm or more. In these assemblies, due to large clearances, greater rattle, wear, fatigue leading to early part failure might be possible.

5. SUMMARY

This paper introduced the notion of tolerance transfer in process planning. A comparison of tolerance transfer for a part produced using traditional and additive manufacturing was presented. The comparison highlighted several challenges related to tolerance transfer in AM processes. When performing tolerance transfer, a process planner needs to consider (a) design intent, (b) build direction (c) process variation and (d) datum references.

Disclaimer: *Any mention of commercial products, software or websites is for information only; it does not imply recommendation or endorsement by NIST.*

REFERENCES

[1] Kemmerer, S. J., 1999, STEP: the grand experience, US Department of Commerce, Technology Administration, National Institute of Standards and Technology.

[2] ISO, S. A. H., 2006, STEP Application Handbook, North Carolina, SC: SCRA.

[3] ISO 1101:2012 - Geometrical product specifications (GPS) -- Geometrical tolerancing -- Tolerances of form, orientation, location and run-out, ISO.

[4] ASME Y14.5-2009: Dimensioning and Tolerancing, ASME, New York, NY.

[5] Srinivasan, V., 1999, "A geometrical product specification language based on a classification of symmetry groups," Comput.-Aided Des., **31**(11), pp. 659–668.

[6] Walker, R. K., and Srinivasan, V., 1994, "Creation and evolution of the ASME Y14. 5.1 M standard," Manuf. Rev., **7**(1), pp. 16–23.

[7] Hong, Y. S., and Chang, T. C., 2002, "A comprehensive review of tolerancing research," Int. J. Prod. Res., **40**(11), pp. 2425–2459.

[8] Zhang, B. C., 1992, "Geometric modeling of dimensioning and tolerancing," Arizona State University.

[9] Desrochers, A., 2003, "A CAD/CAM representation model applied to tolerance transfer methods," J. Mech. Des., **125**, p. 14.

[10] Desrochers, A., and Verheul, S., 1999, "A three dimensional tolerance transfer methodology," Global Consistency of Tolerances, Springer, pp. 83–92.

[11] Xi, M., Lehtihet, E. A., and Cavalier, T. M., 2001, "A Mathematical Optimization Approach to a Subset of Location Tolerance Transfer Problems," J. Comput. Inf. Sci. Eng., **1**(2), pp. 180–185.

[12] Jiang, K., Davidson, J. K., Liu, J., and Shah, J. J., "Using tolerance maps to validate machining tolerances for transfer of cylindrical datum in manufacturing process," Int. J. Adv. Manuf. Technol., pp. 1–14.

[13] Williams, C. B., Mistree, F., and Rosen, D. W., 2011, "A functional classification framework for the conceptual design of additive manufacturing technologies," J. Mech. Des., **133**, p. 121002.

[14] Gibson, I., Rosen, D. W., and Stucker, B., 2010, Additive manufacturing technologies, Springer.

[15] Standard, A., "F2792. 2012. Standard Terminology for Additive Manufacturing Technologies," ASTM F2792-10e1.

[16] Ameta, G., Witherell, P., Moylan, S., and Lipman, R., 2015, "Tolerance Specification and Related Issues for Additively Manufactured Products," ASME 2015 International Design Engineering Technical Conferences & Computers and Information in Engineering Conference, ASME, Boston, MA.

[17] Alexander, P., Allen, S., and Dutta, D., 1998, "Part orientation and build cost determination in layered manufacturing," Comput.-Aided Des., **30**(5), pp. 343–356.

[18] Cheng, W., Fuh, J. Y. H., Nee, A. Y. C., Wong, Y. S., Loh, H. T., and Miyazawa, T., 1995, "Multi-objective optimization of part-building orientation in stereolithography," Rapid Prototyp. J., **1**(4), pp. 12–23.

[19] Wodziak, J. R., Fadel, G. M., and Kirschman, C., 1994, "A genetic algorithm for optimizing multiple part placement to reduce build time," Proceedings of the Fifth International Conference on Rapid Prototyping, University of Dayton Dayton, OH, pp. 201–210.

Laser polishing of laser additive manufactured surfaces made from Inconel 718 and ASTM F75

Ingo Ross[1], Judith Kumstel[1], Sebastian Bremen[1], Edgar Willenborg[1]
[1]Additive Manufacturing and Functional Layers
Fraunhofer Institute for Laser Technology ILT
Aachen, Germany.

INTRODUCTION

The additive manufacturing technologies Laser Metal Deposition (LMD) and Selective Laser Melting (SLM) offer almost unlimited freedom in design for the production of complex shaped, customized parts made from series-identical materials. In the light of increasing resource scarcity these technologies can play a key role in the development of new economic and ecologic solutions for innovative products optimized for weight and function. Due to the layer-by-layer build-up strategy with powder material, LMD and SLM parts usually show a, compared to machined surfaces, high roughness of Ra = 10-40 μm. This is a critical challenge for the industrial implementation of Laser Additive Manufactured (LAM) parts. Currently, parts are often built in near net shape technique and are subsequently finished by time-consuming machining, grinding and polishing operations. Conventional polishing processes are based on mechanical or chemical abrasion, e. g. manual polishing, slide grinding, lapping and electrolytic polishing. These processes often consist of several operations with multiple cleaning steps and can exhibit several drawbacks, e. g. regarding accessibility of complex shaped parts, lack of shape retention especially at function-relevant edges, processing speed or health risks for the operator. One innovative approach to finishing metallic freeform surfaces is laser polishing.

LASER POLISHING

Laser polishing of metallic surfaces is based upon a micro remelting process, optimized for smoothing the initial topography: A thin layer is molten by laser radiation and surface structures are reduced in the molten state by the surface tension in the melt pool. In contrast to conventional grinding and polishing processes the material is not removed, but only redistributed. [1]
Areal polishing is achieved by scanning the laser spot in a meander pattern over the work piece surface. Figure 1 shows the schematic of the laser polishing process and the main process parameters, which are to be chosen depending on the material, the initial roughness and the target roughness. [1]

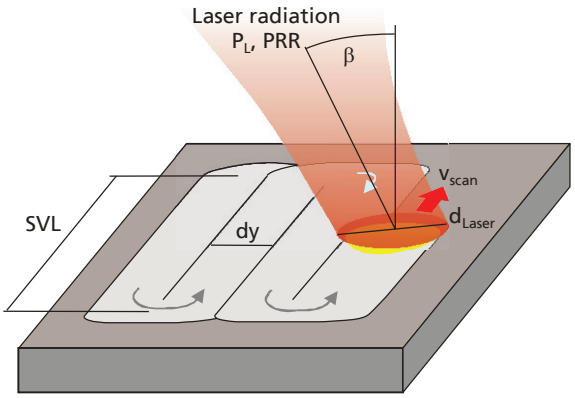

FIGURE 1. Schematic of the laser polishing process with the main process parameters: laser power P_L, pulse repetition rate PRR, spot size d_{Laser}, scan velocity v_{scan}, track offset dy, scan vector length SVL, angle of incidence β.

For laser polishing of metals there are two process variants: macro polishing, using continuous wave (cw) laser radiation (Figure 2a) and micro polishing with pulsed laser radiation (Figure 2b). Typical remelting depths for macro polishing range from 20-100 μm allowing the smoothening of coarse surface structures such as milling and turning tracks or grinding marks, whereas the micro polishing process leads to remelting depths of less than 5 μm [2,3]. Consequentially, micro polishing enhances the micro roughness and glossiness while leaving bigger structures untouched [4]. The initial roughness of a work piece can be Ra 1.0 μm or higher for macro polishing and should typically be less than Ra 0.8 μm for micro polishing.
Due to the big initial roughness of SLM surfaces macro polishing with continuous wave laser radiation is used for the following investigations.

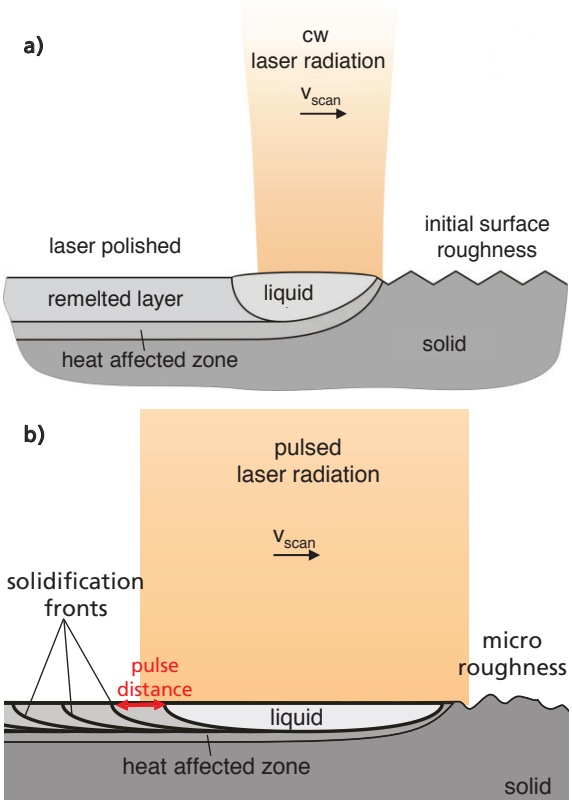

FIGURE 2. Process principle of the laser polishing process: a) macro laser polishing with continuous wave laser radiation; b) micro laser polishing with pulsed laser radiation

SURFACE CHARACTERIZATION

For the evaluation of a surface's quality, profile or areal roughness parameters such as Ra, Rq, Rz respectively Sa, Sq, Sz are widely used. Although these parameters are sufficient for the comparison of surfaces with similar characteristic, the limits become evident when comparing surfaces which were processed with different technologies, e. g. milled, ground and laser polished surfaces. All of these might show the same areal roughness Sa, but can be distinguished visibly by their respective structural characteristics. By analyzing the surfaces in regard of the predominance of structures with specific spatial wavelengths, i.e. a spectral roughness analysis, a more detailed comparison and evaluation of experimental results is possible. For this, the surface topography of a work piece is measured optically by white light interferometry (Zygo NewView7300) or focus variation (Alicona InfiniteFocus). The data is then analyzed using phase-correct band pass filters, thus allowing the calculation of the areal roughness for discrete ranges of spatial wavelength of the different surface structures [4]. Figure 3 gives an overview of this method: The measurements are performed at various magnifications, each of which is used for the analysis of a different set of spatial wavelengths, and the results are plotted as a roughness spectrum, reflecting the surfaces characteristics. E.g. the roughness spectrums of milled or turned surfaces will typically show a local maximum at the spatial wavelength that represents the used track offset.

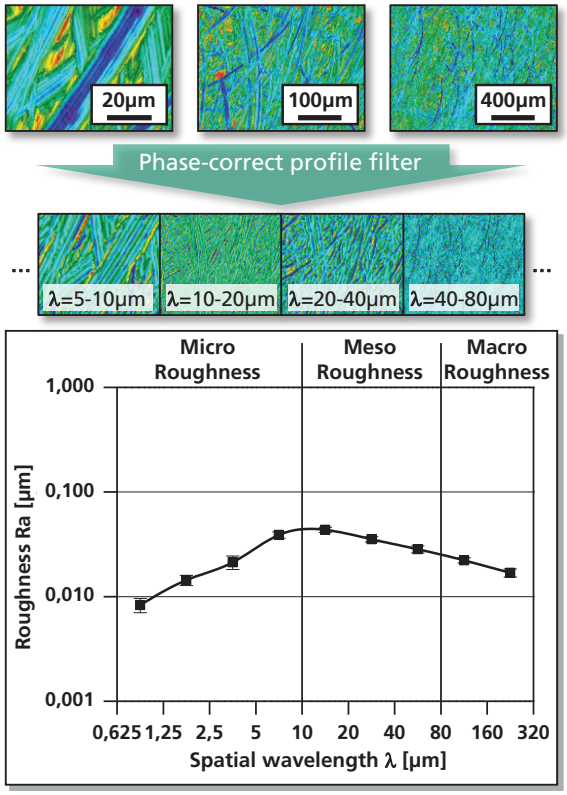

FIGURE 3. Schematic of the roughness spectrum analysis with white light interferometry surface measurements at different magnifications.

MACHINE TECHNOLOGY

The experiments are performed on a 8-axis 3D laser polishing machine developed by the Fraunhofer-Institute for Laser Technology (ILT), Aachen, Germany, in cooperation with Maschinenfabrik Arnold, Ravenburg, Germany. The base machine uses five mechanical axes for continuously reorienting the work piece to the optical system, while a 3-axis galvanometer mirror system by Scanlab performs the laser polishing process by moving the laser spot three-dimensionally over the work piece surface. The laser source is a diode pumped Yb:YAG disc laser TruDisk1000 by Trumpf with a

maximum laser power of 1 kW. In order to reduce oxidation, experiments are performed in a process chamber with inert gas and typically less than 1000 ppm residual oxygen. NC programming for the 3D parts was done using Delcam PowerMill for track generation and subsequent conversion of the trajectories into laser polishing tracks using the Technology Module, a specialized post processor with graphical user interface developed at the ILT [5].

EXPERIMENTAL RESULTS

Laser polishing of Inconel 718

The test specimens are 100x50x10 mm³ slabs, orthogonally built on a SLM Solutions 280HL. The initial surface topography is measured optically by focus variation. The surface roughness in accordance with DIN EN ISO 25178 is Ra = 25.5±2.8 μm.

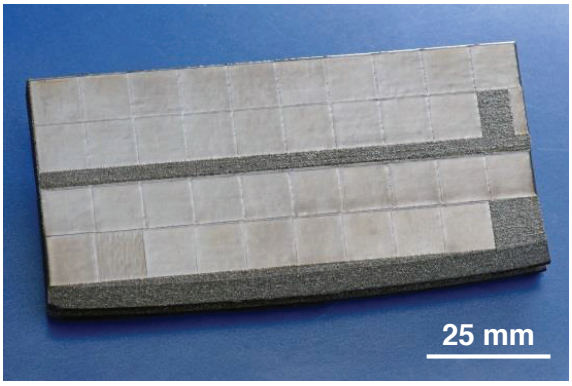

FIGURE 4. Parameter variation on an Inconel 718 SLM test specimen.

In order to determine the parameter set leading to the smallest roughness 10x10 mm² test fields are polished with systematically varied process parameters.
In a first set of experiments laser spot sizes between d_L = 250-800 μm are tested, with the laser power P_L being adapted to the spot size. The parameters scanning velocity v_{scan} = 250 mm/s, number of iterations n = 2 and track offset dy = 50 μm are constant. With a spot size of d_L = 600 μm and a laser power between P_L = 550-650 W roughness values down to Ra = 0.25 μm can be achieved. Thus, the spot size d_L = 600 μm is used in the following investigations on the influence of the scan velocity.
Figure 5 shows an overview of the polishing results with scan velocities between v_{scan} = 50-850 mm/s. The shade of each square represents the mean roughness after laser polishing for the given combination of laser power and scan velocity. The ellipse marks the parameter combinations which lead to the smallest roughness values.

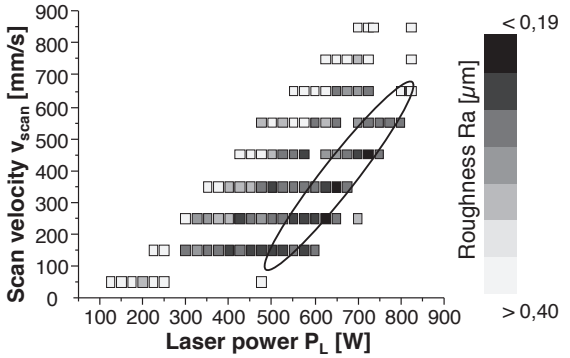

FIGURE 5. Surface roughness after laser polishing with systematically varied scan velocity and laser power.

The best result, Ra = 0.19±0.03 μm, is achieved with a scan velocity of 350 mm/s and a laser power of 650 W. The polishing rate is 5.25 cm²/min. Polishing tests with more than n = 2 iterations with the same parameter set show no further improvement in surface roughness, but instead lead to an increased waviness of the surface.

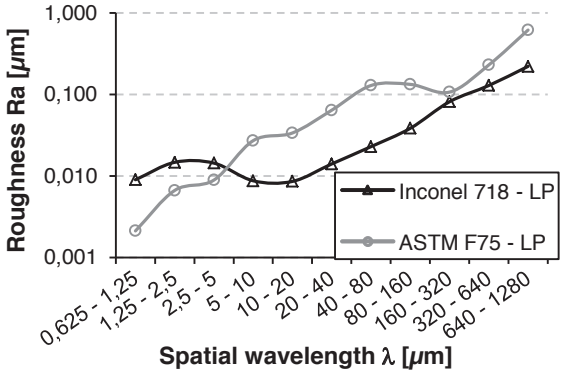

FIGURE 6. Roughness spectrum of an Inconel 718 and an ASTM F75 specimen, laser polished with the respectively optimized process parameters.

The roughness spectrum of the optimized parameter set (Figure 6, Inconel 718 - LP) shows a local minimum at spatial wavelengths between 5-20 μm and a local maximum between 1.25-5 μm, the latter representing the micro roughness or glossiness. The increase of roughness for bigger spatial wavelengths indicates some amount of waviness.

Laser polishing of ASTM F75

The laser polishing tests for the CoCr alloy ASTM F75 were performed on orthogonally built slabs with the dimensions 40x50x8 mm³. The initial roughness of the specimens is Ra = 10.7±1.8 μm, measured using focus variation.

As has been done above with the Inconel 718 specimens, parameter variations (Figure 7a) with different laser spot sizes and scan velocities are performed, leading to a minimum roughness of Ra = 0.71±0.03 μm using the parameter combination: d_L = 400 μm, P_L = 200 W, v_{scan} = 200 mm/s, number of iterations n = 2 and track offset dy = 50 μm.

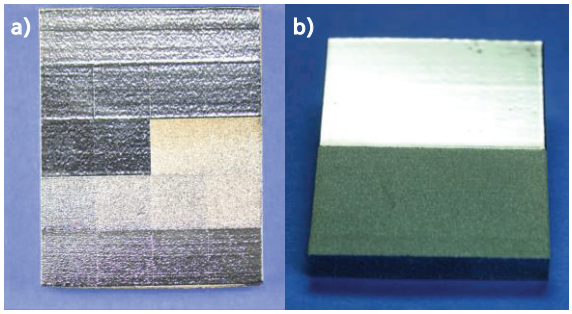

FIGURE 7. ASTM F75 SLM test specimen: a) parameter variation and b) half polished with optimized process parameters.

In contrast to Inconel 718, the surface roughness of ASTM F75 SLM parts can be further improved by increasing the number of iterations (Figure 8). Using the above determined parameter combination, the surface roughness is reduced to Ra = 0.27±0.04 μm after eight iterations with a resulting polishing rate of 0.75 cm²/min. Figure 7b shows a specimen half polished with the optimized parameters.

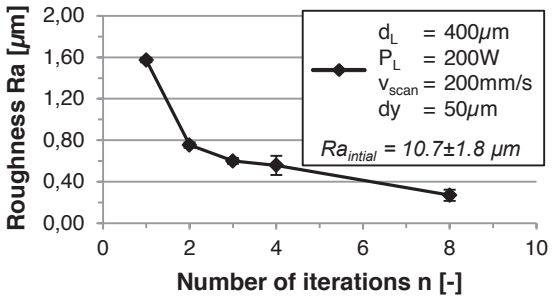

FIGURE 8. Surface roughness after laser polishing of SLM-built ASTM F75 with multiple iterations.

The second roughness spectrum in Figure 6 shows the described parameter set with n = 8 iterations. For spatial wavelengths $\lambda > 5$ μm, the roughness of the F75-spectrum is higher than the Inconel-spectrum, just as the conventional Ra values indicate. Difference in spectral roughness in the range $\lambda < 5$ μm between the two graphs represents the perceptible difference in micro roughness of the parts, the F75-specimen having a glossier appearance than the Inconel-specimen.

Laser polishing of 3D parts

If the laser beam axis is not parallel to the surface normal, the projection of the laser spot on the work piece is elliptically distorted. This leads to an increase of the interaction area by a factor of $\cos(\beta)^{-1}$ and thus a decrease in energy density and ultimately to increased roughness values. By adapting the laser power depending on the angle of incidence this loss in quality can be reduced or prevented [6].

The results of the power adaption tests are summarized in Figure 9. With the power adaption, the surface roughness of the Inconel 718 is almost constant for angles of incidence up to β = 60°. For ASTM F75, the roughness increases from Ra = 0.27 μm at perpendicular beam incidence to Ra =0.36 μm at β = 60°.

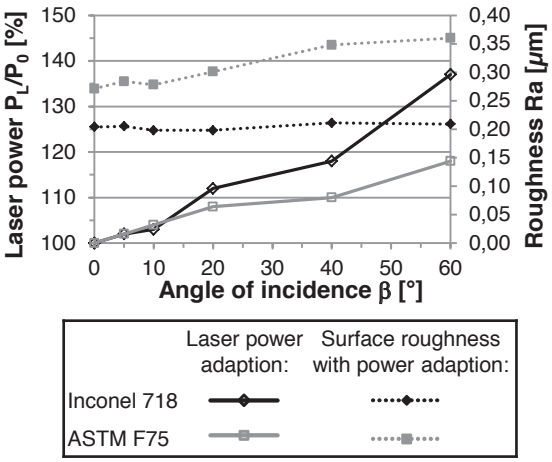

FIGURE 9. Laser power adaption curve and surface roughness with power adaption.

In Figure 10 first results on 3D laser polishing of complex shaped SLM parts, using the optimized process parameters for Inconel 718 and ASTM F75 as well as the respective power adaption curves, are presented.

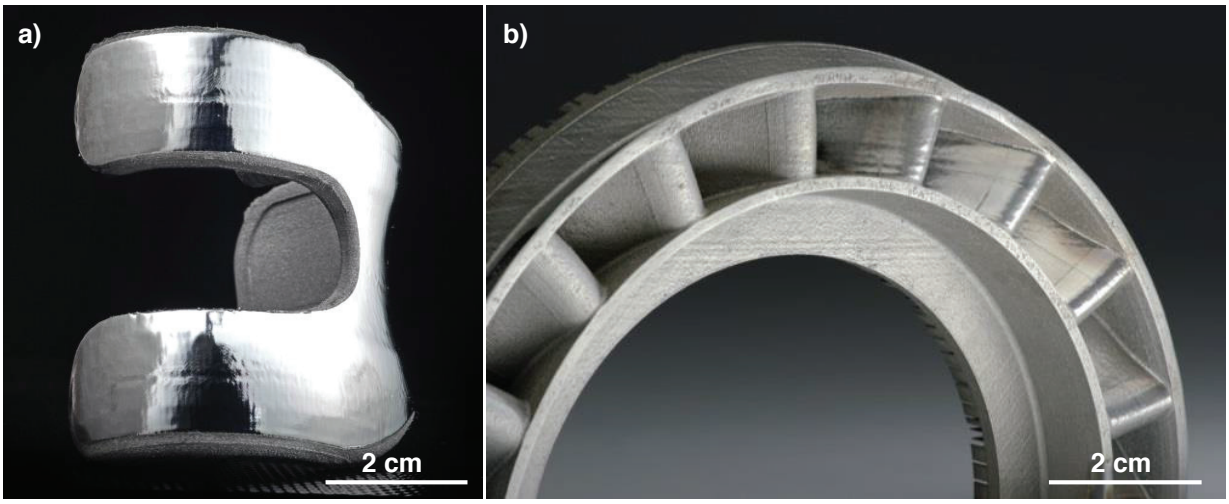

FIGURE 10. Partially laser polished SLM parts: a) knee joint made from ASTM F75; b) Segment of turbine guide vane made from Inconel 718

CONLUSION

In this work laser polishing is introduced as a finishing operation for complex SLM parts. Due to its innovative process principle, this new automated approach on polishing very rough surfaces offers vast new possibilities in the series production of additively manufactured parts. With the respectively optimized laser polishing parameters a roughness reduction of up to 99% for Inconel 718 and 97% for ASTM F75 can be achieved. The adaption of the process parameters for non-perpendicular beam incidence allows 3D laser polishing with minimized loss of quality compared to flat surfaces.

Future investigations will focus on the reduction of inhomogeneous areas by developing process strategies specifically designed for laser polishing SLM parts. Due to the remelting process, investigations concerning the mechanical properties, e.g. micro hardness, micro structure, tensile and fatigue strength will be taken into consideration.

ACKNOWLEDGEMENT

The authors wish to acknowledge support from the AMAZE Project, which is co-funded by the European Commission in the 7th Framework Programme (Contract # FoF.NMP.2012-4-313781), by the European Space Agency and by the individual partner organisations.

REFERENCES

[1] Willenborg E. Polieren von Werkzeugstählen mit Laserstrahlung. Dissertation, RWTH Aachen University: 2006.

[2] Bordatchev E, Hafiz A, Tutunea-Fatan O. Performance of laser polishing in finishing of metallic surfaces. International Journal of Advanced Manufacturing Technology. 2014; 73: 35-52.

[3] Nüsser C, Kumstel J, Kiedrowski T, Diatlov A, Willenborg E. Process- and Material-Induced Surface Structures During Laser Polishing. Advanced Engineering Materials. 2015; 17: 268-277.

[4] Temmler A. Selektives Laserpolieren von metallischen Funktions- und Designoberflächen. Dissertation, RWTH Aachen University: 2013.

[5] Osthold R. Laserpolieren metallischer Freiformflächen. Dissertation, RWTH Aachen University: 2011.

[6] Flemmer J, Ross I, Willenborg E, Fröba H. Machine Tool and CAM-NC Data Chain for Laser Polishing Complex Shaped Parts. Advanced Engineering Materials. 2015; 17: 260-267.

SHAPE ADAPTIVE GRINDING (SAG) OF COMPLEX ADDITIVELY MANUFACTURED PARTS

Anthony T. Beaucamp[1], Yoshiharu Namba[1], Phillip Charlton[2], Samyak Jain[2], Arthur A. Graziano[2]
[1]Department of Mechanical Engineering, Chubu University, Kasugai, Aichi, Japan
[2]Zeeko Ltd, Coalville, Leicestershire, UK

INTRODUCTION

Electron beam melting (EBM) [1-2] and selective laser sintering (SLS) [3] are cutting-edge additive manufacturing (AM) processes used to produce three dimensional shapes by melting metal powder layer by layer. These technologies have recently become widely adopted in applications such as dental and prosthetic implants, or the prototyping of aeronautical components such as shown in Figure 1 [4-5].

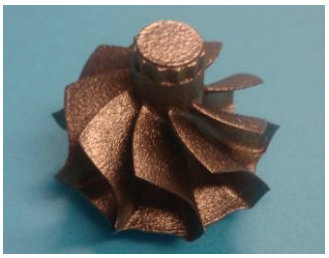

FIGURE 1. Example of "complex" rapidly prototyped component.

The final surface roughness produced by AM however, is unsatisfactory for many applications, demanding a post-finishing process to improve the surface quality prior to usage. One such method involves conformal grinding and polishing of complex additively manufactured shapes such as aero-engine blisks, but usually only achieve roughness around 0.5 μm *Ra* [6]. Although current finishing methods may have a distinct advantage, such as being able to finish porous structures, their resulting surface roughness is still limited. To expand on AM's many applications, it is necessary to further improve the surface roughness of components while limiting the number of finishing operations.

In this paper, we introduce a novel process called Shape Adaptive Grinding (SAG) that combines an elastically compliant tool with small grinding pellets. The process was applied to post-processing of titanium alloy (Ti6Al4V) additively manufactured by EBM and SLS.

SHAPE ADAPTIVE GRINDING

The shape adaptive grinding (SAG) process builds upon the precessed bonnet concept whereby an inflated, spherical, membrane tool is used to machine a surface at a tilted (precessed) orientation [7]. This bonnet (elastic tool) is typically covered with a polishing cloth, and a stream of abrasive slurry is constantly supplied to the tool. As the bonnet presses against the surface of the workpiece (controlled by the tool-offset), the contact-spot diameter increases.

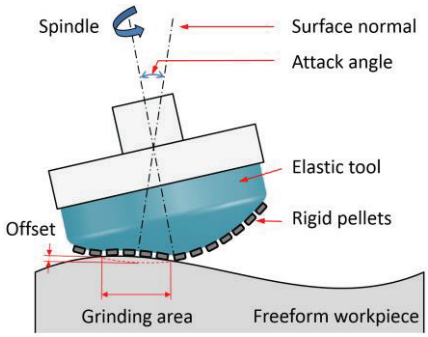

FIGURE 2. Principle of shape adaptive grinding.

However, in the SAG process, instead of being covered with a polishing cloth, the rubber bonnet is covered with nickel bonded (NBD) or resin bonded (RBD) diamond pellets, as shown in Figure 2 [8], with water used as a coolant. The deformability of the elastic layer allows the tool to conform to freeform surfaces featuring any convex or concave curvature larger than about twice the radius of the spherical SAG tool. Simultaneously, at smaller scale, the diamond pellets act as a rigid tool and allow for grinding to take place. The result is a shape adaptive grinding process with the benefits of both polishing and grinding techniques. This allows for greater material removal than standard polishing techniques, while achieving low surface roughness on complex freeform shapes. A 7-axis CNC machine actively controls the spindle speed, attack angle, tool offset, and surface speed of the tool as it traverses the surface of the workpiece; allowing for control of the grinding spot in terms of contact area and removal rate.

STUDY OF GRINDING PROCESS

Experimental procedure

Flat Ti6Al4V samples produced by EBM and SLS were procured in order to perform a series of experiments to determine the range of surface roughness and removal rates achievable with the SAG process. The initial surface roughness of the flat samples ranged between 4 and 5 μm *Ra*.

A series of 5 x 45 mm sub-sections of the titanium sample were ground using the machining parameters shown in Table 1. For the surface roughness experiments, the work spindle was operated at 75% of the maximum speed in order to achieve optimal productivity and to limit the thermal expansion of the spindle (i.e. frictions in the mechanical bearings). Tool pressure of 1.0 bar, attack angle of 20°, and tool offset of 0.3 mm were selected in accordance with previous experience of the SAG process [8]. The tool feed rate was allowed to vary across the sub-sections, with step values of 25, 50, 100, 200, and 400 mm/min. For each sub-section, when the rate of improvement in surface roughness diminished, the optimal feed was recorded. From one sub-section to the next, the nominal size of final diamond abrasives in the SAG pellets was decreased from 40 μm down to 3 μm, until a smooth surface could be obtained.

For the removal rate experiments, another sample of titanium was ground using the machining parameters shown in Table 1, which were selected in accordance with previous experience of the SAG process. The tool feed rate was kept constant in these experiments, and after each grinding pass the removal rate was determined by generating influence spots (dwelling of the tool at a static location).

TABLE 1. Parameters of surface roughness and removal rate experiments.

Parameter	Surface roughness test	Removal rate test
Shape Material Process	Flat Ti6Al4V EBM and SLS	Freeform SLS
Attack angle Spindle speed Tool pressure Tool offset Raster spacing Surface feed	20° 1500 rpm 1.0 bar 0.3 mm 0.3 mm 25, 50, 100, 200, and 400 mm/min	20° 750 rpm 1.0 bar 0.2 mm 0.21, 0.20, 0.19 mm 200 mm/min
Tool radius Abrasive size Abrasive type	10 mm 40, 9 and 3 μm Diamonds bonded in nickel and resin pellets	

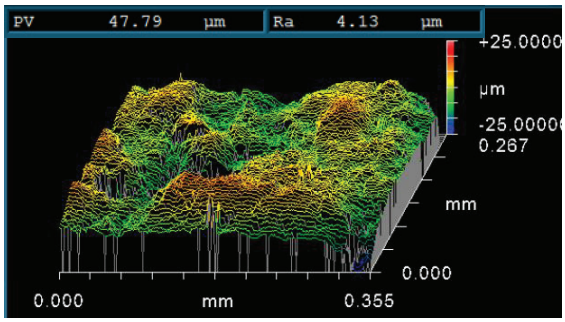

(a) As received

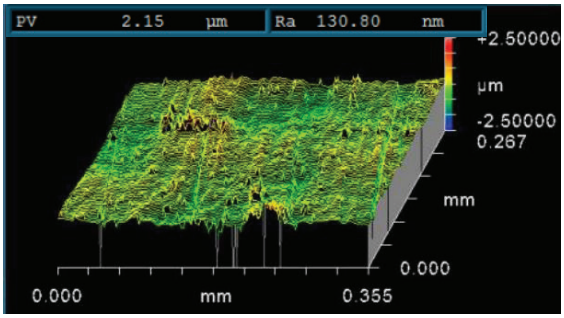

(b) Nickel bonded 40 µm

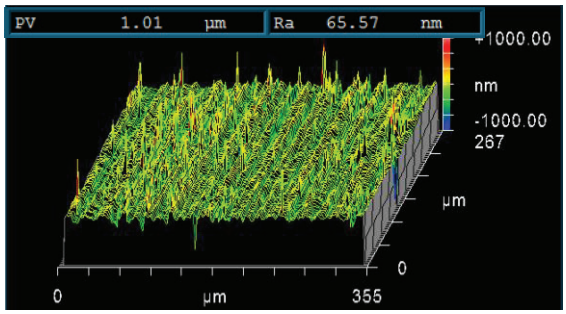

(c) Nickel bonded 9 µm

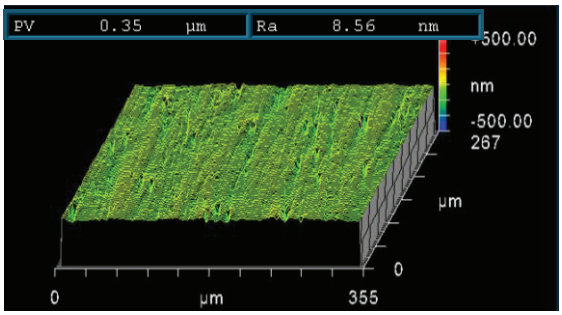

(d) Resin bonded 3 µm

FIGURE 3. 3D measurements of surface at 10x magnification, after successive grinding runs.

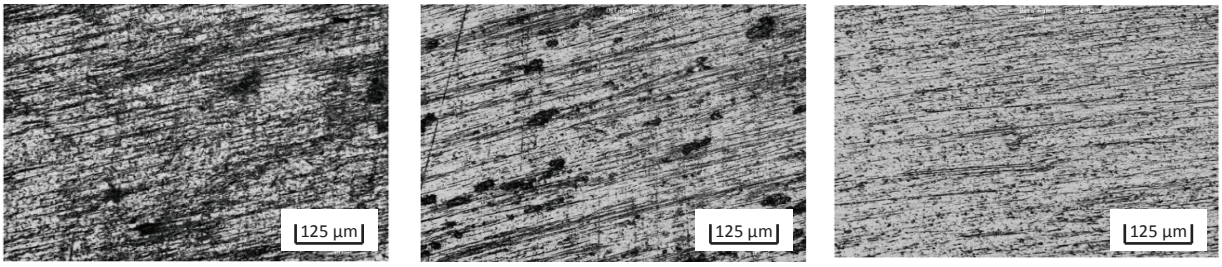

(a) Nickel bonded 40 µm (b) Nickel bonded 9 µm (c) Resin bonded 3 µm

FIGURE 4. Laser microscope images taken at 20X after successive runs.

Surface roughness

Figure 3 shows three-dimensional profiles of the surface taken with a white light interferometer at 10x magnification. Figure 4 shows laser microscope images of the same areas at 20x magnification, after reaching optimal surface roughness on the EBM samples with each SAG tool (progression on the SLS samples was similar). Due to the rough initial condition of the surface, a coarse 40 μm NBD SAG tool was first used to remove the micro-structured surface layer. Figure 3(b) and 4(a) show the resulting surface, in which the structured layer was mostly removed, allowing for finer grinding with subsequent SAG tools.

The next sub-section was prepared by pre-grinding at optimal feed rate with the 40 μm NBD tool. A 9 μm NBD tool was then used. Figure 3(c) and 4(b) show a reduction in the surface micro-structure, but the emergence of a directional surface texture could also be observed. The next sub-section was prepared by pre-grinding with the 40 μm and 9 μm NBD tools at optimal feed. Then, a 3 μm RBD SAG tool was used for final smoothing. The grinding direction was aligned perpendicular to that of the previous 9 μm NBD tool. The final surface shows attenuation of the directional scratches, and low surface roughness below 10 nm *Ra*, as seen in Figure 3(d) and 4(c). These results show substantial improvement by more than one order of magnitude when compared with other methods for post-processing AM titanium.

Figure 5 shows the evolution of surface roughness *Ra* at 10x magnification with successive SAG tools, as a function of grinding time across the 5 x 45 mm sub-sections (the observed surface roughnesses were consistent between EBM and SLS samples). The markers on each spline regression curve, indicate the progressive decrease of feed rate from 400, 200, 100, 50, down to 25 mm/min.

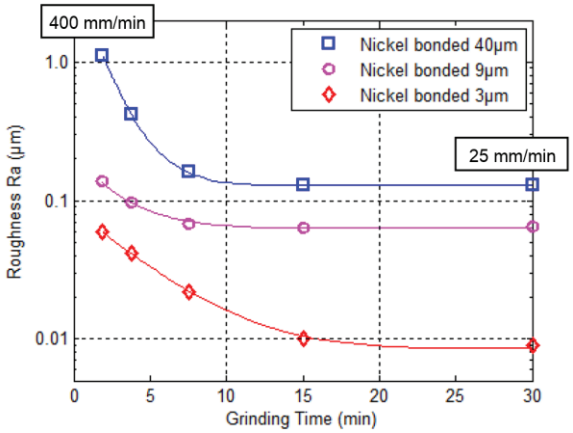

FIGURE 5. Evolution of surface roughness Ra.

Based on these results, it was found that optimal grinding could be obtained by using the following steps: 100 mm/min with 40 μm and 9 μm NBD SAG tools, and 50 mm/min with 3 μm RBD SAG tool (30 min total).

Removal rate

In order to determine the extent to which the SAG process can be used to finish artifacts without degradation of the dimensional accuracy, an accurate estimate of the removal rate must be determined. For this reason, the various SAG tools were used to grind a workpiece for 60 minutes each, and the removal rate was determined every 30 minutes by generating influence spots (dwelling a few seconds at static locations). The spot depth was then measured with a profilometer, and used to compute the equivalent volumetric removal rate, as shown in Figure 6 (the observed removal rates were consistent between EBM and SLS samples, and are plotted here with linear regressions).

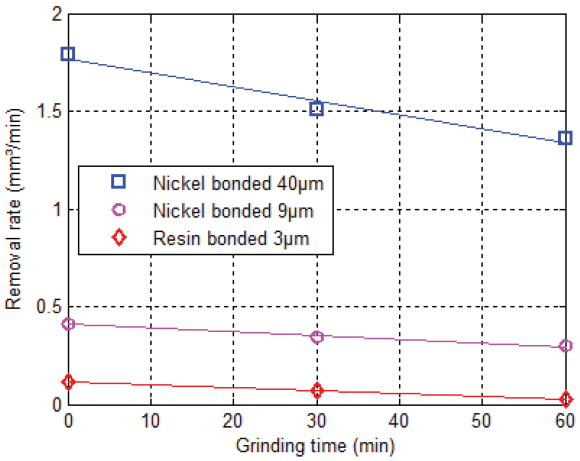

FIGURE 6. Evolution of removal rate as a function of grinding time for each SAG tool.

The volumetric removal rates ranged from about 0.1 mm^3/min for the 3 μm RBD up-to 2 mm^3/min for the 40 μm NBD. The removal rate of the SAG tools was found to follow a linear decline over time, which was consistent from tool to tool. It was found that the removal rate could be scaled up by either increasing the radius of the SAG tools (current SAG tools had 10 mm radius) or manipulating the CNC controller variables such as higher spindle rotation, or increased attack angle.

APPLICATION TO FREEFORMS

Experimental procedure

The application of the SAG process to freeform shapes was demonstrated on an SLS prepared complex sample shown in Figure 7(a). The sample consists of convex, concave, and saddle shaped areas with curvature ranging from 30 mm radius (concave) to 10 mm radius (convex). Figure 7(b) shows a rendering of the corresponding CAD model, with the area to be finished in blue. The SAG grinding process was performed on a 7-axis CNC controlled machine built by Zeeko Ltd.

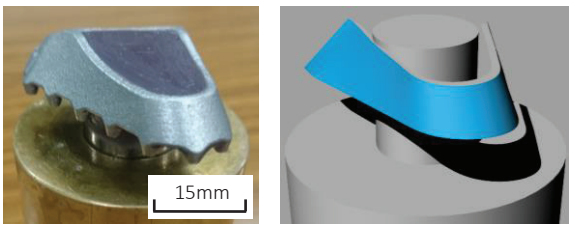

(a) As received (b) Area to be ground (blue)

FIGURE 7. Freeform sample prepared by SLS.

An on-machine probing system was used to characterize and compensate the deviation between CAD model and actual workpiece. A soft probe was mounted on the tool spindle, and used to detect the surface by touch/trigger sensing mode. Figure 8(a) shows a 3D array of points that was used to probe the surface by the machine software. The resulting data was then freeform fitted to the CAD model to determine the workpiece location inside the machine, and the residual form deviation against the CAD model. This data was used to compensate the CNC toolpath.

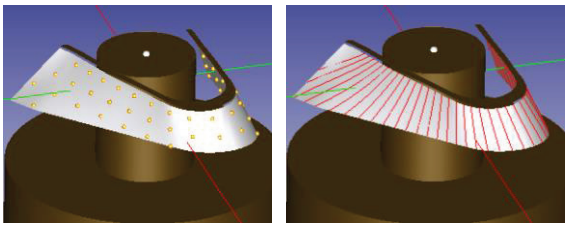

(a) Grid of probe point (b) Tracks of raster path

FIGURE 8. Definition of the probing and toolpath in the CAD/CAM software.

Since the positioning errors of the CNC machine had not been fully calibrated, this method could not be used to provide absolute measurements of the freeform shape. Nevertheless, the probing repeatability was determined to be better than 0.5 μm *rms* prior to the grinding experiments. Therefore, relative changes in the form error could be tracked between grinding runs by subtracting before and after measurements, which provided an estimate of the 3D removal function with an accuracy better than 0.5 μm rms.

In order to produce the toolpath for finishing, the freeform shape was sectioned with a series of planes along the length of the surface to generate the raster path, as seen in Figure 8(b). Three SAG passes were performed with toolpath parameters very similar to those shown in the removal rate section of Table 1.

The process parameters were chosen to produce a toolpath within the dynamic range of the machine. They also reflected the faster processing condition of SLS material compared to EBM. The total grinding time was 45 minutes, consisting of 14 min with 40 μm NBD, 15 min with 9 μm NBD, and 16 min with 3 μm RBD.

(a) As received *(b) SAG machining* *(b) Final condition*

FIGURE 9. Condition of freeform sample after successive grinding runs.

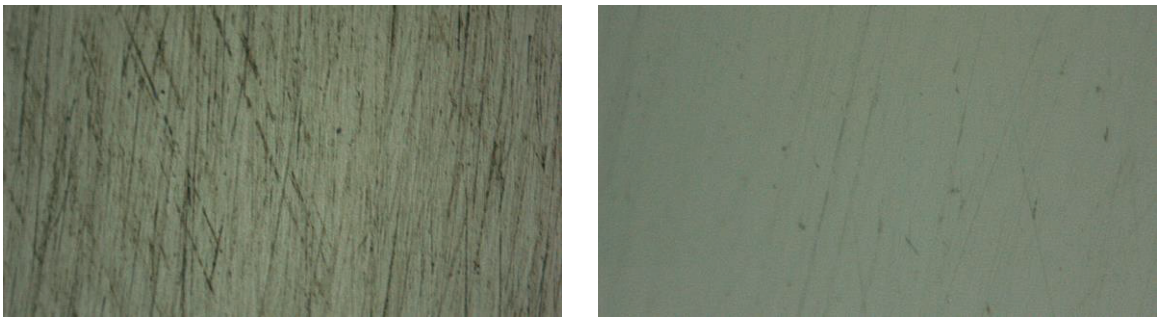

(a) After grinding with resin bonded 3 μm (b) After final polishing with 1 μm diamond paste

FIGURE 10. Optical microscope images of freeform surface taken at 100x magnification.

Surface roughness

Figure 9 shows photographs of the surface before, during, and after grinding. A mirror-like surface was achieved after only 3 SAG grinding runs were performed on the original AM surface condition (with roughness above 5 μm *Ra*). The improvement in surface reflectivity can be easily observed. The surface roughness was measured using white light interferometry to be 12.8 nm *Ra*.

Figure 10(a) shows the resulting surface after the third grinding run by 3 μm RBD (measured at 100x via optical microscope). The residual grinding marks observed after grinding on the freeform surface were very similar to those observed on the flat sample prepared by SLS. It can also be noted that substrates produced by state-of-the-art SLS technology delivered finishing with fewer residual pores than EBM, which would indicate a superior melting condition.

In order to further improve the surface condition, a final smoothing run was performed using the precessed bonnet polishing process, on the same machine and with a bonnet of similar shape and dimension as the SAG tools. A felt polishing cloth was employed together with 1 μm diamond paste. The polishing toolpath parameters were altered slightly: spindle speed of 400 rpm, attack angle 10 degrees, and track spacing 0.18 mm were selected based on previous experience with diamond polishing [9]. After a 17 min bonnet polishing run, the surface was measured again as shown in Figure 10(b). The grinding marks were mostly removed, leaving a very smooth surface with roughness below 3 nm *Ra*.

SUMMARY

The novel shape adaptive grinding process has been applied to post-process surface finishing of titanium alloy (Ti6Al4V) additively manufactured by EBM and SLS. It has been shown that the micro-structured surface layer resulting from the melting process can be removed using nickel

bonded 40 μm and 9 μm diamond SAG tools. The surface can then be further improved to approximately 10 nm *Ra* roughness by finishing with a resin bonded 3 μm diamond SAG tool. Thus, using only 3 different tools, the surface can be improved from 5 μm down to about 10 nm *Ra*; a decrease of almost 3 orders of magnitude. The process is lubricated with water, requiring only a simple tool change between successive runs.

The SAG process was also validated on a freeform sample, thus showing the ability of the tool to adapt to varying curvature from convex to concave. The finishing process maintained a shape deviation of less than +/- 5 μm, which is acceptable when compared to the typical accuracy after additive manufacturing. Finally, further bonnet polishing with diamond abrasives showed that the roughness can be easily brought further down to 3 nm *Ra*.

It was found that SLS samples finished by this process displayed fewer pores than EBM samples, which would indicate that state-of-the-art SLS technology is capable of delivering substrates with better material uniformity than standard EBM technology. The SAG technology is expected to find many applications in the post-process finishing of rapidly prototyped titanium alloy components for such applications as aeronautics and medical components.

ACKNOWLEDGEMENTS

This work was supported by the JSPS Grant-in-Aid for Scientific Research (B) No. 22360063 and the Post-Doctoral program for foreign researchers from the Japan Society for the Promotion of Science. SLS samples were kindly provided by Renishaw plc, and EBM samples by Matthieu Kobilinsky Design.

REFERENCES

[1] Murr L, Gaytan S, Ramirez D, Martinez E, Hernandez J, Amato K. Metal fabrication by additive manufacturing using laser and electron beam melting technologies. Journal of Materials Science and Technology. 2012; 28(1): 1-14.

[2] Cormier D, Harrysson O, West H. Characterization of H13 steel produced via electron beam melting. Rapid Prototyping Journal. 2004; 10(1): 35-41.

[3] Mukesh A, Bourell D, Beaman J, Marcus H, Barlow J. Direct selective laser sintering of metals. Rapid Prototyping Journal. 1995; 1(1): 26-36.

[4] Guo N, Leu M. Additive manufacturing: technology, applications and research needs. Frontiers of Mechanical Engineering. 2013; *8*(3): 215-243.

[5] Chahine G, Koike M, Okabe T, Smith P, Kovacevic R. The design and production of Ti-6Al-4V ELI customized dental implants. Journal of Metals. 2008; 60(11): 50-55..

[6] Duan J, Shi Y, Lin X, Dong T. Flexible Polishing machine with dual grinding heads for aeroengine blade and blisk. Advanced Materials Research. 2011; 317: 2454-2460.

[7] Walker D, Freeman R, Morton R, McCavana G, Beaucamp A: Use of the 'Precessions'™ process for pre-polishing and correcting 2D & 2½D Form. Optics Express. 2006; 14(24): 11787-11795.

[8] Beaucamp A, Namba Y, Combrinck H, Charlton P, Freeman R. Shape adaptive grinding of CVD silicon carbide, Annals of the CIRP. 2014; 63(1): 317-320.

[9] Beaucamp A., Namba Y., Inasaki I., Combrinck H., Freeman R. Finishing of optical moulds to λ/20 by automated corrective polishing, Annals of the CIRP. 2011; 60(1): 375-378.

[10] Gibson I, Rosen D, Stucker B. Additive manufacturing technologies. New York: Springer, 2010.

SPATIAL ACCURACY OF EMBEDDED SURFACE COLORING IN COLOR 3D PRINTING

David B. Pedersen[1], Hans N. Hansen[1], and Eyþór R. Eiríksson [2]
[1]Department of Mechanical Engineering
[2]Department of Applied Mathematics and Computer Science
Technical University of Denmark
Kgs Lyngby, Denmark

INTRODUCTION

Recent years, the industrial market for full-color AM is growing rapidly. In the AM industry, most of the major technology providers are developing new systems with improved color capabilities and with improved materials. In the last 12 months alone, 5 new technology platforms have been revealed capable of full-color printing in polymers[1]. Industrial service providers increasingly expand their product-range of full-color print services, and as of today, the industry for full-color parts has grown rapidly, into a million-dollar industry [2]. With a new market emerging at such pace, it is believed a necessity to consider a new surface-metrological issue. To what accuracy are colors embedded to the surface of geometries, with relation to where specified from input data? This paper investigate the accuracy of surface coloring, by adopting a well-known metrological approach from calibrating Coordinate Measurement Machines (CMM's) and Machine Tools, that already has been transferred to be applicable for AM machine tools, [3] in order to determine the spatial accuracy of embedded color features to artifacts printed on a zCorp 650 color 3D Printer. The spatial color verification artifact is a flat plate with a series of checkered fields on the surface.

METHOD

Following an approach developed by Hansen et al.[3] for geometrical verification of 3D printers in the horizontal plane, a series of four checkered plates was generated. Each artifact contains a series of checkered fields in one of the z650 printer's base colors, as illustrated in *figure 1*.
Upon printing the checkered artifacts, one for each base-color, these can subsequently be mapped by means of an optical CMM. A calibrated DeMeet 220 from Schut Geometrical Metrology was used to find the centre of each checkered field in order to determine the spatial position of these. The measured positions are compared to the ideal of the CAD body, and the differences are mapped. The mapping of the geometrical coloring accuracy in the horizontal plane is finally plotted, in order to describe the spatial color performance of each color channel of the zCorp printer.

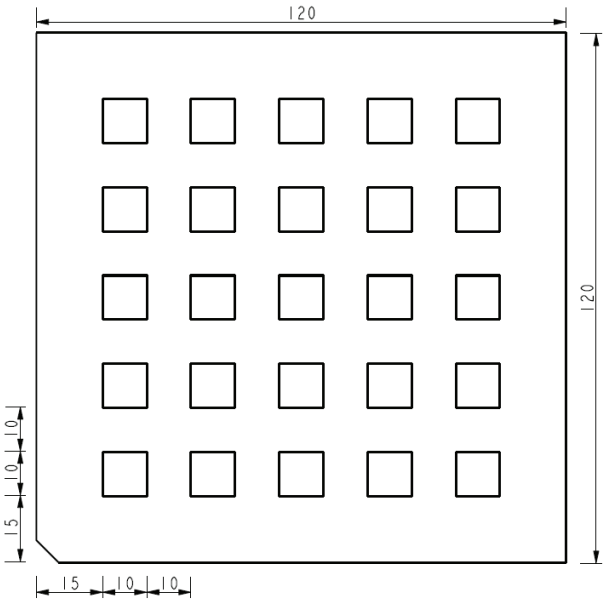

FIGURE 1. Color calibration artifacts. Each checkered field represent a field colored in one of the base colors of the 3D printer.

ARTIFACT GENERATION

A common method for embedding colors to 3D geometries is by texturing. If textures are applied to geometry, the spatial accuracy of the color representation is governed on-screen by the texture file format. Image textures on CAD bodies are often handled in image file formats employing lossy image compression that will introduce a pixilation effect known as compression artifacts.[4] As a result of this, the subsequent printing of the geometry will be carried out by multiple inkjet print heads, using more than one base-color. Furthermore the

capabilities of the engine in the software renderer used to display the geometry affect the accuracy of the rendered geometry, predominant when texture wrapping occur. Following this analogy, there is a risk that the accuracy of the color representation on the printed verification artifacts will be affected by the proprietary job generation software of the printer if a textural coloring of the calibration artifacts was used. To prevent this, it was decided to generate the checker board geometries by means of a tailored python script. This makes it possible to output the 3D geometries in the .OBJ with a per-face color definition, as seen in *figure 2*, to serve as the calibration artifacts. With this approach, it can be ensured that no issues related to texture interpretation and misalignment in the proprietary printer software can occur as each checkered field was generated as facet pairs, with a per-face base color defined. This eliminates the risk of error sources from the 3D body that may be transferred to the print job.

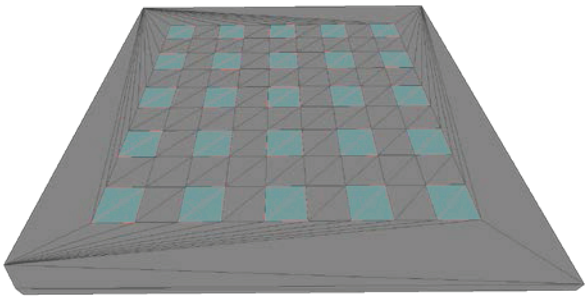

FIGURE 2. Per-face coloring of checkers. Each checker is comprised of a facet-pair in one of the CMYK base colors.

ARTIFACT MANUFACTURING

A series of four artifacts was 3D printed. Each artifact was manufactured on the z650 ink-jet based powderbed printer. z151 powder was used and the print was carried out at 0.89mm layer height with a specified 540x600 - XY DPI resolution, which corresponds to a theoretical horizontal resolution of 4.7μm. All four plates were manufactured in one print-job, and stacked in the vertical plane, so that the same kinematic characteristics in the horizontal plane was present during the manufacture of all four artifacts. *Figure 3* shows the four printed artifacts upon removal from the build-chamber of the 3D printer. No infiltration or other post-processing was carried out, in order to prevent the colors to bleed and deteriorate with respect to spatial accuracy. All artifacts have been manufactured in an orientation so that within the context of this paper, the X direction is in the direction of the print head carriage, whereas the Y direction is in the travel direction of the gantry of the printer.

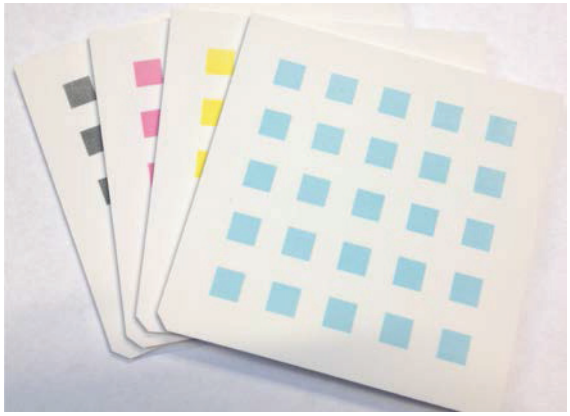

FIGURE 3. 3D printed CMYK color calibration artifacts

SPATIAL PLACEMENT

Each artifact in the CMYK color space, was measured, and for every checker, the spatial center position was determined. Measurements were carried out on a DeMeet 220 from Schut Geometrical Metrology, with x5 optics, maintained with a budgeted uncertainty of approx. ~16μm. The choice to define the spatial position of each checker by its center is in order to limit measurement uncertainties from the effect of ink bleeding out from the deposited area and into the surroundings. As seen in *figure 4* (right), it can be difficult to determine the exact outline of the checkers, whereas for yellow color (left), it can be hard to distinguish the color pigment from the background. Yet, the center of each checker is unaffected with respect to where along the boundary gradient, that the measurement is taken, if kept constant.

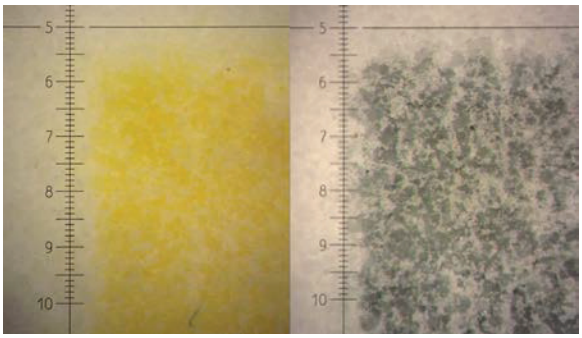

FIGURE 4. Microscopy of gradients from checker to background, K and Y color channel.

With the DeMeet 220, an NC programme was defined to allow for the construction of four lines following the sides of each checker. The line intersections define the corners of the checker, and is exported to a data file. From the four corners, two new lines are constructed. Since these four lines will not be perfect diagonals, their intersection is calculated from equations (1) and (2), for the intersection of two lines, and following the diagram in *figure 5.*

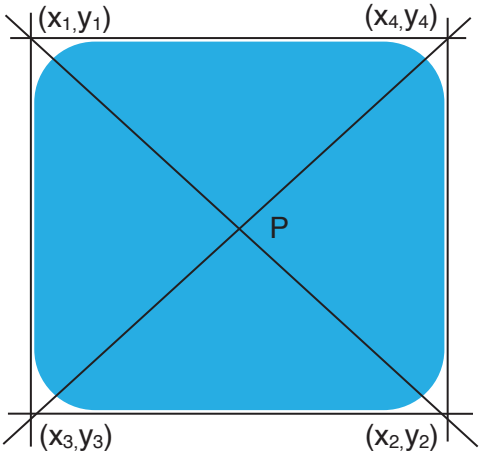

FIGURE 5. Diagram showing the center point definition (P) of a checker.

$$Px = \frac{(x_1y_2 - y_1x_2)(x_3 - x_4) - (x_1 - x_2)(x_3y_4 - y_3x_4)}{(x_1 - x_2)(y_3 - y_4) - (y_1 - y_2)(x_3 - x_4)} \quad (1)$$

$$Py = \frac{(x_1y_2 - y_1x_2)(y_3 - y_4) - (y_1 - y_2)(x_3y_4 - y_3x_4)}{(x_1 - x_2)(y_3 - y_4) - (y_1 - y_2)(x_3 - x_4)} \quad (2)$$

Finally the spatial position of every checker and thus the spatial color representation capabilities can be mapped in one plot, showing how well the z650 printer perform on the CMY and K color channel.

RESULTS

Figure 6 show the complete mapping of geometrical position errors within the four color-fields in the CMYK-space, magnified by a factor of 50, with a common origin in the lower left corner of the space. For each color channel, a grid show the position errors of each square centre, relative to the ideal position, which is shown as slashed gridlines. This makes it possible, in a single graph, to study the behavior of the z650 in the color- and the spatial domain.

An evident general trend, is that for all color channels, the scaling in both the X and Y directions of the machine are too short, resulting in an under-shoot. The error is seemingly linear, and of a magnitude of approx. 100μm in the X-direction (print head travel direction) and approx. 150μm in the Y direction (gantry travel direction). Thus, it will be extremely simple to compensate for this error contribution, if manual machine calibration will be allowed by the machine manufacturer.
Second, it can be seen that the grid lines for all color channels are skewed to the left. This is an indication of the machine axes not being orthogonal. The contribution from this error is largest in the point farthest from the common origin, with a spatial error component of app. 100μm The maximum combined position error cross the 80x80mm artifact error was found to be approx. 350μm.

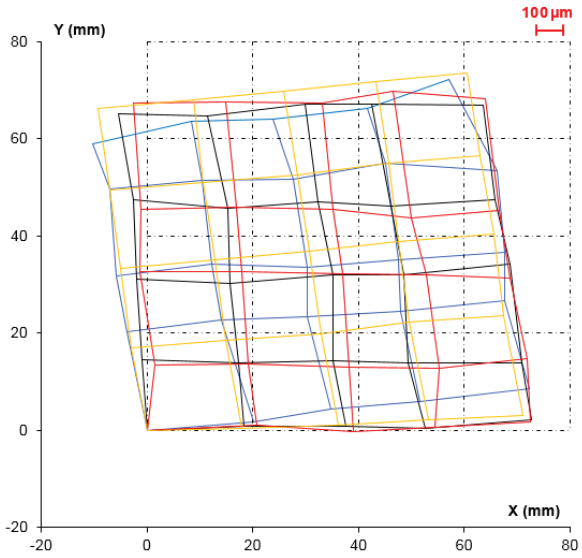

FIGURE 6. Center position of checkers compared to the ideal per color channel. Spatial position errors magnified 50 times.

The error mapping plot does also reveal errors inherent to the individual base colors, and thus the alignment of the print-heads within the tool-head of the printer. Since each color channel has been plotted with a normalized common origin, each color plot should theoretically be identical. When this is not the case, it can be

ruled down to one of two causes. First, it can be measurement errors from the measurements of the artifacts, which in this case has been carried out on accredited equipment. Second, and more plausible given the magnitude of the variance within the color-space is that it can be related to the printer having trouble with compensating for print head misalignment in software. The z650 printer has an automated print head alignment routine The routine is constituted by first, the print of a multi-colored grid spanning over the entire build plane of the machine. Subsequently a photo-sensor detects the grid, and computes a compensation matrix, that is superimposed over the machine movement, to ensure correct color deposition for all color channels. When each color channel of the verification plot in figure 6 share common origin, then it is then evident that variance between the different color channels could be directly linked to performance of the color calibration of the printer itself. Any variance within the CMY & K color can originate from this built-in routine for compensation of print head misalignment. Indications are therefore that the print heads in the z650 is aligned to ±100 μm over the area of the verification artifact.

CONCLUSIONS

Aimed to bring attention to the spatial color accuracy of Additive Machine Tools with full-color capabilities, a study was carried out to determine the spatial coloring accuracy of a zCorp 650 color capable 3D printer in the horizontal plane. The global spatial accuracy of the machine was found to be no more than 350 μm within the extent of the calibration artifact. The main error components was identified to be general axis scaling errors and skewness of the axes, affecting all color channels. A lower, yet significant error component relates to the individual color channels of the printer, and can be seen as the variance of the CMY & K grids in figure 6. Since all color channels share a common gantry and carriage, the variance between the grids from the different colored artifacts was expected to only reflect the measurement uncertainty of the CMM used for the mapping of the verification artifacts. The variance was however found to be approx. ±100 μm, well beyond the measurement uncertainty, and a suspected source of this variance has been proposed, relating to the built-in print head alignment routine of the printer. It is too early to conclude if this indeed is the direct contributor, yet a sub-standard print head alignment strategy will be a valid explanation to the cause behind the variance seen.

FUTURE WORK

It is believed that in order to achieve better spatial coloring accuracy of ink-jet based full-color AM technologies, further attention to the importance of machine calibration and verification this must be raised, and routines for correcting and optimizing color deposition must be improved. A variance between color channels of the manufactured verification artifacts indicated that better spatial coloring accuracy can be achieved by implementing a better print head alignment strategy than the one used in the machine subjected to this study. It is suggested to expand on the analysis to span over the entire horizontal build-envelope, and to expand the study to multiple artifacts for each color channel in order perform statistical hypothesis testing. Finally, this study aimed to propose a general method for spatial color verification within full color Additive Manufacturing. Vertical spatial color verification has not been carried out yet, but will yield more evidence of the capabilities of the method proposed.

REFERENCES

[1] Davide S., *Something3D Announces the Chameleon Full Color Desktop 3D Printer.* 3D Printing Industry Ltd., February 6, 2015

[2] Hooves Inc., *Company Information Register*, Accessed feb 2015. Key figures taken from Shapeways Inc, Twinkind GmbH et al.

[3] H.N. Hansen et al., *Performance Verification of 3D Printers,* ASPE Spring Topical Meeting 2014, Berkeley, California

[4] Mei-Yin Shen, C.-C.Jay Kuo, *Review of Postprocessing Techniques for Compression Artifact Removal,* Journal of Visual Communication and Image Representation, Volume 9, Issue 1, March 1998, Pages 2–14

IN-SITU MONITORING OF DIMENSIONAL ACCURACY IN ADDITIVE MANUFACTURING BY LAYERWISE DETECTION OF GEOMETRIC ERRORS

Masoumeh Aminzadeh and Thomas Kurfess
The George W. Woodruff School of Mechanical Engineering
Georgia Institute of Technology
Atlanta, GA, USA 30332

INTRODUCTION

Additive Manufacturing (AM) is a layerwise manufacturing technique with the ability to make near-net-shape parts. The capability of making complicated geometries, lower raw material usage, no requirement of tooling, and consequently reduced cost and lead manufacturing time are its important advantages over conventional manufacturing methods such as machining. The drawback to AM, however, is its lack of dimensional precision and accuracy. The efficiency of laser powder fusion process in AM processes such as laser metal deposition and laser powder-bed fusion (L-PBF) is highly affected by process errors, powder irregularities as well as geometric factors. Formation of defects such as lack of fusion and over-fusion due to the aforementioned factors causes dimensional errors that significantly damage the precision.

This paper addresses in-situ monitoring of dimensional accuracy of parts made by AM. By layerwise inspection of each layer, geometric errors and defects impairing the dimensional accuracy are identified in each layer. The detected geometric errors can then be repaired and corrected, before the deposition of the next layer, by taking appropriate corrective actions. To achieve layerwise in-situ monitoring of dimensional accuracy, this paper proposes a framework for layerwise detection of geometric errors and their causing defects from 2D measurement data. Techniques from image processing and metrology as well as information form the target geometry are effectively incorporated into the framework. The framework is described and an example of implementation of the framework is given for a geometric object made by L-PBF where the geometric errors are identified by implementing image processing techniques.

FRAMEWORK FOR IN-SITU MONITORING OF DIMENSIONAL ACCURACY

FIGURE 1 shows a schematic diagram of the proposed framework with the three levels of processing. The framework, from a machine vision perspective [1], consists of three levels of processing: low-level (segmentation), intermediate-level (feature extraction), and high-level (identification).

In the first level, a 2D measurement data (image) is acquired from the sensor; the image is pre-processed by noise removal and smoothing filters. Since the layer may consist of fused objects in a powder platform, the solidified fused regions first need to be detected before inspecting geometric errors. Image segmentation algorithms are used to detect all fused regions from the powder background. However, some of these fused regions may be defects due to the machine malfunction that should not be confused with true geometric objects; therefore, a geometric model of the target layer is incorporated into the framework. The target layer is the target geometry for the current layer which is formed by intersection of the plane corresponding to the current build layer with the 3D model. Detected fused regions that correspond with a valid geometric object from the target model are regarded as true geometric objects and those that do not correspond are signified as defects.

The true geometric objects should now be inspected for dimensional accuracy; the true geometric objects of the part should match the desired geometry of the target layer. Various methods in metrology such as point-to-point comparison or comparison of synthetic parameters [2] can effectively be used. For this work, synthetic parameters method is utilized which can be considered as the feature extraction level in the machine vision system. Synthetic parameters can be calculated by a variety of methods such as least squares,

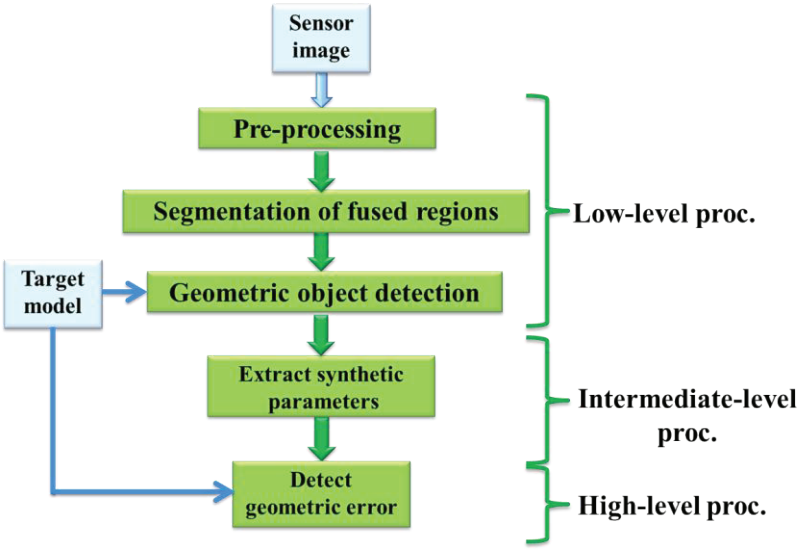

FIGURE 1- A schematic diagram of the proposed framework for layerwise monitoring system for dimensional accuracy.

minimal zone, maximum inscribed / minimum subscribed features from metrology field. In addition to metrology methods, methods from image processing such as pattern matching techniques or Hough transform can be used to extract the parameters of the object. The synthetic parameters may include shape parameters (such as roundness and ratios), size, location, angles, and relative spacing and orientation. Once synthetic parameters are extracted, they can be compared with those of the target layer to calculate geometric errors in the identification level.

To clearly identify out-of-tolerance geometric errors, acceptable process tolerance is accounted by developing control charts. The variation of synthetic parameters in each layer during the build of a high-quality part (with desired dimensional accuracy, built by proper machine operation) can be studied. The variation of the parameters is used to develop a normal statistical distribution and the control limits. During the normal machine operation, layerwise variations of the synthetic parameters signify existence of the geometric errors if they exceed the control limits or show deviations from the normal distributions (see FIGURE 2). FIGURE 2(a) shows an example of a synthetic parameters, roundness that lies out of the control limits or accepted tolerance. FIGURE 2(b) shows an example of a synthetic parameter, in this case the spacing between two objects, that shows irregular diverging behavior despite being within tolerance. This behavior also signifies a geometric error.

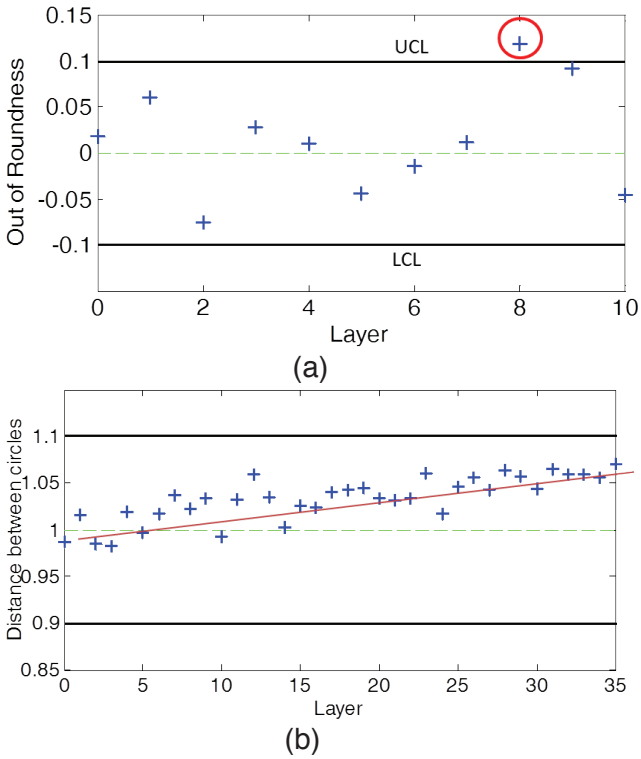

FIGURE 2- Variations of synthetic parameters that signify existence of an error: a) out-of-control limit; UCL and LCL stand for upper/lower control limits, respectively, b) deviation from normal statistical distribution- divergence of error.

DETECTION OF GEOMETRIC ERRORS USING IMAGE PROCESSING TECHNIQUES

In this section, image processing techniques are developed and used to detect geometric errors of a block made by L-PBF. FIGURE 3 shows an image of the square cross section of the block in one layer during the build. The image gray level is not a representative of the color, but it represents the height information. A 2D array of height map was measured using an interferometer and was appropriately scaled to gray range for purposes of visualization and image processing. The desired square is to be perfectly aligned with the axes shown in the figure. The in-situ monitoring system of dimensional accuracy requires the square to be automatically detected in the powder region and the geometric parameters be found. To achieve this objective, image processing algorithms are effectively implemented. Among existent image processing techniques for object detection, edge detection was found to be effective. Thresholding, in both forms of local and global, failed to provide satisfactory results due to the low contrast between the fused region and the powder region. However, the square seems to have sharp edges that can be used to detect the square. Although more sophisticated edge detection techniques such as Canny edge operator exist, Sobel edge detector [3] was used for this purpose as a lower-computational edge-detection operator, since we are only interested in detecting edges that are close to horizontal and vertical alignments.

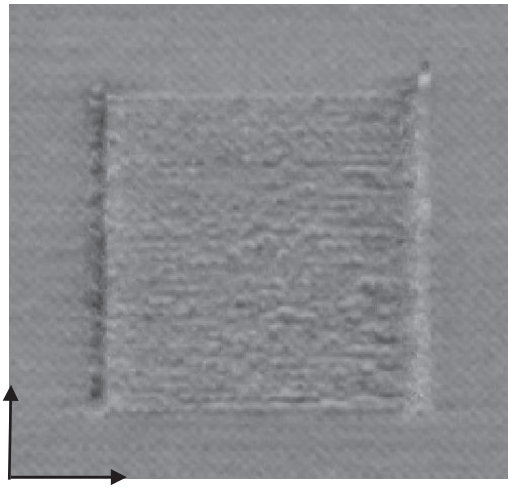

FIGURE 3- image of the square cross section of a block made by L-PBF; the image is the height measurements transformed to gray-scale image (see acknowledgement for the image source).

It was seen that although vertical edges are detected by Sobel more precisely, horizontal edges of the square are confused with the horizontal marks that laser scanning has caused within the square. Wiener noise removal filter was then used to fade the horizontal marks due to laser path while keeping the square horizontal edges detectable. FIGURE 4 shows the result of implementing Sobel edge detector.

(a)

(b)

FIGURE 4- Application of Sobel edge detector to the image of the square. a) vertical edge detector, b) horizontal edge detector applied to filtered image.

After edges are detected, the dominant edges which are equivalent to the sides of the square should be found. The dominant edges are those lines that pass through most detected edge points. There are several techniques that can

help with finding the dominant edges, however, they are usually very computationally expensive. Example of such a technique is to make an initial assumption of the edge slope and location and incrementally change both slope and location once at a time to reach maximum number of detected edge points that pass through this edge. Hough transform [3], however, is known as an effective computationally-efficient technique to detect dominant edges. Hough transform calculates all the possible lines passing through a detected edge point and finds a line that is passed through by largest number of edge points. Hough transform was implemented to detect the two dominant edges in each Figure 4 (a) and (b). FIGURE 5 shows the result of applying Hough transform in which the four sides of the square have been effectively detected. Dashed lines represent the detected edge segments that pass through largest number of edge points.

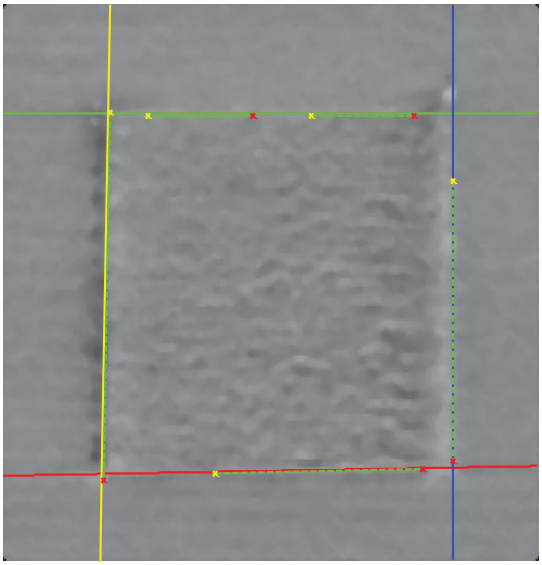

FIGURE 5- Application of Hough transform to detect edges of the square. Dashed lines represent the detected edge points that lie on the dominant edges found by Hough transform.

After the lines were detected, the intersections were automatically found to locate the vertices of the square and consequently the line segments corresponding to the square sides. The result of the detected square is shown in FIGURE 6 which shows satisfactory detection.

Once the square sides are detected, it is possible to measure the synthetic parameters of the square such as angles. Using the line information found by Hough transform, the alignment angle of the edges were calculated as 0 and 5 degrees for the top and bottom horizontal sides, and 90 and 87 degrees for the right and left vertical sides, respectively. Therefore, about a 5 degree error and 3 degree error was seen in alignments of bottom side and left side of the square. Given, the desired tolerance or control limits for this specific part, it can be investigated whether a geometric error must be reported for this layer of the build to be corrected or the process can be continued to the next layer without any corrective actions.

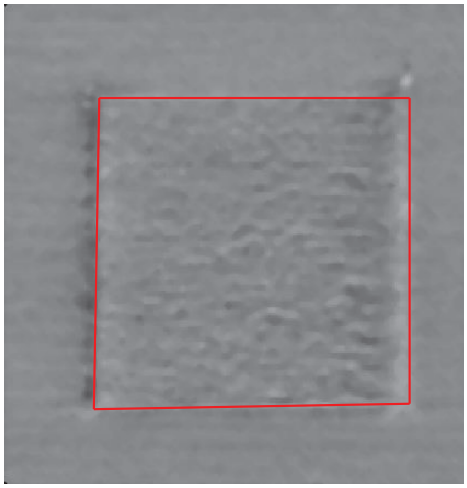

FIGURE 6- The detected square using Hough transform that best represents the square sides in the image.

ACKNOWLEDGEMENT

In accomplishing this work, we acknowledge the helpful contributions of Dr. John Ziegert's team from university of North Carolina, Charlotte, in providing the interferometry height map. We are also thankful to Edison Welding Institute for providing funding for this research.

REFERENCES

[1] D. Vernon, *Machine Vision; Automated Visual Inspection and Robot Vision*, 1991.

[2] B. M. Colosimo and N. Senin, *Geometric Tolerances: Impact on Product Design, Quality Inspection and Statistical Process Monitoring*: Springer Science & Business Media, 2010.

[3] Gonzalez, R.C. and R.E. Woods, Digital Image Processing. 3rd ed. 2008: Addison-Wesley Longman Publishing Co., Inc. 716.

PRELIMINARY STUDY OF CORONA-ASSISTED ADDITIVE MANUFACTURING PROCESS OF PIEZOELECTRIC THERMOPOLYMER

Chabum Lee, Rajib Mahamud, Tanvir Farouk, and Joshua A Tarbutton
Department of Mechanical Engineering
University of South Carolina
Columbia, SC, United States

INSTRUCTIONS

Piezoelectric materials are especially promising for a variety of devices because they can transform precise deformations over many length scales induced by small force and pressure, mechanical vibration, elongation/compression, bending or twisting into useful power or information. Such devices can be used for sensing and actuation applications as well as energy harvesting applications [1-3]. Piezoelectric devices are commonly used in nearly every sector of the economy from computers, mobile, data recording, home appliance and automotive applications. However, such devices have been are a concern in many commercial applications due to the potential toxic lead content. Thus, research and development of lead-free piezoelectric materials is presently one of the hottest topics in the field of piezoelectricity. There are two reasons for this interest: one is scientific (origins of the high piezoelectricity) and technological (processing, reliability), the other is related to environment and health. The scientific challenge is to produce lead-free systems which exhibit MPB (morphotropic phase boundary) with properties comparable to those in lead-based system. Environmental and health issues related to lead-based materials are well documented. According to RoHS, any homogeneous component containing more than 0.1 weight % of lead is subjected to restrictions; and hence, the fact that the best piezoelectric materials contain lead up to 60 weight %, may in the future, seriously hamper their use in everyday applications. This presents a significant material science challenge to create novel designs of new piezoelectric materials and how to engineer those materials to achieve similar performance to their lead-based toxic counterparts.

CURRENT MANUFACTURING PROCESSES

As depicted in Figure 1, current PVDF processing technologies (mechanical stretching, contact poling, corona poling and electrospinning processing) cannot produce realistic piezoelectric devices with large areas of sensitivity and high degrees of alignment and uniformity in a continuous fabrication process [2,6]. Realistic device functionality under small

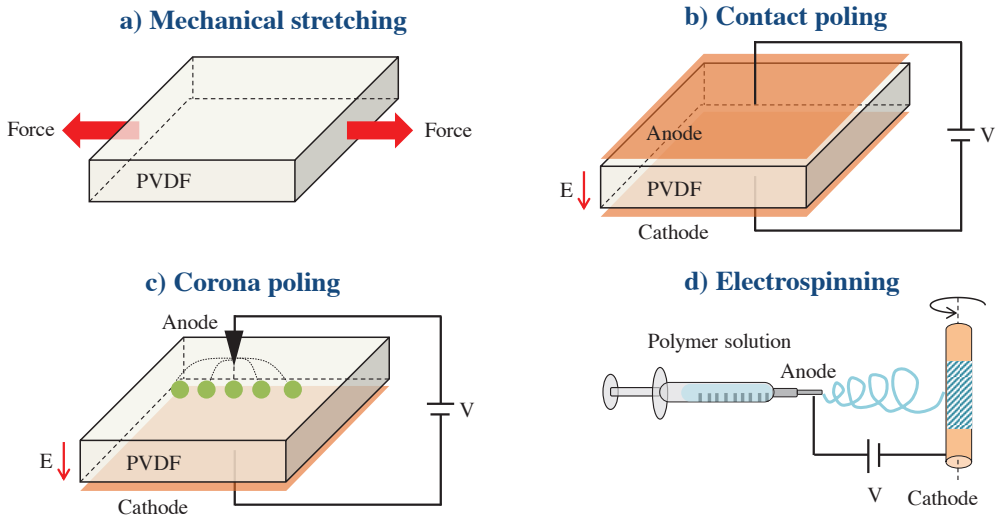

Figure 1. Current PVDF printing processes

mechanical motion can be achieved with high volumetric densities. However, the state-of-art piezoelectric polymer processing can only produce 1D or 2D devices such as thin films or small diameter (millimeter scale) fibers and cover an area of only tens of cm^2 maximum. There are currently no known piezoelectric polymer processes possible to fabricate 3D structured piezoelectric devices with large areas of sensitivity and high degrees of alignment and uniformity.

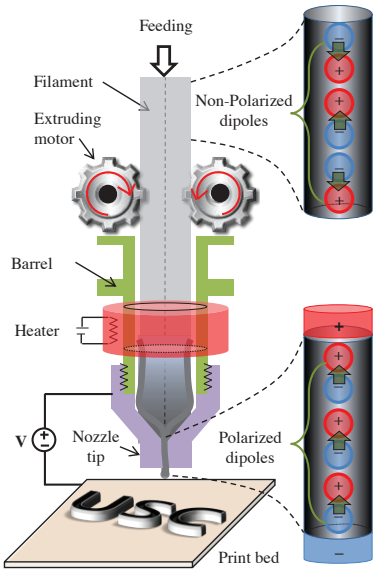

Figure 2. EPAM PVDF printing process [7].

Many researchers have studied various PVDF polymer processing methods [2,4-6]. However, the multi-material and its process make the fiber expensive and difficult to scale for continuous and large area production. Moreover, the current outputs of devices produced with arrays of electrospun fiber of PVDF polymer are less than 5nA and the voltages are in the range of 1~20mV [2]. Realistic device functionality under small mechanical motion can be achieved with high volumetric densities of aligned arrays of fibers. Current PVDF processing technologies cannot produce realistic piezoelectric devices with large areas of sensitivity and high degrees of alignment and uniformity in a continuous fabrication process. The state-of-the-art piezoelectric polymer processing can only produce thin films or millimeter scale fiber types of devices even though there is high demand in low cost 3D structured piezoelectric devices such as multi-axis dynamometers for force measurement, multi-axis actuators for nanopositioning and fiber alignment, and multi-axis energy harvester [2,5]. However, there are currently no known piezoelectric polymer processing processes capable of fabricating freeform-shaped piezoelectric devices with large areas of sensitivity and high degrees of alignment and uniformity.

EPAM PROCESS

The electric poling-assisted additive manufacturing (EPAM) process presented in Figure 1 combines AM and electric poling processes to fabricate free-form devices continuously while maintaining uniform dipole alignment of the PVDF polymer over a large area in a single design, production and fabrication step [6]. The fused deposition modeling (FDM) process as one of AM processes was chosen for experiment. The FDM process begins with a software process that processes a stereolithography file by mathematically slicing and orienting the model for the build process. Assuming that the PVDF polymeric filament is non-reactive and its dipoles are randomly distributed in the solid, a high electric field is applied to the molten polymer column between the nozzle tip and printing bed, which provides molecular chain alignment and transforms the polymer from an predominantly α phase crystalline structure to a β phase crystalline structure. Here the FDM machine (Solidoodle Corp.) was modified to be able to apply a high electric field between a nozzle tip of extruder and printing bed while printing. The PVDF polymer filament is inserted into an extruder along the feeding direction. The extruder is a stepper motor-driven filament feeding mechanism, heater, temperature sensor and nozzle tip. The PVDF polymer is heated by a heater as it is extruded by the motor through the nozzle tip with a diameter of 0.4mm. Temperature is feedback controlled. High voltage is applied between the nozzle tip as an anode and the printing bed as a cathode. The printing bed is heated by an internal heater to help the molten polymer adhere to the object and avoid thermally induced cracks. Kapton tape (0.2mm thickness) on the printing bed is applied for thermal and electrical insulation. This process indicates that the semi-molten polymer column in the gap between the nozzle tip and printing bed has all the dipole moments pointing along the same biased direction and maintains polarity while printing structures. During the EPAM process, the molten PVDF polymer undergoes mechanical stress by the leading nozzle while being subjected to a strong electric

field under specific high temperature. The semi-molten polymer hardens immediately after extrusion from the nozzle. PVDF polymer experiences drawing at high temperature, electric poling at high electric field and annealing at high pressure. This unique combination of processes all contribute to the creation of the β phase crystalline structure.

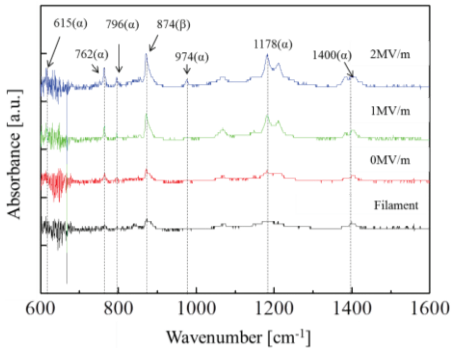

Figure 3. FTIR measurement results

The crystalline phase of samples fabricated under three different electric poling conditions was characterized. A Fourier Transform Infrared Spectroscopy (FTIR, Galaxy series FTIR 5000) was used to obtain an infrared spectrum of absorption of each PVDF polymer sample fabricated by the EPAM process under different electric poling conditions as shown in Figure 3. The results indicate that samples without the electric field applied show nearly identical results with those of PVDF polymeric filament before extrusion. On the other hand, new peak, 974cm^{-1}, was found in the samples fabricated under the strong electric field. In addition, existing peaks became sharp at certain wavenumbers, 762, 796, 874, 1178, and 1400cm^{-1}. In the samples fabricated under a strong electric field, the peaks could be clearly seen at the wavenumber, 87 cm^{-1}, whose crystalline structure is a known β phase, and the wavenumber 1178 a known α phase. In addition, it was found that those peaks show the tendency to being sharper as the strength of electric field increases.

Performance of PVDF polymer samples fabricated by AM process under different electric poling conditions was tested, respectively. PVDF polymer device was self-suspended between two fixtures, 50mm distance away, and both ends of piezoelectric device were securely fixed with high conductive Cu adhesive tape as electrodes. The current was measured while pushing down and pulling up the printed PVDF polymer samples. From the measurement results in Figure 4, it can be seen that PVDF polymer sample fabricated under higher electric field condition, 2.0MV/m, produces the higher current, ±0.37nA with respect to displacement direction when the sample is subjected to cyclic loading, which indicates that the total charge was generated approximately 7.0nC. On the other hand, it did not produce the current when it was stationary. The current output of the sample printed under the electric field condition, 1.0MV/m, was measured ±0.25nA when it was in motion, and its total charge was generated approximately 4.0nC.

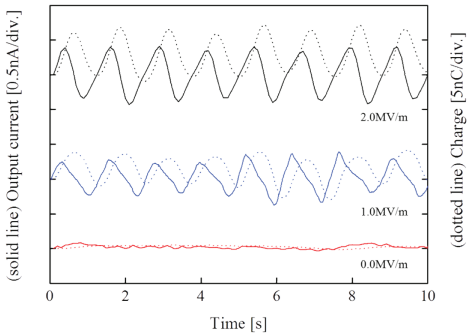

Figure 4. Piezoelectricity test.

CAM PROCESS

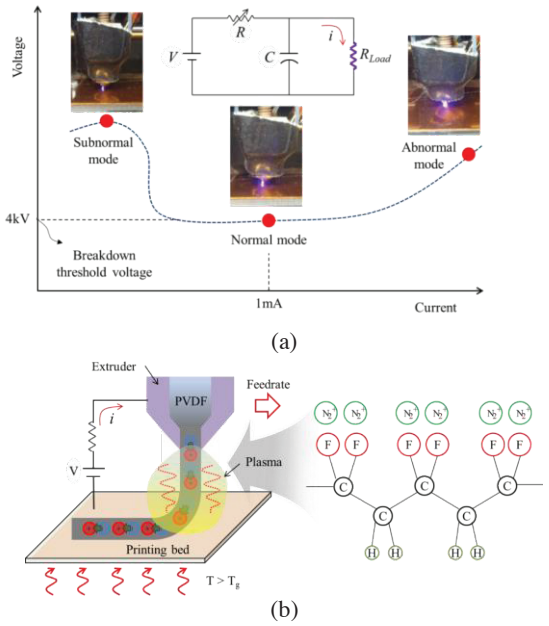

Figure 5. CAM process under different current conditions.

The corona-assisted additive manufacturing (CAM) process is capable of printing PVDF and transforming its polycrystalline structure and phase alignment to cause it to become piezoelectric while under a strong electric field

during the print. Corona discharge is a process by which a current flows from an electrode with a high potential into a neutral fluid, usually air, by ionizing that fluid so as to create a region of plasma around the electrode. The ions generated eventually pass charge to nearby areas of lower potential, or recombine to form neutral gas molecules. It is commonly used in various surface treatment applications.

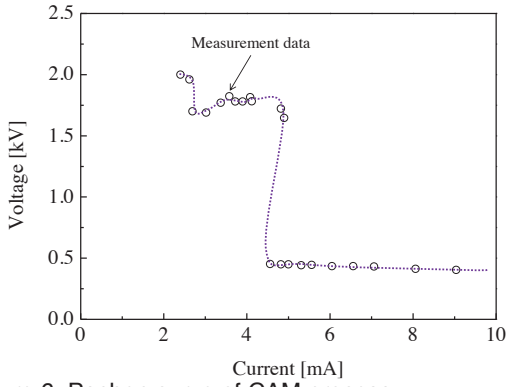

Figure 6. Pachen curve of CAM process

In this research, the corona discharge was made between printing nozzle tip and printing bed by controlling electric field (voltage and current) and printing gap (~0.2mm) while printing the PVDF as seen in Figure 5. The minimum power principle derived from fundamental physical laws cannot accurately predict this behavior making it necessary to experimentally determine operating conditions. Thus, the Paschen curve for CAM process (~200^{O}C and fixed gap distance ~0.2mm conditions) was experimentally obtained to find corona discharge regimes at low currents as seen in Figure 6. Each positive and negative corona effect between two electrodes was characterized by using ultrafast CCD (charge-coupled device) camera and each discharge characteristics was studied, and extruding nozzle geometry (sharp and round) effects on corona discharge was characterized as an early stage research. At a current experiment setup, the piezoelectric properties (crystalline β-phase and piezoelectric output) of PVDF specimens fabricated by CAM process will be characterized by the FTIR and XRD (X-ray diffraction) and CAM process effectiveness will be addressed by comparing the results obtained by EPAM process.

CONCLUSION

A transformative AM-based novel process was presented to fabricate freeform-shaped volumetric piezoelectric devices by combining AM and electric poling processes in a single processing and fabrication step. Piezoelectric samples were successfully printed by the EPAM process. Also, CAM process as an early stage research was proposed to print PVDF and transform its polycrystalline structure and phase alignment to cause it to become piezoelectric while under a strong electric field during the print. This work will lead to a better understanding of phase boundary effects due to plasma treatment in thermoplastics and inform novel sensor and actuator design leading to new methods to create lead free sensors for medical, aerospace, defense, research and development.

REFERENCES

[1] Kawai, H., The Piezoelectricity of poly (vinylidene fluoride), Japan. J. Appl. Phys. **1969**, 8, 975-976.

[2] Persano L, Dagdeviren C, Su Y, Zhang Y, Girardo S, Pisignano D, Guang Y, and Rogers J A, High performance piezoelectric devices based on aligned arrays of nanofibers of poly(vynylidenefluoride-co-trifluoroethylene), Nat. Commun. **2013**, 4:1633 doi: 10.1038/ncomms2639.

[3] Sirohi J, Chopra I, Fundamental understanding of piezoelectric sensors, Intell. Mater. Sys. Struct. **2000**, 11, 246-257.

[4] Chang C, Tran V. H, Wang J. Fuh Y-K, Lin L, Direct-write piezoelectric polymeric nanogenerator with high energy conversion efficiency, Nano Lett. **2010**, 10, 726-731.

[5] Hadimani R L, Bayramol D V, Sion N, Shah T, Quan L, Shi S, Siores E, Continuous production of piezoelectric PVDF fibre for e-textile applications, Smart Mater. Struct. **2013**, 22, 075017.

[6] Egusa S, Wang Z, Chocat N, Ruff Z M, Stolyarov A M, Sorin D, Rakich P T, Joannopolulos J D, Fink Y, Multimaterial piezoelectric fibres, Nature Mater. **2010**, 9, 643-648.

[7] C. Lee, J. A. Tarbutton, Electric poling-assisted additive manufacturing process for PVDF polymer-based piezoelectric device application, Smart Mater. Struct., **2014**, 23, 095044.

X-RAY COMPUTED TOMOGRAPHY FOR THE CHARACTERISATION OF PORES IN AN ADDITIVE MANUFACTURING PROCESS

Ian Maskery
Manufacturing and Process Technologies Research Division
University of Nottingham
Nottingham, NG7 2RD United Kingdom

ABSTRACT
X-ray computed tomography (CT) has been used to examine aluminium alloy parts manufactured by selective laser melting (SLM), an additive manufacturing (AM) process. This non-destructive technique revealed the size, shape and spatial distribution of the interior pores, each of which play a role in determining the mechanical properties and failure mechanisms of the material. Unlike conventional cross-sectioning and microscopy, X-ray CT can deliver information on statistically-significant numbers of defects. We explore and demonstrate the applicability of X-ray CT for assessing the quality of SLM parts (and AM parts, in general) and improving their processing conditions.

Model – Support material interaction inspection by X-ray Computed Tomography in FDM Additive Manufacturing Process

Leopoldo Ruiz-Huerta*, Alberto Caballero-Ruiz, Leticia Vega-Alvarado, Roque Yañez-Sanvicente, Homero Castro-Espinosa

Laboratorio Nacional de Manufactura Aditiva, Digitalización 3D y Tomografía Computarizada (MADiT)
Centro de Ciencias Aplicadas y Desarrollo Tecnológico (CCADET)
Universidad Nacional Autónoma de México (UNAM)
Circuito Exterior S/N, Ciudad Universitaria AP 70-186, C.P. 04510, México D. F. México
leoruiz@unam.mx

ABSTRACT
Additive Manufacturing (AM) is a layer-based automated fabrication process for making 3-dimensional physical objects directly from 3D-CAD data without using part-depending tools. Material extrusion systems represent the largest installed base of AM machines. Fused Deposition Modeling (FDM) is a material extrusion process in which model material is selectively dispensed through a nozzle tip or orifice. According to the geometry, manufacturing orientation, material and building strategy, the devices produced by FDM technology would require a second nozzle tip that extrudes another thermoplastic support material to allow the upper model material to be located [1,2].

The authors, studied the surface and inner structure of parts produced by AM FDM technology and detected possible material or manufacturing defects as a consecuense of model and support material interaction by means of an X-ray CT system. The studied material was polycabonate (PC). The machine used for the test was a Stratasys Fortus 400 with T16 nozzle tip and PC-S support material.

BACKGROUND
X-ray Computed Tomography (CT) is essentially based on the measurement of the different absorption coefficient of the materials crossed by a penetrating beam such as X rays. So far, dimensional X-ray CT metrology is the only technology able to measure the inner as well as the outer geometry of a component without the need to cut it through and destroy it. As such, it is the only technology for industrial quality control of workpieces having non-accessible internal features (e.g., components produced by additive manufacturing) or multi-material components (e.g. injection molded plastic parts or plastic parts with metallic inserts). Another major advantage of industrial CT technology is that it allows performing dimensional and material quality control simultaneously [3,4].

FDM technology has different parameters that affect the final result of the manufacturing such as the tip size, model material, support material, internal and external raster conditions, air gap, among others. FDM technology builds parts using joint wires by layers with a final roughness between 8 and 50 Ra (μm). The main characteristics that define this roughness are the tip size and the angle of construction. These characteristics are called “stair stepping effect”; the authors also show a prediction model related to the roughness based on the height of the layer and the angle of construction [5].

The aim of the present work is to show some results of the relation between the surface finishing obtained as the result of the contact interface between model and support materials. This relation was measured as a dimensional consecuence of manufacturing the same device with the same machine and materials by changing the manufacturing parameters.

MATERIALS AND METHODS
A device with variations of 5 degrees among “*arms*” from 0 to 90 degrees was designed and is shown in Figure 1. This device was

manufactured under three different conditions of manufacturing (shown in Table 1) using a Stratasys Fortus 400 loaded with a PC, PC-support and T16 nozzle. For the 3D manufacturing output, the Stratasys Fortus Insight v10.1 software was used.

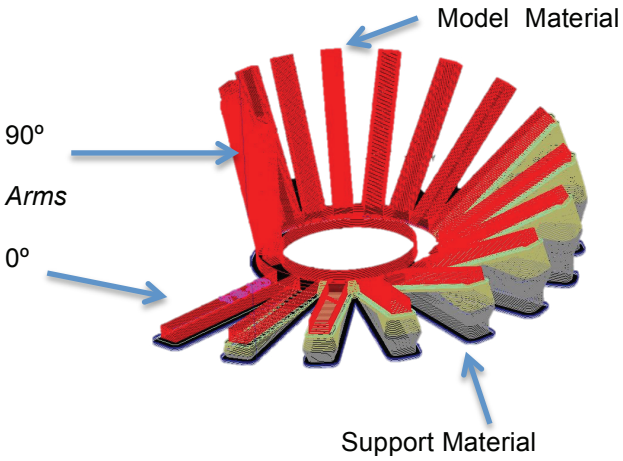

a)

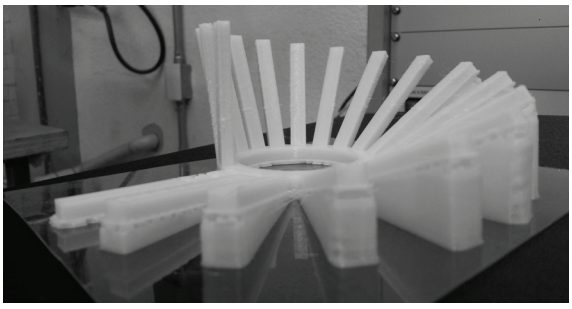

b)

FIGURE 1. a) Designed device; b) manufactured device.

TABLE 1. Manufacturing conditions

Parameter	GF	GFS	EH
Support Style	Basic	Smart	Smart
Slice height	0.254 mm	0.254 mm	0.254 mm
Visible surface style	Normal	Normal	Enhanced
Contour width	0.5080 mm	0.5080 mm	0.4064 mm
Part raster width	0.5080 mm	0.5080 mm	-
Internal rasters	-	-	0.7064 mm
Visible surface rasters	-	-	0.4064 mm
Raster-to-raster air gap	0.0 mm	0.0 mm	0.0 mm
Contour-to-raster air gap	0.0 mm	0.0 mm	0.0 mm
Raster angle	45°	45°	45°
Part fill style	One contour	One contour	One contour
Part interior style	Solid – Normal	Solid – Normal	Solid – Normal

GF means "green flag", which represents default values for the Fortus 400 machine with PC model material, T16 tip and basic support material deposition strategy. The GFS apply the same parameters as the GF but smart support material strategy deposition was used. The EH mode represents manually modified parameters with support material deposition strategy in smart mode. The CT system employed was a Nikon Metrology XT H225ST with the following parameters: 220KV, 11.7W, exposure of 267 ms and 3142 images.

TESTS AND RESULTS

For GF, GFS and EH, it is possible to observe a more pronounced stair stepping effect near horizontal values of manufacturing. Figure 2 shows this condition.

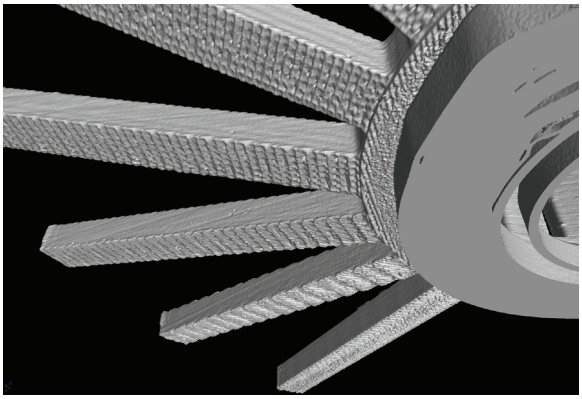

a)

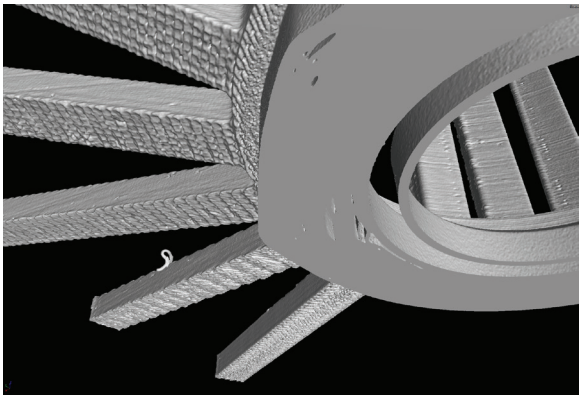

b)

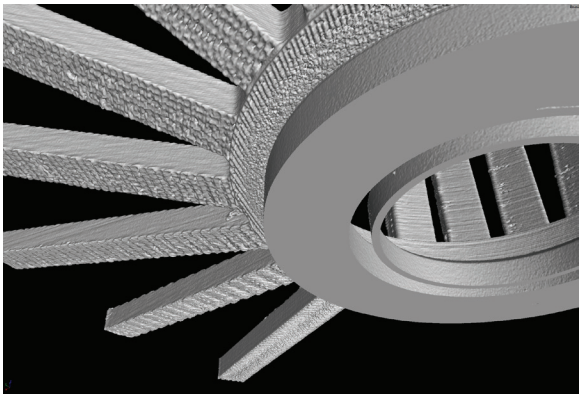

c)

FIGURE 2. a) CT images of GF manufacturing conditions; b) CT images of GFS manufacturing conditions; c) CT images of EH manufacturing conditions.

As a result of the building process, the 5-degree arm presents the main stair stepping effect. This arm was selected as a study case for the rest of this work. The interaction of the model support material is shown in Figure 3.

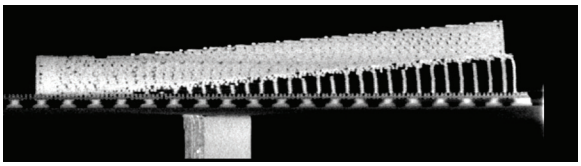

a)

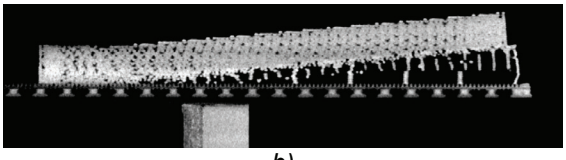

b)

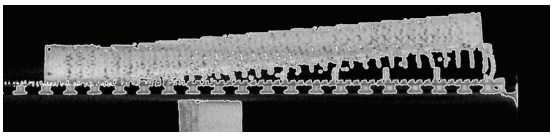

c)

FIGURE 3. a) CT images of model and support material interaction for GF manufacturing conditions; b) CT images of model and support material interaction for GFS manufacturing conditions; c) CT images of model and support material interaction for EH manufacturing conditions.

Because of the density similarity between model and support material, it was necessary to remove the support material to obtain a better view of the resulting surface.

To measure the dimensional characteristics of the three building conditions, GF, GFS and EH, the angular value of the 5-degree arm was measured using the Volume Graphis MAX 2.2 software. The results are shown in Figure 4 and reported in Table 2.

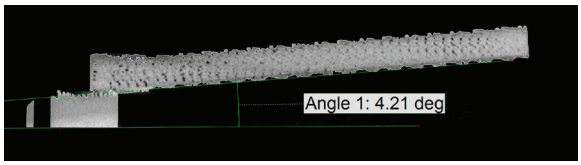

a)

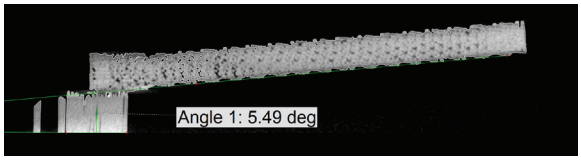

b)

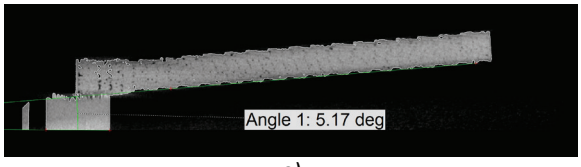

c)

FIGURE 4 a) CT images of the angular measured value for GF manufacturing conditions; b) CT images of the angular measured value for GFS manufacturing conditions; c) CT images of the angular measured value for EH manufacturing conditions.

TABLE 2. Measured values

Manufacturing Condition	Measured Value	Difference
GF	4.21	0.79
GFS	5.49	-0.49
EH	5.17	-0.17

DISCUSSION

The stair stepping effect is one of the major disadvantages of the FDM technology. Different autosupport angles were observed according to diferent manufacturing conditions. Low-angle values (near zero) are affected more by the stair stepping effect and, according to the manufacturing conditions, it is possible to decrease the dimensional error.

The time and quantity of material required to manufacture the same device with the same machine, type of material and tip size is also reported. These characteristics could be employed to compare it with dimensional performace. In Table 3, some manufacturing diferences are reported.

TABLE 3. Manufacturing diferences

Parameter	GF	GFS	EH
Self-supporting angle	43°	43°	51.34°
Building time	3h 34m	3h 39m	4h 10m
Model Volume	35.288 cm^3	34.39 cm^3	35.994 cm^3
Support Volume	18.262 cm^3	16.374 cm^3	21.782 cm^3

Thus, for the manufactured device as a study case in this work, to decrease from 0.79º to -0.17º, the difference between the angular designed value and the measured one, it is necessary to spend 17% more time, 2% more model material and 19% more support material.

CONCLUSIONS

This work shows different images related to the interaction between model and suport materials in a specifically designed and manufactured device.

Better manufacturing features produced by FDM technology would likely be obtained if it is possible to asume the cost associated with the extra material consumption and additional use of machine time.

The designer and the manufacturer related with FDM technologies have to be careful in terms of the balance between performance and cost.

ACKNOWLEDGEMENTS

This work has been financed by DGAPA-UNAM through grant PE-104014. The financial support from CONACYT LN-232719 and INFR-205502 is also acknowledged.

REFERENCES

[1] Wohlers Report 2014, 3D Printing and Additive Manufacturing State of the Industry, Annual Worldwide Progress Report, Wohlers Associates, ISBN 978-0-9913332-0-2

[2] Andreas Gebhardt, Understanding Additive Manufacturing, Carl Hanser Verlag, Munich, 2011, ISBN 978-3-446-43162-1

[3] Horst Czichos, Tetsuya Saito, Tsukuba, Ibaraki Leslie Smith, Handbook of Metrology and Testing, Second Edition, Springer, 2001, ISBN: 978-3-642-16641-9

[4] J.P. Kruth, M. Bartscher, S. Carmignato, R. Schmitt, L. De Chiffre, A. Weckenmann, Computed tomography for dimensional metrology , CIRP Annals - Manufacturing Technology, Volume 60, Issue 2, 2011, Pages 821–842

[5] Ahn D., Jin-Hwe k, Soonman k, (2009) Representation of surface roughness in fused deposition modeling, Journal of Materials Processing Technology, Elsevier, 209, 5593-5600.

[6] Ruiz-Huerta, L., Ortega-Rodriguez, A., Caballero-Ruiz, A.; Relation between tip size, deposition speed and roughness in FDM technology, Proceedings - ASPE 2014 Spring Topical Meeting: Dimensional Accuracy and Surface Finish in Additive Manufacturing pp. 214-218

DIMENSIONAL METROLOGY OF COMPLEX INNER GEOMETRIES BUILT BY ADDITIVE MANUFACTURING

Herminso Villarraga[1, 2, 4], ChaBum Lee[5], Steven P. Charney[4], Joshua A. Tarbutton[5], and Stuart T. Smith[1, 2, 3]
[1]Center for Precision Metrology, [2]Department of Physics and Optical Science, and [3]Department of Mechanical Engineering and Engineering Science
University of North Carolina at Charlotte, NC, USA.
[4]Carl Zeiss Industrial Metrology, LLC, USA.
[5]Department of Mechanical Engineering
University of South Carolina, Columbia, SC, USA.

The aim of this work is to evaluate the metrology results of dimensional measurements performed on the internal geometries of artifacts produced by an additive manufacturing (AM) process. The objects of study are shown in Figure 1. With rapid technology growth, AM-based precision engineering devices such as sensors, actuators, or precision mechanisms can be easily designed and manufactured at low cost. However, many questions about AM quality control, AM tolerance limits and AM material characterizations remain unanswered because those devices are in general 3-dimensional, complex, or even hollow inside. They have internal structures to enable free standing or delicate layers to be supported as the object is 'grown' in the vertical direction. There even exists a number of supporting layers or columns automatically generated by the slicing algorithm from 3D digital generating software.

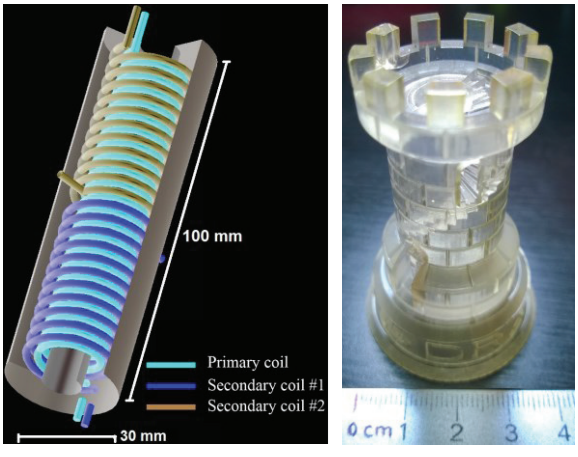

FIGURE 1. AM artifacts for the study. Left: Winding coils. Right: Chess rook with a spiral staircase and a double-helix twist in the center.

To study complex structures produced by AM process, with the current metrology technologies, computer tomography (CT) promises a non-destructive method to dimensionally characterize internal geometries of parts, and it might be the only available option to extract component dimensions of inner or hidden structures in an assembled product [1, 2]. This is important because with a destructive method the dimensions extracted from the disassembled state of a product may differ from the actual geometrical dimensions in the original assembled state. This is relevant for parts built by AM.

In this study, two test specimens were fabricated by using the stereolithography (SLA) process, and X-ray CT scanning methods were used to characterize AM tolerances of the two specimens. The scanning method and the AM dimensional limits are discussed. For dimensional evaluation of geometries of the AM artifacts, CT data was analyzed with three different methods: actual to nominal comparison to compare dimensional measurement data with reference geometry data and to evaluate tolerances achieved by the AM process; evaluation of single measurement features such as diameters, distances, etc. for dimensional characterization of the part (particularly of inner geometries); and wall thickness analysis. Also, with the aim of verifying the repeatability and reproducibility (R&R) of the CT method for dimensional measurements, and to be able to estimate the uncertainty of the results, several CT scans were performed on the same samples by two different operators, and by evaluating single measurement features with two different methods (global threshold – determined by the best iso-surface, and local adaptive or dynamic gradient threshold).

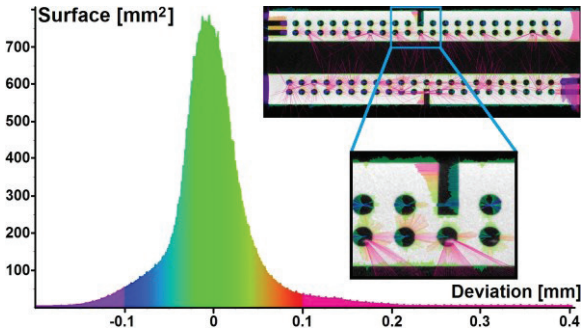

FIGURE 2. Variance distribution for deviations from nominal values for the winding coils artifact. An axial cut shows the internal details.

THE WINDING COILS

Figure 2 shows the actual-to-nominal comparison for the winding coils artifact using CT data as the actual measurements for the part and a CAD model as the nominal values for the artifact's surface locations. This part was designed to determine if AM can produce continuous multiple internal channels suitable for bio-fluidic sensing or actuation applications. It can be seen that the majority of the surfaces have geometric deviations between ± 0.1 mm, with a big portion of the surfaces varying only around ± 0.05 mm, but there are also parts of the surfaces exceeding these tolerance limits, particularly around the corners or in the inside of the winding coils with large deviations from nominal values (around ± 0.2 mm mainly). Figure 2 (left) highlights these details by color coding and by zooming into the coils. An interesting view from the interior of the winding coils can be reached by unwrapping the surface data points lying on a cylindrical surface that pass through the inside of the extracted part's volume as indicated by Figure 3. The non-planar view obtained this way, reveals features that develop during the growth of material during the AM process, particularly the presence of material inclusions in the inside of expected empty spaces. It seems that the deposition of polymeric materials along the Z-axis require of supporting structures to build the part. The supporting structures were automatically generated by the slicing algorithm generated by the 3D CAD model. While this may be user-defined, the default setting was applied in this research.

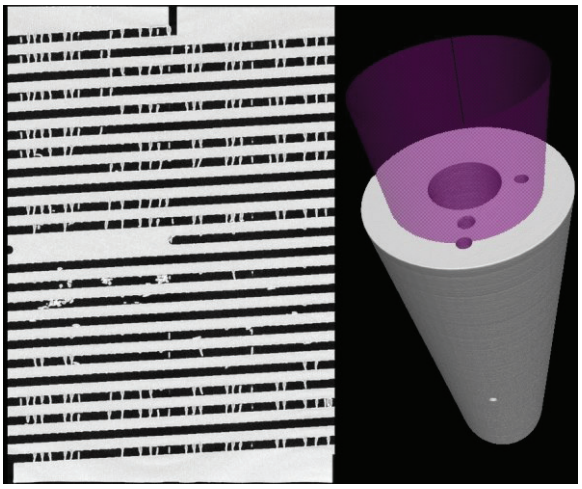

FIGURE 3. Non-planar view unwrapped from a cylindrical surface as indicated for the winding coils artifact showing internal material inclusions.

Figure 4 shows the wall thickness analysis of the winding coils artifact, showing thicknesses between 1 mm and 3.5 mm, and although a very pronounced peak is shown around 0.25 mm, this region is representing the thickness of the small inclusions inside of the coils.

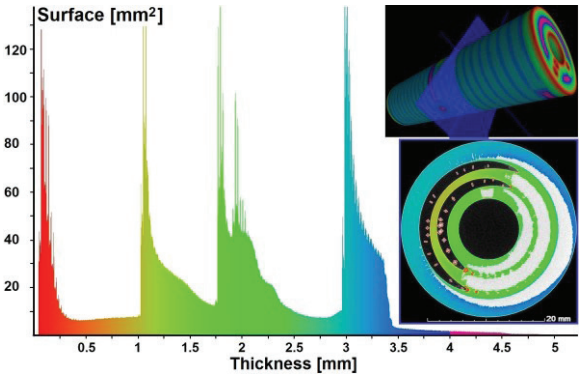

FIGURE 4. Wall thickness distribution for the winding coils artifact. A planar cut perpendicular to the rotational axis is shown (right-down side).

THE CHESS ROOK

A chess rook from the souvenir market built with AM process was CT imaged, and the results of wall thickness distribution are shown in Figure 4. This figure also shows the details of a non-planar view extracted from unwrapping a cylindrical view through the inside of the CT extracted part's volume. It is interesting to see how the non-planar view reveals details from the interior of the artifact's design like the doorman or guard standing at the entrance of the chess rook castle.

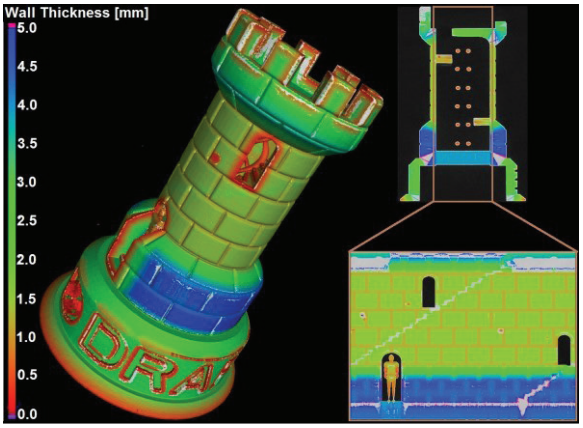

FIGURE 5. Wall thickness distribution for the chess rook artifact. A planar axial cut is shown as well as a non-planar view unwrapped from a cylindrical surface as indicated.

A smaller version (about half the size) of the chess rook artifact shown in Figure 5 was built in the laboratory by AM process. The part-to-CAD variance distribution for the new chess rook (again using CT data as actual measurement for the part) is shown in Figure 6, with details from the interior of the artifact revealed by a clipping view of the 3D CT image. While the majority of the external tolerances (or deviation from nominal geometry) seem to be in the range ± 0.1 mm, the internal geometry seems affected by material inclusions (stalagmites/stalactites looking) hanging out from the castle's roof (or growing out from the bottom floor) and growing from the bottom/up sides in the internal stairs. Figure 7 shows CT and microscopic images at different resolutions. A 28 μm CT scan seems to wash out some details from the structural roughness on the surfaces which are revealed by microscopy images. This is a disadvantage of the CT technologies that can only be partially compensated by selecting a small region of interest during the scanning, reducing thus the optimum voxel size captured (and increasing resolution) for image acquisition in the CT system as shown in Figure 7 (top right). However, in the modern industrial microfocus CT, this is limited by a minimum voxel size provided by the CT system, typically in the order of 1 to 5 μm (although nanometer level resolution can also be reached with some X-ray CT scanners [3, 4, 5]).

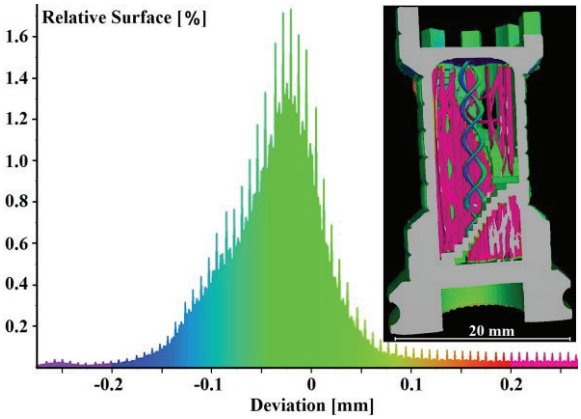

FIGURE 6. Variance distribution for deviations from nominal values for the chess rook artifact. A clipping view shows internal details.

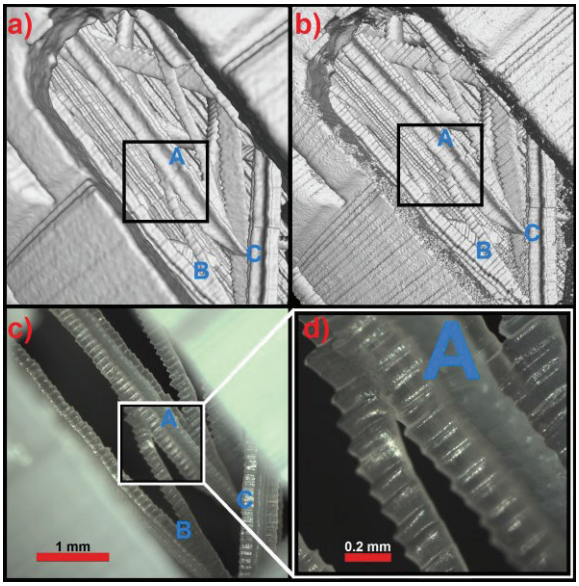

FIGURE 7. Intrusive internal structures grown in an AM rook chess artifact: a) 28 μm CT scan, b) 10 μm CT scan c) 68x microscopic image d) 228x microscopic image. A, B, and C represent common features in the images.

The chess rook artifact cannot be inspected using conventional coordinate measuring machines (CMMs) due to its complex internal geometry, but CT allows full three-dimensional characterization. CT measuring systems are able to completely capture the inaccessible or hidden features, particularly the spiral staircase and a double-helix twist in the center of this artifact. Dimensional characterization against nominal geometry for these internal structures is shown in Figure 6, but with the aim of verifying the repeatability and

reproducibility (R&R) of the CT method for dimensional measurements, and to be able to estimate the uncertainty of the results, evaluation of single measurement features with two different methods was also performed. The first method (SW1) uses a global CT threshold determined by the best iso-surface (ISO50%), and a Gauss (least-squares) fitting construction method with approximately 1000 fit points on each feature's surface. This is implemented by VGStudio MAX 2.2.4 software from Volume Graphics GmbH, which determines the part's surface on the original scan voxel data [6, 7]. The second method (SW2) employs a local adaptive or dynamic gradient CT threshold by using a least-square evaluation method for fitting surfaces, with low-pass filter of 0.8 mm wavelength and 50 undulations per revolution for fitting planes and circles (or cylinders) respectively. This is implemented by Calypso 5.6 software from Carl Zeiss Industrial Metrology, LLC, which uses a geometrical evaluation derived on the original volumetric voxel data [8]. Although an advanced surface determination algorithm using a local adaptive approach is available in VGStudio MAX, in this research only the ISO50% was implemented with the SW1 method to make it substantially different from SW2. Results from the evaluation of single measurement features with the two different methods, SW1 and SW2, performed by two different operators, CT user1 and CT user2, are presented in Figure 9 and Figure 10.

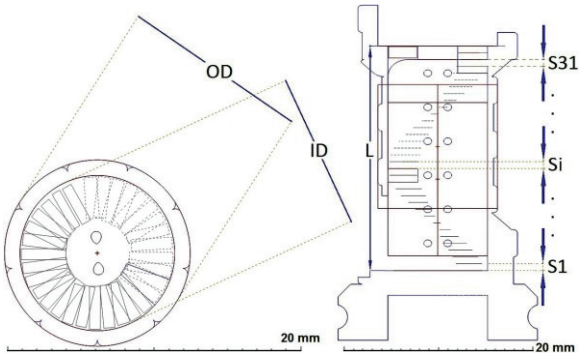

FIGURE 8. Characteristics of interest for CT dimensional measurement evaluation in the chess rook artifact. OD=outer diameter, ID=internal diameter, L=length from floor to floor, and Si represent the height of the i^{th} staircase step.

Because internal features in the chess rook artifact are inaccessible with tactile or optical CMMs, there are only two reliable possibilities as reference values for the CT measurements here: nominal geometry and a pooled mean from CT measurements. Figure 9 shows deviations of CT measurements from the pooled mean, while Figure 10 shows deviations of CT measurements from nominal values. In the majority of the cases, the measurements from two different users evaluated by two different methods seem to agree between them within the uncertainties of measurement of around 8 to 12 μm estimated by the quadrature sum [9],

$$U \approx 2 * \sqrt{{u_m}^2 + {u_p}^2 + {u_w}^2}$$

Here u_m is the machine uncertainty stated by the manufacturer in a calibration certificate, that is the standard calibration uncertainty of the measurement instrument calculated as $MPE/2$, where the MPE is the maximum permissible error for length measurement of the CT machine corresponding to $(8 + L/100)$ μm for the Zeiss Metrotom 800, with the length L in mm [10]. The standard deviation of repeated measurements after calibration of any instrument should not be more than half of its maximum permissible error, so $u_m \approx MPE/2$ is a fair assumption according to [11]. The uncertainty (of repeatability) of the measurement procedure u_p is calculated as $u_p = t_{1-\alpha,\nu}(s/\sqrt{n})$, where $t_{1-\alpha,\nu}$ is the t-statistic safety factor multiplier for the Student's distribution [12, 13], and s is the sample standard deviation of the n repeated measurements (it is important to highlight here that the number of measurement repetitions used was only $n = 3$, typical from CT metrology for which a single precision measurement can take from 45 minutes to a couple of hours). The uncertainty u_w is associated with variations in the workpiece caused by expansion due to temperature deviations, vibrations, form or roughness deviations, or any other changes in the workpiece material composition or material-manufacturing-measuring dispersion. Particularly for a temperature deviation δT and a coefficient of expansion β, u_w can roughly be estimated as $u_w \sim \beta L|\delta T|/\sqrt{3}$ where $|\delta T|/\sqrt{3}$ is the standard uncertainty resulting from a rectangular error distribution for temperature (all values of error within the band $\pm\delta T$ being equally probable). Lastly, the factor 2 computes the expanded uncertainty U with a confidence level of approximately 95% [9, 11].

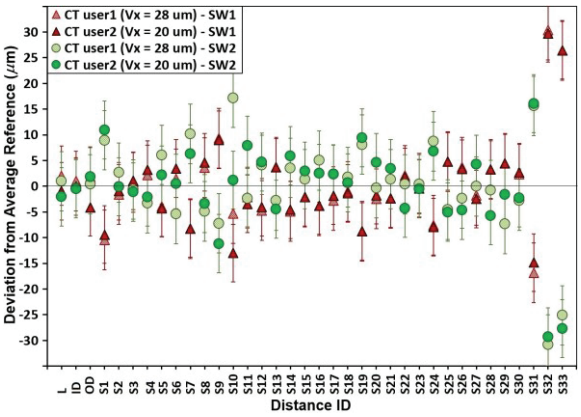

FIGURE 9. Deviations of CT measurements from the pooled mean for the distances indicated in Figure 8. SW1 and SW2 represent different CT computation software.

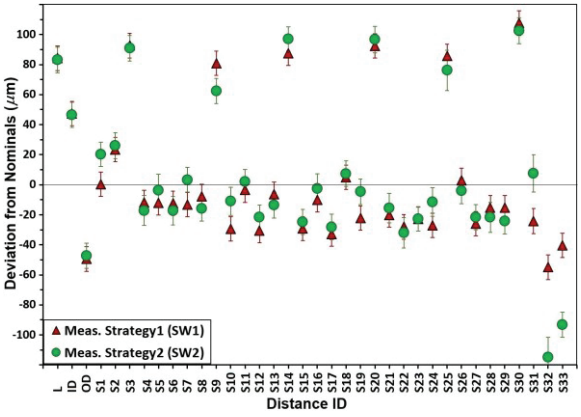

FIGURE 10. Deviations of CT measurements from nominal geometry indicated in Figure 8.

The CT measurements reported in Figure 9 and Figure 10 by user1 and user2 seem consistent within the reported uncertainties, with deviations between respective reported values less than 5 μm in the majority of the cases (with exception of the staircase step height S10). The measured values reported by SW1 and SW2 software show also this level of agreement for the diameters ID and OD, and length L (from floor to floor); but for the staircase step heights the differences between measurements computed by the software SW1 and SW2 are higher. Although the variation is not bigger than the computed uncertainties of measurement for the majority of the cases (less or approx. equal to 8 μm), there are some exceptional cases as can be seen in Figure 9: S1, S7, S10, S24, S31, S32, and S33. The high differences in these particular cases might be due to subtle differences in the practical definition of distance between two planes used by the SW1 and SW2 software, but also by possible instability of free standing spiral staircase feature inside the chess rook artifact. Lastly, from the evaluation of single measurement features reported in Figure 10, deviations up to 100 μm from nominal values have been detected for the AM artifact (the chess rook), which is in agreement with what is reported by the part-to-CAD comparison reported in Figure 6.

CONCLUSIONS

This paper demonstrates the current capabilities of X-ray CT as a tool for dimensional metrology characterization of internal geometries in parts built by AM process. Two different parts were studied: an artifact with internal winding coils, and a chess rook with a spiral staircase and a double-helix twist in the center. From the measurements of actual to nominal comparison obtained in this work, variation in dimensional geometry were detected for the AM parts with tolerances of around ± 0.1 mm with respect to reference geometry (nominal data) – see Figure 2 and Figure 6. Material inclusions in the internal cavities were also detected as remnants (either intended or unintended) from the AM process – see for example Figure 3 and Figure 7. On the other hand, wall thicknesses analysis showed minimum and maximum wall thickness of around 0.25 mm and 7.5 mm respectively for the winding coils part, and a wall thickness mostly between 0.25 mm and 5 mm for the chess rook artifact from Figure 4.

The overall dimensional measurements for single features of inner geometries show consistency with the R&R measurement tests performed in the laboratory by different operators, and by evaluating the single measurement features with two different methods (iso-surface threshold, and dynamic gradient threshold). This is reflected by the small deviations between the respective measurement values reported by two different users (less than 5 μm), and also the small differences (less or approx. equal to 8 μm in the majority of the cases) between measurements computed by two different software. Although there were some exceptional reported cases with bigger deviations, the majority of the CT comparable measurements have differences falling within the claimed uncertainties of around 4 to 8 μm for modern microfocus CT systems.

ACKNOWLEDGMENTS

The authors would like to express their appreciation to Carl Zeiss Industrial Metrology, LLC, for providing the CT measuring machine and Calypso software, and to Volume Graphics GmbH for providing VGStudio MAX. This study could not have been completed without their collaboration.

REFERENCES

[1] Kruth J. P., Bartcher M., Carmignato S., Schmitt R., De Chiffre L., and Weckenmann A. Computed tomography for dimensional metrology. CIRP Annals, Manufacturing Technology 60 (821-842), 2011.

[2] Villarraga H., Morse E. P., Hocken R. J., and Smith S. T. Dimensional metrology of internal features with X-ray computed tomography. Proc. of ASPE Annual Meeting, Vol 59, 2014.

[3] Firsching, M., Nachtrab, F., and Uhlmann, N. Concept for a nanometer-resolution X-ray computed tomography system for non-destructive testing based on room temperature semiconductor detector modules. Nuclear Science Symposium and Medical Imaging Conference (NSS/MIC), IEEE, October, 2012.

[4] Holler M., Diaz A., Guizar-Sicairos M., Karvinen P., Färm E., Härkönen E., Ritala M.,Menzel A., Raabe J., and Bunk O. X-ray ptychographic computed tomography at 16 nm isotropic 3D resolution. Scientific Reports 4: 3857, 2014.

[5] Holzner C., Feser M., Vogt S., Hornberger B., Baines S. B., and Jacobsen C. Zernike phase contrast in scanning microscopy with X-rays, Nature Physics, 883-887, 2010.

[6] Reinhart C, Industrial computer tomography – A universal inspection tool. 17th World Conference on Nondestructive Testing, Oct 2008, Shanghai, China.

[7] Reinhart C., Poliwoda T, Guenther T., Roemer W., Maass S., and Gosch C. Modern voxel based data and geometry analysis software tools for industrial CT. 16th World Conference on Nondestructive Testing, 2004, Montreal, Canada.

[8] Lettenbauer H., Lotze A., and Kunzmann S. Method and device for identifying material boundaries of a test object, Patent US 8,045,806 B2. Oct, 25 2011.

[9] Villarraga H., Thousand J. D., Morse E. P., and Smith S. T. CT Measurements and their estimated uncertainty: The significance of temperature and bias determination. Proc. of 15th International Conference on Metrology and Properties of Engineering Surfaces, Charlotte, NC 2015.

[10] Lettenbauer H., Georgi B., and Weiß D. Means to Verify the Accuracy of CT Systems for Metrology Applications (In the Absence of Established Internation al Standards), International Symposium on Digital industrial Radiology and Computed Tomography, Lyon, France) pp 25–7 2007.

[11] Gupta S. V. Measurement Uncertainties: Physical Parameters and Calibration of Instruments, Berlin Heidelberg, Springer-Verlag, 2012.

[12] Bonamente M. Statistics and Analysis of Scientific Data, New York, NY Springer, 2013.

[13] Dietrich C. F. Uncertainty, Calibration and Probability. Boca Raton, FL, Taylor & Francis Group, 1991.

Authors Index

Aanaes, Henrik 95
Ameta, Gaurav. 129
Aminzadeh, Masoumeh 151
Anderson, Andrew T.. 58
Arroave, Raymundo. 106
Ayas, Can 15
Bao, Chao*
Bartkowiak, Tomasz 77
Bate, David J. 110
Battaile, Corbett C. 22
Bauza, Marcin B. 54
Beaucamp, Anthony Tadeus 141
Bergmann, André 5, 59, 83
Bhogaraju, Raghuram 54
Biyikli, Emre. 32
Blacker, Ted D.. 22
Boulware, Paul C. 46
Boyce, Brad 22
Bremen, Sebastian 136
Browar, Allison Eileen Marie 72
Brown, Christopher A.. 77
Burns, Stephen J. 72
Caballero-Ruiz, Alberto 160
Castro-Espinosa, Homero 160
Charlton, Phillip 141
Charney, Steven P.. 164
Chen, Yanqiu*
Clark, Brett W. 22
Corbett, Taylor 116
Cronley, Lance. 46
Davies, Angela D. 47
Dehoff, Ryan R.. . . . . 54, 66
Deng, Yongqiang*
Eiríksson, Eythor R. 95, 147
Ellis, Jonathan D.. 72
Elwany, Alaa 106
Farouk, Tanvir 155
Ferencz, Robert M. 58
Firestone, Greg 46
Galovskyi, Bogdan. 89
Gerlitzky, Georg 83
Goudsmit, Frans-Willem 10
Graf, Benjamin. 5
Graziano, Arthur A. 141
Green, William E. 72
Gridin, Watalij 59
Hansen, Hans Norgaard 77, 147
Harrysson, Ola L. A. 40
Hausotte Dr.-Ing., Tino Rene 89
Herderick, Edward C. 4
Hodge, Neil E.. 58
Hyde, Joyce. 77
Jain, Samyak 141
Jamshidinia, Mahdi 46
Jared, Bradley H.. 22
John, Patrick 83
Jones, Jason 122
Kamath, Chandrika 58
Karaman, Ibrahim 106
Kashveko, Vasyl. 83
Kelly, Shawn M.. 46
Kersting, Robert 5
Khairallah, Saad A.. 58
Khanna, Maneesh 3
King, Wayne E. 58
Kirka, Michael M. 54, 66
Knoop, Frederick 26
Kumstel, Judith 136
Kurfess, Thomas R.. 151
Land II, William Stafford 47
Lane, Brandon M. 123
Lau, Woon-Ming*
Lee, ChaBum 36, 116, 155, 164
Lee, Sun-Kyu 36
Leggett, Perry 47
Lehner II, James T. 77
Lim, Hojun. 22
Lipman, Robert 129
Liu, Yu*
Love, Lonnie E. 54
Lowe, Larry E. 54
Mahamud, Rajib 155
Marchal, Jacob 46
Maskery, Ian 159

**** No Abstract Available***

McDonough, Jake 17
Medina, Frank 66
Mei, Jun*
Moussa, Khalil 17
Moylan, Shawn P. 100, 123, 129
Namba, Yoshiharu Y 141
Nguyen, Hop 17
Oosterhuis, Gerrit 10
Pedersen, David Bue 77, 95, 147
Peijnenburg, Antonius T. 10
Reichert, Connie 46
Rethmeier, Michael 5
Richardson, Bradley S. 54
Robbins, Joshua 22
Ross, Ingo 136
Rubenchik, Alexander 58
Ruiz-Huerta, Leopoldo 160
Sames, William 66
Schoeppner, Volker 26
Smith, Stuart T. 116, 164
Srinivasan, Harshad 40
Stempky, Travis 46
Tang, Changyu*
Tarbutton, Joshua 36, 116, 155, 164
Taylor, John S. 70
To, Albert C. 32
Tran, Hy D. 22
Tummala, Praveen 17
Uhlmann, Eckart 5, 59, 83
van Keulen, Fred 15
Vega-Alvarado, Leticia 160
Villarraga-Gómez, Herminso 116, 164
Wang, Xue 32
Wang, Zhijie 77
Whitenton, Eric P. 123
Willenborg, Edgar 136
Witherell, Paul 129
Wysk, Richard 40
Xu, Keqin*
Yan, Hui*
Yañez-Sanvicente, Roque 160
Zhan, Hao-ran*
Zhang, Bin 47
Ziegert, John C. 47

**** No Abstract Available***

Volume 60
ISBN 978-1-887706-67-4